Study of the Electronic Structure of InSb by Electron Spectroscopy

Thesis submitted in accordance with the requirements of the University of Liverpool for the degree of Doctor in Philosophy by Abdulrahman N Al Sawi.

April 2017

Study of the Electronic Structure of InSb by Electron Spectroscopy

Abdulrahman N Al Sawi

Abstract

III-V semiconductors continue to receive great scientific and technological attention as photodetectors and emitters, photovoltaic materials and electronic components. Better understanding of their fundamental electronic structure might lead to improvements in their performance.

Electron spectroscopy is inherently sensitive to the electronic structure, and using atomic structure calculations as a mean of interpreting spectroscopic results in terms of local atomic charge and atomic core hole screening has proven to provide insight in charge transfer between atoms in binary alloys and the polarisability of the surrounding medium.

This work employs the potential model developed by Cole, Gregory, and Weightman to interpret the chemical shifts of the binding energies of photoelectrons and the kinetic energies of the Auger electrons of In and Sb between their solid elemental samples and InSb. The value of the charge transfer was found to be 0.25 ± 0.41 of an electron from In to Sb; in close agreement with other studies. The value of the core hole screening length was found to be 1.75 ± 0.05 Å which is $\sim 20\%$ larger than half the inter-nuclear distance in InSb, a value which arises from the low concentration of charge carriers and the polarisation of the nearest neighbour ions.

By this finding, a new approach to the study of the electronic structure of III-V semiconductors has been established which can be extended to include II-VI and other semiconductors.

Acknowledgements

This work would not have been accomplished without valuable contributions from many people to whom I express my deepest gratitude.

First of all, I thank my parents for their unlimited love, and prayers. I also thank my wife Hajar for her love and support, and my son Moayad who asked me every time I collected him from school: how was your work? And how was your university?

I am also thankful to my sponsor; Qassim University of Saudi Arabia.

Prof Peter Weightman, my supervisor, has always made me feel welcome, and dedicated a lot of time and effort to my project. For this I express sincere thankfulness.

I acknowledge the contribution of my collaborators in providing the spectroscopic results described in this work; Dr Paul Unsworth who provided the results of In, Sb and Sb/InSb, and Dr David Hesp of the Stevenson Institute for Renewable Energy, University of Liverpool, who carried out the experiment of InSb under the direction of Dr Vin Dhanak and Dr Tim Veal. I also thank the Department of Physics of The University of Warwick, who provided the InSb specimen.

I finally thank members and students of the Department of Physics of The University of Liverpool, who always offered their greetings and wishes, particularly Dr Caroline Smith, Paul Harrison, Dr David Joss the Director of Postgraduate Research at the Faculty of Science and Engineering, and Dr Jon Coleman.

Contents

List of Figures

Glossary

Atomic relaxation: Reorganisation of electrons in an atom as a consequence of the creation of a core hole.

Auger electron spectroscopy (AES): The spectroscopic study of the kinetic energies of the electrons emitted by the Auger process.

Auger parameter (AP): The sum of the kinetic energy of the strongest Auger transition, in an electron spectrum, and the binding energy of the strongest photoelectron peak.

Auger process: The emission of an electron by the energy from an irradiative atomic transition.

Central field approximation (CF): An approximation of the many-electron atom problem, wherein each electron is assumed to evolve independently in a spherically symmetric field due to the nucleus, and a spherical average of other electrons charge distribution.

Chemical shift: A shift of the energy of an Auger electron, a photoelectron, or the value of the Auger parameter, between different chemical states.

Electron Spectroscopy for Chemical Analysis (ESCA): Using the shifts of the XPS and AES values to distinguish different chemical states.

Extra-atomic relaxation: Reorganisation of electric charges in the surroundings of an atom as a consequence of the creation of a hole in the core of the atom.

Hartree-Fock method (HF): The application of the CF with taking into account the antisymmetry of the atomic wave function.

Irradiative transition: The transition of an electron from an atomic level to a lower one without emitting a photon.

Multi-configuration Dirac-Fock Method (MCDF): A method of calculating the atomic structure using the HF with the relativistic corrections made by Dirac, and including all possible electron configurations.

Peak fitting: The construction of a model of synthetic peaks to fit all the XPS and AES components in a spectrum.

Screening: Blocking an atomic core hole by atomic and extra-atomic relaxation.

Screening length: The distance from a core ionised atom, after which the core hole charge is obscured.

Self-consistent field approximation (SCF): An iterative method of solving the Schroedinger equation by initialising a guess of the basis set to form an initial Hamiltonian, and then solving the individual set of Schroedinger equations simultaneously. The individual solutions are used to update the initial Hamiltonian. This is repeated until the final solutions converge.

X-ray photoelectron spectroscopy (XPS): The spectroscopic study of the energies of the electrons emitted from a certain material by the photoelectric process induced by x-ray.

Chapter 1
Introduction

1.1. Introduction:

Electron spectroscopy is a useful technique for obtaining information about the structure of atoms and their surrounding environments [1-3]. It involves the analysis of the kinetic energy spectrum at which electrons are emitted from a sample when it is bombarded by x-rays or electron beams of a known energy. The energies of the emitted electrons depend on the energy of the excitation source and the energy with which the electrons are bound in the sample (the binding energy BE). This is described by Einstein's equation for the photoelectric effect [4]:

$$KE = h\nu - BE \qquad (1.1)$$

where KE is the kinetic energy with which the electron is emitted, $h\nu$ is the energy of the excitation source (an x-ray photon in this case), and BE is the binding energy.

BE depends on the structure of the atom and the interaction between the atom and the surrounding medium i.e. the atomic levels of a particular element are affected by the chemical state of this element; hence the electron spectroscopy is sensitive to the chemical state. BE is determined by three factors:

a) The structure of the atom [3, 5-7].
b) The Coulomb interaction between the atom and the neighbouring atoms [1, 7].
c) The change of the electrostatic energy of the system (the studied atom and the atoms around it) after the emission of the electron [3, 7]. This is called the relaxation energy (R) which increases the kinetic energy of the emitted electron. Therefore, the value of BE obtained by (Eq.1.1) is less than the amount by which the electron is bound in the sample by the value of R.

There is no direct way of distinguishing the contributions of the three factors (a, b, and c) to the value of BE. However, when the technique (electron spectroscopy) is applied to free atoms, as in a vapour for example, then the factors b and c are eliminated and BE is considered to be dependent on the intrinsic state of the atom only ($BE_{free\ atom}$) [8-11]. Then, when the technique is also applied to the atom (of the same element) within a medium (interacting with other atoms either in single vaporous molecules or in a condensed state), the factor a can be eliminated by subtracting $BE_{free\ atom}$ from the resulting BE [8-11]. The task, then, becomes the finding of a mathematical model that distinguishes the effects of factors b and c. Such a model would provide information about the electronic structure of the sample. Many models [7, 12, 13] have been proposed and refined since the development of electron spectroscopy by Siegbahn and co-workers [3, 7, 14]. Among the models is the one developed by Cole, Weightman and co-workers [11, 15, 16] which yielded good results for the valence atomic charge and the relaxation energy in metallic Na, Mg and Zn [11]. The key step towards the development of such a model was turning the problem from investigating the contributions of the factors a, b and c to the value of BE into investigating the contributions of changes of b and c to the change of BE (ΔBE) between two chemical states of the same element i.e. applying the electron spectroscopy to an element in two different chemical states, then analysing the differences of BE between the two states. Employing the gaseous state (as explained above) is an example.

In this work, the model developed by Weightman, Cole and co-workers as reported in [15] is used to interpret the electron spectroscopy measurements of ΔBE for indium and antimony between their pure elemental metallic states and their states in the InSb semiconducting compound.

In summary, the aim of this chapter is to explain four aspects and how they are linked together to be used in the analysis of electronic structure of matter. These aspects are:

- Electron spectroscopy.
- Atomic structure calculations.
- A model that links the spectroscopic results to the electronic structure of solids (or other many-atom media) through the atomic structure calculations.
- Potential applications of such a model in understanding the fundamental electronic structure of III-V semiconductors (and other compound semiconductors).

This work establishes a method by which information about the electronic structure of a many-atom system is derived from the study of electrons emitted from the cores of the constituent atoms.

1.2. The development of electron spectroscopy as a probe of electronic structure in solids:

The basis of electron spectroscopy is the photoelectric effect which involves the ejection of an electron from a material by the interaction with a photon. The phenomenon was explained by Einstein [17] (Eq.1.1). If the energy of the electromagnetic source $h\nu$ is known and the kinetic energy of the photoelectron KE is measured, information about the energy levels of the emitting atom can be deduced. This leads to the identification of the constituent elements of the material and their chemical states since the atomic energy levels are sensitive to the surrounding medium as mentioned in (Sec.1.1)

Kai Siegbahn and his group pioneered the advancement of XPS, at the beginning of the second half of the last century [3, 14], by improving resolution of the measurements of the energies of the emitted electrons. They discovered that x-ray photoelectron spectroscopy is sensitive to the chemical state of the elements and used the name ESCA, Electron Spectroscopy for Chemical Analysis.

XPS has received wide interest as a non-destructive surface analysis technique. The sampling depth (the depth at which a measureable portion of the emitted electrons escape from the sample without losing energy) depends on the kinetic energy of the electron and on the structure of the sample. The sampling depth is around $100\ \text{Å}$ for Al $K\alpha$ x rays whose energy is $1486.6\ eV$ [7]. Such a depth can be considered within the bulk of the material, therefore photoelectron (and Auger) peaks contains surface and bulk sensitive components as seen in the spectra in (Ch. 4,5). The escape depth becomes higher if a higher energy source is used. The escape depth varies with the emission angle where the normal emission ($0°$ degrees from the normal on the surface of the specimen) is the least sensitive to the surface. This adds an analytical feature to the electron spectroscopy which is the depth profiling (how the structure of the sample changes with depth).

XPS also has a quantitative property as the intensities of the peaks are proportional to the concentration of the constituent elements. There is, however, a certain limit of atomic concentration less than which an element cannot be detected. This is called the detection limit and it is 0.1-1% [7].

1.2.1. X-ray photoelectron spectroscopy XPS:

The relation between the kinetic energy of the emitted electron (KE) and its binding energy (Eq. 1.1) must be corrected to include the instrument work function which is the energy difference between the Fermi level of the instrument and the vacuum level [7] (Sec.1.2.4):

$$KE_i = h\nu - BE_i - \phi_i \qquad (1.2)$$

where KE_i is the kinetic energy of the photoelectron ejected from the ith atomic level, BE_i is the binding energy of the ith electron referenced to the Fermi level, ϕ_i is the instrument work function. (Eq. 1.2) applies for a conducting sample in contact with the instrument to prevent accumulation of electric charge on the surface of the specimen, which changes the value of the measured KE_i. For non-conducting samples a correction may be needed for surface charging.

1.2.1.1 Theoretical explanation of the binding energy:

Electron spectroscopy involves the ejection of a core electron i using an x-ray or electron source of a known energy. So, by measuring the kinetic energy KE_i of the ejected electron its binding energy BE_i can be directly calculated. A simple relation for KE_i and BE_i was first proposed by Koopmans where BE_i is equal to the eigenvalue of the ith electron:

$$BE_i = h\nu - KE_i = -\epsilon_i \qquad (1.3)$$

where ϵ_i is the eigenvalue of the ith electron (in the ith orbital defined by the nlj quantum numbers as described in (Sec.1.2.3). BE_i is conventionally taken as positive, hence the (–) sign before the negative eigenvalue ϵ_i. The relation between the measured kinetic energy and the core atomic level made the x-ray photoelectron spectroscopy XPS a useful tool in identifying the elemental constitution of the measured sample.

Koopmans' theorem employs the frozen orbital approximation [3] in which the spectator electrons left in the atom after photoemission do not respond to the change in the atomic potential by the creation of a hole state. Koopmans theorem of the binding energy was found to disagree with the experimental results apart from those of the outermost electrons [3]. That is, due to screening by the core electrons, the effective nuclear potential felt by the valence electrons is much reduced and these electrons are not as sensitive to changes in the occupation of core orbitals as are the more bound electrons [3].

The value of ϵ_i in (Eq. 1.3) results from solving the Schroedinger equations of each electron in the atom simultaneously in the self-consistent field method SCF described in (Sec. 1.3.1.1).

Due to employing the frozen orbital approximation, Koopmans interpretation of the binding energy failed to account for the relaxation of spectator electrons (R^a). R^a is called the atomic relaxation, and arises from the decrease of the energies of the spectator electrons. This energy is added to the KE of the emitted electron making the BE smaller. R^a is larger in the case of the emission of a core electron since more outer electrons are affected. By taking the relaxation into account, BE_i is rewritten as follows [3]:

$$BE_i = -\epsilon_i - R_i^a \qquad (1.4)$$

R_i^a can be accounted for (in the atomic structure calculations) by defining BE_i in (Eq. 1.4) to be equal to the difference in the total energy of the atom of N electrons before photoionization calculated by the SCF method (Sec.1.3.1.1) and the total energy of the ion of $(N-1)$ electrons:

$$BE_i = ETOT_{(N-1)} - ETOT_{(N)} \qquad (1.5)$$

(Eq. 1. 4, 5) apply for a free atom, in the case of a vapour for example. However, in the case of solids and molecules the extra-atomic relaxation significantly reduces the value of BE_i which is written as follows [3]:

$$BE_i = -\epsilon_i - R_i^a - R_i^{ea} \qquad (1.6)$$

where R_i^{ea} is the extra-atomic relaxation which is defined as the response of the surrounding environment to the creation of the core hole. The significance of R_i^{ea} is appreciated when the chemical shift of BE between two different environments is studied.

The energy of the photoelectron is described to have initial and final state effects. The former is determined by the structure of the atom and its interaction with the surrounding environment (before the emission), and is expressed by the eigenvalue of the electron (ϵ_i in (Eq.1.6)). Whereas, the final state involves the screening of the hole left after the emission by the atomic and the extra-atomic relaxations.

1.2.2. X-ray excited Auger electron spectroscopy AES:

A second type of x-ray excited electron spectroscopy is the Auger electron spectroscopy. The kinetic energy of the electron emitted by the Auger process is characteristic of the emitting atom and independent of the x-ray source as explained in the following section.

1.2.2.1. Theoretical explanation of the Auger kinetic energy:

The excited atom left following a photoemission event decays by either radiating an x-ray photon, or by a non-radiative transition where an outer electron fills the hole and gives its energy to another electron which is ejected with a kinetic energy characteristic of the atom

(Fig. 1.1). The latter process is called the Auger process which is known to be significantly more sensitive to the chemical environment than photoemission because its final state (the state of the system after the emission) involves the existence of two holes in contrast to one hole in the final state of photoemission.

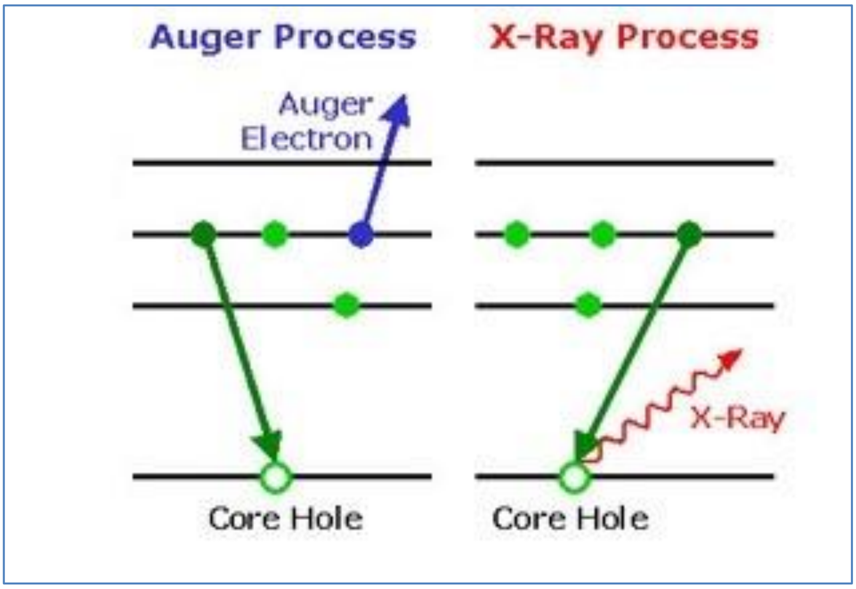

Fig. 1.1. Schematic of the two processes by which a core hole state decays. Right is the emission of an x-ray photon. Left is the non-radiative transition the energy from which is used to eject another electron (Auger). Source: http://www.lpdlabservices.co.uk/ analytical _techniques/surface_analysis/aes.php

By equivalence to (Eq. 1. 5) the kinetic energy of the Auger electron is calculated as the difference in total energy between the initial and final state of the atom. The initial state of the Auger process is the relaxed atom after the creation of a core hole in the i level by electron emission and the final state is an atom having two holes; a hole in j level from which an electron filled the original hole in i level, and a second hole ejected from k level by $i - j$ transition energy. Therefore, the kinetic energy of the electron emitted by the Auger process involving the ijk levels is:

$$KE(ijk) = ETOT_{ion}(i) - ETOT_{ion}(jk) \qquad (1.7)$$

where $ETOT_{ion}(i)$ is the total energy of the ion having a hole in level i and $ETOT_{ion}(jk)$ is the total energy of the ion having a hole in level j and a hole in level k. Similarly, using (Eq. 1.5), (Eq. 1.7) can be written as follows:

$$KE(ijk) = (ETOT_{ion}(i) - ETOT_{atom}) - (ETOT_{ion}(jk) - ETOT_{atom}) \qquad (1.8.a)$$

$$KE(ijk) = BE_i - BE_{jk} \qquad (1.8.b)$$

(Eq. 1.7, 8) shows that the Kinetic energy of the Auger electron is an atomic property and not affected by the source of the excitation.

From (Eq. 1.6) the kinetic energy of the Auger electron is written as follows:

$$KE(ijk) = (-\epsilon_i - R_i^a - R_i^{ea}) - \left(-\epsilon_j - \epsilon_k - R_{jk}^a - R_{jk}^{ea}\right) + U(jk{:}\,{}^{2S+1}L_J) \qquad (1.9)$$

U includes the Coulombic interaction between the j and k electrons as well as the spin-orbit coupling between the two holes left in j and k levels (Sec. 1.2.3). S and L are the total atomic spin and orbital angular momenta. J is the total atomic angular momentum. The term symbol ${}^{2S+1}L_J$ is explained in (Sec. 1.2.3). R_i^{ea} is the extra-atomic relaxation due to the creation of a core hole in level i. R_{jk}^{ea} is the extra-atomic relaxation due to the creation of holes in levels j and k. Relaxation is a change to the Coulombic interaction of the atom with the environment, hence R_{jk}^{ea} and R_i^{ea} are proportional to the square of the atomic charge [10, 18] which is equal to e^+ in the final state of a photoemission, and $2e^+$ in the final state of an Auger process. Therefore:

$$R_i^{ea} \propto (e^+)^2,$$

$$R_{jk}^{ea} \propto (2e^+)^2 \qquad (1.10)$$

Therefore, for a core-core-core Auger process (only core levels are involved) the extra-atomic relaxation is written as follows [19]:

$$R_{jk}^{ea} = 4R_i^{ea} \qquad (1.11)$$

Then (Eq. 1.9) can be rewritten as follows:

$$KE(ijk) = -\epsilon_i + \epsilon_j + \epsilon_k - R_i^a + R_{jk}^a + 3R_i^{ea} + U(jk{:}\,{}^{2S+1}L_J) \qquad (1.12)$$

In the central field approximation of the potential in the atomic core (Sec. 1.3.1.1) where the atom is assumed to be a charged sphere, the following expression applies to the shifts of the eigenvalues of core atomic levels [19]:

$$\Delta\epsilon_i = \Delta\epsilon_j = \Delta\epsilon_k \qquad (1.13)$$

The shift of the Auger kinetic energy between two chemical environments is then:

$$\Delta KE(ijk) = \Delta\epsilon_i + 3\Delta R_i^{ea} \qquad (1.14)$$

assuming that ΔR_i^a is negligibly small [18, 20]. This shows the great sensitivity of the shift in the core-core-core Auger electron kinetic energy to the difference in the chemical environment. Compare this to the shift of the binding energy of a core hole from (Eq. 1.6):

$$\Delta BE_i = -\Delta\epsilon_i - \Delta R_i^{ea} \qquad (1.15)$$

$\Delta\epsilon_i$ in (Eq.1.14, 15) is the shift of the core atomic levels between different chemical environments, whereas ΔR_i^{ea} is the change of the extra-atomic relaxation between the two environments. Since ΔR_i^{ea} is multiplied by three in (Eq.1.14), the shift of the Auger electron kinetic energy is more sensitive to the change in chemical environments than the shift of the photoelectron binding energy.

1.2.3. Energy levels and angular momentum coupling:

A one electron energy level is described by four quantum numbers n, l, m_s, m_j or alternatively n, l, j, m_j, where n is the principal quantum number which takes the values $1, 2, 3, \ldots$; l is the orbital angular momentum quantum number and takes the values $0, 1, 2, \ldots, n-1$; m_s is the spin magnetic quantum number which takes the values $\pm 1/2$; j is the total angular momentum quantum number ($j = l \pm 1/2$); m_j is the total magnetic quantum number and takes the values $-j, -j+1, \ldots, j$. To a first approximation, electrons that have the same n and l have the same orbital energies. However, photoelectrons that are emitted from the same shell nl are split into two XPS lines with different energies due to the spin-orbit coupling of the core hole left after the ejection of electron. Therefore, a full description of a photoelectric line is nlj. For example, $4f_{7/2}$ and $4f_{5/2}$ (Fig. 2.6) are photoelectric lines ejected from the subshells designated by $n = 1$, $l = 3$ and $j = l \pm 1/2 = 7/2, 5/2$. The $4f_{7/2}$ line has a higher kinetic energy than the $4f_{5/2}$.

In the Auger process three shells may be involved (Sec. 1.2.2.1) and the x-ray notation is used. Principal quantum numbers $1, 2, 3, \ldots$ are designated $K, L, M, \ldots$,. Subshells with a specific principal quantum number n are ordered in numbers from lower to higher energies. An Auger process designated as $M_4N_4N_4$ involves the emission of an Auger electron from the subshell $4d_{3/2}$ by an irradiative transition of an electron from the same subshell to fill a hole in $3d_{3/2}$.

The angular momenta of the two core holes left in the Auger process couple in different ways. Each of such ways results in a different total angular momentum of the final state of the atom leading to various final state energies. Therefore, an Auger process involving the same atomic levels produces a complex structure of multiple spectroscopic lines. This is called the multiplet splitting which is described below and dealt with in the spectroscopic analysis in (Ch.4, 5, 6).

The total atomic angular momentum is calculated by two different schemes, the $j-j$ and the $L-S$ coupling schemes. The latter is used to describe the profile of the Auger spectra of indium and antimony. In the $L-S$ scheme the total orbital angular momentum for the two holes L, and the total spin angular momentum S are calculated. Then, L and S are summed. This can be illustrated using the $M_{4,5}N_{4,5}N_{4,5}$ transition observed for In and Sb in this work. The total atomic orbital quantum number is:

$$\vec{L} = \overrightarrow{l_1} + \overrightarrow{l_2} = \vec{2} + \vec{2} = 0, 1, 2, 3, 4 \equiv S, P, D, F, G \qquad (1.16)$$

and the total atomic spin quantum number is:

$$\vec{S} = \overrightarrow{s_1} + \overrightarrow{s_2} = \frac{\vec{1}}{2} + \frac{\vec{1}}{2} = 0, 1 \qquad (1.17)$$

The total atomic angular momentum quantum number is:

$$\vec{J} = \vec{L} + \vec{S} = 0, 1, 2, \ldots., 5 \qquad (1.18)$$

Different values of the total angular momentum are designated by the so called term symbol ${}^{2S+1}L_J$ where S is the total spin quantum number, L is the total orbital quantum number, and J is the total atomic quantum number. The value of $2S+1$ determines the degeneracy on a specific orbital quantum number L. The most likely term symbol of an atom is that of the highest L and lowest degeneracy ($2S+1$). So, in the case of the above example ${}^1G_4$ component is expected to be of the highest intensity in the Auger profile. This was observed experimentally [10],[21].

1.2.4. The importance of the Auger parameter:

Measuring the chemical shifts of the binding energies of different samples and different experiments requires referencing them to a specific point in the energy scale that is independent to the sample [7]. In the following, the problem of referencing is explained, as well as how it is avoided by the concept of the Auger parameter.

The Fermi level of the instrument can be used as a reference point to the measured kinetic energies. An emitted electron loses energy that is equal to the work function of the specimen:

$$KE = h\nu - \phi_s - BE \qquad (1.19)$$

where KE is the measured kinetic energy, $h\nu$ is the energy of the x-ray photon, ϕ_s is the work function of the specimen, BE is the binding energy of the emitted electron which is the difference between the energy level from which the electron was ejected and the Fermi level (Fig.1.2). Making an electrical contact between a conducting specimen and the instrument makes their Fermi levels equal by flow of charge between one to the other. This cancels the effect of differences of the Fermi levels between different specimens on the measured KEs i.e. if the Fermi level of the specimen is initially higher than that of the instrument, then the electric contact will make electric charge flow from the specimen to the instrument. The opposite happens if the Fermi level of the specimen is lower than that of the instrument. Therefore, the electric contact neutralises the effect of the specimen work function, but leaves the experimentalist with a task of measuring the instrument work function (ϕ_i) (Fig1.2).

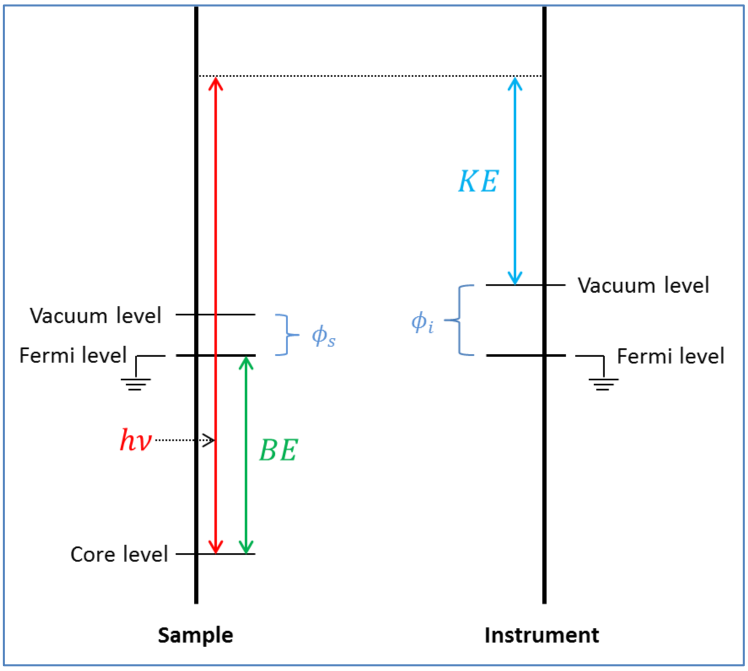

Fig.1.2. A schematic diagram of the energy levels of a conducting sample with an electrical contact with the instrument. The contact causes a flow of charge which makes the Fermi levels equal and leaves the specimen electrically charged. The electron needs an energy equal to the binding energy BE plus the instrument function ϕ_i to reach the vacuum level (becomes free to move). Both the instrument and the sample must be earthed to avoid the accumulation of charge which would cancel the change on the sample work function (text).

The kinetic energy of the emitted electron (Eq.1.19) is, then, rewritten as follows:

$$KE = h\nu - \phi_s - (\phi_i - \phi_s) - BE = h\nu - \phi_i - BE \qquad (1.20)$$

where ϕ_i is the work function of the instrument, $(\phi_i - \phi_s)$ is the difference between the work function of the instrument and that of the sample, which is called the contact potential [7] which is due to the charge on the specimen resulting from the contact with the instrument. Comparing (Eq.1.20) to (Eq.1.2), it can be said that the energy that an electron needs to reach the vacuum level (free to move) is equal to its binding energy added to the instrument work function (Eq.1.20). The method of measuring the instrument work function is shown in (Ch.2).

The instrument and the specimen must be earthed. Otherwise, the flow of charge between them causes accumulation of charge which would cancel the change of the Fermi level i.e. when a charge flows from the specimen to the instrument, its Fermi level is reduced leading to lower work function , but a positive charge would accumulate causing deceleration of the emitted electrons.

In the case of an insulating sample there are no free electrons, hence the Fermi level is not occupied. Moreover, an arbitrary amount of static electric charge accumulates on the surface of the specimen causing shifts to the measured energies. Therefore, a different referencing method is needed. This is addressed in (Ch.2).

The referencing problem causes uncertainty in the measurements of the KEs of the emitted Auger and photo-electrons. The uncertainty becomes greater when the chemical shifts of elements at different environments are studied, especially if the results are obtained at different instruments. Therefore, the concept of the Auger parameter (AP) was introduced by C. D. Wagner in 1971 [1] . AP is defined as the difference in KE between a strong photoelectric line and the highest peak in the Auger profile [7] (Fig.1.3):

$$\alpha = KE(C_1C_2C_3) - KE(C_1) \qquad (1.21)$$

The Auger parameter is independent of energy referencing or surface charging. (Eq. 1.21) can result in negative values, so C. D. Wagner introduced, in 1979 [1], a modified version of the Auger parameter by adding the photon energy of the excitation source [7]:

$$\alpha' = KE(C_1C_2C_3) - KE(C_1) + h\nu = KE(C_1C_2C_3) + BE(C_1) \qquad (1.22)$$

The work function correction and charge compensation cancels in (Eq. 1.22). The modified Auger parameter is characteristic of the studied material and independent to the energy of the x-ray used or to the instrument [18, 22]. The initial definition of the Auger parameter is abandoned; hence the symbol α is used for the modified version defined in (Eq.1.22).

The chemical shift of the Auger parameter is defined from (Eq. 1.14, 15) as follows:

$$\Delta\alpha = 2\Delta R^{ea} \qquad (1.23)$$

So, the shift of AP as defined in (Eq. 1.22) is sensitive to the change in the surrounding environment only [23].

Different definitions of the AP have been introduced to study different chemical features [1, 11, 24].

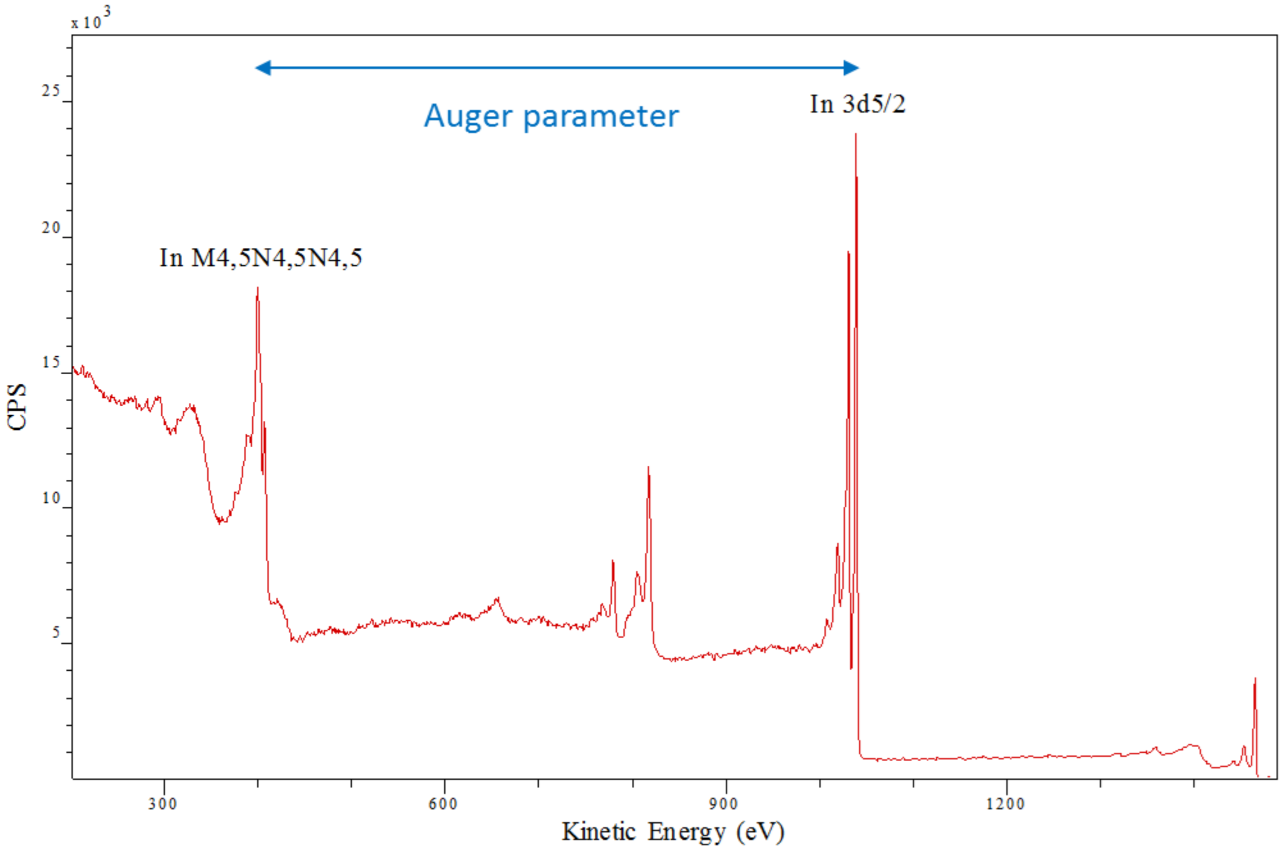

Fig.1.3. Kinetic energy spectrum obtained for a metallic indium foil. It shows the strong $3d_{5/2}$ photoelectric line and the $M_{4,5}N_{4,5}N_{4,5}$ Auger spectrum. The difference between the kinetic energy of $3d_{5/2}$ and the highest peak in $M_{4,5}N_{4,5}N_{4,5}$ is a characteristic Auger parameter value defined by (Eq.1.21). Such a value is independent to the referencing point, so it is appropriate for comparing the indium spectra taken for different samples and different instruments. All the features of this spectrum are analysed in (Ch.4, 5, 6).

1.3. Atomic structure calculations:

The main problem in the interpretation of chemical shifts is distinguishing between the factors that affect the value of the measured shift, which includes changes in valence charge and valence electron configuration and relaxation.

There is no way of directly measuring the values of valence charge and the relaxation. So, several approaches have been used to establish a theoretical link between the measured spectroscopic shifts and changes to the values of valence charge and relaxation through the atomic wavefunction calculations. Such calculations are far from straight forward, because of the interaction of the wave functions of the many electrons (within an atom) and many atoms. This is explained in this section.

1.3.1. The problem of the many-electron atom:

Since the beginning of the study of atomic structure using quantum mechanics by Schroedinger and Heisenberg, the electronic structure of matter has received great attention and many advances have been made in the treatment of this many-electron problem [25]. The Hartree-Fock self-consistent field (SCF) approach was a turning point by which the Schroedinger equation for a many-electron atom has been solved for all elements using computational methods. However, extending the calculation to condensed matter and complicated molecules faces the "exponential-wall problem" [25] where the number of bits required to solve the equations rises exponentially with the number of electrons.

The structure of matter at the atomic level can be thought of as a many-body problem which involves nuclei and electrons which are quantum mechanical objects that are described by Schroedinger equations. For a stationary nucleus in isolation from other nuclei the Schroedinger equation of an atom of N electrons is written as follows [26]:

$$\mathcal{H}\psi_{Atom} = E_{Atom}\psi_{Atom} \qquad (1.24a)$$

$$\mathcal{H} = \left[\sum_{i=1}^{N}\left(-\frac{\hbar^2}{2m}\nabla_i^2 - \frac{Ze^2}{4\pi\varepsilon_0 r_i}\right) + \frac{1}{2}\sum_{i=1}^{N}\sum_{j\neq i}^{N}\frac{e^2}{4\pi\varepsilon_0 r_{ij}}\right] \qquad (1.24b)$$

where ψ_{Atom} is the wave function of the atom, $\mathcal{H}$ is the Hamiltonian of the atom and E_{Atom} is the total energy of the atom. The Hamiltonian consists of three terms each of which is a sum over the number of electrons (N). The first term represents the kinetic energy; the second is the potential energy due to the Coulomb field of the nucleus which depends on its atomic number Z and on the distance r_i between it and the ith electron. The third term is the repulsive energy of all the pairs of electrons; r_{ij} is the distance between electron i and electron j [26]. The $\frac{1}{2}$ in the third term is to cancel the duplication in considering the interaction between each electron pair (ij and ji for example).

The electron-electron Coulomb interaction term prevents the separation of the Hamiltonian (Eq. 1.24b) into a set of one-electron Hamiltonians. Therefore, there is no analytical solution of (Eq. 1.24a). It cannot also be solved numerically without further assumptions due to the number of independent electron coordinates. Each electron will have a radial coordinate r and angular coordinates θ and φ. Thus for the Zn atom for example, which has 30 electrons, the solution to equation (Eq. 1.24a) will require a table with 90 dimensions. Thus with a rough grade of 10 entries per dimension, the table would have 10^{90} entries. Therefore, approximations were needed in order for the many-electron atom Schroedinger equation to be solved.

1.3.1.1: Hartree method:

In order to solve the problem of the many-electron atom Hartree formulated the independent particle model where each electron moves independently of all others in an average potential due to the nucleus and the average charge distribution of all other electrons. This leads to the Central Field (CF) approximation where each electron moves in a spherically symmetric field due to nucleus and spherical average of other electrons charge distribution. This enables the Schroedinger equation of the atom (Eq.1.24) to be rewritten with separable Hamiltonians:

$$\sum_{i=1}^{N}\left(-\frac{\hbar^2}{2m}\nabla_i^2-\frac{Ze^2}{4\pi\varepsilon_0 r_i}+V(r_i)\right)\psi_{Atom}=E_{Atom}\psi_{Atom} \qquad (1.25)$$

where $V(r_i)$ is the average potential affecting an electron i due to the repulsive Coulomb force of all other electrons [26]. The Hamiltonian in (Eq.1.25) can be separated into N Hamiltonians. Thus, the Schroedinger equation of the N-electron atom is separated into N Schroedinger equations in the following form:

$$\mathcal{H}_i\phi_{nl}(i)=\left(-\frac{\hbar^2}{2m}\nabla_i^2-\frac{Ze^2}{4\pi\varepsilon_0 r_i}+V(r_i)\right)\phi_{nl}(i)=\varepsilon_i\phi_{nl}(i) \qquad (1.26)$$

The second and the third terms in this single electron Hamiltonian are the average potential felt by individual electron i; and can be written together as:

$$V_i=-\frac{Ze^2}{4\pi\varepsilon_0 r_i}+V(r_i) \qquad (1.27)$$

The separation of the Hamiltonians enables writing the atomic wave function as a product of the single electron wave functions as follows:

$$\psi_{Atom} = \prod_{i=1}^{N} \phi_{nl}(i) \qquad (1.28)$$

$\phi_{nl}(i)$ is also called the spin orbital of electron i. The spin orbital is a function of the coordinates of electron i and is written as a product of three wave functions:

$$\phi_{nl}(i) = R_{nl}(r_i) Y_{lm_l}(\theta_i, \varphi_i) \chi_{m_s}(\sigma) \qquad (1.29)$$

where R_{nl} is the radial wave function which is determined by the principal n and the orbital l quantum numbers, Y_{lm_l} is the angular wave function which is described by l and the magnetic quantum number m_l, χ_{m_s} is the spin wave function which is determined by the spin magnetic quantum number m_s. Hartree did not include the spin function in his original method [27] and the Pauli principle was accounted for by not allowing more than two electrons to occupy an atomic orbital (Sec.1.3.1.2).

After the separation of the single electron Hamiltonians the task becomes to find solutions of the Schroedinger equations (Eq.1.26) that minimises the total atomic energy i.e. finding the ground state of the atom. The problem is that (Eq.1.26) cannot be solved for one electron (electron i for example) until the Hamiltonian is known, but the Hamiltonian cannot be known without knowing the wave functions of all other electrons which, in turn, depend on the wave function of the electron i ($\phi_{nl}(i)$). That is, the Schroedinger equation of each individual electron cannot be solved without knowing the charge distributions (electric fields) of the other electrons. The solution of this problem is to apply the Self-consistent Field (SCF) method proposed by Hartree in 1928 [27]. The first step of SCF is to guess initial values of all the individual wave functions (ϕ_{nl}) simultaneously. These wave functions are used to obtain initial individual Hamiltonians which can be written from (Eq.1.26) as follows [28]:

$$\mathcal{H}_i = -\frac{\hbar^2}{2m}\nabla_i^2 - \frac{Ze^2}{4\pi\varepsilon_0 r_i} + \sum_{j\neq i}^{N} \int \frac{|\phi_{nl}(j)|^2}{r_{ij}} d\tau_j \qquad (1.30)$$

This Hamiltonian contains the complete description of the energy of an electron in an atom having N electrons where the first term is the kinetic energy of the electron, the second term is the potential due to the electric field of the nucleus, the third term is the total potential due to all the other electrons. The integration in the third term is over the coordinates of an electron j. $|\phi_{nl}(j)|^2$ is the charge density of the electron j:

$$|\phi_{nl}(j)|^2 = \rho_j \qquad (1.31)$$

From (Eq.1.27) into (Eq.1.30):

$$\mathcal{H}_i = -\frac{\hbar^2}{2m}\nabla_i^2 + V_i \qquad (1.32)$$

V_i was defined in (Eq.1.27) as the average potential affecting electron i. To find the exact potential (Eq.26) must be solved [27]. By solving (Eq.1.26) for all electrons the total atomic energy is obtained as sum of the individual electron eigenvalues (ε) as follows:

$$E_{Atom} = \sum_{i=1}^{N} \varepsilon_i \phi_{nl}(i) - \frac{1}{2}\sum_{i=1}^{N}\sum_{j\neq i}^{N} \frac{e^2}{4\pi\varepsilon_0 r_{ij}} \qquad (1.33)$$

where the second term prevents accounting for the interaction between a pair of electrons twice.

By completing the first step of the SCF method N equations in the form of (Eq.1.26) are obtained of known values of ε_i. The second step is applying the variational principle to obtain the ground state of the atom (where E_{Atom} is minimum). It is out of the scope of this work to explain the underlying mathematics of the application of the variational principle; however it is achieved by differentiating each of the N equations and setting the values of the derivatives to zero. After that, these derivatives are solved together to find a new set of the individual electron wave functions $\phi_{nl}(i)$. If this new set is the same as that of the initial guess made in the first step (within some tolerance range), then the initial atomic wave function (ψ_{Atom}) is the ground state of the atom. Otherwise, the new values of $\phi_{nl}(i)$ are used to modify the initial guess, and the process is repeated. The process is iterated until the solution agrees with the guess of ψ_{Atom} . In this case, the solution is described to be self-consistent. The SCF marked a breakthrough in the atomic structure calculations which enabled the construction of various models to interpret the chemical shifts in the electron spectroscopy [3].

Although Hartree's approach was a success in terms of separating the Hamiltonian of the atom, it suffered from three major over-simplifications which are: neglect of the Pauli Exclusion Principle; the electron-electron correlation; and relativistic effects, especially for the cores of heavy atoms.

1.3.1.2: Hartree-Fock method:

As electrons are Fermions, no two electrons can occupy the same state at the same time. Therefore, the atomic wave function must be made antisymmetric to electron exchange i.e. it should change its sign when two electrons are exchanged. V. Fock introduced the antisymmetry to the atomic wave function through the Slater determinant (Eq. 1.34) which expresses the atomic wave function as a superposition of all possible electron-electron exchanges:

$$\psi_{Atom} = \frac{1}{\sqrt{N!}} \begin{vmatrix} \phi_1(1) & \phi_2(1) & \cdots & \phi_N(1) \\ \phi_1(2) & \phi_2(2) & \cdots & \phi_N(2) \\ \vdots & \vdots & \ddots & \vdots \\ \phi_1(N) & \phi_2(N) & \cdots & \phi_N(N) \end{vmatrix} \qquad (1.34)$$

$\phi_i(j)$ notation means describing the state of electron j by the coordinates (or the quantum numbers: n, l, m_l, m_s) of electron i. The Slater determinant equals zero if any ϕ_i equals ϕ_j [29] i.e. the one electron wave functions are orthogonal.

With the introduction of electron exchange to Hartree's method the Self-Consistent Field approach was known as the Hartree-Fock method. The SCF procedure described in (Sec. 1.3.1.1) applies to the Hartree-Fock wavefunction (Eq. 1.34). This is a lengthy process, but with the help of computer programs (such as the MCDFGME by Desclaux [30] used in this work (Sec. 2.4) it became a useful process and tabulations have been made for the orbital eigenvalues and relaxation, as well as different approaches in describing the extra-atomic relaxation for molecules and solids.

1.3.2: Major improvements to the Hartree-Fock method:

The underlying maths of the SCF method and the following improvements are complicated, but well established. This section discusses the major concepts that were used to improve the Hartree-Fock method. Understanding such concepts helps in interpreting the output of the atomic structure calculations made in (Ch.3, 7).

1.3.2.1. The relativistic corrections:

Relativistic corrections to the atomic Schroedinger equation lead to significant changes from the concept of electron spin to the fine structure and Breit energy as explained below. Fine structure was accounted for in atomic structure, before the application of relativistic corrections, by applying the Pauli theory [31].

The energy-momentum relation in special relativity is:

$$E = \sqrt{p^2c^2 + m^2c^4} \qquad (1.35a)$$

By Taylor expansion:

$$E = mc^2 + \frac{p^2}{2m} - \frac{1}{8}\frac{(p^2)^2}{m^3c^2} + \cdots, \qquad (1.35b)$$

where the first term is the rest energy, the second is the classical kinetic energy and the third is the relativistic correction to the kinetic energy which is taken as a first order perturbation to the Hamiltonian of the one electron state (Eq. 1.26). This leads to a breaking of the degeneracy in the principal quantum number n by a value which is dependent on the angular momentum [32]:

$$\langle \hat{H}_1 \rangle = -\frac{mc^2}{2}\left(\frac{Z\alpha}{n}\right)^4 \left(\frac{n}{l+1/2} - \frac{3}{4}\right) \qquad (1.36)$$

Z is the atomic number, l is the orbital quantum number, and α is the fine-structure constant:

$$\alpha = \frac{e^2}{4\pi\epsilon_0}\frac{1}{\hbar c} \simeq \frac{1}{137}$$

The value of the spin-orbit coupling is a relativistic entity which is described by adding the following term to the one electron Hamiltonian:

$$H_{s-o} = \frac{1}{4c^2}\frac{1}{r}\frac{dV}{dr}\hat{L}.\hat{S} \qquad (1.37)$$

where V is the central potential (Eq. 1.27), $\hat{L} = l(l+1)$ and $\hat{S} = s(s+1)$.

Further studies revealed that for heavy atoms the electron energy is best described by n and the total angular momentum number j rather than l. Whereas for most of the atoms the energy is evaluated by the intermediate scheme [31].

Relativistic corrections would clearly extend to hyperfine structure which results from coupling between the nuclear and electron orbital magnetic moments where the latter is a function of the angular momentum.

Another relativistic correction to the electron-electron interaction is the Breit interaction which is described by the following equation:

$$\hat{B}_{ij} = -\frac{1}{2r_{ij}}\left\{\alpha_i.\alpha_j + \frac{(\alpha_i.r_{ij})(\alpha_j.r_{ij})}{{r_{ij}}^2}\right\} \qquad (1.38)$$

which can be written as follows:

$$\hat{B}_{ij} = -\frac{1}{r_{ij}}\left\{\alpha_i.\alpha_j - \frac{1}{2}\left(\alpha_i.\alpha_j - \frac{(\alpha_i.r_{ij})(\alpha_j.r_{ij})}{{r_{ij}}^2}\right)\right\} \qquad (1.39)$$

where α_i and α_j are the Dirac matrices for electron i and j respectively. The first term of the Breit interaction (Eq. 1.39) is called the Gaunt interaction and the second term is a retardation interaction. The first is a magnetic interaction due to the exchange of a virtual photon and the second is due to the finite time of travel for the virtual photon carrying the Coulombic force between two electrons.

Relativistic treatment of the N-electron problem has involved tremendous theoretical work which lead to great precision in atomic structure calculations. This is manifested in (Ch. 8) where physically reasonable values of extra- atomic relaxation are obtained for metallic In and Sb and in (Ch. 9) which investigates the relaxation in InSb.

The first to introduce special relativity to quantum mechanics was Dirac, therefore the relativistic Hartree-Fock method is often called the Dirac-Fock method.

1.3.2.2. Lamb Shift:

The Lamb shift is a quantum electrodynamic (QED: a field that studies electromagnetic interactions) effect that is due to the interaction of electrons in the atom with the free space field. Due to the uncertainty principle, there is an electromagnetic fluctuations in free space which affect any quantum system and has to be taken into account by considering a single photon to be continuously created and annihilated. In the case of the atomic structure calculations, the electromagnetic fluctuations are taken into account by considering the electrons to continuously emit and absorb a photon. Lamb shift causes the energy levels of the same total angular momentum quantum number (j) and different orbital quantum number (l) to be different. This shift was first observed for the Hydrogen atom in which the levels $2s_{1/2}$ and $2p_{1/2}$ whose principal quantum number is the same ($n = 2$) and orbital quantum numbers are 0 and 1 respectively, and total angular quantum numbers are $1/2$ (hence of term symbols ${}^2S_{1/2}$ and ${}^2P_{1/2}$ as explained in (Sec.1.2.3)) to have different energies. Lamb shift mainly affects the energies of $l = 0$ orbitals making $2s_{1/2}$ orbital in hydrogen atom higher than $2p_{1/2}$ [33].

1.3.2.3. Electron correlation and configuration interaction:

The ionisation energies of light atoms calculated by the Hartree-Fock (HF) method tend to conflict with the measured data [34]. This is due to the adoption of the independent particle approximation explained in (Sec. 1.3.1.1) i.e. ignoring the electron correlation.

$$E_{correlation} = E_{exact} - E_{HF} \qquad (1.40)$$

where E_{exact} is the exact solution of the Schroedinger equation [34].

In reality, electron motions are correlated. The electron correlation is described as the change of the expected eigenstate of an electron $\phi_i(i)$ due to the presence of another electron in a specific eigenstate $\phi_j(j)$ [27].

One way of including electron correlation in the total energy is by writing the atomic wave function as a superposition of eigenfunctions of the type in (Eq. 1.34):

$$\Psi_{Atom} = C_0\psi_0 + \sum_{i=1}^{ND} C_i\psi_i \qquad (1.41)$$

where ψ_0 is the ground state of the atom constructed of the lowest spin-orbitals ($\phi_{nl}(i)$). i in (Eq. 1.41) denotes the ith excited atomic state. ND is the number of the excited states included in the atomic wavefunction Ψ_{Atom}. Increasing ND improves the accuracy of the determination of the correlation [27].

(Eq. 1.41) can be utilised to account for configuration interaction (CI). The excited states ψ_i involve one electron (or more) that is occupying a spin-orbital higher than those in the ground state. Configuration interaction is included by writing the atomic wavefunction as a superposition of atomic eigenstates in the form of (Eq. 1.41) with each eigenstate involving a specific number of excited electrons [27].

1.4. The development of using the atomic core potential shift in interpreting chemical shifts:

Chemical shifts of the energies of the Auger and photo-electrons contain contributions from changes to the *initial* and the *final* state of the emitting atom and the surrounding medium. The initial state (also called ground state) of the atom in a certain chemical environment involves the following aspects of the atom *before* the process of Auger or photo-emission:

a) the valence charge of that atom i.e. the amount of charge in the valence levels. This is not necessarily an integer multiplied by the charge of the electron since valence electrons can be shared between atoms,
b) the electron configuration,
c) the electrostatic interaction of the atom with the surrounding atoms.

Each of these three factors affect the electric potential in the core of the atom (Eq.1.27) leading to change to the binding energies, hence the energies of the emitted Auger and photo-electrons. The final state of the atom and the surrounding medium includes the atomic and extra-atomic relaxations as introduced in (Sec. 1.2.1.1). Relaxation can be defined as the change of the energy of the atom and the surrounding medium in response to the creation of a core hole (by photoelectron emission) or two core holes (by the Auger emission) (Sec.1.2.2.1). Relaxation is also called screening in that the spectator electrons left in the atom as well as the electric charges in the surrounding medium redistribute to screen the positive charge created in the emitting atom after the emission. So, screening can occur by the following processes:

a) atomic relaxation, where the electrons left in the emitting atom reduce their energy and become closer to the ionised core [16],
b) extra-atomic relaxation by either the attraction of an electron from the free electron gas (in the cases of a conducting or a semiconducting material) to the core-ionised atom, or change to the dipole moment of the neighbouring molecules [16].

Relaxation (the final state effect) also changes the potential in the core of the atom and hence, the binding energies of electrons. Therefore, these two relaxation processes as well as the three initial-state factors (a,b,c mentioned above) make five factors that contribute to the observed shifts of the kinetic energies of the Auger and photo-electrons between different chemical environments. Distinguishing between the contributions of these factors to the chemical shifts has been the subject of substantial amount of research [5, 7, 11, 24, 35]. Successful quantitative description of the contribution of each factor to the chemical shift would lead to knowledge in the electronic structure of materials. This involves knowledge of the valence charge in atoms (initial state effect), and charge mobility (which is related to the screening by free electrons), as well as the response of the environment to sudden creation of a positive charge (screening by change of polarisation). All such applications to the analysis of chemical shifts are discussed in (Sec.1.5).

A link has to be found between the chemical shifts in electron spectroscopy and the change to the electronic structure of the studied material. The most appropriate link is the electric potential in the core of the atom, because it is directly related to the observed energies of the emitted electrons and to the electronic structure of the medium [7]. These relations are explained as follows:

1- The potential in the core of the emitting atom determines the binding energies of electrons (as explained in the atomic structure calculations (Sec.1.3.1.1)), and hence the energies with which Auger and photo-electrons are emitted.

2- The wave function of an atom changes by interacting with other atoms in a molecule or a condensed matter. This interaction makes the structure of the atom and hence the potential in its core sensitive to the structure of the surrounding medium.

The atomic structure calculations as overviewed in (Sec.1.3) have been used to formulate theoretical models that link the chemical shifts in electron spectroscopy to changes of the electronic structure of the chemical environment through the atomic core potential as described above. Such models are known as the potential models and have seen advancements by the development of computer programs that perform the atomic calculations. Such advancements have led to the development of a model by a group based in the department of Physics at the University of Liverpool [15]. This model was refined through the last two decades of the twentieth century [5] and resulted in physically meaningful values for screening and valence charge (Sec.1.4.2). This model is implemented in studying the electronic structures of pure metallic indium (In) and antimony (Sb) as well as the $InSb$ compound semiconductor (Ch.7,8,9). The following section describes the model that was the first attempt to interpret chemical shifts in terms of electronic structure [7, 36]. The potential models stemmed from that first model [1, 11, 15].

It has been emphasized during the previous discussion that electron emissions that involve core electrons only are to be used as probes of the atomic wave function and the potential resulting from it. This is because such electrons do not interact with the neighbouring atoms, so their quantum states are solely described by the wave function of the studied atom [1].

1.4.1. The point charge model:

This early primitive model linked the shift of a core hole binding energy ΔBE_i (between two chemical environments) to changes in the atomic core potential ΔV due to the difference in valence atomic charge Δq and the point charges in the surrounding medium [7, 11]:

$$\Delta BE_i \approx \Delta V_i = \Delta V_{valence}(i) + \Delta V^{ea} \qquad (1.42)$$

where $\Delta V_{valence}$ and ΔV^{ea} are changes to the potential in the core of the atom due to change in valence charge and to the charges of the surrounding ions. $\Delta V_{valence}$ is written as:

$$\Delta V_{valence}(i) = k_i \Delta q \qquad (1.43)$$

where k (a constant obtained theoretically from atomic structure calculations) describes the change of BE_i caused by a change of amount e of the valence charge, and Δq is the difference in valence charge between the two environments. k is inversely proportional to the average radius of valence level:

$$k \approx 1/\langle r_i \rangle \qquad (1.44).$$

ΔV^{ea} is the shift in the Madelung potential (the electric potential due to the electrostatic interaction of the studied ion with the neighbouring ions [37]) evaluated by considering the ions in the surrounding medium as point charges.

$$\Delta V^{ea} = -e\Delta q \sum_j \frac{z_j^*}{R_j} \qquad (1.45)$$

where ($z_j^* e$) is the effective charge of the ion j which is equal to the charge of the nucleus added to the charge of the core electrons, and R_j is the distance between it and the atom from which the photoelectron is emitted.

The point charge model ignores the final state effects which dominate the binding energy shift in solids. Moreover, its dependence on BE makes it subject to referencing differences.

The shift of the core potential in (Eq. 1.42) is equated to the shift of the binding energy of a single electron on the basis that the charge of an electron $e = -1$ in the atomic units, and BE is considered to be positive.

1.4.2. The Auger parameter and screening analysis:

The advantage of using chemical shifts of the Auger parameter α rather than shifts in core hole binding energies was discussed in (Sec. 1.2.4). (Eq. 1.23) shows that the shift of the modified Auger parameter ($\Delta\alpha$) is sensitive to final state (screening) only.

By Taylor expanding the total atomic energy in the number of core holes (occupation number) [38], Thomas [19] was able to include the relaxation in the binding energy of a core hole [11]:

$$BE_i = V_i - \frac{1}{2}\left(\frac{\partial V_i}{\partial N}\right)_{N=0} + \frac{1}{6}\left(\frac{\partial^2 V_i}{\partial N^2}\right)_{N=0} - \cdots, \qquad (1.46)$$

Similarly for two core holes state:

$$BE_{ii} = 2V_i - 2\left(\frac{\partial V_i}{\partial N}\right)_{N=0} + \frac{4}{3}\left(\frac{\partial^2 V_i}{\partial N^2}\right)_{N=0} - \cdots, \qquad (1.47)$$

From this, Thomas [19] developed a model which links the shift of the Auger parameter $\Delta\alpha$ (Eq. 1.22) to the difference in screening between chemical environments as well as the difference in the valence charge Δq.

$$\Delta\alpha = \Delta\left[q\frac{dk}{dN} + \left(k - 2\frac{dk}{dN}\right)\frac{dq}{dN} + \frac{dU}{dN}\right] \qquad (1.48)$$

k describes the change of the core potential due to change of valence charge (Eq.1.43). Therefore, dk/dN describes how the creation of a core hole changes the dependency of core potential on valence charge. N is the number of core holes multiplied with -1. . dq/dN is screening of a core hole by the attraction of a free charge to the core ionised atom. dU/dN is screening of a core hole by polarisation of the medium. The introduction of (Eq. 1.48) made the problem of interpreting the chemical shifts mainly a matter of describing the shifts of the core hole screening. Shift in the intra-atomic screening between different chemical environments is negligible [15]. However, the extra-atomic screening is rather a subtle effect that has attracted a great deal of research.

Thomas and Weightman [39] corrected the value of k to account for the compression of the valence wavefunction in solids relative to free atom due to the interaction with the valence levels of other atoms within the Wigner-Seitz cell. The relation of the value of k in a solid material to its value in a free atom is:

$$\gamma = \frac{k_{solid}}{k_{atom}} \qquad (1.49)$$

The Thomas-Weightman model achieved success in studying charge transfer in binary alloys [39]. To apply the model to the analysis of auger parameter shift between a free atom and a metal, screening by polarisation of the surrounding medium (dU/dN) is cancelled from (Eq. 1.48), because screening in metals occurs by the attraction of a free electron to localised orbitals of the core-ionised atom [1]. Extra-atomic screening for a free atom is equal to zero. Therefore, (Eq. 1.48) is written for free-atom to metal shifts as follows:

$$\alpha_{metal} - \alpha_{atom} = \left(q_{metal}\frac{dk_{metal}}{dN} - q_{atom}\frac{dk_{atom}}{dN}\right) + \left(k_{metal} - 2\frac{dk_{metal}}{dN}\right)\left(\frac{dq}{dN}\right)_{metal} \qquad (1.50)$$

substituting (Eq. 1.49) in (Eq. 1.50) and considering valence charge of an atom in metal to be equal to the valence charge of a free atom ($q_{metal} = q_{atom}$) gives:

$$\alpha_{metal} - \alpha_{atom} = q\frac{dk}{dN}(\gamma - 1) + \gamma\left(k - 2\frac{dk}{dN}\right)\left(\frac{dq}{dN}\right)_{metal} \qquad (1.51)$$

where k is k_{atom} which is calculated from the atomic structure results (Ch.7).

Using experimental results for $\alpha_{metal} - \alpha_{atom}$ where α_{atom} is the for the element in gaseous state, and equating the value of $\left(\frac{dq}{dN}\right)_{metal}$ to unity due to screening by the attraction of a free electron to the core ionised atom (perfect local screening), γ was obtained empirically for metallic Mg, Zn and Na [15]. Empirical γ values for metals were found to be less than 1 which is unphysical given the shrinkage of valence level radius in solids which leads to $\gamma > 1$ according to (Eq. 1.44,49). Cole and co-workers [15] attributed the failure of the Thomas-Weightman model to the assumption of k being linear with N and independent to q. They constructed a new potential model through an investigation of the atomic structure calculations of Xe in terms of the eigenvalues of core levels, valence charge configuration and number of core holes. This model depends on the description of the core potential due to valence charge as follows:

$$V_{valence}(N_{nl}, q) = \int_0^q k(N_{nl}, q')\ dq' \qquad (1.52)$$

and describes k through five parameters:

$$k(N_{nl}, q) = a + bN_{nl} + cN_{nl}{}^2 + (d + eN_{nl})q \qquad (1.53)$$

where N_{nl} is the number of holes in the core level nl multiplied by -1, q is the valence charge. The parameters a, b, c, d and e are obtained theoretically using the Dirac-Fock calculations. From (Eq. 1.46, 47, 52, 53), [15] described the relation between the shift of the Auger parameter and the shifts in valence charge and screening as:

$$\Delta\alpha = \Delta\left\{qb + \frac{dq}{dN}\left[a - 2b + d\left(q - \frac{dq}{dN}\right)\right] + \frac{dV^{ea}}{dN}\right\} \qquad (1.54)$$

where the magnitudes of parameters c and e are negligibly small as seen for In and Sb in (Ch. 7).

This model has predicted values of screening (dq/dn) in Mg, Zn and Na metals close to 1 which is expected because of the attraction of an electron from the electron gas [11]. Similar results were found for metallic In and Sb (Ch. 8) by this work. The model was also applied to InSb, the III-V semiconductor, and predicted physically meaningful results of screening and valence charges (Ch. 9).

1.5. The Auger parameter analysis and development of compound semiconductors:

Analysis of the shifts of the Auger parameter (AP) is a type of fundamental research that provides answers to long lasting questions such as charge transfer between the constituent atoms in compounds (e.g. between In and Sb in InSb), and the screening distance around a core-ionised atom (how far from the ionised atom does the surrounding medium respond to the core hole charge (Ch.9)). Obtaining experimental values of these fundamental electronic properties holds potential applications in the field of the III-V, II-VI and other compound semiconductors [40, 41]. A new method of analysing AP based on the potential model described in (Sec.1.4.2) is applied to InSb which is a III-V semiconductor (Ch.9). Further research is expected to follow this method, and it is the plan in the Department of Physics of The University of Liverpool in collaboration with Stevenson Institute for Renewable Energy to carry out research depending on this work.

Some attempts have been already made to investigate the electronic structures of compound semiconductors using AP shifts [40-42]. [43] and [44] found a proportional relation between AP shift and band gap in compound semiconductors, and [45] reported proportionality of the band gap of compound semiconductors to charge transfer and anion electronegativity. Charge transfer is also linked to carrier mobility [16] .

The value of the Auger parameter in solids is dominated by the screening of core holes. Screening depends on the carrier density and the polarisability of the medium around the core ionised site. This provides a method of investigating doping, both in terms of the type of dopant and its concentration [46, 47]. Screening is also related to carrier mobility. Screening distance and the efficiency of local screening (the attraction of a free electron to the ionised atom) provide insight on how ions and defects are screened in the studied material, and hence how much the charge carriers are scattered (Coulomb scattering [48]).

The effect of doping can, also, be simulated using the equivalent cores approximation [40]. Core ionising the group III element of a III-V semiconductor is equivalent to doping with group IV element. Similarly, core ionising the group V element is equivalent to doping with group VI element.

The potential model can also be extended to buried interfaces and layered semiconductors [49]. Charge transfer occurs between layers across the interface where different screening mechanisms also exist. [50] Explained band structure at graphene compound-semiconductor interfaces depending on the amount of charge transfer.

1.6. Thesis structure:

This introduction (Chapter.1) explained the research problem which is finding a link between chemical shifts of electron spectroscopic values and the electronic structure of the studied materials through the electric potential in the core of the atom. This link required the explanation of the x-ray excited photoelectron spectroscopy (XPS) and the Auger electron spectroscopy (AES) as well as the concept of Auger parameter. The development of atomic structure calculations, since the early development of quantum mechanics through relativistic correction and configuration interaction, has been overviewed to the extinct needed to interpret the output of the atomic structure program MCDFGME. The mathematical model (the potential model) that will be used in interpreting spectroscopic results of In, Sb and InSb was also explained. Ch.7 includes the derivation of the potential model parameters in (Eq.1.53, 54) for In and Sb atoms using atomic calculations by MCDFGME and following the method explained in [15].

Chapter.2 explains the methods and techniques used in this work. This includes aspects about the electron spectroscopy and its instrumentation. This chapter also introduces CasaXPS; the program used in analysing spectra, and MCDFGME the atomic structure calculation program.

Chapter.3 explores the results of atomic structure calculations of the In and Sb atoms, by MCDFGME, using different methods. The calculations concentrate on the spectroscopic features important to this study. These are the In and Sb $3d$ and $4d$ photoelectric lines and the $M_{4,5}N_{4,5}N_{4,5}$ Auger transitions. The aim of this chapter is establishing good knowledge in the atomic structure calculations and how the total energy of the atom and the orbital energies of electrons are affected by different electron configurations and ionisations states. This knowledge is vital for both understanding the output of the MCDFGME program and how it was used in making the potential model, as well as future analysis of electron spectroscopic results and how they are affected by different bonding.

Chapter.4 contains an electron spectroscopic study of metallic elemental In and Sb. The Auger parameters of both elements are obtained to be used in (Ch.9) as explained below.

Chapter.5 thoroughly investigates the electron spectroscopic study performed on Sb/InSb sample. Cleaning and decapping procedure was followed through gradual heating processes of the sample up to $375\ ℃$. This procedure resulted in a clean In-rich surface of the Sb overlayer, but failed to expose the InSb underlayer.

Chapter.6 reports an electron spectroscopic experiment performed on an indium antimonide (InSb) sample. The sample was treated by Ar^+ ion bombardment at moderate energy followed by annealing. The APs of In and Sb in InSb obtained in this chapter are used together with the APs of metallic In and Sb (obtained in Ch.4) to investigate the electronic structure of InSb (Ch.9)

Chapter.7 involves the calculation of the five potential parameters for In and Sb to obtain two formulas in the form of (Eq.1.54). These formulas are used to evaluate screening and valence charge of metallic In and Sb (Ch.8) and of In and Sb sites in InSb (Ch.9).

Chapter.8 involves the application of the potential model [15] to metallic In and Sb. The model was found to predict nearly complete local screening (by the attraction of free electron from the free electron gas) for both elements, and valence charges close to those of free atoms (-3 and -5 for In and Sb, respectively). Such results are expected since both elements are metals. The model also predicts solid state parameter (γ) greater than one for the two elements. These results support the validity of the potential model used for predicting electronic structures of solids.

In (Ch.9) the model is used to predict local charge and screening mechanism of In and Sb atoms in InSb which is a more subtle problem, as will be seen, since InSb is a semiconductors, hence screening in it cannot be assumed to be completely local. However, reasonable results of local charges and screening distance were obtained which shows the potential of this model to advance the study of electronic properties of semiconductors.

References

1. Moretti, G., *Auger parameter and Wagner plot in the characterization of chemical states by X-ray photoelectron spectroscopy: a review.* Journal of electron spectroscopy and related phenomena, 1998. **95**(2): p. 95-144.
2. Suga, S. and A. Sekiyama, *Photoelectron spectroscopy: bulk and surface electronic structures*. Vol. 176. 2013: Springer.
3. Weightman, P., *X-ray-excited Auger and photoelectron spectroscopy.* Reports on Progress in Physics, 1982. **45**(7): p. 753.
4. Vickerman, J.C. and I.S. Gilmore, *Surface analysis : the principal techniques*. 2009: Chichester : Wiley, 2009. 2nd ed.
5. Weightman, P., *The Development of Auger Spectroscopy as a Probe of Local Electronic Structure.* Microscopy Microanalysis Microstructures, 1995. **6**(3): p. 263-288.
6. Cole, R., B. Macdonald, and P. Weightman, *Relative core level shifts in XPS: a theoretical study.* Journal of electron spectroscopy and related phenomena, 2002. **125**(2): p. 147-152.
7. Briggs, D. and J.T. Grant, *Surface analysis by Auger and x-ray photoelectron spectroscopy*. 2003, Chichester, West Sussex, U.K.: IM Publications. xi, 899 p.
8. Nefedov, V., et al., *Determination of effective atomic charge, extra-atomic relaxation and Madelung energy in chemical compounds on the basis of X-ray photoelectron and auger transition energies.* Journal of electron spectroscopy and related phenomena, 1988. **46**(2): p. 381-404.
9. Aksela, S., et al., *Free-atom—metal shifts in theM4,5N4,5N4,5Auger spectra of Ag, Cd, In, Sn, Sb, and Te.* Physical Review B, 1981. **23**(9): p. 4362-4368.
10. Pessa, M., et al., *Solid-state effects inM4,5N4,5N4,5Auger spectra of elements fromIn49toTe52.* Physical Review B, 1979. **20**(8): p. 3115-3123.
11. Cole, R. and P. Weightman, *Separating ground state and screening contributions to chemical shifts.* Journal of Physics: Condensed Matter, 1994. **6**(29): p. 5783.
12. Cole, R., J. Matthew, and P. Weightman, *Extra-atomic relaxation energy calculations using an extended potential model.* Journal of electron spectroscopy and related phenomena, 1995. **72**: p. 255-259.
13. Siegbahn, K., *ESCA applied to free molecules*. 1969: North-Holland Pub. Co.
14. Siegbahn, K., *Electron spectroscopy for chemical analysis*, in *Atomic Physics 3*. 1973, Springer. p. 493-522.
15. Cole, R.J., D.A.C. Gregory, and P. Weightman, *Analysis of Auger-parameter and XPS shifts: Application of potential models.* Physical Review B, 1994. **49**(8): p. 5657-5661.
16. Waddington, S.D., et al., *Charge transfer and core-hole screening in PbTe.* Physical Review B, 1989. **39**(14): p. 10239-10245.
17. Einstein, A., *Concerning an heuristic point of view toward the emission and transformation of light: Translation into English.* American Journal of Physics, 1965. **33**(5): p. 367.
18. Wagner, C., *Chemical shifts of Auger lines, and the Auger parameter.* Faraday Discussions of the Chemical Society, 1975. **60**: p. 291-300.
19. Thomas, T., *Extra-atomic relaxation energies and the Auger parameter.* Journal of Electron Spectroscopy and Related Phenomena, 1980. **20**(1): p. 117-125.
20. Guittet, M., J. Crocombette, and M. Gautier-Soyer, *Bonding and XPS chemical shifts in ZrSiO 4 versus SiO 2 and ZrO 2: Charge transfer and electrostatic effects.* Physical Review B, 2001. **63**(12): p. 125117.
21. Parry-Jones, A., P. Weightman, and P. Andrews, *The M4, 5N4, 5N4, 5 Auger spectra of Ag, Cd, In and Sn.* Journal of Physics C: Solid State Physics, 1979. **12**(8): p. 1587.

22. Gaarenstroom, S. and N. Winograd, *Initial and final state effects in the ESCA spectra of cadmium and silver oxides.* The Journal of Chemical Physics, 1977. **67**(8): p. 3500-3506.
23. Wagner, C. and A. Joshi, *The auger parameter, its utility and advantages: a review.* Journal of electron spectroscopy and related phenomena, 1988. **47**: p. 283-313.
24. Moretti, G., *The Wagner plot and the Auger parameter as tools to separate initial- and final-state contributions in X-ray photoemission spectroscopy.* Surface Science, 2013. **618**: p. 3-11.
25. Fulde, P., *Wavefunction-based electronic-structure calculations for solids.* Nature Physics, 2016. **12**(2): p. 106-107.
26. Froese Fischer, C., T. Brage, and P. Jönsson, *Computational atomic structure : an MCHF approach*. 1997, Bristol, UK ; Philadelphia, Penn: Institute of Physics Publ. xi, 279 p.
27. Kohanoff, J., *Electronic structure calculations for solids and molecules: theory and computational methods*. 2006: Cambridge University Press.
28. Gupta, V.P., *Principles and applications of ouantum chemistry*. 2016, Academic Press is an imprint of Elsevier,: London, UK. p. 1 online resource.
29. Woodgate, G.K., *Elementary atomic structure*. Oxford science publications. 1980: Oxford: Clarendon Press, 1980.2nd ed.
30. Desclaux, J.P., *A multiconfiguration relativistic Dirac-Fock program.* Computer Physics Communications, 1975. **9**(1): p. 31-45.
31. Grant, I., *Relativistic calculation of atomic structures.* Advances in Physics, 1970. **19**(82): p. 747-811.
32. Simons, B. *Advanced Quantum Physics*. 2009 06/09/2009 [cited 2016 01/04/2016]; Available from: http://www.tcm.phy.cam.ac.uk/~bds10/aqp.html.
33. Foot, C.J., *Atomic physics*. Oxford master series in physics. 2005, Oxford ; New York: Oxford University Press. xiii, 331 p.
34. Drake, G.W.F., *Springer handbook of atomic, molecular, and optical physics*. 2006, New York: Springer. lviii, 1504 p.
35. Darrah Thomas, T. and P. Weightman, *Valence electronic structure of AuZn and AuMg alloys derived from a new way of analyzing Auger-parameter shifts.* Physical Review B, 1986. **33**(8): p. 5406-5413.
36. Streubel, P., et al., *Chemical state information from photoelectron and Auger electron lines-investigation of potential and relaxation effects of solid silicon and phosphorus compounds.* Journal of electron spectroscopy and related phenomena, 1991. **57**(1): p. 1-13.
37. Kittel, C., *Introduction to solid state physics*. 8th ed. 2005, Hoboken, NJ: Wiley. xix, 680 p.
38. Lang, N. and A. Williams, *Theory of Auger relaxation energies in metals.* Physical Review B, 1979. **20**(4): p. 1369.
39. Thomas, T.D. and P. Weightman, *Valence electronic structure of AuZn and AuMg alloys derived from a new way of analyzing Auger-parameter shifts.* Physical Review B, 1986. **33**(8): p. 5406.
40. Weightman, P., *Auger spectroscopy and the electronic structure of semiconductors.* Journal of electron spectroscopy and related phenomena, 1998. **93**(1): p. 165-174.
41. Turner, N.H. and J.A. Schreifels, *Surface analysis: X-ray photoelectron spectroscopy and auger electron spectroscopy.* Analytical chemistry, 2000. **72**(12): p. 99-110.
42. Woodbridge, C., X. Gu, and M. Langell, *Extra-atomic relaxation energies and auger parameters of titanium compounds.* Surface and interface analysis, 1999. **27**(9): p. 816-824.
43. Moretti, G., *Relationship between the auger parameter and the energy gap.* Journal of electron spectroscopy and related phenomena, 1990. **50**(2): p. 289-293.
44. Mejias, J., et al., *Interpretation of the binding energy and auger parameter shifts found by XPS for TiO2 supported on different surfaces.* The Journal of Physical Chemistry, 1996. **100**(40): p. 16255-16262.
45. Zaanen, J., G. Sawatzky, and J. Allen, *Band gaps and electronic structure of transition-metal compounds.* Physical Review Letters, 1985. **55**(4): p. 418.

46. Dobler, D., S. Oswald, and K. Wetzig, *Changes of Auger Parameter in doped SnO.*
47. Egdell, R., et al., *Competition between initial-and final-state effects in valence-and core-level x-ray photoemission of Sb-doped SnO 2.* Physical Review B, 1999. **59**(3): p. 1792.
48. Kasap, S.O. and P. Capper, *Springer handbook of electronic and photonic materials*. 2006, New York: Springer. xxxii, 1406 p.
49. Jimenez, V., et al., *Interface effects for metal oxide thin films deposited on another metal oxide II. SnO 2 deposited on SiO 2.* Surface science, 1996. **366**(3): p. 545-555.
50. Xu, L., et al., *Interfacial Interactions of Semiconductor with Graphene and Reduced Graphene Oxide: CeO2 as a Case Study.* ACS applied materials & interfaces, 2014. **6**(22): p. 20350-20357.

Chapter 2

Methods and Techniques

2.1. Introduction:

Achieving the goal of probing the electronic structure of InSb using the method described in (Ch.1) required the use of two computer programs. The first is the CasaXPS program which is used to analyse and model the electron spectra to precisely determine the positions of the peaks and hence the values of the Auger parameters of In and Sb in their elemental metallic states and in InSb. The second program is the MCDFGME V 2005.10 [1] which was used to carry out atomic structure calculations of In and Sb atoms. The output of these calculations was used to derive the parameters of the potential model described in (Sec.1.4.2). This chapter illustrates the experimental aspects of electron spectroscopy first, then explains how the CasaXPS and MCDFGME programs were used.

Four sets of electron spectroscopic data were studied in this work. Three of these sets which were of the metallic In and Sb as well as Sb/InSb (antimony on indium antimonide) were obtained in the Oliver Lodge Laboratory of the Department of Physics at The University of Liverpool with help from Dr. Paul Unsworth. The fourth was of InSb and provided by Dr. David Hesp of Stevenson Institute for Renewable Energy at The University of Liverpool.

2.2. Electron Spectroscopy:

The theories of the Auger and photo-electron spectroscopy as well as the concept of the Auger parameter were explained in (Ch.1). This section explains the experimental setup of the electron spectroscopy in addition to the properties of the photoelectric line and the calibration of the energy scale of the spectrometer.

2.2.1. The experimental setup:

A typical XPS instrumental setup (Fig. 2.1) includes stainless steel specimen preparation and measurement chambers separated by valves and connected to a pumping system to provide ultrahigh vacuum. The preparation chamber can contain an ion gun used to sputter the surface of the specimen for cleaning or removal of the top layer of multilayer specimens.

An x-ray source (Sec.2.2.1.2) is connected to the measurement chamber where the specimen is analysed. Vertically above the specimen is the lens system which focuses the emitted electrons into the hemispherical analyser.

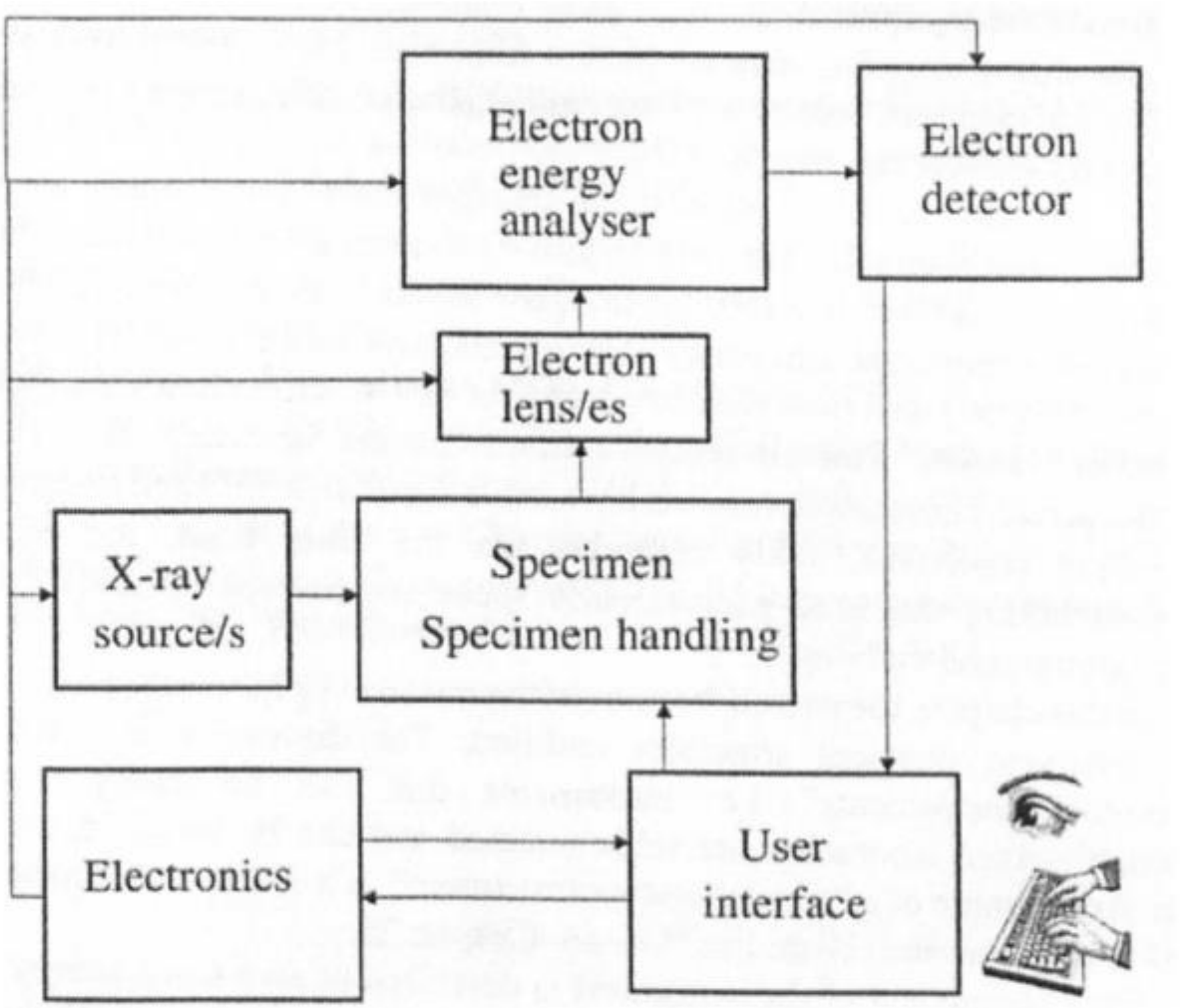

Fig. 2.1. A block diagram of the XPS instrument setup. The specimen is entered into the ultrahigh vacuum system where it is irradiated with x-ray. Part of the emitted electrons enters into a lens system which focuses them and adjusts their energy to chosen values. Then, electrons enter into the electrostatic energy analyser (concentric hemispherical analyser in this experiment) where they are guided to the detector slit. Diagram is taken form [2]

(Fig. 2.2) shows a photo of the VSW ESCA instrument at the Oliver Lodge Laboratory in which three of the specimens were scanned by this work.

2.2.1.1. The ultrahigh vacuum:

As electron spectroscopy is very surface sensitive, making the measurement in ultrahigh vacuum (UHV) is necessary to minimise surface contamination. In chemically active materials like metals, the formation of an oxide monolayer requires seconds in pressure of

10^{-4} Pa. A minimum pressure of 10^{-8} Pa needs to be maintained during the experiment to prevent oxidation [2]. Reducing the pressure below 10^{-8} Pa requires baking the instrument at ~ 200 ℃ to desorb water from the stainless steel walls. C and CO remain after baking.

Measurements of metallic In and Sb, and InSb were made at a pressure of 10^{-9} Pa. Clean specimen surfaces were achieved by Ar^+ ion bombardment of metallic In and Sb (Ch. 4). Sb/InSb specimen was treated by successive heating processes up to 375 ℃ after which very small amounts of C and O detected (Ch.5).

UHV is achieved by reducing the pressure to 1 Pa by mechanical rotary pumps, then using ion and turbo-pumps, backed by rotary pumps, to achieve UHV.

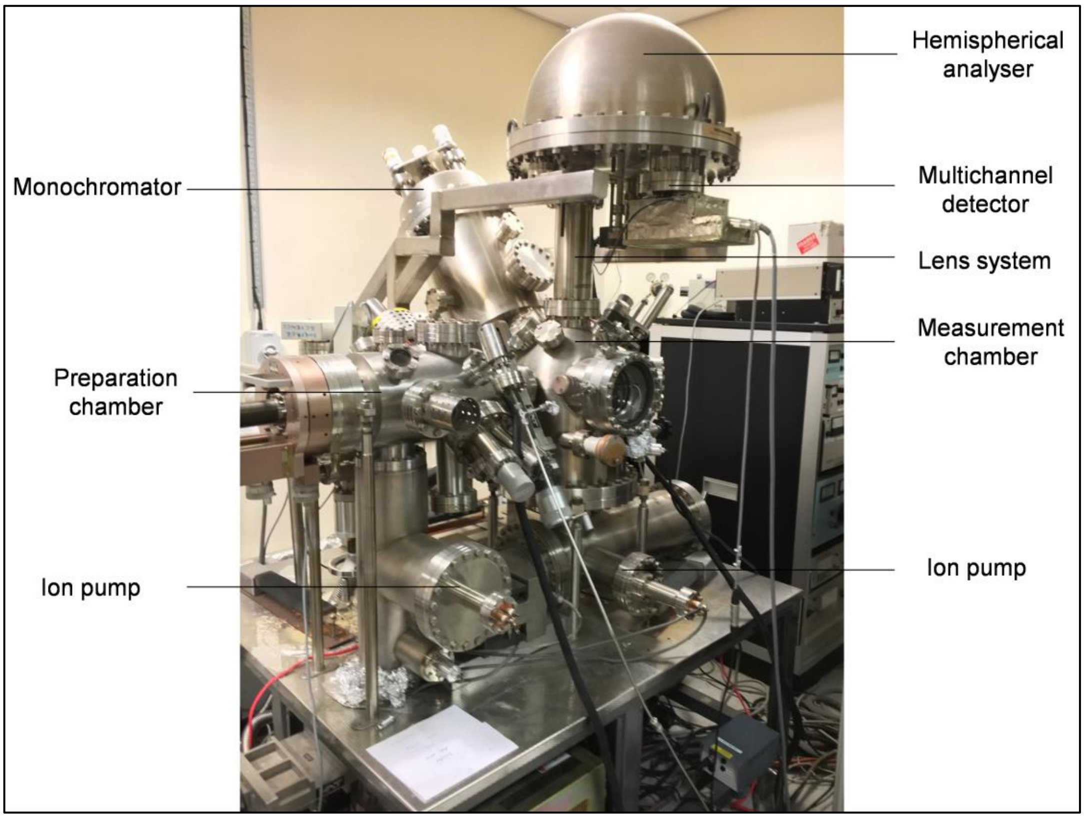

Fig. 2.2. The VSW ESCA instrument at Oliver Lodge building in the University of Liverpool. It shows the preparation and the measurement chambers and the pumping system. The electric lens system is vertically above the position of the sample holder in the measurement chamber. The lenses change the energy of the electrons to the pass energy required and focus them into the hemispherical analyser. The difference between the voltages applied on the inner and outer hemispheres drives the electrons to deferent channels of the multichannel detector depending on their energy.

2.2.1.2. X-ray sources:

The most commonly used x-ray sources are Al and Mg. The characteristic peaks of these elements are $K\alpha$ whose energies are $1486.6\ eV$ and $1253.6\ \ eV$ respectively. The characteristic lines are accompanied by the Bremsstrahlung continuous spectrum as well as satellites which increase the widths of the emitted photoelectric peaks, and reduce the energy resolution in the spectra and cause the emission of additional unwanted peaks. Therefore, it is desirable to obtain a monochromatic x-ray source which is achieved for Al $K\alpha$ by the constructive diffraction using α-quartz crystals (Fig.2.3).

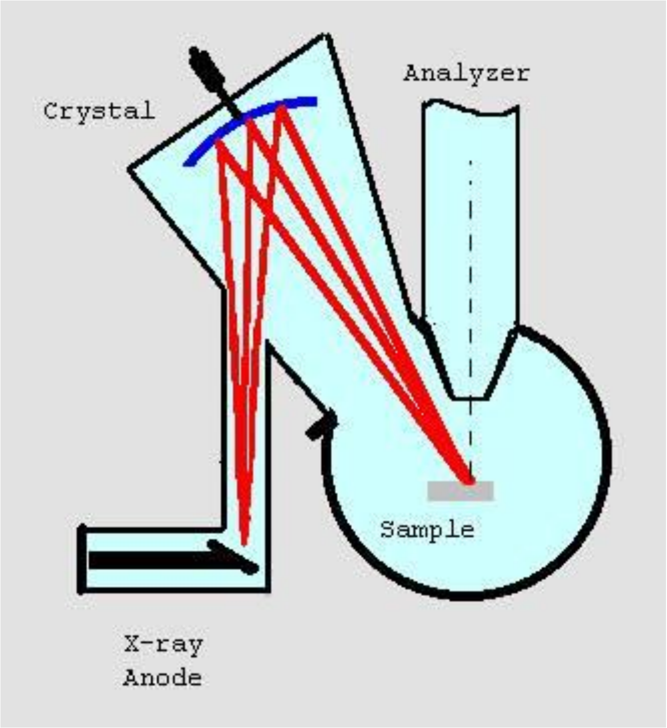

Fig.2.3. A diagram of the method the monochromatic Al $K\alpha$ x-ray is produced by the diffraction of the x-ray beam from the Al target at the α-quartz crystal. The incidence angle (of the x-ray beam on the crystal) is adjusted according to Bragg's law to achieve constructive interference of the $K\alpha$ line. Image source: www.casaxps.com/help_manual/XPSInformation/XPSInstr.htm

Higher energy sources are needed to extract core electrons whose binding energies are larger than that of Al $K\alpha$. Bremsstrahlung radiation can be used or other targets such as Ag $L\alpha$ and Cr $K\beta$ whose energies are 2984.3 and $5946.7\ eV$ respectively. Synchrotron radiation is another choice which provides several advantages such as tunability where the energy of the x-ray can be chosen and varied [2]. Moreover, synchrotrons provide polarised, very high intensity x-rays. The yield of electron emission depends on the polarisation of the x-ray which can be exploited in various ways such as studying the orientation of the chemical bonds [2].

A monochromated Al Kα x-ray is used in the VSW ESCA instrument (Fig.2. 2, 3).

2.2.1.3. Retardation and the analyser resolution:

The VSW instrument includes a concentric hemispherical analyser (CHA) with central radius (the radius of the central sphere between the inner and the outer spheres) $R = 150\,mm$ (Fig.2.4).

The resolution of the CHA, which is defined as the standard deviation of the distribution of the energies of the detected electrons around the chosen value, is:

$$\Delta E = E\frac{S}{2R} \qquad (2.1)$$

where E is called the pass energy which is the energy at which the electrons enter the analyser and S is the width of the entrance slit of the analyser.

A retardation voltage is applied by the lens system to control the energies of the electrons entering the analyser. There is a choice between operating the analyser at a fixed pass energy or a fixed retardation ratio. The first requires synchronising the retardation potential to the kinetic energy of the electrons that are desired to be detected. The retardation potential V_r is given as follows:

$$V_r = KE - E \qquad (2.2)$$

where E is the pass energy as in (Eq.2.1). For example, if the pass energy is chosen to be $10\ eV$; then to detect the electrons emitted at KE of $200\ eV$ a retardation of $190\ eV$ is applied. (Eq.2.1) shows that operating the analyser at a fixed pass energy results in the same resolution for the peaks of all energies. Choosing a low pass energy increases the energy resolution of the analyser, but then the intensity of the detected electrons decreases.

Operating at a fixed retardation ratio means maintaining a constant ratio of the energies of the electrons before and after retardation:

$$\frac{E}{KE} = constant \qquad (2.3)$$

(Eq.2.1) also shows that operating the analyser at a fixed retardation ratio leads to the degradation of resolution for the electrons emitted at high energies i.e. the spectroscopic peaks of these electrons will be broader.

All the measurements in this work were performed with fixed pass energies i.e. the same pass energy is maintained throughout the measurement. The lowest possible values of the pass energies were chosen depending on the strength of the measured lines. High pass energies were chosen in the survey scans (broadscans) that are performed at the beginning of measuring each specimen to detect any small constituent element and surface contamination.

During the setup of an experiment the operator chooses the pass energy, the range of KE to be scanned, the energy step and dwelling time. These settings are entered through the computer software of the instrument.

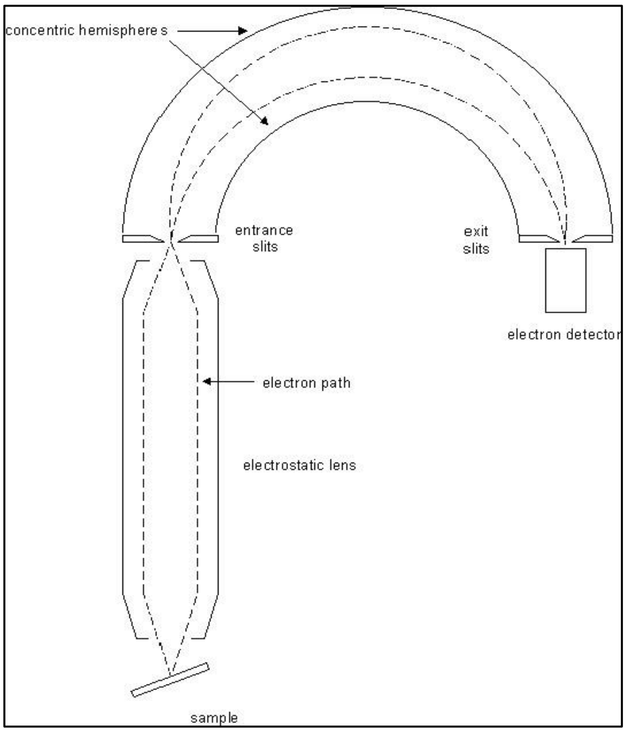

Fig.2.4. A diagram of the path of the emitted photo- and Auger electrons from the specimen to the detector. The electrons pass through an electrostatic lensing system where their energies are adjusted to either a chosen energy (pass energy) with which they enter the analyser, or to energies with fixed ratio to their original energies (fixed retardation ratio). The lens also focuses the electrons on the entrance slit of the analyser. The analyser shown is called the concentric hemispherical analyser whose inner and outer hemispheres are connected to an electrical kit so that they produce electric fields that focus the electrons with the chosen energies on the exit slits, to the multichannel detector. Source of the image: mcc.lsu.edu/images/XPS%20conf.jpg

In this experiment, the energy step was $0.488\ eV$ in broadscans and $0.092\ eV$ in narrow regions of specific lines. These values are chosen so that there is a constant offset in the kinetic energy of electrons hitting each of the sixteen detectors in the multichannel system. It is determined by the relationship between the central radius of the analyser, the kinetic energy of the analyser and the physical separation of the sixteen detectors. The energy steps lead to a systematic error (uncertainty) in reading measurements in the energy scale equal to half the step.

2.2.2. Properties of the photoelectric line:

The intensity of the photoelectron line is proportional to the atomic density of the element. The intensity also depends on the ionisation cross section of the measured atomic level. The cross section depends on the atomic structure and the energy of the x-ray source. Tabulations of cross sections calculated theoretically of different energy levels have been made such as that of Scofield [3].

Photoelectrons are not emitted from a certain energy level with a certain kinetic energy, but with a Lorentzian distribution (around the main value) which is called natural broadening. This broadening is related to the lifetime of the hole left in the energy level as described by the uncertainty principle:

$$\Gamma = \frac{\hbar}{\tau} \qquad (2.4)$$

where Γ is the FWHM of the Lorentzian, τ is the lifetime of the hole, $\hbar$ is the reduced Planck constant.

The XPS line also contains contributions of Gaussian nature from the x-ray source and from the resolution of the analyser. This is called the instrument resolution. So, the width of the line is:

$$FWHM = \sqrt{{\Gamma_\tau}^2 + {\mathrm{FWHM}_M}^2 + {\mathrm{FWHM}_A}^2} \qquad (2.5)$$

where Γ_τ is the natural broadening, FWHM_M is the width of the x-ray which is in a monochromated source related to the Monochromator, FWHM_A is the resolution of the energy analyser. The overall resolution of the instrument can be calculated using (Eq.2.6) by studying an XPS peak with a well-known natural broadening:

$$\mathrm{FWHM}_I = \sqrt{(FWHM)^2 - \Gamma_\tau{}^2} \qquad (2.6)$$

where the overall instrument resolution FWHM_I is defined as:

$$\mathrm{FWHM}_I = \sqrt{\mathrm{FWHM}_M{}^2 + \mathrm{FWHM}_A{}^2} \qquad (2.7)$$

The Au $4f$ photoelectron spectrum, which consists of the $4f_{5/2}$ and $4f_{7/2}$ components, was analysed using CasaXPS. The FWHM of $4f_{7/2}$ line was found to be $0.76 \pm 0.07\ eV$ and the natural broadening is reported to be $0.329 \pm 0.009\ eV$ [4]. So, the instrument resolution (FWHM_I) is $0.68 \pm 0.06\ eV$. The Au $4f$ spectrum was acquired at a pass energy at the analyser equal to $10\ eV$. Knowing that the width of the entrance slit of the analyser is $5\ mm$, and the length of the central radius (the radius of the central sphere between the outer and the inner hemispheres of the analyser) is $150\ mm$, the resolution of the analyser at the pass energy of $10\ eV$ is calculated using (Eq.2.1) and is equal to $0.17\ eV$. This is the standard deviation of the Gaussian broadening of the energy analyser (σ_A) which is related to the standard deviations of the total instrumental broadening (σ_I) and the standard deviation of the monochromatic x-ray beam (σ_m) as follows:

$$\sigma_I = \sqrt{\sigma_M{}^2 + \sigma_A{}^2} \qquad (2.8)$$

The relation of the standard deviation of the Gaussian distribution to FWHM is

$$\sigma = \mathrm{FWHM}/2.35 \qquad (2.9)$$

So, σ_I is $0.29 \pm 0.03\ eV$, and from (Eq.2.8): σ_M is $0.23 \pm 0.01\ eV$

2.2.3. Energy scale calibration:

Before conducting an XPS experiment, the work function of the instrument must be measured as explained in (Sec.1.2.4). This is called the energy scale calibration which involves measuring the binding energy of a photoelectric line of a well-known value and correcting the measured value according to the recommended one. The calibration is performed by shifting the whole energy scale by the same correction value.

As the Auger electron is not ejected directly by the x-ray, its KE and shape are not affected by those of the x-ray. The value of the kinetic energy of the Auger electron is corrected in the same way for that of a photoelectron (Eq.1.20).

The Au $4f_{7/2}$ and Ag $3d_{5/2}$ and Cu $2p_{3/2}$ lines are widely used to calibrate the energy scales in Al $K\alpha$ x-ray electron spectroscopy. They are prominent lines of metals which do not suffer from surface charging which also affects the measured kinetic energies (Sec.1.2.4).

Measurement was taken of an Au foil after cleaning by Ar^+ ion sputtering for 1 hour. The broadscan taken of the sample before cleaning (Fig. 2.5) shows strong C $1s$ and O $1s$ lines as well as O KLL Auger line. This contamination was removed by the Ar sputtering (Fig. 2.5).

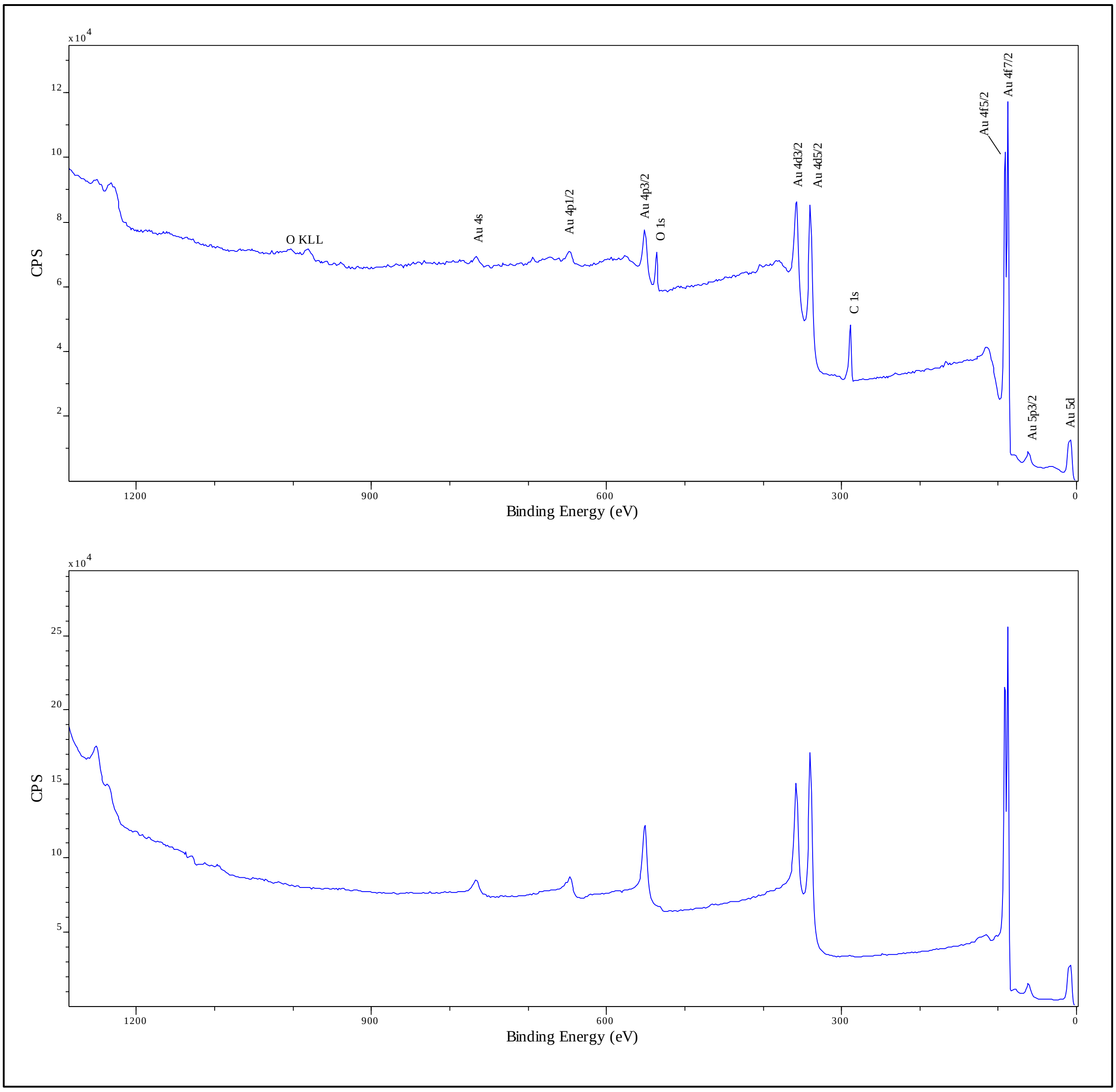

Fig. 2.5. Top: The broadscan spectrum obtained on the Au foil before cleaning. It shows the presence of C and O contamination. Bottom: the broadscan performed after Ar ion bombardment for 1 hr.

A narrow scan was performed on the $4f$ region at pass energy of $10\ eV$ and analyser entrance hole with a diameter of $5\ mm$ which results in a nominal resolution of $0.17\ eV$ (Fig. 2.6). The binding energies (BE) of $4f_{7/2}$ and $4f_{5/2}$ components are $88.32 \pm 0.05\ eV$ and $91.99 \pm 0.05\ eV$ respectively. The BE of $4f_{7/2}$ recommended by [5] is $83.96 \pm 0.01\ eV$ which suggests a correction to the energy scale of $4.36 \pm 0.05\ eV$. This correction applies to any measurement of a conducting sample in contact with the instrument.

For non-conducting samples, the $1s$ line of adventitious carbon is used for calibration to account for the surface charging. Adventitious carbon is in the hydrocarbons, from organic debris, which contaminate the surface of any specimen exposed to air [2]. C forms different chemical bonds in hydrocarbons, a dominant one of which results in C $1s$ binding energy of $284.8\ eV$ [6].

If the Fermi level is clear in the studied sample and can be measured, it is favourable to reference the binding energies to it.

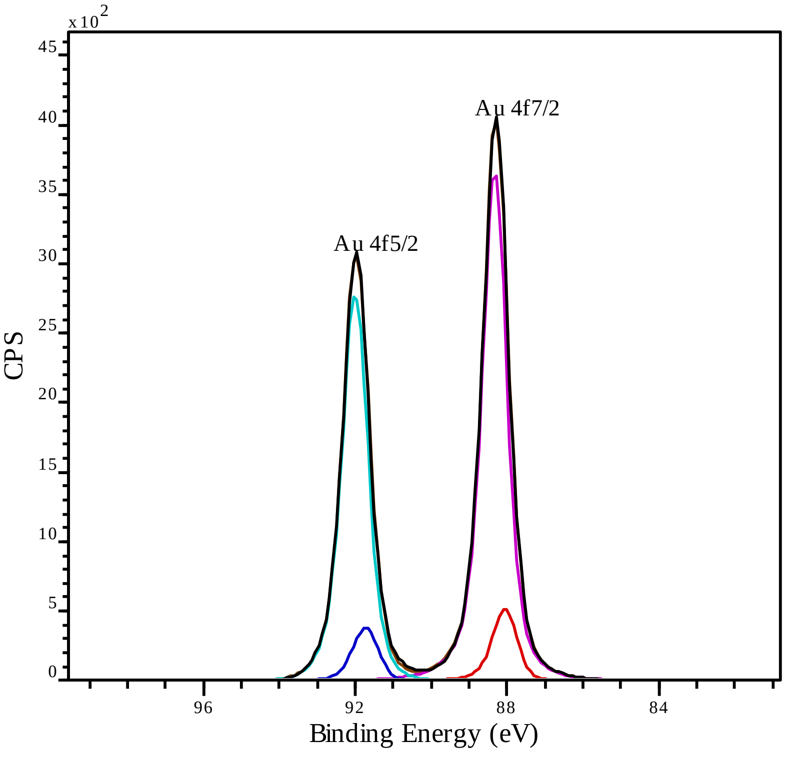

Fig. 2.6: Au $4f$ spectrum. Background corrected by Shirley method. Peaks associated with the surface core level shift are present at $-0.30 \pm 0.07\ eV$ binding energies from the more intense bulk sensitive peaks of both lines.

2.3. The CasaXPS program:

CasaXPS is a commercial program which is able to read XPS and AES data from the software of various instruments and convert them to a specific form by which the spectra can be analysed. The version 2.3.16 of the program was used in this work for peak fitting to distinguish different species (chemical states of elements) present and locate the maxima of their peaks.

2.3.1. Element identification:

CasaXPS contains a library of XPS and AES line positions which can be used in primary identification of the elements present in a sample and their different lines and species (if there is more than one). The spectra must be corrected for the work functions and surface charging before using the library.

2.3.2. Quantification of spectra:

After the main spectroscopic features in a sample have been identified, narrow scans are performed on them with small pass energy for better resolution, and small energy step to reduce the systematic measurement error. The spectrum of a narrow scan is quantified by fitting it to a synthetic spectrum constructed depending on knowledge in the spectroscopic lines involved in terms of their relative positions, intensities and widths. Relative positions involve splittings between components (such as the Au $4f_{7/2}$ and $4f_{5/2}$ components), or the chemical shifts between different species if they have been previously reported. Relative intensities include those of doublet components i.e. the electron populations of the Au $4f_{7/2}$ and $4f_{5/2}$ levels are 8 and 6 respectively leading to relative intensities of the two peaks of $4{:}\,3$. Quantification of Auger emissions is substantially more difficult than that of photoemissions (Sec.1.2.3). However, models of the multiplet structure of Auger emissions such as In and Sb $M_{4,5}N_{4,5}N_{4,5}$ are available from previous work [7-10].

Quantification of spectra is performed in the *Quantification Parameters* dialog window (Fig. 2.7, 8). At the beginning, quantification region is created with specific *beginning* and *end*. Then, the type of background subtraction method is chosen from various types provided. Backgrounds result from inelastic scattering of electrons in the specimen. Shirley and Tougaard are the most commonly used methods. The Tougaard background is more appropriate when a wide spectral region is studied. More than one region can be used in a spectrum for better evaluation of the background.

After the background is subtracted, synthetic peaks are created to account for different species and components in the quantification region (or regions). Extra peaks may be needed to account for the surface core-level shift. The surface of a sample is a moderately different chemical environment from the bulk. This results in the energies of the electrons emitted from the cores of the atoms near the surface to be shifted from the bulk energies. Gold spectrum is known to show surface shift [4], which was accounted for when the $Au\ 4f$ model was constructed (Fig.2.6). (Ch.4, 5) contains investigations of the spectra of metallic In and Sb as well as $InSb$ to detect the existence of any surface components.

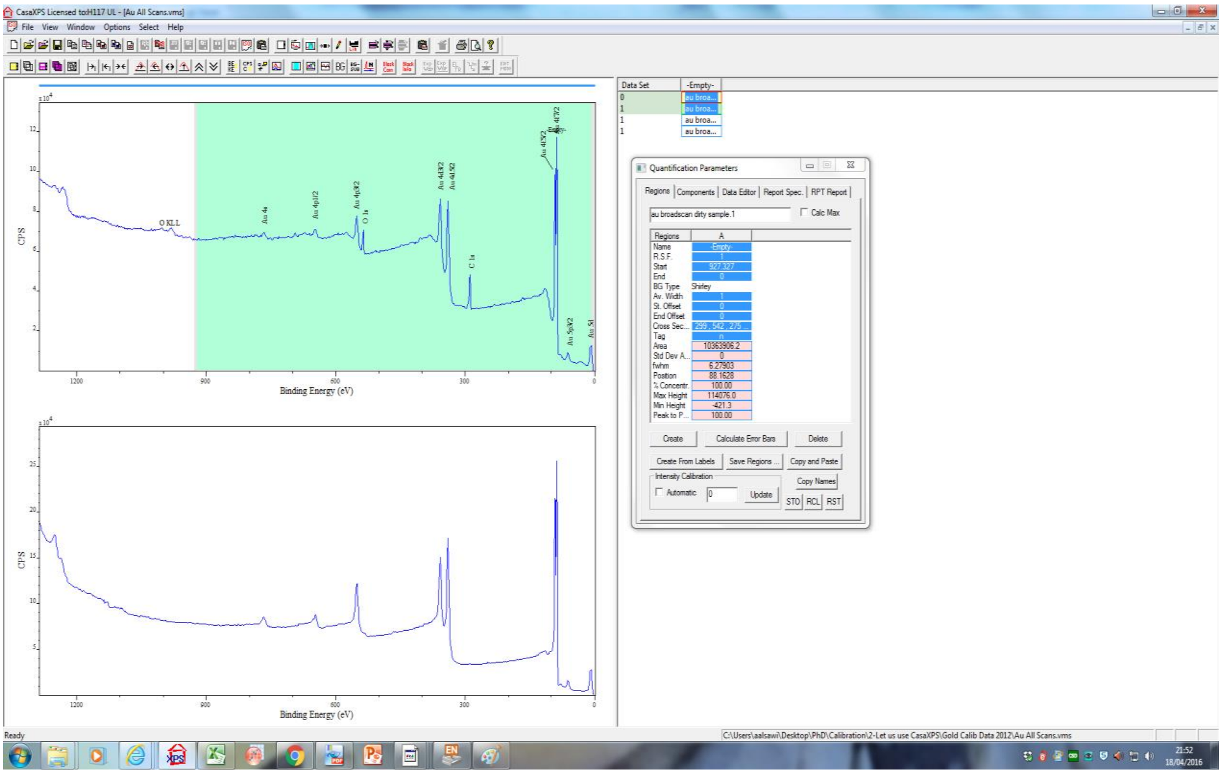

au broadscan dirty sample.1

☐ Calc Max

Regions	A
Name	-Empty-
R.S.F.	1
Start	927.327
End	0
BG Type	Shirley
Av. Width	1
St. Offset	0
End Offset	0
Cross Sec...	299 , 542 , 275 ...
Tag	n
Area	10363906.2
Std Dev A...	0
fwhm	6.27903
Position	88.1628
% Concentr.	100.00
Max Height	114076.0
Min Height	-421.3
Peak to P...	100.00

Intensity Calibration

☐ Automatic 0

C:\Users\aalsawi\Desktop\PhD\Calibration\2-Let us use CasaXPS\Gold Calib Data 2012\Au All Scans.vms

Fig. 2.7. The main window of the CasaXPS program with the *Quantification Parameters* dialog box is open. The part of the spectrum whose background is green coloured is the quantification region created.

After the creation of the synthetic peaks an elementary fit is run by clicking *Fit Components* (Fig.2.8). In fitting, the program modifies the synthetic peaks to achieve the lowest residual i.e. lowest difference between the model and the real spectra, which may result in a model that is mathematically a good fit, but not physically meaningful. To avoid that, constraints must be applied to the positions, intensities and widths of the synthetic peaks before running the fit. After the first fit, constraints can be relaxed to account for any unaccounted for factors, such as the errors in the background subtraction and differences in the emission cross sections. The fit is repeated until the best model is achieved. Fitting process is also illustrated when In and Sb spectra are studied in (Ch.4, 5, 6).

The shapes of the photoelectric peaks are Gaussian-Lorentzian convolution (Sec. 2.2.2) where the Lorentzian component is due to the natural broadening and the Gaussian is a property of the Monochromator and the energy analyser. CasaXPS provides various line shapes in which the convolution parameter can be specified.

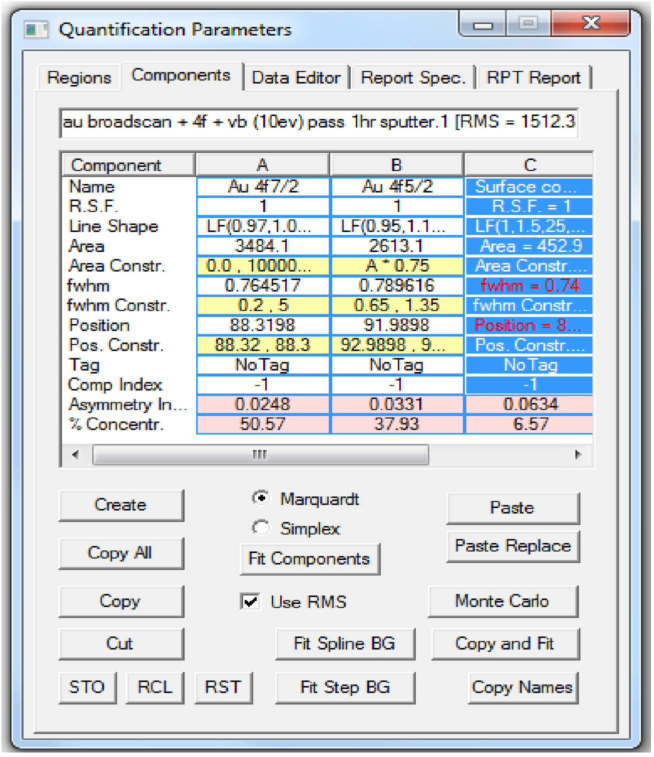

au broadscan + 4f + vb (10ev) pass 1hr sputter.1 [RMS = 1512.3

Component	A	B	C
Name	Au 4f7/2	Au 4f5/2	Surface co...
R.S.F.	1	1	R.S.F. = 1
Line Shape	LF(0.97,1.0...	LF(0.95,1.1...	LF(1,1.5,25,...
Area	3484.1	2613.1	Area = 452.9
Area Constr.	0.0 , 10000...	A * 0.75	Area Constr....
fwhm	0.764517	0.789616	fwhm = 0.74
fwhm Constr.	0.2 , 5	0.65 , 1.35	fwhm Constr...
Position	88.3198	91.9898	Position = 8...
Pos. Constr.	88.32 , 88.3	92.9898 , 9...	Pos. Constr....
Tag	NoTag	NoTag	NoTag
Comp Index	-1	-1	-1
Asymmetry In...	0.0248	0.0331	0.0634
% Concentr.	50.57	37.93	6.57

● Marquardt
○ Simplex

☑ Use RMS

Fig. 2.8. The *Quantification Parameters* dialog window with the *Components* property page open. In this page, peaks are created and constrained and their shaped are specified.

A specific line shape (LF line shape) which was introduces in the version 2.3.15 of the program was used for all the peaks in this work. It includes parameters for asymmetry that can be set to zero for symmetric peaks. The Gaussian component in this shape is defined as:

$$G(x\colon e,f,m) = exp\left[-4ln2\left(1-\frac{m}{499}\right)\left(\frac{x-e}{f}\right)^2\right] \qquad (2.10)$$

where e is the maximum, f is the FWHM, m is the convolution parameter which is an integer between 0 and 499 that is entered by the user. (Eq.2.10) describes how the energies of the electrons emitted from a certain atomic level are distributed around their expected value e

($e \equiv KE = hv - BE - \phi_i$) due to the instrumental broadening (Sec.2.2), where ϕ_i is the instrument work function (Sec.1.2.4). So, neglecting the natural broadening, the intensity of photoelectrons measured at kinetic energy x is:

$$I(x\colon e, f) = I_e exp\left[-4ln2\left(\frac{x-e}{f}\right)^2\right] \qquad (2.11)$$

where I_e is the intensity at the centre of the peak. This is a Gaussian function.

Similarly if the instrument broadening is neglected, then the distribution of the energies of the emitted electrons is written as a Lorentzian function:

$$L(x\colon e, f,) = I_e \frac{1}{1+4\left(\frac{x-e}{f}\right)^2} \qquad (2.12)$$

The Lorentzian component in the LF line shape is:

$$L(x\colon e, f, m) = \frac{1}{1+4\frac{m}{499}\left(\frac{x-e}{f}\right)^2} \qquad (2.13)$$

The convolution of the Lorentzian and the Gaussian distributions is called the Voigt function [2], which is written as a product of (Eq.2.10, 13) with the amplitude I_e:

$$LF(x, e, f, m) = I_e\ exp\left[-4ln2\left(1-\frac{m}{499}\right)\left(\frac{x-e}{f}\right)^2\right] / \left[1+4\frac{m}{499}\left(\frac{x-e}{f}\right)^2\right] \qquad (2.14)$$

Choosing m (the convolution parameter) to be 499 results in a pure Lorentzian peak and choosing it to be 0 results in in a Gaussian peak.

XPS peaks are usually asymmetric [2] i.e. the tail of the peak is extended at one side more than the other. The asymmetry is introduced by raising the Lorentzian part to different power at $x > e$ and $x < e$ [11]:

$$LF(x, \alpha, \beta, e, f, m) = \begin{cases} [L(x, e, f, m)]^{\alpha} & x \le e \\ [L(x, e, f, m)]^{\beta} & x > e \end{cases} \qquad (2.15)$$

Setting the powers (α or β) to value greater than one supresses the Lorentzian tail, while setting them to values less than one increases the tail. During the fitting processes α was given values smaller than β to introduce the core level asymmetries that results from shake-up to the unfilled one-electron levels above the Fermi level [2]. This shake-up results in energy loss which appears as a tail in the low energy side of the peak. During the fitting process, the values of α and β are varied together with the convolution parameter and the width of the peak until a good model is achieved.

2.3.3. Savitzky-Golay method:

The Savitzky-Golay method was used to obtain the differential form (dI/dE) of some of the Auger spectra (Ch. 4, 5, 6). Such a type of spectra does not require background subtraction and makes it easy to visualise the highest peaks with which the Auger KE's and the Auger parameters of the studied elements at different chemical states are associated.

The Savitzky-Golay method is a way of smoothing spectra by simulating each data bin with a set of equal number of data represented by polynomials (Eq. 2.16) whose coefficients are determined by performing the least square principle.

$$p(x_i) = a_0 + a_1 x_i + a_2 {x_i}^2 \qquad (2.16)$$

The differential form of a spectrum is obtained by replacing the resulting polynomials with their first derivatives.

2.3.4. Determination of the Fermi level:

CasaXPS provides a function, of four parameters, that can be fitted to the Fermi edge (Fermi step). The intensity of the photoelectrons at the edge is equal to a half of the magnitude of the edge a_0 multiplied by an error function ($erfc$) which depends on the position of the Fermi level a_1 and the standard deviation of the total instrumental broadening a_2:

$$I_{edge} = \frac{a_0}{2} erfc\left(\frac{(a_1 - KE)}{a_2}\right) + a_3 \qquad (2.17)$$

a_3 is an offset representing the intensity of the continuum at the higher energy side of the edge. Fitting this function to the Fermi level involves visually adjusting the values of the four parameters (a_0 to a_3). Knowledge of the instrumental broadening reduces the number variables in the fitting process. However, if this broadening is unknown, then fitting the Fermi level provides another way of obtaining the instrumental broadening in addition to the use of photoelectron lines as described in (Sec.2.2.2).

The Fermi level was used to correct the spectra of elemental In and Sb (Ch.4), and of the Sb/InSb (Ch.5).

2.4. The multi-configuration Dirac-Fock program:

The atomic structure calculations were carried out by the *MCDFGME V 2005.10* program [1]. The basic principles of the multi-configuration Dirac-Fock calculations were explained in (Sec. 1.3). The program can be run with a type of calculations called *mdf* by which multi-configuration calculations are performed for a specific total atomic angular momentum number J and magnetic quantum number m_j. Another type of calculations is called *eal* which stands for 'extended average energy level'. In this case, the total atomic energy is averaged over different configurations and total angular momenta. So, when the *eal* type is used, there is no need for the total atomic angular momentum to be entered. Different types of calculations for different purposes are reported in (Ch. 3).

(Fig. 2.9) shows the input file of the MCDFGME program optimised for the purpose of this work depending on the input data manual [12]. At each run of the program, the atomic number (number of protons) of the atom is entered (nz), as well as the number of electrons (nbel) and the electron configuration. If the mdf mode is used, the total atomic angular momentum number multiplied by 2 is entered for the value (jjt) (Fig. 2.9), and the total atomic magnetic quantum number m_j multiplied by 2 is entered for the value (mjt). Choosing these four values (nz, nbel, jjt, mjt) is all that is needed to perform the atomic structure calculations (using the optimised input text file (Fig.2.9)) for any atom with any ionisation state and any electron configuration and total angular momentum.

Running the MCDFGME produces an output text file which contains a description of the procedure of the Self-Consistent Field (SCF) process and the parameters and matrices used. What is of the interest in this work from the output file are two categories which are shown in the screenshot (Fig.2.10). The first is the total energy of the atom which is used in this work, as mentioned in (Sec.1.6), to explore the SCF method and how the total energies of atoms are affected by different ionisation and configuration. The total energies are also used to theoretically explore the binding energies of different orbitals and the kinetic energies of the $M_{4,5}N_{4,5}N_{4,5}$ Auger process in In and Sb using (Eq.1.5, 7). The second output category which is more important for the aim of this work is the orbital energy of any specific core level. The value of this energy level is read and tabulated from the atomic calculations performed for In and Sb atoms at different core ionisation states (from closed core to a core containing four holes). For each core ionisation state the atomic calculations are repeated for all valence charge values i.e. from $5s^0\ 5p^0$ to $5s^2\ 5p^6$ for In and Sb. Change of the energy of the core level between the different values of core ionisation and valence charge is due to change of the electric potential in the core of the atom. This potential was assigned the letter

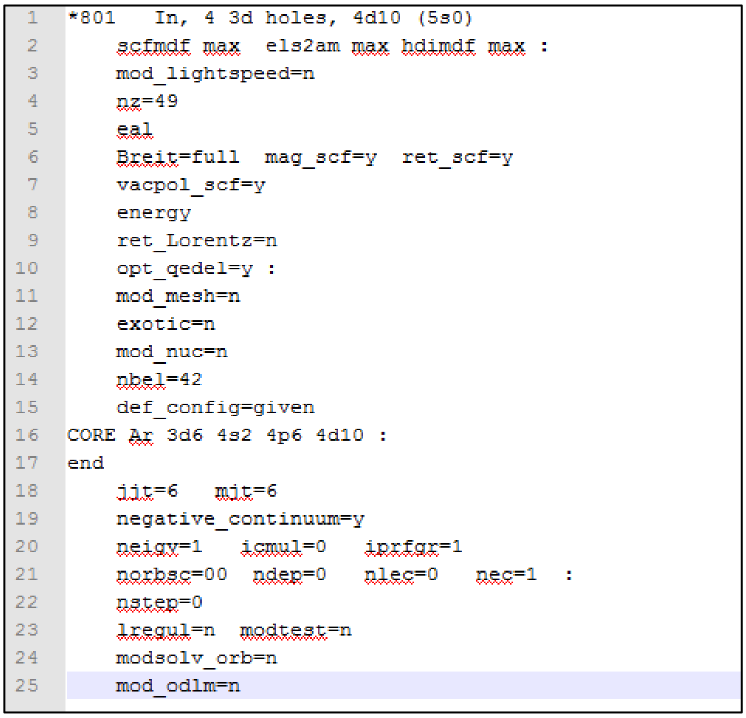

```
 1  *801   In, 4 3d holes, 4d10 (5s0)
 2       scfmdf max  els2am max hdimdf max :
 3       mod_lightspeed=n
 4       nz=49
 5       eal
 6       Breit=full  mag_scf=y  ret_scf=y
 7       vacpol_scf=y
 8       energy
 9       ret_Lorentz=n
10       opt_qedel=y :
11       mod_mesh=n
12       exotic=n
13       mod_nuc=n
14       nbel=42
15       def_config=given
16  CORE Ar 3d6 4s2 4p6 4d10 :
17  end
18       jjt=6   mjt=6
19       negative_continuum=y
20       neigv=1   icmul=0   iprfgr=1
21       norbsc=00  ndep=0   nlec=0   nec=1   :
22       nstep=0
23       lregul=n  modtest=n
24       modsolv_orb=n
25       mod_odlm=n
```

Fig.2.9. The input file of the MCDFGME program for an atom of atomic number (`nz=49`) i.e. indium atom. Number of electrons (`nbel`) is assigned the value `42` which means there are `7` electrons messing in this atom. Number of electrons entered in the configuration (line `16`) has to agree with the `nbel` value. The configuration shows that there are `4` holes in the core level `3d` (`d` level takes 10 electrons), and that the valence electrons ($3s^2$ $3p^1$) are removed. The type of calculations entered (in line 5) was `eal`, so the values of the total atomic angular momentum number `jjt` and the total atomic magnetic quantum number `mjt` will not affect the output which is averaged over different configurations and total angular momenta.

k in (Eq.1.53) when the potential model was introduced. (Ch.7) contains the derivation of k and the atomic potential parameters a, b and c (of In and Sb atoms) to obtain two formulas in the form of (Eq.1.54) which are then used in (Ch.8) to investigate the electronic structure of metallic In and Sb, and in (Ch.9) to investigate the electronic structure of $InSb$. The procedure of obtaining the potential parameters was introduced by [13] and applied for Xe.

A shot of the output file showing the self-consistent results of the total atomic energy and the orbital energies is in (Fig.2.10). $\mathrm{nl}*$ denotes the subshell shell of $j = l - 1/2$ i.e. $2\mathrm{p}*$ denotes $2p_{1/2}$, while $2\mathrm{p}$ denotes $2p_{3/2}$.

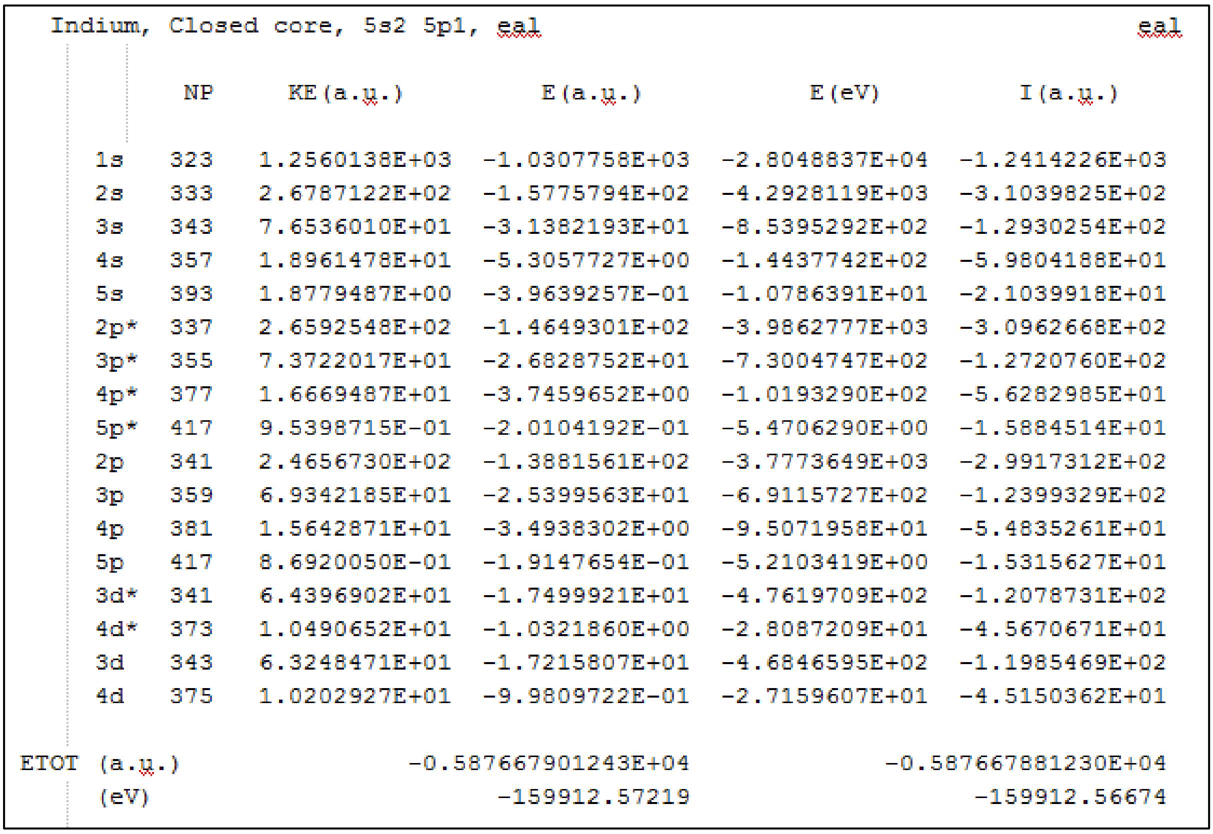

```
  Indium, Closed core, 5s2 5p1, eal                                           eal

          NP     KE(a.u.)          E(a.u.)           E(eV)            I(a.u.)

     1s   323   1.2560138E+03  -1.0307758E+03  -2.8048837E+04  -1.2414226E+03
     2s   333   2.6787122E+02  -1.5775794E+02  -4.2928119E+03  -3.1039825E+02
     3s   343   7.6536010E+01  -3.1382193E+01  -8.5395292E+02  -1.2930254E+02
     4s   357   1.8961478E+01  -5.3057727E+00  -1.4437742E+02  -5.9804188E+01
     5s   393   1.8779487E+00  -3.9639257E-01  -1.0786391E+01  -2.1039918E+01
     2p*  337   2.6592548E+02  -1.4649301E+02  -3.9862777E+03  -3.0962668E+02
     3p*  355   7.3722017E+01  -2.6828752E+01  -7.3004747E+02  -1.2720760E+02
     4p*  377   1.6669487E+01  -3.7459652E+00  -1.0193290E+02  -5.6282985E+01
     5p*  417   9.5398715E-01  -2.0104192E-01  -5.4706290E+00  -1.5884514E+01
     2p   341   2.4656730E+02  -1.3881561E+02  -3.7773649E+03  -2.9917312E+02
     3p   359   6.9342185E+01  -2.5399563E+01  -6.9115727E+02  -1.2399329E+02
     4p   381   1.5642871E+01  -3.4938302E+00  -9.5071958E+01  -5.4835261E+01
     5p   417   8.6920050E-01  -1.9147654E-01  -5.2103419E+00  -1.5315627E+01
     3d*  341   6.4396902E+01  -1.7499921E+01  -4.7619709E+02  -1.2078731E+02
     4d*  373   1.0490652E+01  -1.0321860E+00  -2.8087209E+01  -4.5670671E+01
     3d   343   6.3248471E+01  -1.7215807E+01  -4.6846595E+02  -1.1985469E+02
     4d   375   1.0202927E+01  -9.9809722E-01  -2.7159607E+01  -4.5150362E+01

ETOT (a.u.)                 -0.587667901243E+04               -0.587667881230E+04
     (eV)                         -159912.57219                     -159912.56674
```

Fig.2.10. A shot of the output file of the MCDFGME. The first column from left contains the symbols of the atomic orbitals where nl* is the orbital of the term $nl_{l-1/2}$ (see the text). The fourth and fifth columns shows the energy of each orbital in atomic units ($a.u.$) and electron volt (eV) respectively. The energies of the $3d$ orbitals are used in (Ch.7) for the potential model calculations. `ETOT` is the total energy of the atom.

2.5. Summary:

Combining the use of CasaXPS for precise determination of the positions of the electron spectroscopic lines of In and Sb in their metallic states and in the semiconducting InSb with the use of the MCDFGME program to derive the atomic potential parameters in (Eq.1.53) makes it possible to formulate (Eq.1.54) for both elements and then solve the equations using different approximations. This makes it possible to examine the ability of the potential model proposed by [13] to determine charge transfer and screening mechanisms in metals and compound semiconductors.

References

1. Desclaux, J. and P. Indelicato, *The relativistic atomic program MCDFGME V 2005.10.* Published at http://dirac. spectro. jussieu. fr/mcdf/on August, 2005. **17**: p. 2005.
2. Briggs, D. and J.T. Grant, *Surface analysis by Auger and x-ray photoelectron spectroscopy*. 2003, Chichester, West Sussex, U.K.: IM Publications. xi, 899 p.
3. Scofield, J.H., *Hartree-Slater subshell photoionization cross-sections at 1254 and 1487 eV.* Journal of Electron Spectroscopy and Related Phenomena, 1976. **8**(2): p. 129-137.
4. Citrin, P.H., G.K. Wertheim, and Y. Baer, *Surface-atom x-ray photoemission from clean metals: Cu, Ag, and Au.* Physical Review B, 1983. **27**(6): p. 3160-3175.
5. Seah, M., I. Gilmore, and G. Beamson, *XPS: binding energy calibration of electron spectrometers 5—re-evaluation of the reference energies.* Surface and Interface Analysis, 1998. **26**(9): p. 642-649.
6. NIST, X., *Database,< h ttp.* srdata. nist. gov/xps/Default. aspx.
7. Pessa, M., et al., *Solid-state effects inM4,5N4,5N4,5Auger spectra of elements fromIn49toTe52.* Physical Review B, 1979. **20**(8): p. 3115-3123.
8. Aksela, H., J. Väyrynen, and S. Aksela, *Vapour phase M 4, 5 N 4, 5 N 4, 5 Auger electron spectra of antimony and tellurium.* Journal of Electron Spectroscopy and Related Phenomena, 1979. **16**(3): p. 339-350.
9. Parry-Jones, A., P. Weightman, and P. Andrews, *The M4, 5N4, 5N4, 5 Auger spectra of Ag, Cd, In and Sn.* Journal of Physics C: Solid State Physics, 1979. **12**(8): p. 1587.
10. Aksela, S., et al., *M4, 5N4, 5N4, 5 Auger electron spectrum of In from In, InCl and InCl3 vapours.* Journal of Physics B: Atomic and Molecular Physics, 1980. **13**(19): p. 3745.
11. John Walton, P.W., Neal Fairley, Alan Carrick, *Peak Fitting with CasaXPS*. 2011, Cheshire: Acolyte Science. 132.
12. J.P. Desclaux, P.I., *Input Data For Relativistic Atomic Program MCDFGME V 2005.10*. 2005. p. 36.
13. Cole, R.J., D.A.C. Gregory, and P. Weightman, *Analysis of Auger-parameter and XPS shifts: Application of potential models.* Physical Review B, 1994. **49**(8): p. 5657-5661.

Chapter 3

Theoretical Calculations of Atomic Structure and Spectroscopic Values

3.1. Introduction:

Analysing the electron spectroscopic features, which are atomic structure properties [1-4], requires a minimum of understanding of the different contributions to these properties. The number of core holes, number of valence electrons, and electron configuration all contribute to the total energy of the atom and to the individual energy levels. This was explained in (Sec.1.3) through the theory of the atomic energy calculations and is manifested experimentally by the chemical shifts of the spectroscopic lines. Therefore, the aim of this chapter is to explore the electronic structure calculations and how the results are obtained using the MCDFGME program [5]. The output of this program includes, as mentioned in (Sec.2.4), the total energy of the atom (at the particular ionisation state and electron configuration entered in the input) and the energies of the atomic levels. The former is used in this chapter, while the latter is used in deriving the formulas of the potential model in (Ch.7). After the exploration of theoretical total atomic energies, theoretical spectroscopic features (binding energies of the $3\mathrm{d}$ and $4\mathrm{d}$ core levels, kinetic energies of the $M_{4,5}N_{4,5}N_{4,5}$ Auger transition together with the Auger parameter) are calculated as functions of different valence electron configurations assumed for the Sb and In atoms. Relations of the theoretical total atomic energies and spectroscopic features with electron configurations and ionisation states are analysed and discussed.

3.2. Sb Calculations:

Theoretical calculations are performed first on the Sb atom, which has in its ground state 5 valence electrons, then repeated for the In atom which is in the same period in the periodic table (has the same number of core electrons) but has 3 valence electrons in its ground state.

3.2.1: Fixed valence electron configuration:

The energies of the Auger and photo-electrons involve contributions from the initial and the final states of the atom during the emission process (Sec.1.2) [6, 7]. In this section valence electron configurations are assumed not to change by the core holes left in the final states.

3.2.1.1: Total energies

The total energies of the closed-core Sb atom and the Sb atom having lost a $3\mathrm{d}$ or a $4d$ electron are calculated by the *eal* and *mdf* calculation types explained in (Sec. 2.4) and plotted against the corresponding valence electron configurations.

3.2.1.1.1: Closed-core atom

An *ETOT* in (Table. 3.1) is the total energy of a closed-core Sb atom or ion, at a specific valence charge and configuration and total angular momentum (J), calculated using the *mdf* approach.

The total energy (*ETOT*) at a specific total angular momentum value (J) is calculated as a superposition of all possible $L-S$ terms. The program does not converge for some J values, and an error message appears in the output file of the *MCDFGME* program stating that there are '*Too many steps for adjusting the energy*'. This is encountered in many cases in this chapter and in (Ch.7), and it can be attributed to the existence of an atomic state having energy eigenvalue that is equal to that of the ground state within the tolerance range mentioned in (Sec.1.3.1.1). This makes the program swing continuously between the two states while performing the self-consistent field (SCF) process hence the appearance of the error message.

Configuration	Term Symbol ($^{2S+1}L_J$)	ETOT(ev)	Configuration	Term Symbol ($^{2S+1}L_J$)	ETOT(ev)
Sb: $5s^2\,5p^3$	$^{2}P_{1/2}$	-176226.12	Sb: $5s^2\,5p^2\,6p^1$	$^{2}F_{7/2}$, $^{4}D_{7/2}$	-176222.03
Sb: $5s^2\,5p^3$	$^{2}D_{3/2}$,$^{2}P_{3/2}$,$^{4}S_{3/2}$	-176228.81			
Sb: $5s^2\,5p^3$	$^{2}D_{5/2}$	-176227.14	Sb: $5s^2\,5p^2\,5d^1$	$^{4}D_{1/2}$, $^{4}P_{1/2}$ $(^{2}P_{1/2})_{1,2}$ $^{2}S_{1/2}$	-176222.01
Sb: $5s^1\,5p^4$	$^{4}P_{1/2}$, $^{2}P_{1/2}$, $^{2}S_{1/2}$	-176220.86			
Sb: $5s^1\,5p^4$	$^{2}D_{3/2}$, $^{4}P_{3/2}$, $^{2}P_{3/2}$	-176220.98			
Sb: $5s^1\,5p^4$	$^{2}D_{5/2}$, $^{4}P_{5/2}$	-176221.27	Sb: $5s^2\,5p^2\,5d^1$	$^{4}F_{3/2}$, $^{4}D_{3/2}$ $(^{2}D_{3/2})_{1,2,3}$ $^{4}P_{3/2}$,$(^{2}P_{3/2})_{1,2}$	-176222.41
Sb: $5s^2\,5p^2\,6s^1$	$^{4}P_{1/2}$, $^{2}P_{1/2}$, $^{2}S_{1/2}$	-176223.63			
Sb: $5s^2\,5p^2\,6s^1$	$^{2}D_{3/2}$, $^{4}P_{3/2}$, $^{2}P_{3/2}$	-176223.32			
Sb: $5s^2\,5p^2\,6s^1$	$^{2}D_{5/2}$, $^{4}P_{5/2}$	-176222.99	Sb: $5s^2\,5p^2\,5d^1$	$^{4}F_{5/2}$, $(^{2}F_{5/2})_{1,2}$ $(^{4}D_{5/2})$, $(^{2}D_{5/2})_{1,2,3}$, $^{4}P_{5/2}$	-176222.09
Sb: $5s^2\,5p^1\,6s^2$	$^{2}P_{1/2}$	-176215.70			
Sb: $5s^2\,5p^1\,6s^2$	$^{2}P_{3/2}$	-176214.93	Sb: $5s^2\,5p^2\,5d^1$	$^{2}G_{7/2}$, $^{4}F_{7/2}$ $(^{2}F_{7/2})_{1,2}$ $^{4}D_{7/2}$	-176222.11
			Sb: $5s^2\,5p^2\,5d^1$	$^{2}G_{9/2}$, $^{4}F_{9/2}$	-176221.85
Sb: $5s^2\,5p^2\,6p^1$	$^{4}D_{1/2}$, $^{4}P_{1/2}$, $(^{2}P_{1/2})_{1,2,3}$ $^{2}S_{1/2}$	-176222.76	Sb^-: $5s^2\,5p^4$	$^{3}P_{0}$, $^{1}S_{0}$	-176228.36
			Sb^-: $5s^2\,5p^4$	$^{3}P_{1}$	-176228.43
			Sb^-: $5s^2\,5p^4$	$^{1}D_{2}$, $^{3}P_{2}$	-176228.75
Sb: $5s^2\,5p^2\,6p^1$	$^{4}D_{3/2}$, $(^{2}D_{3/2})_{1,2}$ $(^{4}P_{3/2})_{1,2,3}$ $(^{2}P_{3/2})_{1,2,3}$, $^{4}S_{3/2}$	-176222.97	Sb^+: $5s^2\,5p^2$	$^{3}P_{0}$, $^{1}S_{0}$	-176220.69
			Sb^+: $5s^2\,5p^2$	$^{3}P_{1}$	-176220.34
Sb: $5s^2\,5p^2\,6p^1$	$^{2}F_{5/2}$, $^{4}D_{5/2}$, $(^{2}D_{5/2})_{1,2,}$ $^{4}P_{5/2}$		Sb^+: $5s^2\,5p^2$	$^{1}D_{2}$, $^{3}P_{2}$	-176219.98

Table. 3.1 ETOT (column 3 and 6) is the total energies of the closed-core Sb atom calculated at specific electron configurations (column 1 and 4) and total angular momenta J (column 2 and 5). The total energy of the atom is calculated for a specific total angular momentum J (calculated by the $j-j$ coupling scheme) as a superposition of all possible $L-S$ terms e.g. ETOT of the Sb atom at ($5s^2\,5p^3$) and $J=\frac{3}{2}$ as entered values is calculated as a superposition of the atom at $L-S$ terms of $^{2}D_{3/2}$,$^{2}P_{3/2}$,$^{4}S_{3/2}$. See (Sec.1.2.3).

(Table. 3.2) compares the maximum and minimum ETOTs of each configuration in (Table. 3.1) with the average ETOT obtained using the *eal* approach which is the other type of calculation available in the *MCDFGME* which calculates the total energy of an atom or ion as an average over the total energies of all the total atomic angular momentum (J) states at a specific charge state and valence electron configuration (Sec.2.4).

At first glance, the differences between the values of the total energy listed in (Table.3.1, 2) may be considered to be insignificant as they range between $\sim 1\ eV$ and $\sim 13 eV$ relative to the value of the Sb ground state ($5s^2\ 5p^3$) which is $176227.14\ eV$ as calculated by the eal type. However in reality, most of these differences are extreme bearing in mind that the chemical shifts of binding energies observed experimentally for the Sb $3d_{5/2}$ photoelectric line range between 0.1 and $4eV$ [8].

Configuration	**ETOT$_{min}$(ev)**	**ETOT$_{max}$(ev)**	**ETOT$_{eal}$(ev)**
Sb$^-$: 5s^2 5p^4	-176228.74	-176228.36	-176228.10
Sb: 5s^2 5p^3	-176228.80	-176226.12	-176227.14
Sb: 5s^2 5p^2 6s^1	-176223.63	-176222.99	-176222.44
Sb: 5s^2 5p^2 5d^1	-176222.41	-176222.01	-176221.15
Sb$^+$: 5s^2 5p^2	-176220.69	-176220.34	-176219.52
Sb: 5s^1 5p^4	-176221.27	-176220.86	-176218.50
Sb: 5s^2 5p^1 6s^2	-176215.70	-176214.93	-176215.19

Table. 3.2 Comparison between the average total energy of the closed core Sb atom at various valence electron configurations obtained using the eal type of calculations and the maximum and minimum values of the total energies associated with the different $L-S$ terms corresponding to that configuration using the mdf type.

It can be noticed from (Table. 3.2) and (Graph. 3.1) that, with exception of the ground state (*5s^2 5p^3*) and the state of the configuration *5s^2 5p^1 6s^2*, the highest total energy calculated by the *mdf* type of calculations ($ETOT_{max}$) is lower than the average total energy calculated by the *eal* type ($ETOT_{eal}$). The likely explanation for this is that since the total angular momentum is not specified in the input of the *eal* type, the program includes higher excited atomic eigenstates in the atomic wavefunction (Eq. 1. 41) leading to higher atomic energy. That is why this type of calculations is described as an "extended average" (*eal*). In the other hand, the atomic wavefunction at the *mdf* type has a contribution from all the $L-S$ terms having the value of the total angular momentum J entered in the input; therefore the SCF method can converge to a solution that is closer to the $L-S$ term having the lowest total energy.

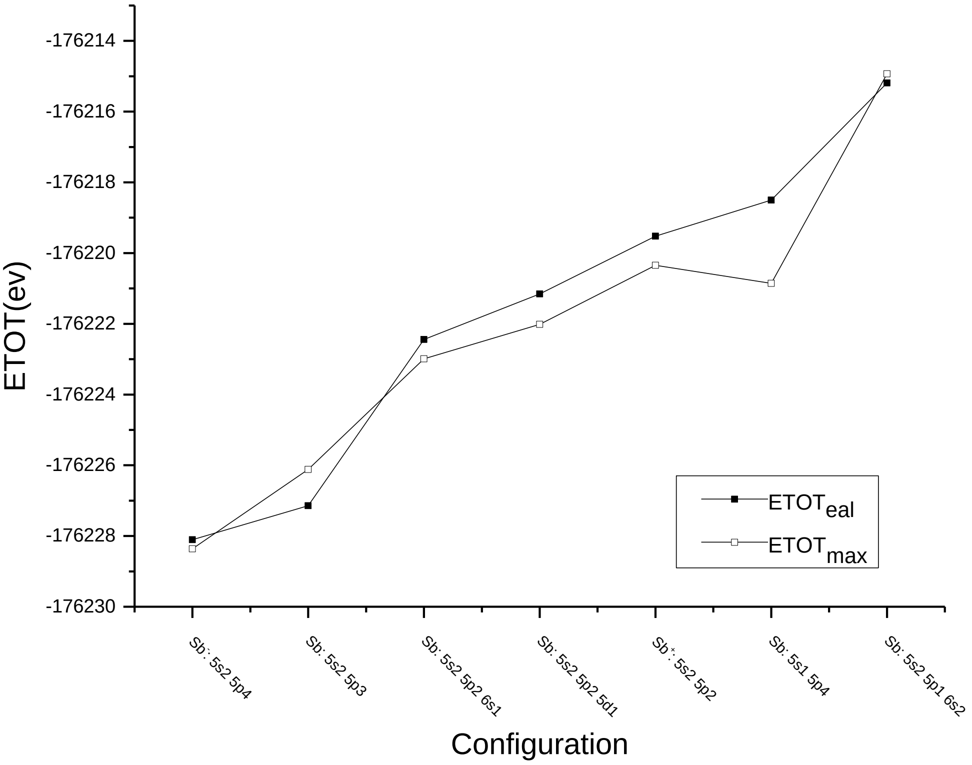

Graph. 3.1 The average total energy of the closed core Sb atom calculated by the eal type at different valence electron configurations, and the corresponding maximum total energies calculated with the mdf type (Table.3.2). Adding an electron to the open 5p shell reduces the average energy of the atom by 0.96 eV, while removing an electron from the same shell increase the atomic energy by 7.62 eV.

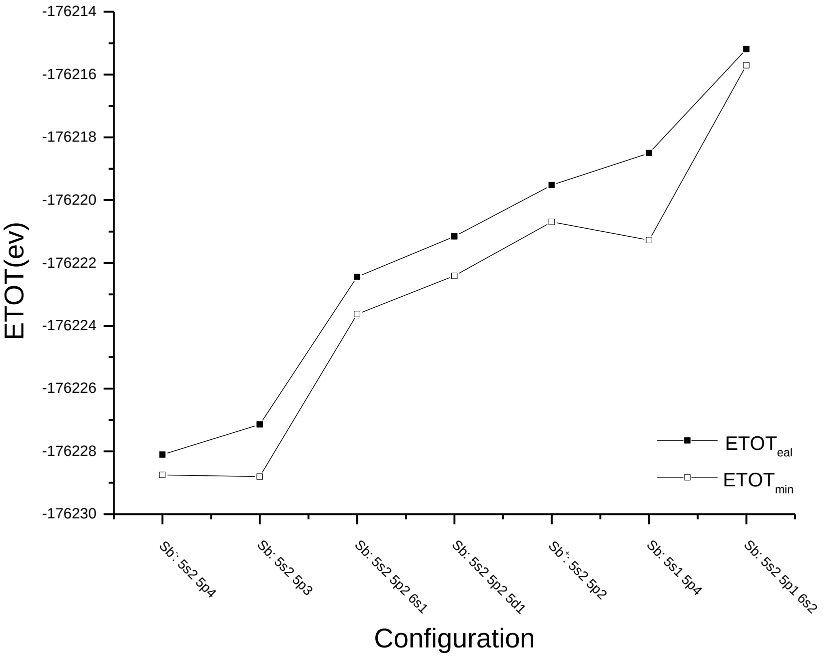

Graph. 3.2 ETOT$_{eal}$ is the average total energy of a closed core Sb atom at different configurations. ETOT$_{min}$ is the energy of the *J* term having the lowest total energy.

The configurations in (Graph. 3.1) are ordered depending on the values of the corresponding average total energies from the lowest to the highest.

3.2.1.1.2: Sb atom with a $3d$ hole

The same total energy calculations are repeated for the Sb atom having a hole in the $3d$ orbital.

Configuration	$ETOT_{min}$(ev)	$ETOT_{max}$(ev)	$ETOT_{eal}$(ev)
Sb: $5s^2\ 5p^4$	-175700.57	-175700.39	-175695.83
Sb^+: $5s^2\ 5p^3$	-175692.78	-175690.73	-175686.95
Sb^+: $5s^2\ 5p^2\ 6s^1$	-175683.14	-175682.01	-175677.81
Sb^+: $5s^2\ 5p^2\ 5d^1$	-175682.78	-175681.94	-175676.71
Sb^+: $5s^2\ 5p^2$	-175683.81	-175683.57	-175676.63
Sb^+: $5s^1\ 5p^4$	-175675.16	-175673.94	-175669.87
Sb^+: $5s^2\ 5p^1\ 6s^2$	-175670.71	-175660.52	-175666.21

Table. 3.3 The average and extreme total energies of the Sb atom or ion with a $3d$ hole at various valence electron configurations.

By comparing (Graph. 3.3) with (Graph. 3.2), it can be seen that there are significant variations in the dependence of the total atomic energies on the valence configuration between the presence or absence of $3d$ core hole. These differences gives rise to variation in the calculated binding energies of the $3d$ level at different configuration states which is utilised by using the shift of the binding energies of core levels as a probe of the chemical state of the element studied.

(Graphs. 3.2, 3) shows that the average total atomic energy ($ETOT_{eal}$) that was calculated using the *eal* mode behaves in roughly the same manner as that calculated using the *mdf* mode ($ETOT_{min}$). This is consistent with the SCF method converging to the lowest total atomic energy at a given electron configuration.

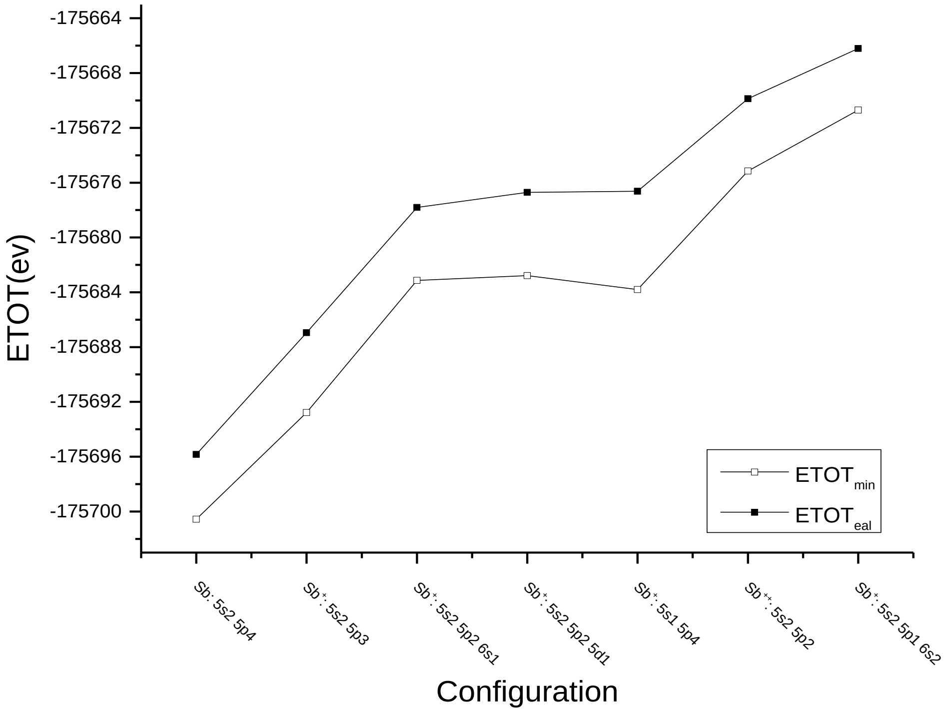

Graph. 3.3: The average and minimum total energies of the Sb atom, having a $3d$-hole, at different number and configuration of valence electrons.

3.2.1.1.3: Sb atom with a $4d$ hole

The total energy of the Sb atom with a hole in the $4d$ level shows a similar dependence on the valence configuration as an atom having a hole in $3d$ core level, which shows that the Sb $4d$ level, like the $3d$ level, is solely an atomic core entity.

Configuration	$ETOT_{min}$(ev)	$ETOT_{max}$(ev)	$ETOT_{eal}$(ev)
Sb: $5s^2$ $5p^4$	-176197.86	-176197.46	-176196.09
Sb^+: $5s^2$ $5p^3$	-176190.08	-176187.92	-176187.29
Sb^+: $5s^2$ $5p^2$ $6s^1$	-176180.70	-176179.51	-176178.27
Sb^+: $5s^2$ $5p^2$ $5d^1$	-176180.43	-176179.24	-176177.16
Sb^+: $5s^2$ $5p^2$	-176172.73	-176171.48	-176170.38
Sb^+: $5s^1$ $5p^4$	-176181.42	-176180.96	-176177.07
Sb^+: $5s^2$ $5p^1$ $6s^2$	-176168.48	-176166.61	-176166.83

Table. 3.4 The average and extreme total energies of the Sb atom with a $4d$ hole at various valence electron configurations.

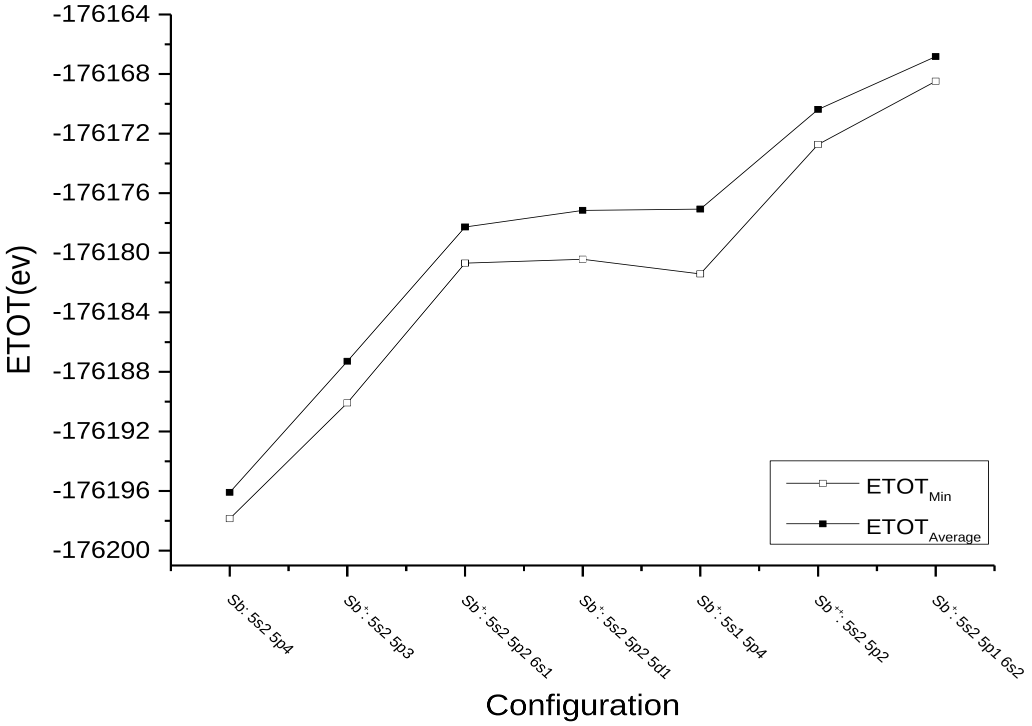

Graph. 3.4 The average and minimum total energies of the $4d$-hole Sb atom. The two curves are similar to those obtained for an Sb atom having a core hole in the $3d$ level which shows that the Sb $4d$ level is solely an atomic core entity.

3.2.1.1.4: Sb atom with $4d^2$ holes:

The $M_{4,5}N_{4,5}N_{4,5}$ Auger emission leaves the Sb atom in the 4d^2 hole state. The total energy of the atom in this case is expected to be strongly affected by the interaction between the two holes and the different ways in which angular momentum of the holes can couple into the term structure (Sec.1.2.3).

V Level Configuration	ETOT (eV)
5s^2 5p^4	-176149.99
5s^2 5p^3	-176131.58
5s^1 5p^4	-176119.93
5s^2 5p^2 5d^1	-176118.25
5s^2 5p^2 6s^1	-176118.08
5s^2 5p^2 6p^1	-176115.32
5s^2 5p^2	-176104.00

Table. 3.5 The average total energy of the Sb atom with $4d^2$ holes at various valence electron configurations.

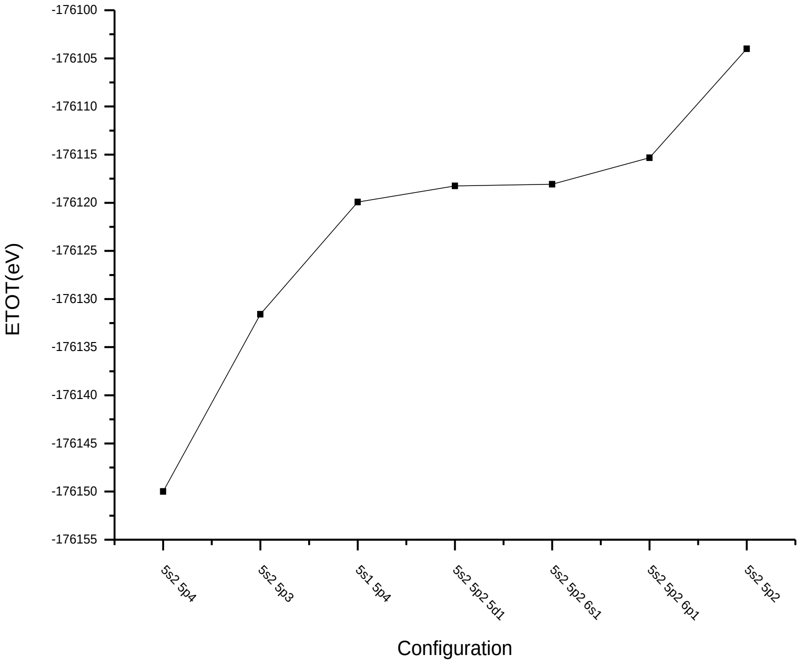

Graph. 3.5: The average total energy of Sb atom, having $4d^2$ holes, at various valence level configurations.

The total energy of the Sb atom having 2 holes in the $4d$ level behaves similarly to that having a single hole in the same level.

3.2.1.2: Sb Binding energy:

The binding energy of an electron in the level i is equal to the difference in total energy between the neutral atom $E_{(N)}$ and the ion containing a hole in the same level $E_{(N-1)}$ as explained in (Sec.1.2.1.1) [9]:

$$BE_i = ETOT_{(N-1)} - ETOT_{(N)} \qquad (3.1)$$

BE_i is not equal to the orbital energy of the electron i, but includes a contribution from the relaxation of the spectator electrons and the surrounding atoms (if the atom is a part of a solid or a molecule) [10]. Thus, (Eq. 3.1) is rewritten as follows:

$$BE_i = h\nu - KE = -\epsilon_i - R \quad (3.2)$$

where $h\nu$ is the energy of the x-ray photon, KE is the kinetic energy of the emitted photoelectron, ϵ_i is the orbital energy of the electron i, R is the relaxation energy which can be described as the reduction of the energy of the atom and its surrounding medium due to the creation of a hole in the level i.

$$R = R^a + R^{ea} \quad (3.3)$$

R^a is the atomic relaxation and R^{ea} is the extra-atomic relaxation which will be revisited later.

(Eq. 3.1) will be used to calculate the binding energies of the Sb $3d$ and $4d$ levels for several configurations.

3.2.1.2.1: $3d$ Binding energy

The average total energies of the Sb atom or ion (calculated by the *eal* method) were used to calculate the binding energy of a $3d$ electron in (Table. 3.6). These binding energy values are plotted against their corresponding configurations in (Graphs. 3. 6,7).

V Level Configuration	BE_{3d} (eV)	BE_{4d} (eV)
$5s^2$ $5p^4$	532.27	32.01
$5s^2$ $5p^3$	540.19	39.85
$5s^2$ $5p^2$ $6s^1$	544.63	44.17
$5s^2$ $5p^2$ $6p^1$	545.59	45.12
$5s^2$ $5p^2$ $5d^1$	544.44	43.99
$5s^2$ $5p^2$	549.65	49.14
$5s^1$ $5p^4$	541.87	41.43
$5s^2$ $5p^1$ $6s^2$	548.98	48.36

Table. 3.6 Binding energies of $3d$ and $4d$ levels for different configurations. Calculated using (Eq. 3.1)

The $3d$ level is split into a doublet because of the spin-orbit coupling of the hole, therefore the $3d$ photoelectron line consists of two components ($3d_{3/2}$, $3d_{5/2}$) separated by the spin-orbit coupling energy. The splitting between the two components cannot be calculated using eal calculations of the MCDFGME program, but it can be obtained from the output of the program in which the orbital energies are included as shown in (Fig. 3.1) which is a caption from the output file of the *eal* calculation of the elemental Sb atom.

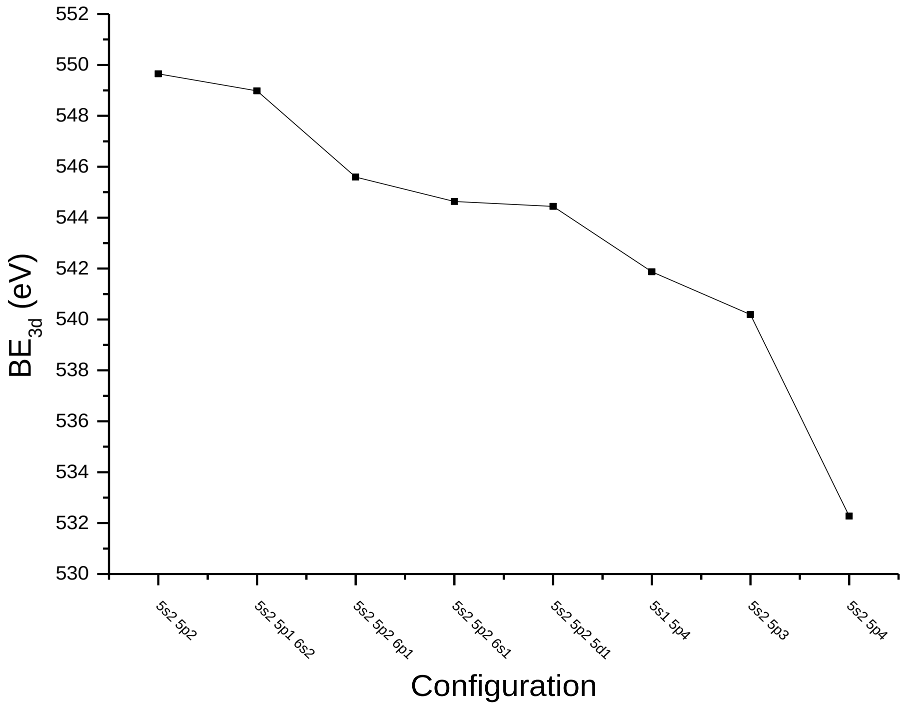

Graph. 3.6 Binding energies of Sb 3d level for different valence electron configurations calculated using (Eq. 3.1) and listed in (Table. 3.6).

The orbital energy (the eigenvalue) of the $3d_{3/2}$ level (3d* in (Fig. 3.1)) is equal to $-563.486\ eV$, and the orbital energy of the $3d_{5/2}$ level (3d in the graph) is $-553.932\ eV$, therefore the splitting between the two levels according to the theoretical calculation is equal to $9.56\ eV$, whereas the splitting obtained experimentally has been reported at values ranging between $9.30 - 9.50\ eV$ [8]. Then, the theoretical and the experimental values are reasonably close given that the former does not account for the effect of the field of the surrounding atoms on the orbital energy and the extra-atomic relaxation. This result when combined with conclusions from (Graphs. 3. 2, 3, 4) that the average total atomic energy (calculated by the *eal* method) at different valence electron configurations changes in accordance with the minimum total energy (calculated by the *mdf* method) supports the validity of using the *eal* method for the theoretical calculations of the spectroscopic features (binding energies, Auger kinetic energies and the Auger parameters) in this chapter, and for the atomic structure calculations for the potential model.

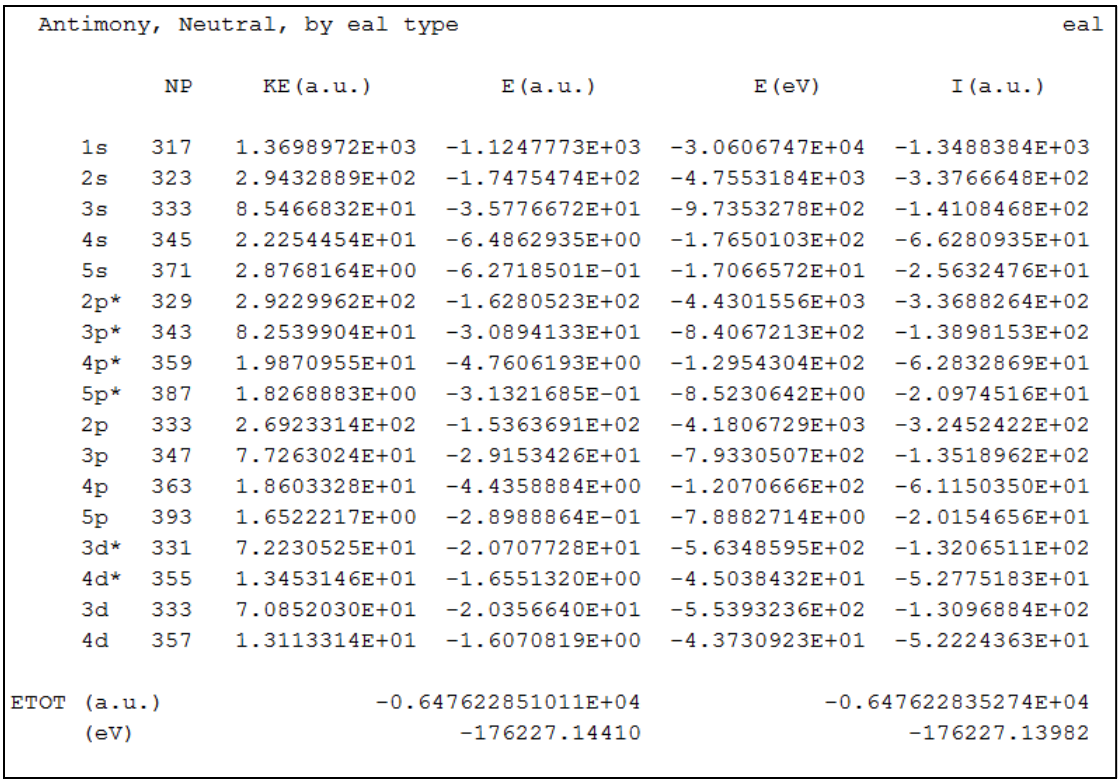

```
 Antimony, Neutral, by eal type                                         eal

           NP     KE(a.u.)         E(a.u.)          E(eV)          I(a.u.)

     1s   317   1.3698972E+03  -1.1247773E+03  -3.0606747E+04  -1.3488384E+03
     2s   323   2.9432889E+02  -1.7475474E+02  -4.7553184E+03  -3.3766648E+02
     3s   333   8.5466832E+01  -3.5776672E+01  -9.7353278E+02  -1.4108468E+02
     4s   345   2.2254454E+01  -6.4862935E+00  -1.7650103E+02  -6.6280935E+01
     5s   371   2.8768164E+00  -6.2718501E-01  -1.7066572E+01  -2.5632476E+01
     2p*  329   2.9229962E+02  -1.6280523E+02  -4.4301556E+03  -3.3688264E+02
     3p*  343   8.2539904E+01  -3.0894133E+01  -8.4067213E+02  -1.3898153E+02
     4p*  359   1.9870955E+01  -4.7606193E+00  -1.2954304E+02  -6.2832869E+01
     5p*  387   1.8268883E+00  -3.1321685E-01  -8.5230642E+00  -2.0974516E+01
     2p   333   2.6923314E+02  -1.5363691E+02  -4.1806729E+03  -3.2452422E+02
     3p   347   7.7263024E+01  -2.9153426E+01  -7.9330507E+02  -1.3518962E+02
     4p   363   1.8603328E+01  -4.4358884E+00  -1.2070666E+02  -6.1150350E+01
     5p   393   1.6522217E+00  -2.8988864E-01  -7.8882714E+00  -2.0154656E+01
     3d*  331   7.2230525E+01  -2.0707728E+01  -5.6348595E+02  -1.3206511E+02
     4d*  355   1.3453146E+01  -1.6551320E+00  -4.5038432E+01  -5.2775183E+01
     3d   333   7.0852030E+01  -2.0356640E+01  -5.5393236E+02  -1.3096884E+02
     4d   357   1.3113314E+01  -1.6070819E+00  -4.3730923E+01  -5.2224363E+01

ETOT (a.u.)               -0.647622851011E+04             -0.647622835274E+04
     (eV)                        -176227.14410                   -176227.13982
```

Fig. 3.1: A caption from the MCDFGME program output shows the orbital and total energies (`ETOT`) of the closed core elemental Sb atom. The first column contains the term symbol of the orbitals, where the orbitals denoted `nl*` are the ($l - 1/2$) doublet components. Column 5 contains the orbital energies in `eV` units. The energies of the $3d_{5/2}$ and $3d_{3/2}$ orbitals are $-553.93\ eV$ and -563.49×10^2 respectively.

3.2.1.2.2: $4d$ Binding energy:

Considering the atomic core as a charged sphere as described in (Sec. 1.3.1.1.), one would expect the BE_{4d} and BE_{3d} to behave in a similar fashion which is the case as shown in (Graphs. 3. 6, 7).

3.2.1.3: $M_{4,5}N_{4,5}N_{4,5}$ Auger kinetic energy:

The kinetic energy of the Auger electron can be calculated using two methods. The first is by considering the binding energies of the three atomic levels involved in the emission process

$$KE_{Auger} = BE_1 - BE_2 - BE_3 \quad (3.4)$$

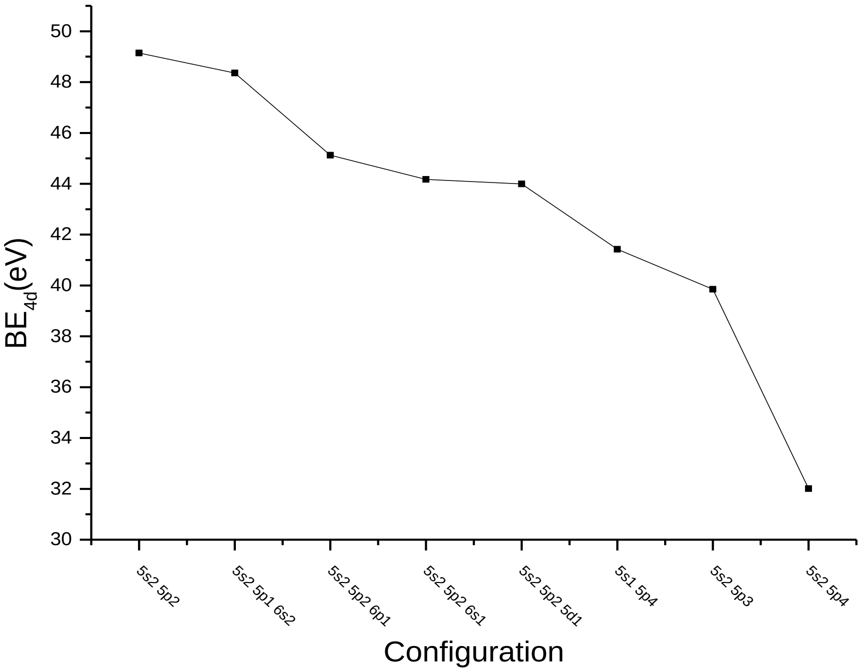

Graph. 3.7 Binding energy of the Sb 4d level for several valence electron configurations calculated using (Eq. 3.1). The results are listed in (Table. 3.6).

For the case of the $M_{4,5}N_{4,5}N_{4,5}$ transitions the two holes in the final state (2 and 3 in (Eq.3.4)) are in the same level. Therefore, the first equation for calculating the Auger energy becomes:

$$KE_{M_{4,5}N_{4,5}N_{4,5}} = BE_{3d} - 2BE_{4d} \qquad (3.5)$$

The second method is to subtract the total energy of the ion with two final state 4d holes from that of the atom with a single 3d hole.

$$KE_{M_{4,5}N_{4,5}N_{4,5}} = ETOT_{ion}(3d) - ETOT_{ion}(4d^2) \qquad (3.6)$$

The first approach ignores the Coulomb repulsion between the two final state holes and only includes atomic relaxation around an atom in a single hole state. Therefore, the second approach should be more realistic.

The difference between the Auger KE calculated by the two methods (Table. 3.7) varies significantly with the valence electron configuration, which means that the atomic relaxation is sensitive to the chemical environment.

Valence electron Configuration	$\boldsymbol{KE^1_{M_{4,5}N_{4,5}N_{4,5}}\ (eV)}$	$\boldsymbol{KE^2_{M_{4,5}N_{4,5}N_{4,5}}\ (eV)}$	$\boldsymbol{\Delta KE_{M_{4,5}N_{4,5}N_{4,5}}\ (eV)}$
$5s^2\ 5p^4$	468.25	454.16	14.09
$5s^2\ 5p^3$	460.49	444.63	15.86
$5s^2\ 5p^2\ 6s^1$	456.28	440.26	16.02
$5s^2\ 5p^2\ 6p^1$	455.35	439.39	15.96
$5s^2\ 5p^2\ 5d^1$	456.46	441.54	14.92
$5s^2\ 5p^2$	451.36	434.13	17.24
$5s^1\ 5p^4$	459.02	443.30	15.72
$5s^2\ 5p^1\ 6s^2$	452.27	436.02	16.24

Table. 3.7 The values of $KE_{M_{4,5}N_{4,5}N_{4,5}}$ calculated using (Eq.3.5, 6): as follows: $KE^1_{Auger} = E_B(1) - E_B(2) - E_B(3)$, $KE^2_{Auger} = E_{ion}(3d) - E_{ion}(4d^2)$. ΔKE is the difference between the Auger kinetic energy calculated by the two methods. This difference arises from the interaction between the two $4d$ holes. This interaction is not accounted for in the first method.

(Graph. 3.9) provides a visual analysis of the relation between the atomic relaxation and the valence electron configuration. The charge state of the atom changes the relaxation significantly. This is clear from comparing $\Delta Auger$ for $5s^2\ 5p^2$ and $5s^2\ 5p^4$ with that of the ground state ($5s^2\ 5p^3$). $\Delta Auger$ differs by $3.14\ eV$ between Sb^+ and Sb^- as in (Table. 3.7). (Graph. 3.9) also shows that 6s and 6p orbitals have similar spatial distributions to 5p, whereas 5d is more localised. In general, (Graph. 3.9) confirms that the Auger KE is an accurate probe of the local charge and the distribution of valence charge as explained in (Sec.1.2.2.1).

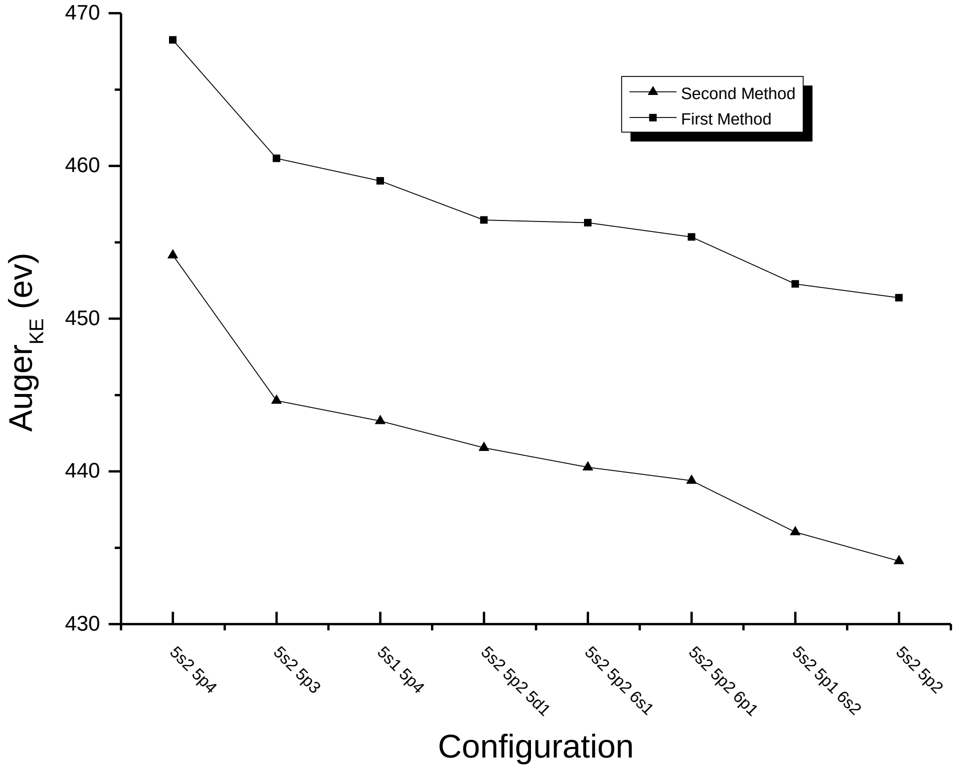

Graph. 3.8 The $KE_{M_{4,5}N_{4,5}N_{4,5}}$ calculated by the two methods for different valence electron configurations.

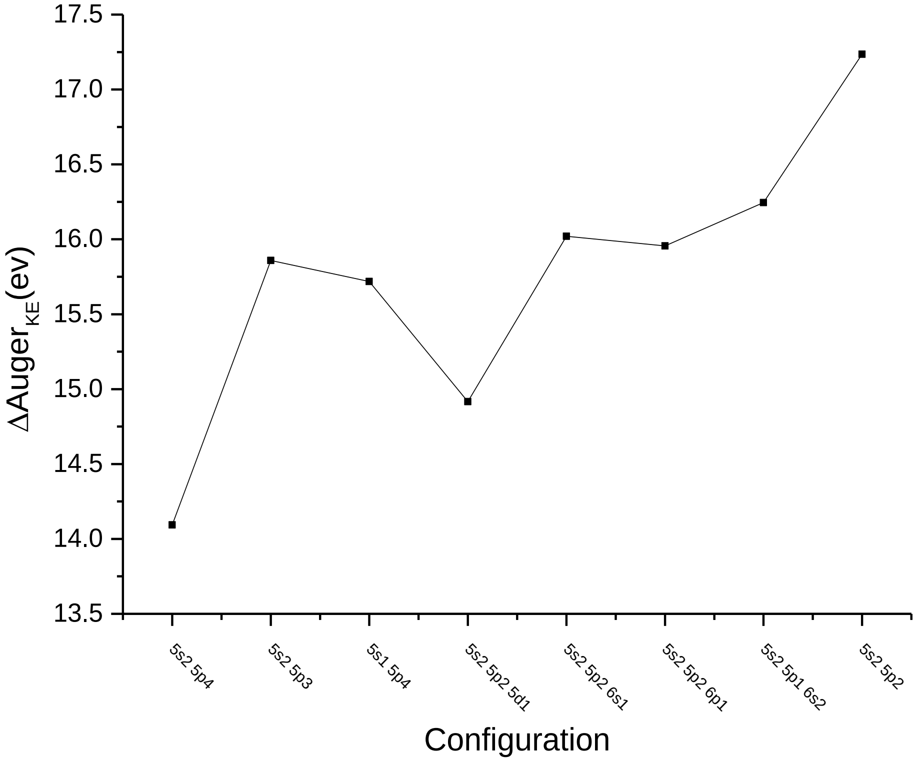

Graph. 3.9 The difference in the $KE_{M_{4,5}N_{4,5}N_{4,5}}$ that is calculated by the two methods (Eq.3.5, 6). This difference is sensitive to the atomic relaxation.

3.2.1.4: The Auger parameter:

The original Auger parameter (α) was defined as the difference between the kinetic energy of an identified component of Auger profile and the binding energy of the sharpest line in the XPS spectrum of an element [11]:

$$\alpha = KE_{Auger} - BE \quad (3.7)$$

The value of α depends on the nature of the element and its chemical state and is independent on the position of the Fermi level or the surface charging of insulators. It is an important tool in identifying chemical states.

The following expression which is called the modified Auger parameter [6, 12-14] will be used in calculating the Auger parameter (AP):

$$\alpha = KE_{Auger} + BE \quad (3.8)$$

where BE and KE_{Auger} are calculated from the atomic structure calculations using (Eq. 3. 1, 6) respectively.

For the cases of Sb and In atoms which are studied in this work, the value of the Auger parameter is given as:

$$\alpha = KE_{M_{4,5}N_{4,5}N_{4,5}} + BE_{3d} \quad (3.9)$$

Configuration	$\boldsymbol{\alpha}$ ***eV*** **from** $\boldsymbol{KE^2_{M_{4,5}N_{4,5}N_{4,5}}}$
$5s^2\ 5p^4$	986.43
$5s^2\ 5p^2\ 5d^1$	985.98
$5s^1\ 5p^4$	985.18
$5s^2\ 5p^1\ 6s^2$	985.01
$5s^2\ 5p^2\ 6p^1$	984.99
$5s^2\ 5p^2\ 6s^1$	984.90
$5s^2\ 5p^3$	984.82
$5s^2\ 5p^2$	983.78

Table. 3.8. The values of the Auger parameter of Sb calculated from the atomic structure calculations using (Eq. 3.9) for different charge states and valence electron configurations.

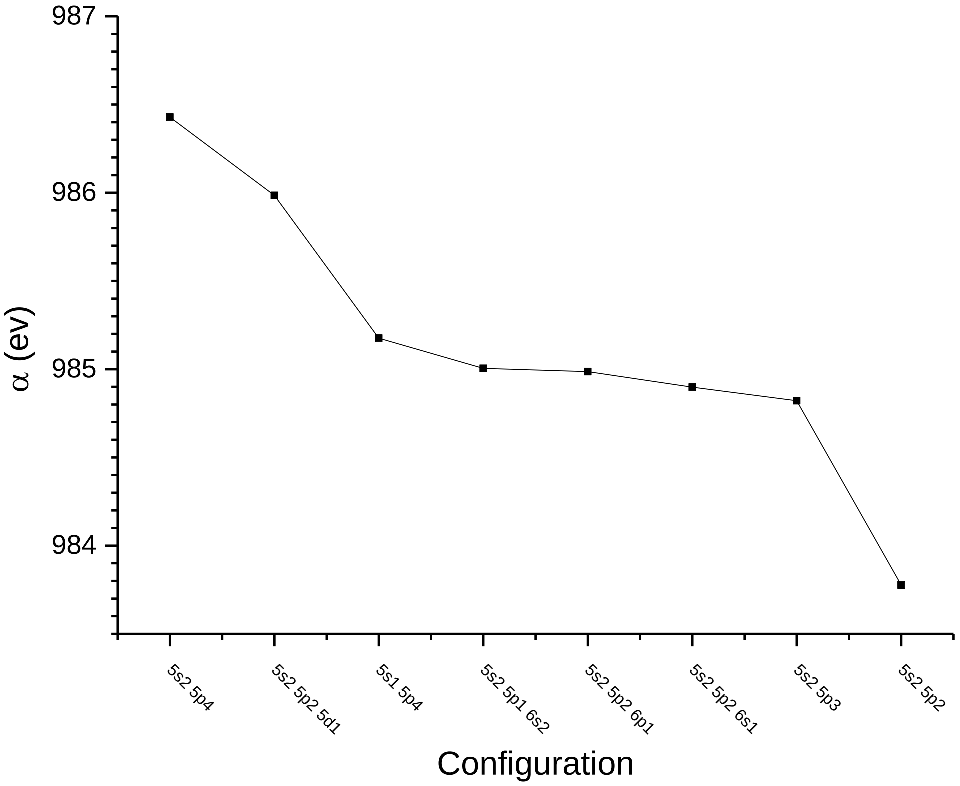

Graph. 3.10. The values of the Auger parameter of Sb calculated from the atomic structure calculations using (Eq. 3.9). The values are listed in (Table. 3.8).

(Table. 3.8) shows the sensitivity of the Auger parameter to the chemical state. The difference between AP of the ground state of Sb ($5s^2$ $5p^3$) and AP of Sb^-: $5s^2$ $5p^4$ is $1.61\ eV$, whereas the difference between the ground state and Sb^+: $5s^2$ $5p^2$ is $-1.04\ eV$.

3.2.2. Valence electron configuration changing with creation of a core hole:

In (Sec. 3.2.1), valence electron configuration was assumed not to be affected by the creation of a core hole following an electron emission, or two core holes following an Auger emission. However, the effective nuclear charge is expected to increase following such events which leads to the attraction of more negative charge to the valence level in solids. Different changes to the valence electron configuration due to core hole creation will be considered as in the (Sec.3.2.1). Then, the relations between the electron configuration and the spectral energies (BE, KE and α) will be plotted as in (Graphs. 3. 6,8,10). (Table. 3.9) lists the theoretical values of Sb (BE, KE and α) calculated using (Eq. 3. 1,6,9). Different ground state configurations were considered, as well as different scenarios of the change in the configuration due to the creation of single core hole (after photoemission), and two core holes (after the Auger process).

Since the *eal* type is used to calculate the total atomic energies from this section onward, the total atomic angular momentum is not entered in the input of the MCDFGME program. Therefore, the occupations of the open (unfilled) subshells are not specified e.g. it is not specified in the input whether the unoccupied orbital in a p^5 shell is $p_{3/2}$ or $p_{5/2}$. In this case, the program calculates the average total energy over all possible configurations and orbital occupations as described in (Sec.3.2.1.1.1).

Configuration			**Energy (eV)**		
Ground State	**After Creation of a 3d hole**	**After Creation of $4d^2$ holes**	BE_{3d}	$KE_{M_{4,5}N_{4,5}N_{4,5}}$	α
Sb^-: $5s^2$ $5p^4$	Sb^-: $5s^2$ $5p^5$	Sb^-: $5s^2$ $5p^6$	530.57	464.91	995.48
		Sb:$5s^2$ $5p^5$	530.57	462.43	993.01
	Sb: $5s^2$ $5p^4$	Sb:$5s^2$ $5p^5$	532.27	464.13	996.41
		Sb^+:$5s^2$ $5p^4$	532.27	454.156	986.43
	Sb^+: $5s^2$ $5p^3$	Sb^{+2}:$5s^2$ $5p^3$	541.15	444.63	985.78
		Sb^{+3}: $5s^2$ $5p^2$	541.15	417.05	958.20
Sb: $5s^2$ $5p^3$	Sb: $5s^2$ $5p^4$	Sb: $5s^2$ $5p^5$	531.31	464.13	995.45
		Sb^+: $5s^2$ $5p^4$	531.31	454.16	985.47
	Sb^+: $5s^2$ $5p^3$	Sb^+: $5s^2$ $5p^4$	540.19	463.04	1003.23
		Sb^{+2}: $5s^2$ $5p^3$	540.19	444.63	984.82
	Sb^{+2}: $5s^2$ $5p^2$	Sb^{+3}: $5s^2$ $5p^2$	557.27	434.13	991.40
		Sb^{+4}: $5s^2$ $5p^1$	557.27	396.73	954.00
Sb^+: $5s^2$ $5p^2$	Sb^+: $5s^2$ $5p^3$	Sb^+: $5s^2$ $5p^4$	532.57	463.04	995.61
		Sb^{+2}: $5s^2$ $5p^3$	532.57	444.63	977.20
	Sb^{+2}: $5s^2$ $5p^2$	Sb^{+2}: $5s^2$ $5p^3$	549.65	461.71	1011.36
		Sb^{+3}: $5s^2$ $5p^2$	549.65	434.13	983.78
	Sb^{+3}: $5s^2$ $5p^1$	Sb^{+4}: $5s^2$ $5p^1$	575.74	422.82	998.55
		Sb^{+5}: $5s^2$	575.74	375.02	950.76

Table. 3.9. Spectral values of Sb at various ground state configurations, and different configurations of the relaxed atom after photoemission and Auger process. The atomic term symbol, which describes the total atomic angular momentum, is not specified, because the eal type of calculations is used. In this type, the total atomic energy is averaged over all possible electron configurations and orbital occupations.

(Graph. 3.11) shows the relation between valence electron configuration (of the ground state of Sb atom and of the relaxed ion after a photoemission of an electron from 3d level) and BE_{3d}. The 5s subshell is considered to be always felled, so it is not included in the configurations in this graph. The values of the binding energy were taken from (Table. 3.9).

Similarly for $KE_{M_{4,5}N_{4,5}N_{4,5}}$, (Graph. 3.12) shows the relation between the kinetic energy of the Auger electron and the valence electron configurations of the initial and final states of the Sb atom. (Graph. 3.13) shows the corresponding results of the Auger parameter.

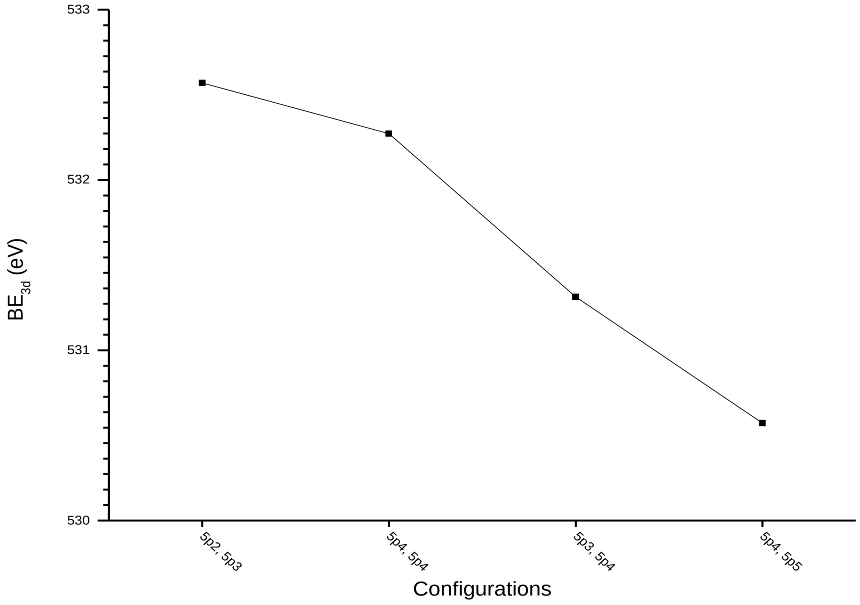

Graph. 3.11. The values of the binding energy of the Sb 3d electrons corresponding to various assumptions of the valence electron configurations in the initial and the final states. The 5s level was assumed to be always filled (5s^{2}), therefore it is not included in the configurations e.g. the set (5p^{2}, 5p^{3}) means that the valence level configuration of the initial state is (5s^{2} 5p^{2}) and that of the relaxed ion after the photoemission of a 3d electron is (5s^{2} 5p^{3}), which means that the atom attracted an electron to its valence level after it was core ionised. It should be noted that the total angular momentum of the electrons in the open 5p shell is (as explained in the text) an average of $5p_{3/2}$ and $5p_{5/2}$ since the eal type of calculations. The same is said for the 3d electron for which the binding energy is calculated. The values of the binding energies are listed in (Table. 3.9)

The theoretical spectral values in (Table. 3.9) are widely spread. So only those which are close to the experimental values (Table.5.3) were used to make the theoretical plots (Graphs.3. 11, 12, 13).

In (Sec.3.2.1.2.1), where the valence level is assumed not to change by the creation of a core hole after the emission of a $3d$ electron, the binding energy of this electron was $540.19\ eV$ for the Sb atom in its ground (neutral) state ($5s^2$ $5p^3$). However in this section, different valence electron configurations were assumed for the final state of the atom after creation of $3d$ hole (Table.3.9). Since solid Sb is semi-metal, it is reasonable to assume the availability of a free electron to be attracted to the valence level when a core hole is created, making the valence level configuration $5s^2$ $5p^4$. In this case, BE_{3d} is $531.31\ eV$. The binding energy of $3d_{5/2}$ line in solid Sb has been reported around $528.20\ eV$ [8], which is a value closer to the theoretical one obtained when Sb atom was assumed to attract a free electron after emitting a $3d$ electron. The difference between the theoretical and the experimental value is expected since the former does not account for the solid state effects such as the compression of the valence level wavefunction and the extra-atomic relaxation (Sec.1.4.2). The binding energy of Sb $3d_{5/2}$ line in gaseous Sb_4 was reported to be $534.6 \pm 0.6\ eV$ [15], which is higher than the theoretical value of $531.31\ eV$. This is because (unlike

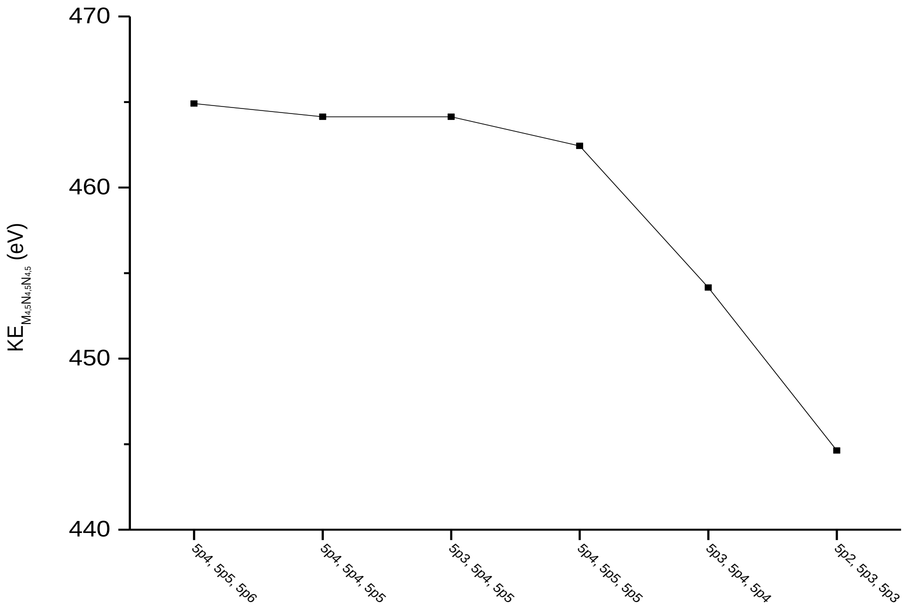

Graph 3.12 The $M_{4,5}N_{4,5}N_{4,5}$ Auger kinetic energy for various initial and final state configurations.

the case of solid), the emitting atom is surrounded by three atoms only leading to a significant reduction in the extra-atomic relaxation.

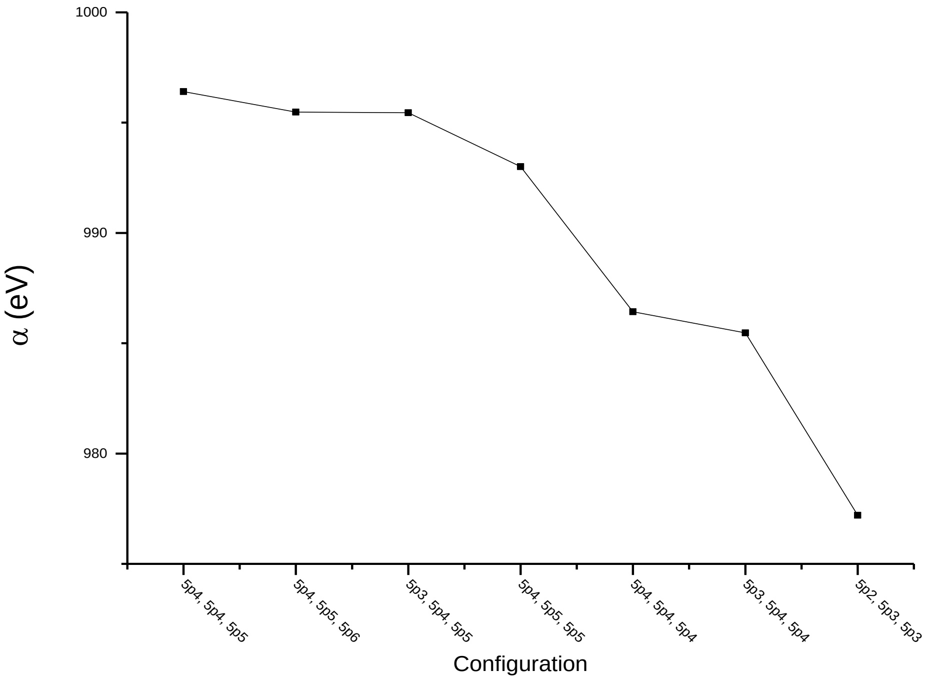

Graph. 3.13 The abscissa is sets of Sb valence level configurations. Each set includes the ground state configuration, the configuration after the creation of a hole in the $3d$ level, and the configuration after the creation of two holes in the $4d$ level. The ordinate is the Auger parameter values corresponding to each set of configurations.

3.3. In Calculations:

All the calculations that were made for the Sb atom are repeated for In in this section.

3.3.1: Fixed valence electron configuration:

In this section the valence electron configuration is assumed not to change by the creation of a core hole.

3.3.1.1: Total energies

The total energies of the In atom at a specific total angular momentum (J) will not be calculated using the *mdf* method since it was concluded in section (3.2.1.2.1) that the calculations of the average total energies using the *eal* type is appropriate to obtain the theoretical spectral features.

3.3.1.1.1: Closed-core atom

(Table.3.10) lists the total atomic energies of a closed core In atom at different valence electron configurations.

Valence Level Configuration	$ETOT\ (eV)$
In^-: $5s^2\ 5p^2$	No convergence
In: $5s^2\ 5p^1$	-159912.57
In: $5s^2\ 5d^1$	-159908.98
In^+: $5s^2\ 5p^0$	-159907.44
In^+: $5s^1\ 5p^1$	-159902.34
In^{2+}: $5s^1$	-159890.41

Table. 3.10. Different closed-core In atom valence level configurations and their corresponding average total atomic energies.

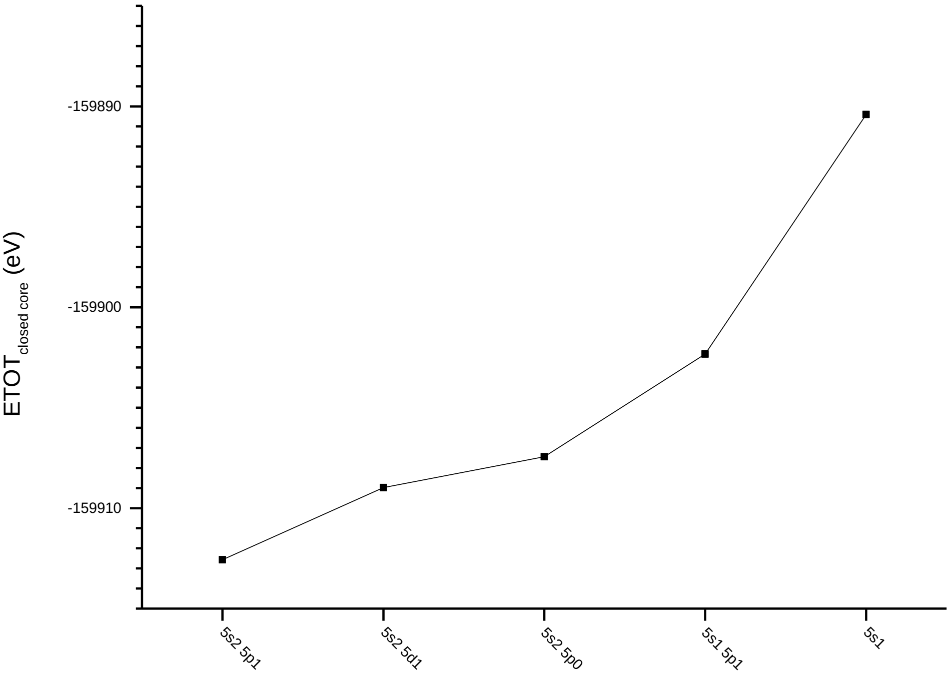

Graph. 3.14 Various closed-core In atom configurations and their corresponding total atomic energies.

The self-consistent field procedure does not converge to a final solution of the wavefunction of the In atom having the valence electron configuration $5s2\ 5p2$.

3.3.1.1.2: An In atom having a $3d$ hole:

Valence Level Configuration	$ETOT_{3d\ hole}\ (eV)$
In: $5s^2\ 5p^2$	-159464.48
In^+: $5s^2\ 5p^1$	-159458.15
In^+: $5s^2\ 5d^1$	-159450.62
In^{2+}: $5s^2\ 5p^0$	-159444.59
In^{2+}: $5s^1\ 5p^1$	-159438.00
In^{3+}: $5s^1$	-159416.43

Table. 3.11. Various valence electro configurations of In atom having a $3d$ hole and their corresponding average total atomic energies.

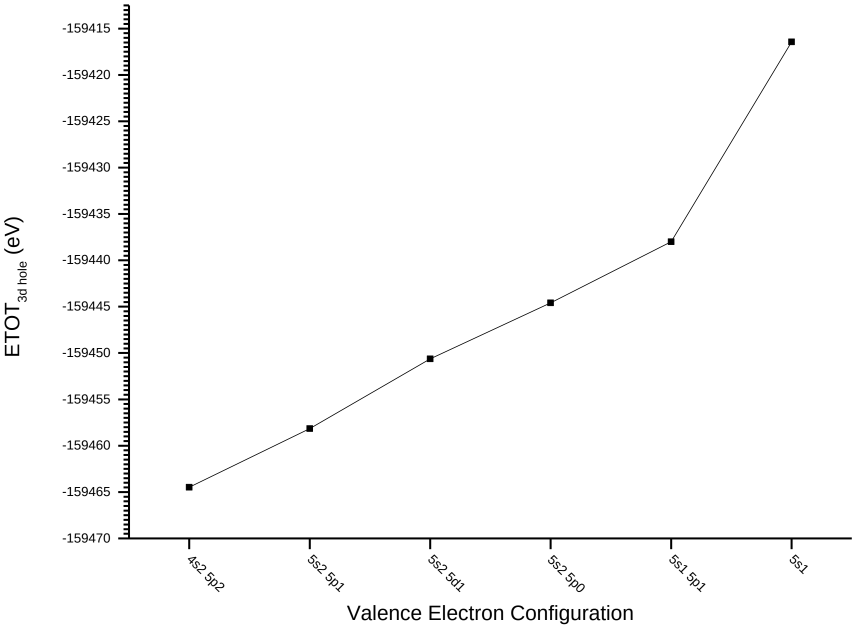

Graph. 3.15 The average total atomic energies at different valence electron configurations of In atom having a hole in the 3d level.

3.3.1.1.3: An atom having $4d^2$ holes:

Valence Level Configuration	$\boldsymbol{ETOT_{4d^2\ hole}\ (eV)}$
In^{+}: $5s^2\ 5p^2$	-159464.48
In^{2+}: $5s^2\ 5p^1$	-159458.15
In^{2+}: $5s^2\ 5d^1$	-159450.62
In^{3+}: $5s^2\ 5p^0$	-159444.59
In^{3+}: $5s^1\ 5p^1$	-159438.00
In^{4+}: $5s^1$	-159416.43

Table. 3.12. Various valence electro configurations of In atom having a $4d^2$ holes and their corresponding average total atomic energies.

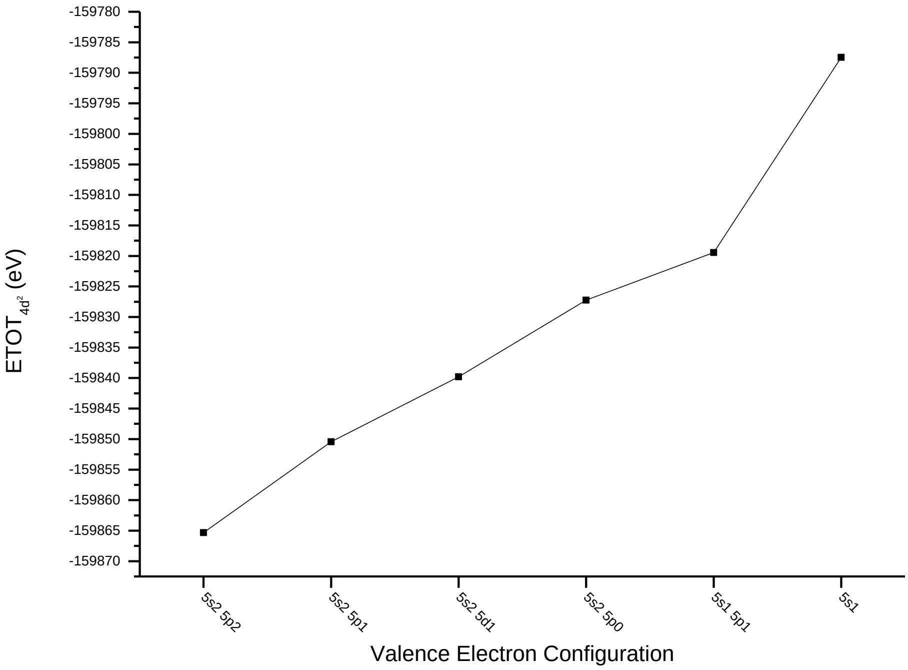

Graph. 3.16 The average total atomic energies at different valence electron configurations of In atom having $4d^2$ holes in the 3d level.

3.3.1.2: Binding Energy:

(Equation. 3.1) was used to calculate the binding energies (BE) of the $3d$ and $4d^2$ hole states for various valence electron configurations of In atom.

3.3.1.2.1. The BE of the In $3d$ hole state:

Valence Electron Configuration	BE_{3d} (eV)
$5s^2\ 5p^1$	454.42
$5s^2\ 5d^1$	458.35
$5s^2\ 5p^0$	462.85
$5s^1\ 5p^1$	464.34
$5s^1$	473.98

Table. 3.13 Indium $3d$ biding energy at different valence electron configurations.

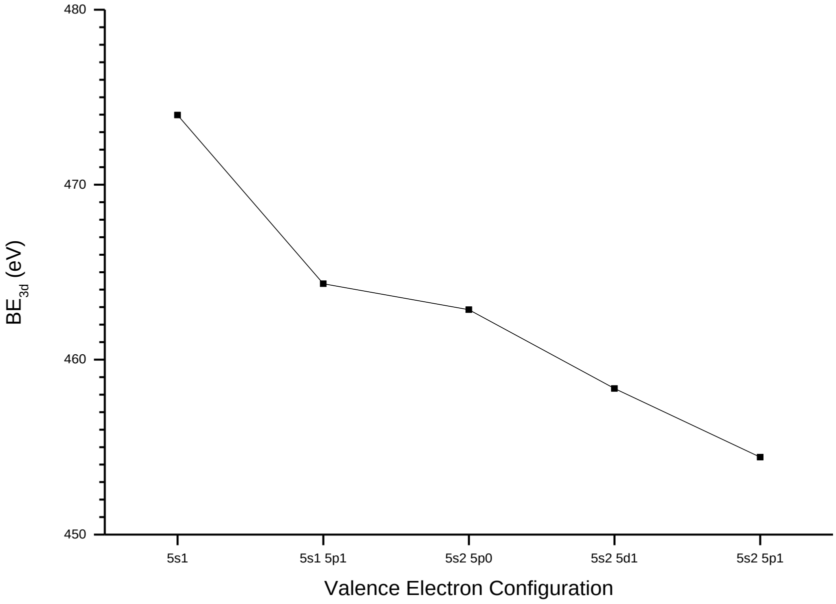

Graph. 3.17 Valence electron configurations of In atom vs. $3d$ level binding energy.

3.3.1.2.2. The BE of the In $4d^2$ hole state:

Valence Electron Configuration	BE_{4d^2} (eV)
$5s^2\ 5p^1$	62.14
$5s^2\ 5d^1$	69.18
$5s^2\ 5p^0$	80.21
$5s^1\ 5p^1$	82.89
$5s^1$	102.93

Table. 3.14. Indium $4d^2$ holes biding energy at different valence electron configurations.

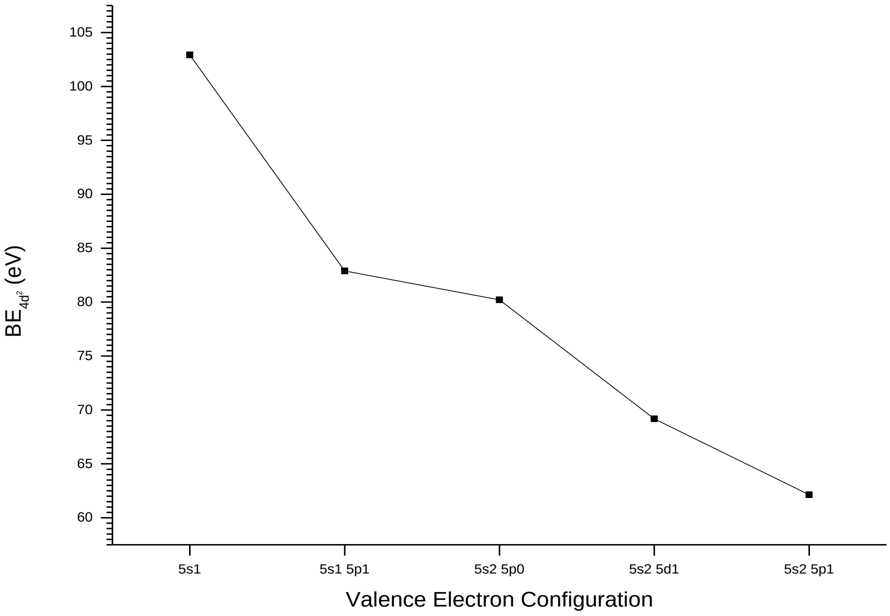

Graph. 3.18. Various valence electron configurations of In atom vs. corresponding $4d^2$ holes binding energy.

3.3.1.3. The In $M_{4,5}N_{4,5}N_{4,5}$ Auger Kinetic Energy:

(Equation. 3.6) was used to calculate the kinetic energy of the $M_{4,5}N_{4,5}N_{4,5}$ Auger line of In atom at various valence electron configurations including $5s^2$ $5p^2$ for which BE_{3d} and BE_{4d^2} were not calculated in the previous two sections because the SCF procedure does not converge for this configuration at the closed core In atom. However, the value of the Auger kinetic energy can be calculated using (Equation. 3.6) without knowledge of the $ETOT_{closed\ core}$.

Valence Electron Configuration	$KE_{M_{4,5}N_{4,5}N_{4,5}}$ (eV)
$5s^2$ $5p^2$	400.84
$5s^2$ $5p^1$	392.28
$5s^2$ $5d^1$	389.17
$5s^2$ $5p^0$	382.65
$5s^1$ $5p^1$	381.45
$5s^1$	371.05

Table. 3.15. The kinetic energy of the $M_{4,5}N_{4,5}N_{4,5}$ Auger line at various valence electron configurations.

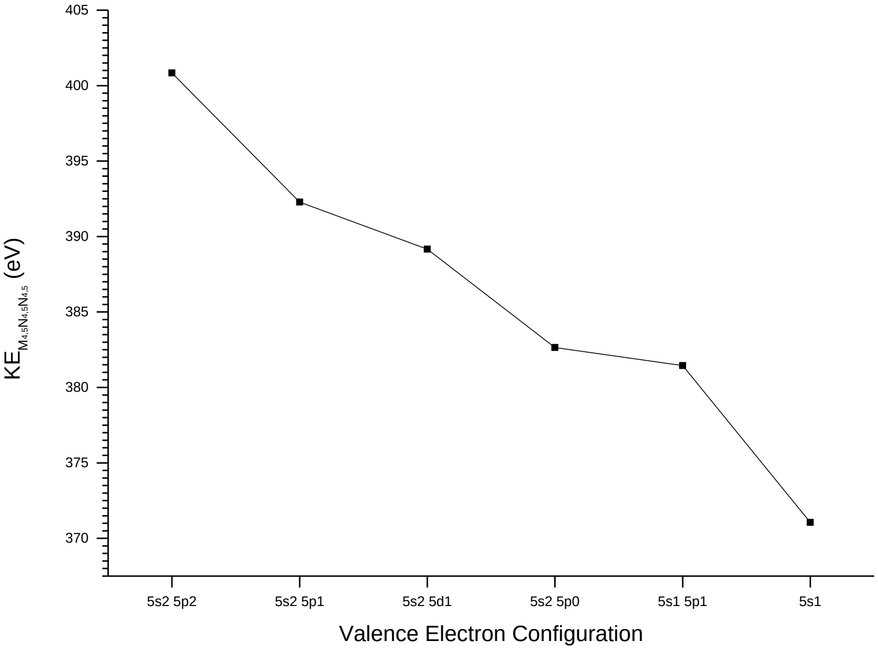

Graph. 3.19. Valence electron configuration vs. the kinetic energy of the $M_{4,5}N_{4,5}N_{4,5}$ Auger line.

3.3.1.4. The In Auger parameter (α):

(Eq. 3.9) was used to calculate the values of the Auger parameter α associated with the valence electron configurations above except the case of $5s2\ 5p2$ as the BE_{3d} cannot be obtained.

Valence Electron Configuration	$\boldsymbol{\alpha\ (eV)}$
In: $5s^2\ 5d^1$	847.52
In: $5s^2\ 5p^1$	846.71
In^+: $5s^1\ 5p^1$	845.79
In^+: $5s^2\ 5p^0$	845.50
In^{2+}: $5s^1$	845.03

Table. 3.16. The Auger parameter values at various valence electron configurations.

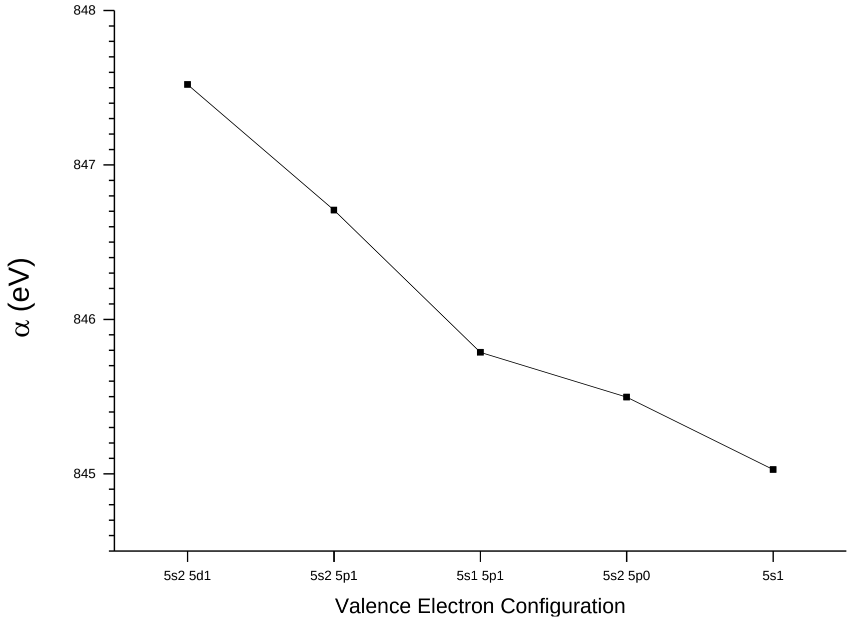

Graph. 3.20. Valence electron configurations vs. the values of the Auger parameter for In atom.

3.3.2. Valence electron configuration changing with hole creation:

As in (section. 3.2.2) for Sb, the spectral values of In are calculated with account is taken of possible change to the valence electron configuration in the final state of the emission.

As indicated in (Sec. 3.3.1.1.1), the total energy of the atom in the ground state at the configuration $5s^2\ 5p^2$ cannot be obtained theoretically, consequently it is not possible to calculate BE_{3d} as the term $ETOT_{(N)}$ in (Eq.3.1) is not available, and hence α cannot be calculated (Eq.3.8). However, the kinetic energy of the $M_{4,5}N_{4,5}N_{4,5}$ Auger line can be calculated as it is independent of the ground state (the initial state) of the photoemission.

The theoretical spectroscopic values in (Table. 3.17) are widely spread. So only those which are close to the experimental values in (Table. 5.3) will be used to make the theoretical plots.

Valence electron configuration			Spectral Energies		
Ground state	After creation of a $3d$ hole	After creation of $4d^2$ holes	$BE_{3d}(eV)$	$KE_{M_{4,5}N_{4,5}N_{4,5}}\ (eV)$	$\alpha\ (eV)$
$5s^2\ 5p^2$	$5s^2\ 5p^3$	$5s^2\ 5p^4$	--	408.91	--
		$5s^2\ 5p^3$	--	407.93	--
	$5s^2\ 5p^2$	$5s^2\ 5p^3$	--	408.26	--
		$5s^2\ 5p^2$	--	400.84	--
	$5s^2\ 5p^1$	$5s^2\ 5p^1$	--	392.28	--
		$5s^2$	--	369.09	--
$5s^2\ 5p^1$	$5s^2\ 5p^2$	$5s^2\ 5p^3$	448.09	408.26	856.35
		$5s^2\ 5p^2$	448.09	400.84	848.93
	$5s^2\ 5p^1$	$5s^2\ 5p^2$	454.43	407.18	861.61
		$5s^2\ 5p^1$	454.43	392.28	846.71
	$5s^2$	$5s^2$	467.98	382.65	850.63
		$5s^1$	467.98	342.89	810.88
$5s^2$	$5s^2\ 5p^1$	$5s^2\ 5p^2$	449.30	407.18	856.48
		$5s^2\ 5p^1$	449.30	392.28	841.58
	$5s^2$	$5s^2\ 5p^1$	462.85	405.84	868.69
		$5s^2$	462.85	382.65	845.50
	$5s^1$	$5s^1$	491.01	371.05	862.06
		$4d^8$	491.01	320.03	811.04

Table. 3.17. Theoretical spectroscopic values of In at different ground and final state configurations.

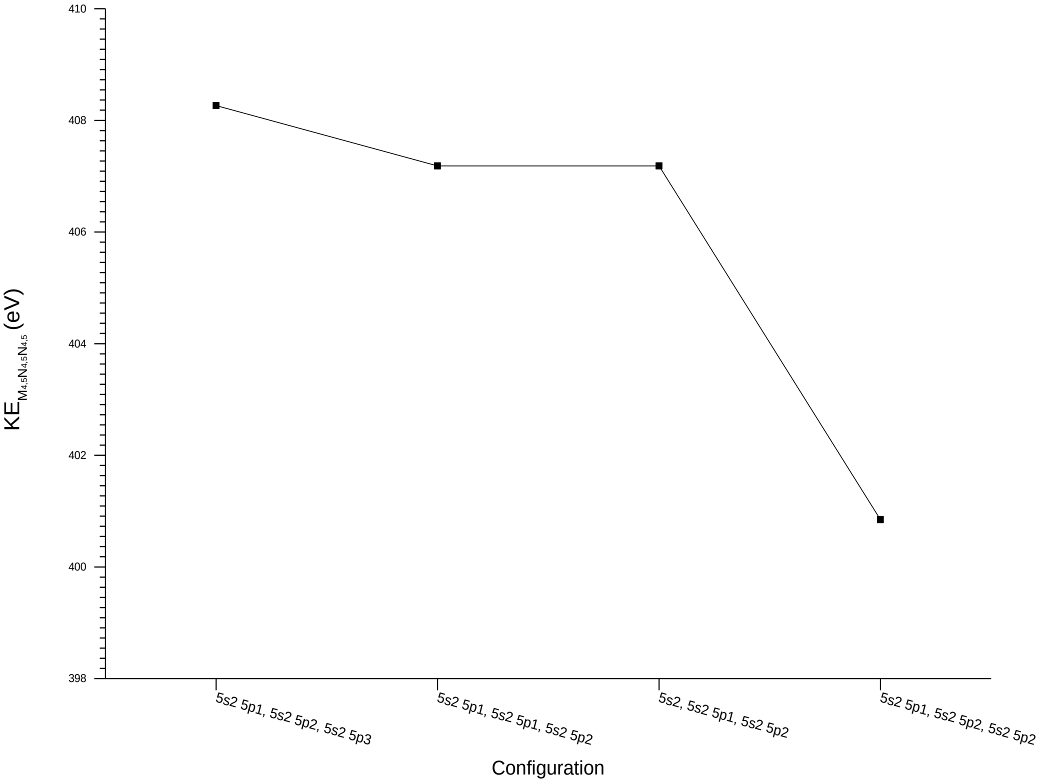

Graph. 3.21. In $KE_{M_{4,5}N_{4,5}N_{4,5}}$ for different sets of valence level configurations. Each set contain the configuration for the closed core In atom, for the atom after the emission of a 3d electron, and the configuration for the atom having 2 4d holes (after the Auger emission of a 4d electron). The second and the third sets result in the same KE value since they have the same configuration for the initial and the final state of the Auger process, yet both are included because they differ in the ground state (the closed core atom).

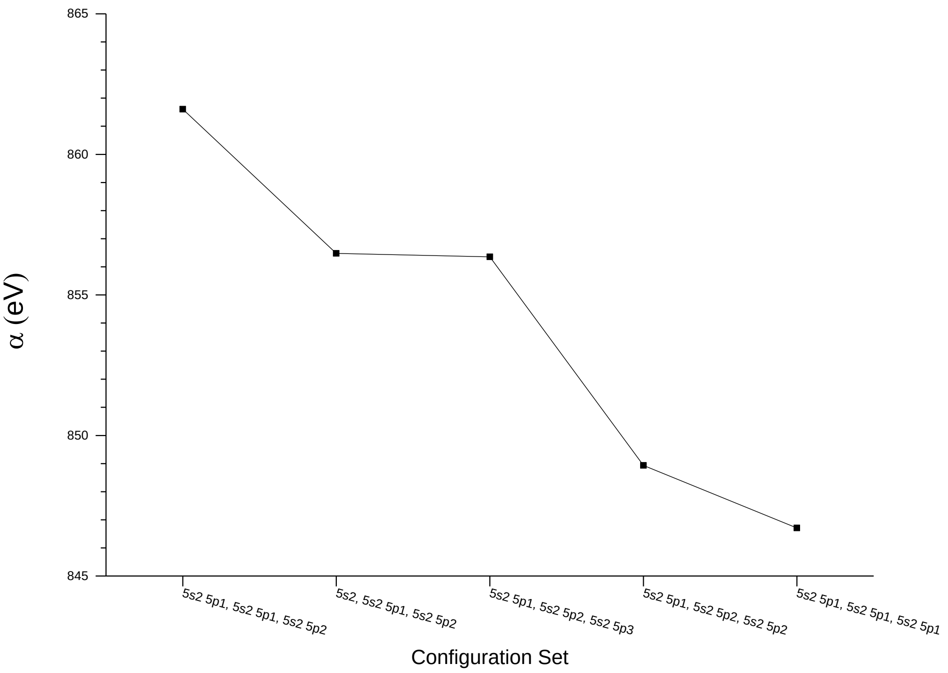

Graph. 3.22. In α for various ground and ionised state configurations.

Since the ground state of the atom (before bombardment by x-ray) is not involved in the Auger process, the kinetic energy of the Auger electron is not sensitive to the charge and configuration of the valence level in a certain chemical state. However, the Auger parameter as defined by (Eq.3.8) is sensitive to the ground state of the atom and to the relaxation.

(Graph.3.22) shows that the two configuration sets ($5s^2$, $5s^2$ $5p^1$, $5s^2$ $5p^2$) and ($5s^2$ $5p^1$, $5s^2$ $5p^2$, $5s^2$ $5p^3$) result in almost equal values of the Auger parameter, although their valence levels in the ground states are different by one electron ($5p^1$) whose binding energy, as obtained from (Table.3.10) using (Eq.3.1), is $5.13\ eV$. Both configuration sets assume the same mechanism of relaxation of In atom; an electron is attracted to the valence level when a core hole is created. In contrast, the configuration sets whose ground states are the same ($5s^2$ $5p^1$) but assume different relaxation mechanisms result in significantly different values of the Auger parameter. This shows that the relaxation contributes to the value of the Auger parameter far more than the initial valence charge. It was shown in (Sec.1.2.4) that the contribution of the valence charge in the ground state is completely eliminated by studying the shift of the Auger parameter ($\Delta\alpha$) between chemical states rather than α itself (Eq.1.23).

3.4. Summary:

Thorough analysis of the atomic structure calculations and how they are performed by the MCDFGME program have been performed. Different features have been discussed including the difference between calculations by the *eal* and the *mdf* types in the program, the effects of relaxation and valence charge on the total energy of the atom, and the energies of the spectroscopic features (binding energies, Auger kinetic energies, and the Auger parameter). This concludes the theoretical discussion of the atomic structure studies which has been put in a solid form. (Ch.7) will include the use of the eigenvalues of the $3d$ levels, in the way described by [16], to calculate the atomic potential parameters of In and Sb atoms discussed in (Sec.1.4.2).

The following three chapters include the analysis of the experimental results of electron spectroscopy performed on metallic elemental In and Sb, $Sb/InSb$, and $InSb$.

References

1. Gregory, D., et al., *Atomic structure calculations for the analysis of Auger parameters of elements K to Kr.* Journal of Physics: Condensed Matter, 1993. **5**(23): p. 3843.
2. Grunthaner, F., et al., *High-Resolution X-Ray Photoelectron Spectroscopy as a Probe of Local Atomic Structure: Application to Amorphous Si O 2 and the Si-Si O 2 Interface.* Physical Review Letters, 1979. **43**(22): p. 1683.
3. Moretti, G., *Auger parameter and Wagner plot in the characterization of chemical states by X-ray photoelectron spectroscopy: a review.* Journal of electron spectroscopy and related phenomena, 1998. **95**(2): p. 95-144.
4. Streubel, P., et al., *Chemical state information from photoelectron and Auger electron lines-investigation of potential and relaxation effects of solid silicon and phosphorus compounds.* Journal of electron spectroscopy and related phenomena, 1991. **57**(1): p. 1-13.
5. Desclaux, J. and P. Indelicato, *The relativistic atomic program MCDFGME V 2005.10.* Published at http://dirac. spectro. jussieu. fr/mcdf/on August, 2005. **17**: p. 2005.
6. Briggs, D. and J.T. Grant, *Surface analysis by Auger and x-ray photoelectron spectroscopy*. 2003, Chichester, West Sussex, U.K.: IM Publications. xi, 899 p.
7. Moretti, G., *The Wagner plot and the Auger parameter as tools to separate initial- and final-state contributions in X-ray photoemission spectroscopy.* Surface Science, 2013. **618**: p. 3-11.
8. NIST, X., *Database,< h ttp.* srdata. nist. gov/xps/Default. aspx.
9. Weightman, P., *X-ray-excited Auger and photoelectron spectroscopy.* Reports on Progress in Physics, 1982. **45**(7): p. 753.
10. Shirley, D., *The effect of atomic and extra-atomic relaxation on atomic binding energies.* Chemical Physics Letters, 1972. **16**(2): p. 220-225.
11. Wagner, C., *Auger lines in x-ray photoelectron spectrometry.* Analytical Chemistry, 1972. **44**(6): p. 967-973.
12. Gaarenstroom, S. and N. Winograd, *Initial and final state effects in the ESCA spectra of cadmium and silver oxides.* The Journal of Chemical Physics, 1977. **67**(8): p. 3500-3506.
13. Wagner, C., *Chemical shifts of Auger lines, and the Auger parameter.* Faraday Discussions of the Chemical Society, 1975. **60**: p. 291-300.
14. Wagner, C. and A. Joshi, *The auger parameter, its utility and advantages: a review.* Journal of electron spectroscopy and related phenomena, 1988. **47**: p. 283-313.
15. Banna, M., et al., *Core binding energies of the gaseous elements: the Sb3d levels of Sb4 from x-ray photoelectron spectroscopy.* Chemical Physics Letters, 1982. **92**(4): p. 362-365.
16. Cole, R.J., D.A.C. Gregory, and P. Weightman, *Analysis of Auger-parameter and XPS shifts: Application of potential models.* Physical Review B, 1994. **49**(8): p. 5657-5661.

Chapter 4

Electron Spectroscopic Analysis of Elemental Indium and Antimony

4.1 Introduction:

The experiment involved performing x-ray excited Auger and photo-electron spectroscopy on elemental indium and antimony.

The energy scales are initially corrected, using the position of the $\mathrm{Au}\ 4f_{7/2}$ line, by adding $4.36 \pm 0.05\ eV$ to the kinetic energies as specified in (Sec. 2.2.3).

The pass energy of the analyser was set to $100\ eV$ in the survey scans, and $20\ eV$ in the narrow scans, yielding energy resolutions of $1.67\ eV$ and $0.33\ eV$ respectively.

The energy step of the analyser was set at $0.49\ eV$ in broadscans and $0.09\ eV$ in narrow scans, which result in measurement errors of $0.24\ eV$ and $0.05\ eV$ respectively.

4.2 Elemental In Spectra:

The survey scans and the raw narrow regions will be considered first, followed by analysis of the characteristic lines.

4.2.1 Overview of the raw data

Broad scans were performed, following an Ar ion bombardment for $40\ minutes$, on an In foil at electron emission angle (takeoff angle) normal to the surface of the specimen ($0°$ from the line perpendicular to the surface), and at $75°$ (from the line perpendicular to the surface) to detect any surface related effect (Sec.1.2). (Fig. 4.1) shows the normal emission scan in which only the In spectrum is present with no clear presence of contamination. The binding energies of the characteristic $3d_{5/2,3/2}$ photoelectron lines are $443.88 \pm 0.24\ eV$ and $451.78 \pm 0.24\ eV$ respectively, and the kinetic energies of the highest peaks in the $M_5N_{4,5}N_{4,5}$ and the $M_4N_{4,5}N_{4,5}$ Auger groups are $402.96 \pm 0.24\ eV$ and $410.35 \pm 0.24\ eV$.

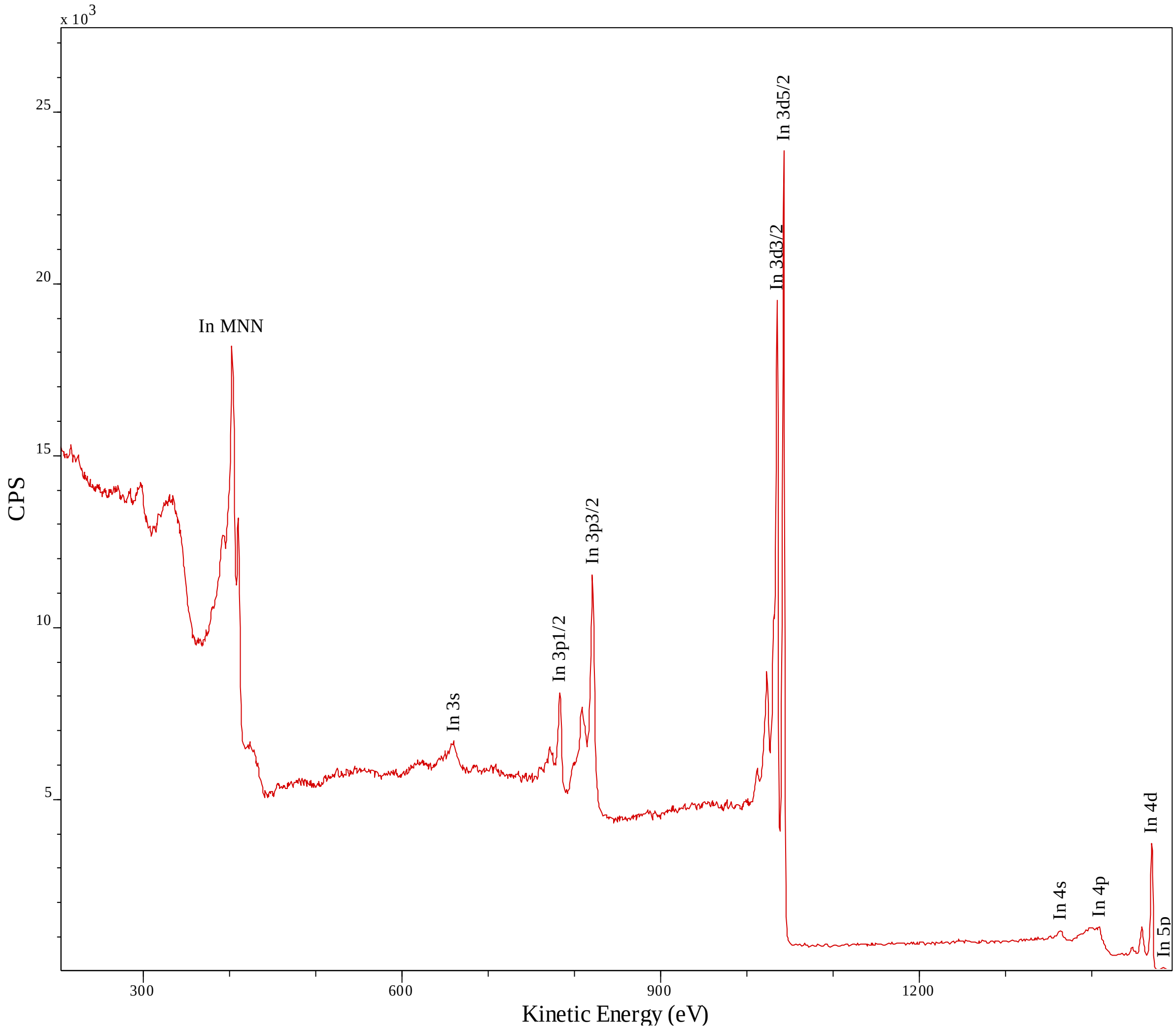

Fig. 4.1: A broad scan spectrum of the Ar ion bombarded In specimen at the normal takeoff. It shows the characteristic $3d$ photoelectron lines and the $M_{4,5}N_{4,5}N_{4,5}$ Auger lines, as well as other less intense lines from levels 3, 4, and 5. Peaks that are not annotated are plasmon loss peaks. There are no signs of contamination such as the C 1s at binding energy of 284.8 eV (kinetic energy of 1201.8 eV where the $Al\ K\alpha$ x-ray is used as an excitation source), or the oxygen KLL Auger profile around KE of 503 eV.

A broad scan performed at the end of the experiment shows the presence of a low intense carbon contamination (Fig.4.2) which provides another method of calibrating the energy scale using the C 1s line, although this method is mainly used in insulators. This can be compared with the correction of $4.36 \pm 0.05\ eV$ determined from the Au $4f_{7/2}$ (Sec.2.2.3). The program CasaXPS provides a method of calibrating the energy scale where a reported line position (C 1s in this case) is entered in a field named '*True*' in the calibration window (Fig. 4.3), and the range in which this line lies within the spectrum is entered in a field named '*Measured*'. When the button *'Apply'* is clicked, the program locates the peak position and corrects the energy scale according to the value interred in the field '*True*'. $284.8\ eV$ [6] was entered in the program as the '*True*' value of the binding energy of C 1s. Subsequently, the program corrected the observed (not corrected) binding energy scale of the raw In spectrum taken at the end of the experiment by subtracting $4.75 \pm .24\ eV$. The difference between this correction and that obtained using the Au $4f_{7/2}$ is considerable ($0.39 \pm .24\ eV$) and can be due to a chemical shift of the C 1s. Therefore, the initial correction of $4.36 \pm .05\ eV$ is more reliable.

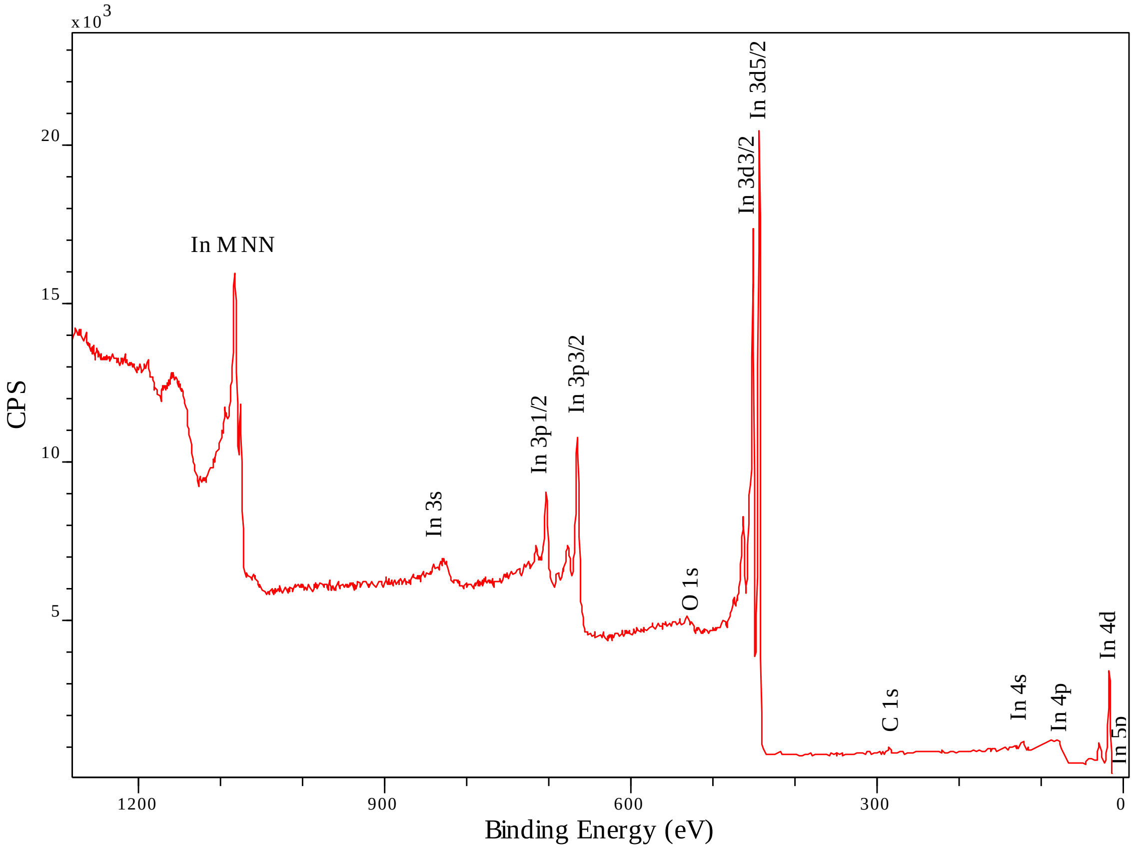

Fig. 4.2: A broadscan spectrum of the In specimen at the end of the experiment. It shows the accumulation of small amounts of oxygen and carbon. The position of C 1s line can be determined, as described in the text, and used to correct the energy scale.

As In is a metal, it is more reliable to reference its spectroscopic lines to the Fermi level. By doing so, the instrumental work function is accounted for as well as energy shifts such as that caused by surface roughening by Ar ion bombardment. Surface roughening is change of surface topography caused by the impact of the accelerated ions. This affects the takeoff angles of the emitted electrons leading to shifts in their observed energies.

The Fermi level can be determined in CasaXPS by fitting the step function (Eq.2.17) to the observed Fermi edge as described in (Sec.2.3.4). By doing so (Fig. 4.4), the Fermi level was determined at:

$$KE_{Fermi} = 1482.36 \pm 0.05\ eV \quad (4.1)$$

hence, the correction that must be applied to the measured KE is:

$$KE_{correction} = h\nu - KE_{Fermi}$$

$$= 1486.6 - 1482.36 \pm 0.05 = 4.24 \pm 0.05\ eV \quad (4.2)$$

The difference between this correction and that made after Au $4f_{7/2}$ is $0.12 \pm .07\ eV$.

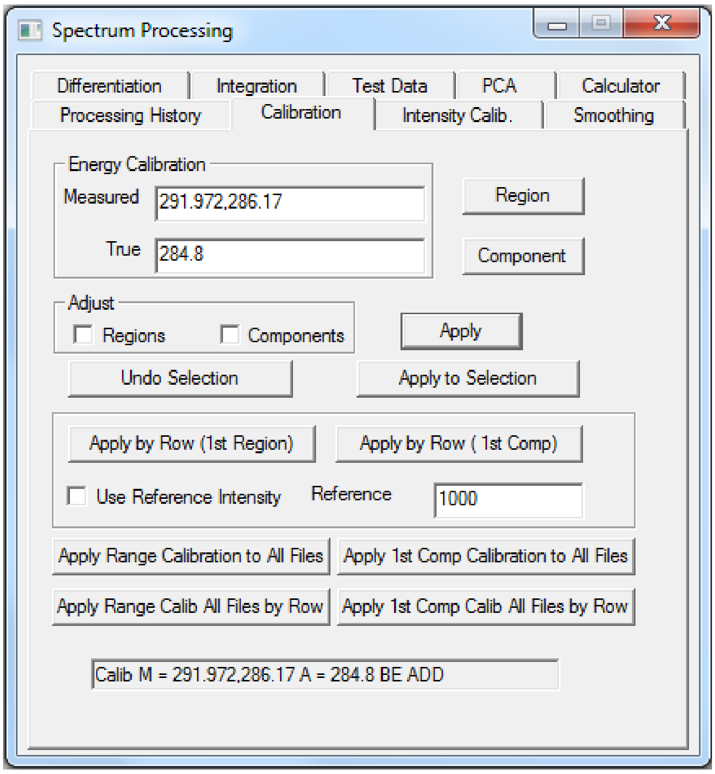

Measured: 291.972,286.17

True: 284.8

☐ Regions ☐ Components

☐ Use Reference Intensity

Reference: 1000

Calib M = 291.972,286.17 A = 284.8 BE ADD

Fig. 4.3: The Energy Calibration window in CasaXPS. A reported value of the energy of an XPS line (C 1s in this case) is entered in the field "*True*", whereas the range (of the spectrum) within which this line was detected is entered in the field "*Measured*". When the button "*Apply*" is clicked, the program locates the peak within the entered range and corrects its energy to the entered value, and applies the same correction to the whole energy scale.

Considering the three methods of energy referencing (Au $4f_{7/2}$, C $1s$ or the Fermi level) the latter is the most reliable, henceforward, its value will be used instead of that obtained from the Au $4f_{7/2}$.

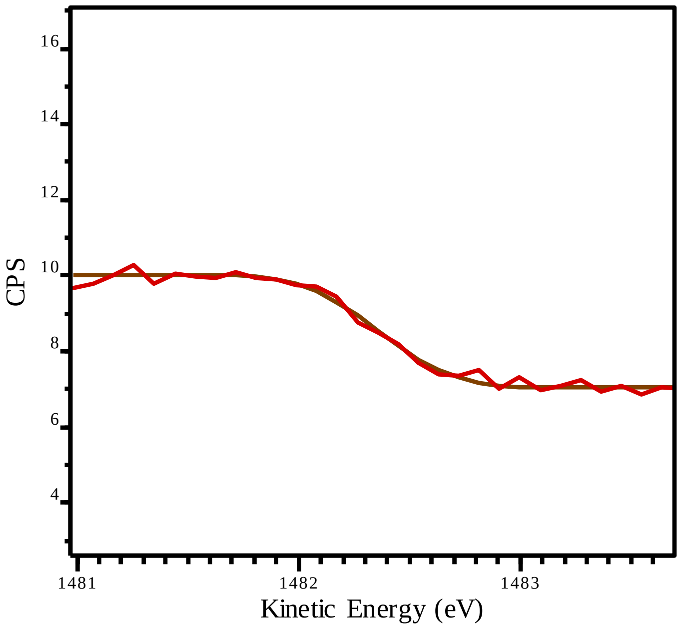

Fig. 4.4: The Fermi edge of the metallic elemental indium (red) scanned after cleaning the specimen by Ar ion bombardment. The black line is the fit of the step function to the Fermi edge. The position of the Fermi level, which is the inflection point of the step function is chosen during the fitting process (at $KE = 1482.36 \pm 0.05\ eV$) alongside the instrumental Gaussian contribution as described in (Sec.2.3.4).

Narrow scans of the $3d$ region were also performed at $0°$ and $75°$ takeoff angles. In order to compare the two spectra they were normalised with respect to the peak maxima (Fig. 4.5). The $3d_{5/2}$ peak is identical at the two takeoff angles, which indicates that there are no components associated with a surface core-level shift. This result was also reported by Williams et al [7]. A very weak shoulder is present at the lower kinetic energy edge of the $3d_{5/2}$ peak which can be attributed to the oxidisation of a very small fraction of the surface atoms. A stronger shoulder appears on the low KE side of the $3d_{3/2}$ peak which is due to the surface plasmon loss of the $3d_{5/2}$ peak. This loss has been reported by Krischok et al [8] and Bouslama et al [9] to be $8.6\ eV$, and found here, from the $3d_{3/2}$ peak maxima (before fitting), to be $8.46 \pm 0.07\ eV$.

The bulk plasmon loss is $11.5\ eV$ according to the same references [7, 8], and found to be $11.63 \pm 0.07\ eV$ and $11.69 \pm 0.07\ eV$ for $3d_{5/2}$ and $3d_{3/2}$ components, respectively. The $3d_{3/2}$ bulk plasmon appears broader in the surface sensitive spectrum (Fig. 4.5) due to overlapping with the $3d_{5/2}$ surface+bulk loss. That is $\hbar(w_{surface} + w_{bulk})$ energy loss.

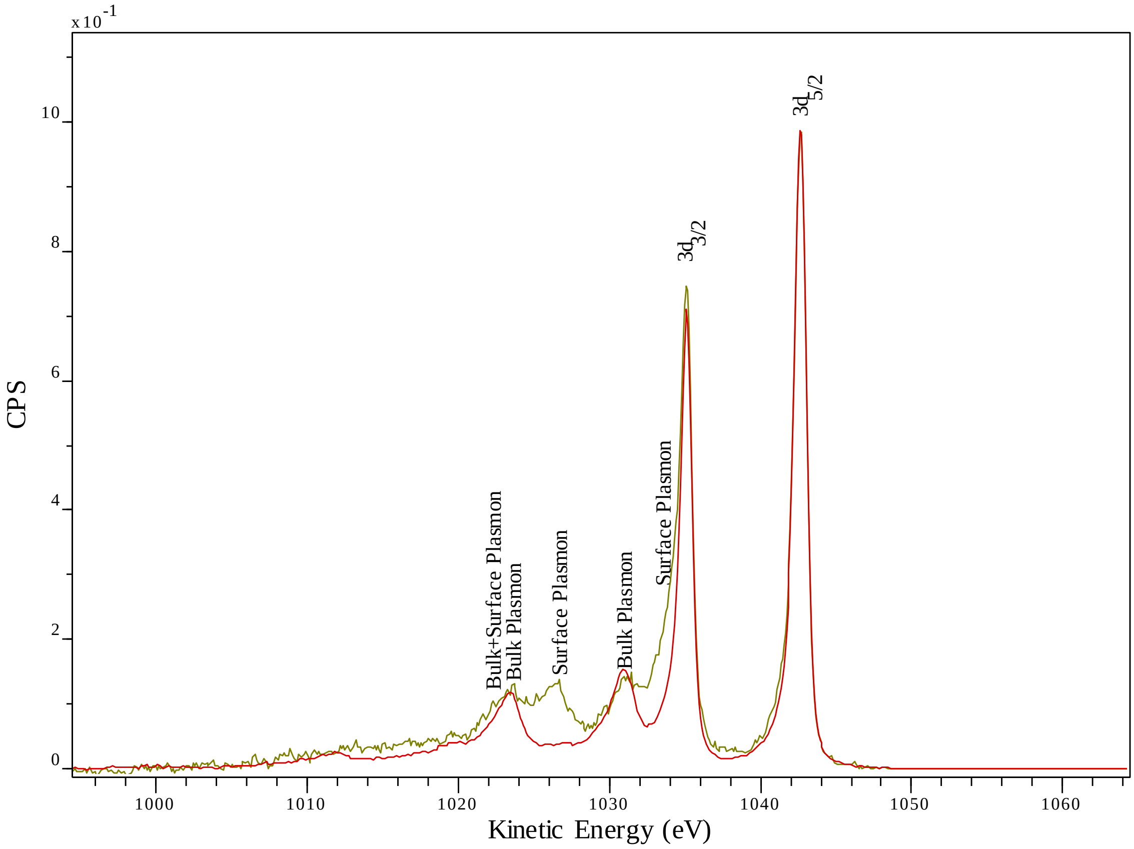

Fig. 4.5 The In $3d$ spectra at normal (red) and surface sensitive (green) takeoff. Both spectra are normalised with respect to the $3d_{5/2}$ peak maxima to detect any broadening that may result from surface core-level shift. The two spectra are identical apart from plasmons. Surface plasmons do not appear in the normal-takeoff spectrum. Shirley method was used to subtract the backgrounds of both spectra.

4.2.2 A model to fit the In $3d$ XPS peaks:

A model for the In $3d$ XPS spectrum was constructed by subtracting a Shirley background from the raw data and using the following parameters:

- The $3d_{5/2}$ to $3d_{3/2}$ intensity ratio was initially set to $3:2$ in accordance with the electron population from the degeneracy of the total angular momentum

$$2j + 1 = 2\left(2 \pm \frac{1}{2}\right) + 1 = 6:4 \quad (4.3)$$

and then allowed to vary in order to reflect small variations in the photoelectron cross sections of the two peaks.

- The spin-orbit splitting between the $3d$ components has been reported at $7.5\ eV$ [10] and $7.6\ eV$ by Sen et al [11] and $7.6 \pm .21\ eV$ Pessa et al [5], therefore the two peaks were separated by $7.6\ eV$ at the beginning of the fitting process, then their separation was allowed to vary.

- The $LF(\alpha, \beta, w, m)$ asymmetric Lorentzian line shape convoluted with a Gaussian described in (Sec. 2.3.2) was used to fit the $3d$ doublets and the plasmons. The FWHM and the four lineshape parameters were varied until the best fit was reached.

This procedure results in a good fit for the experimental results as shown in (Fig.4.6)

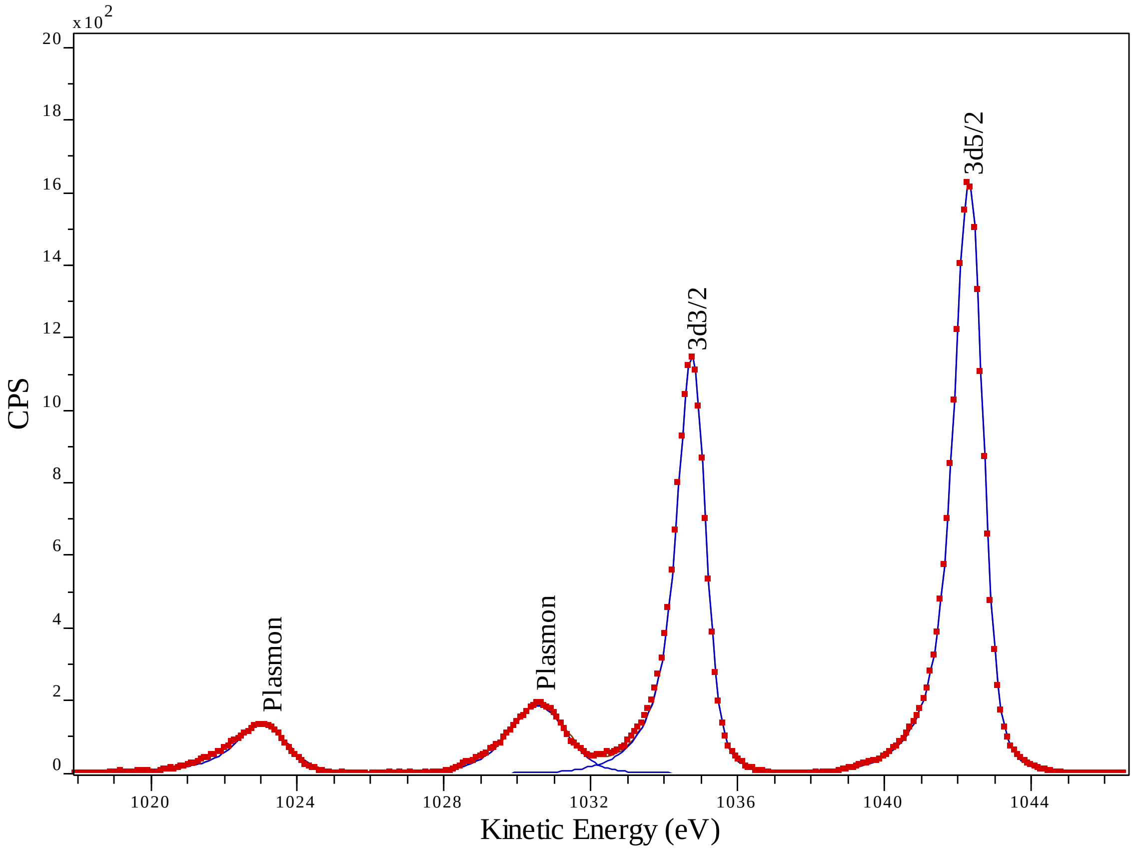

Fig. 4.6: A synthetic peak model of the elemental $\mathrm{In}\ 3d$ region. The red dotted line is the raw data and the blue lines are the synthetic peaks. The widths of $3d_{5/2}$ and the $3d_{3/2}$ are $0.89 \pm 0.07\ eV$ and $0.87 \pm 0.07\ eV$ respectively, whereas the plasmon energy losses are $11.71 \pm 0.07\ eV$ and $11.66 \pm 0.07\ eV$. All peaks are asymmetric because of the shakeup loss explained in (Sec.2.3.2).

The binding energies of $3d_{5/2}$ and $3d_{3/2}$ corrected according to the position of the Fermi level (Eq. 4.2) are 444.04 ± 0.07 and $451.58 \pm 0.07\ eV$ respectively. This results in a spin-orbit splitting of $7.54 \pm 0.07\ eV$. The uncertainty from energy correction is neglected in the spin-orbit splitting because two local values are compared.

4.2.3 In $M_{4,5}N_{4,5}N_{4,5}$ Auger spectra:

A narrow scan of the $M_{4,5}N_{4,5}N_{4,5}$ Auger area was performed at the same normal (to the surface of the specimen) and surface-enhanced takeoff used in the results represented in the previous section for the $\mathrm{In}\ 3d$ XPS spectrum.

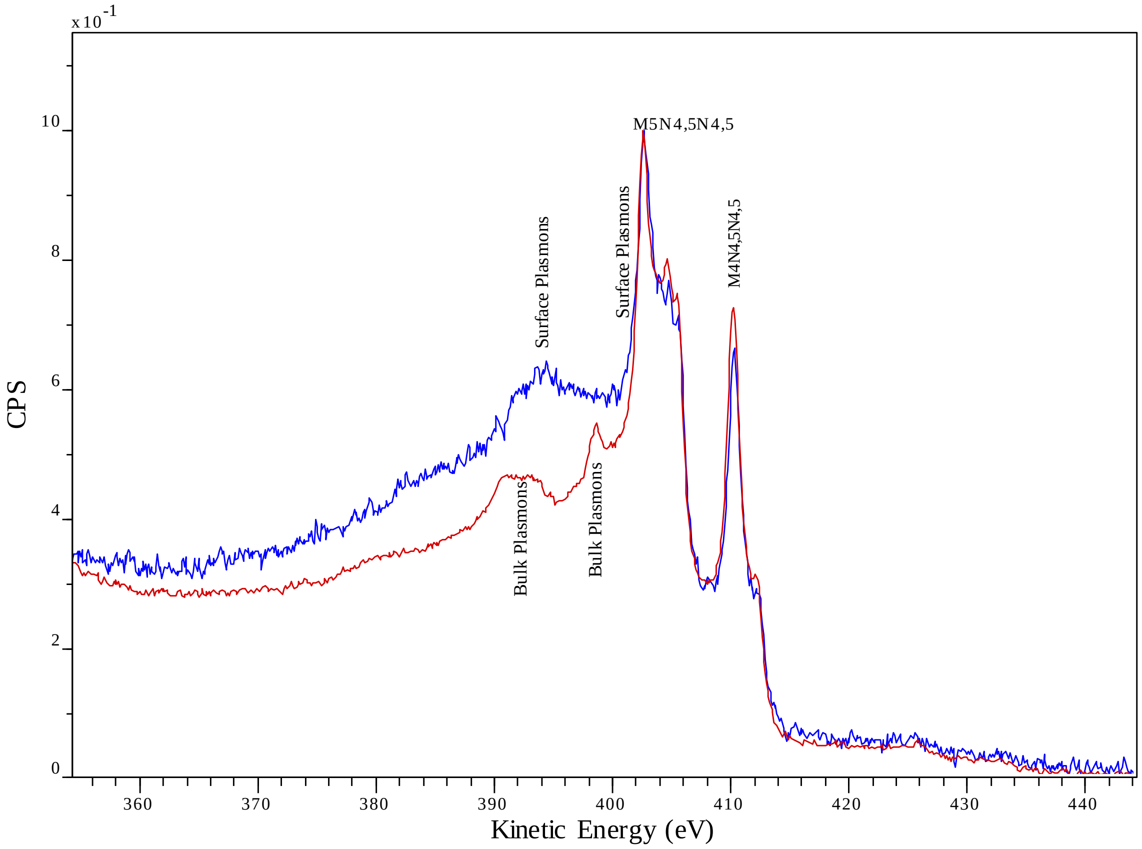

Fig. 4.7: Narrow scans of the metallic In $M_{4,5}N_{4,5}N_{4,5}$ Auger area. The red spectrum was taken at normal takeoff and the blue one was taken at $75°$ of the normal to the surface of the specimen. Both spectra contain the $N_4N_{4,5}N_{4,5}$ and the $N_5N_{4,5}N_{4,5}$ groups whose initial states are the ion having a hole in $3d_{3/2}$ and the ion having a hole in $3d_{5/2}$, respectively. Bulk plasmons do not appear at the surface spectrum, but rather weak surface plasmons are present. The backgrounds are not subtracted.

The $M_4N_{4,5}N_{4,5}$ and the $M_5N_{4,5}N_{4,5}$ Auger groups (described in (Sec.1.2.3)) contain the same multiplet structure which has been modelled by [12] for the solid metallic phase, and by [13] for In, InCl, and $InCl_4$ vapours. The $^1G_4$ transitions are the strongest in the two groups [12, 14], and can be located precisely [5].

Shirley-type background was subtracted from the $M_{4,5}N_{4,5}N_{4,5}$ spectra (Fig 4.8). The sharpest features in the $M_5N_{4,5}N_{4,5}$ and the $M_4N_{4,5}N_{4,5}$ groups, corresponding to the positions of the dominant $^1G_4$ term, are located at $402.56 \pm .07\ eV$ and $410.22 \pm .07\ eV$ respectively. The splitting between the two Auger groups is $7.66 \pm .07\ eV$. This splitting should be equal to the splitting between $3d_{3/2}$ and $3d_{5/2}$ photoelectron lines (since the relaxed atom after the photoemission from these two levels is the initial state of the $M_4N_{4,5}N_{4,5}$ and the $M_5N_{4,5}N_{4,5}$ Auger processes respectively, as explained in (Sec.1.2.3) and demonstrated in the calculations in (Sec.3.2.1.3)), and this is the case as seen when the positions of the ${}^1G_4$ lines are determined precisely from the differential form below. The positions of ${}^1G_4$ at the surface sensitive spectrum are almost the same as in the bulk sensitive spectrum ($402.57 \pm .07\ eV$ and $410.22 \pm .07\ eV$).

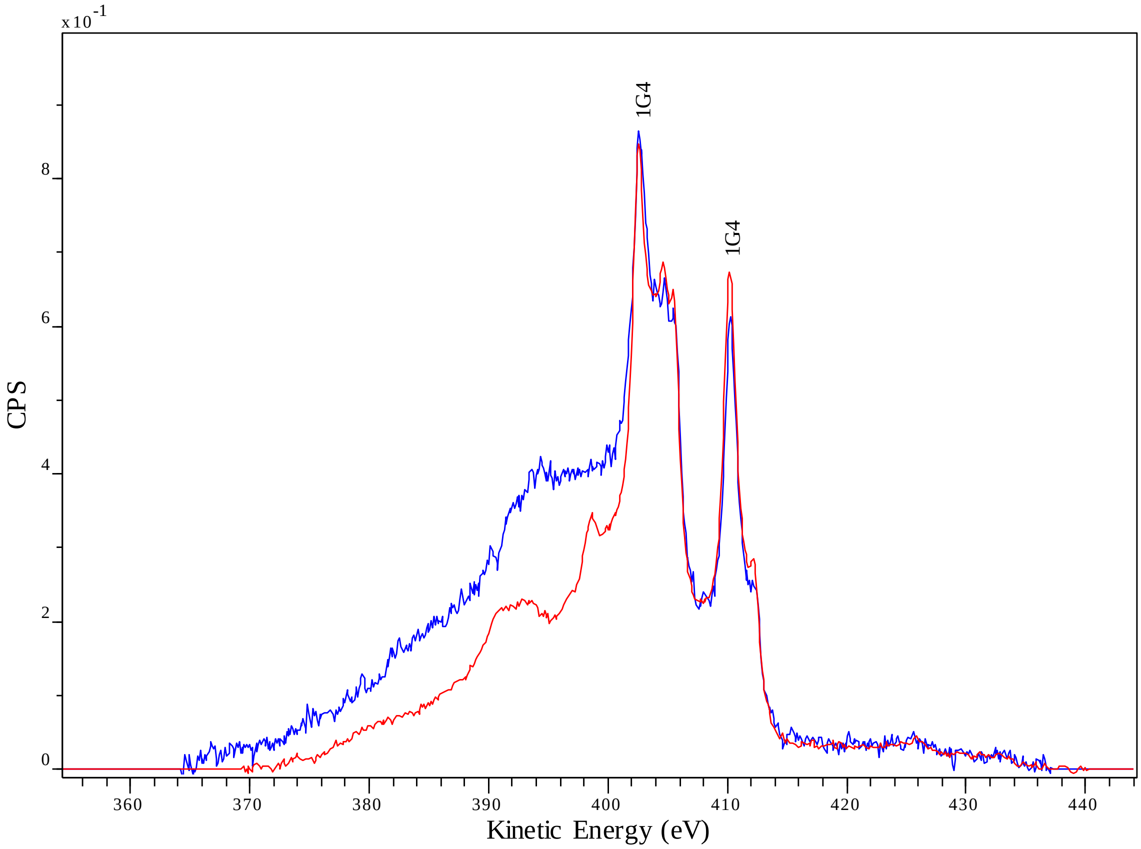

Fig. 4.8: Normal (red) and surface- sensitive (blue) elemental indium $M_{4,5}N_{4,5}N_{4,5}$ Auger spectra corrected for backgrounds using the Shirley method. The highest peaks, which correspond to the ${}^1G_4$ components in the two groups, are annotated. The $M_5N_{4,5}N_{4,5}$ appears significantly more intense due to overlapping with the plasmon peaks of the $M_4N_{4,5}N_{4,5}$ groups.

Auger spectra were recorded in the early stages of the instrumentation development in the differential form [15]. It is easier to visualise and locate the positions of the ${}^1G_4$ components in the differential form [15-17]. Moreover, differentiation supresses the background from the spectrum. Therefore, and since this work is not concerned with the quantitative analysis of the spectra, it is preferable to use the differential form of the Auger spectra. The differentiated form of the $\mathrm{In}\ M_{4,5}N_{4,5}N_{4,5}$ region was obtained using the Savitzky-Golay algorithm explained in (Sec. 2.3.3) with smoothing width of 5 data points (Fig 4.9). The ${}^1G_4$ components of the $M_5N_{45}N_{45}$ and the $M_4N_{45}N_{45}$ groups were found by this method at $402.58 \pm 0.07\ eV$ and $410.21 \pm 0.07\ eV$ respectively. So, the splitting between the two groups is $7.63 \pm 0.07\ eV$. That is equal to the splitting between $3d_{3/2}$ and $3d_{5/2}$ lines considering the measurement error.

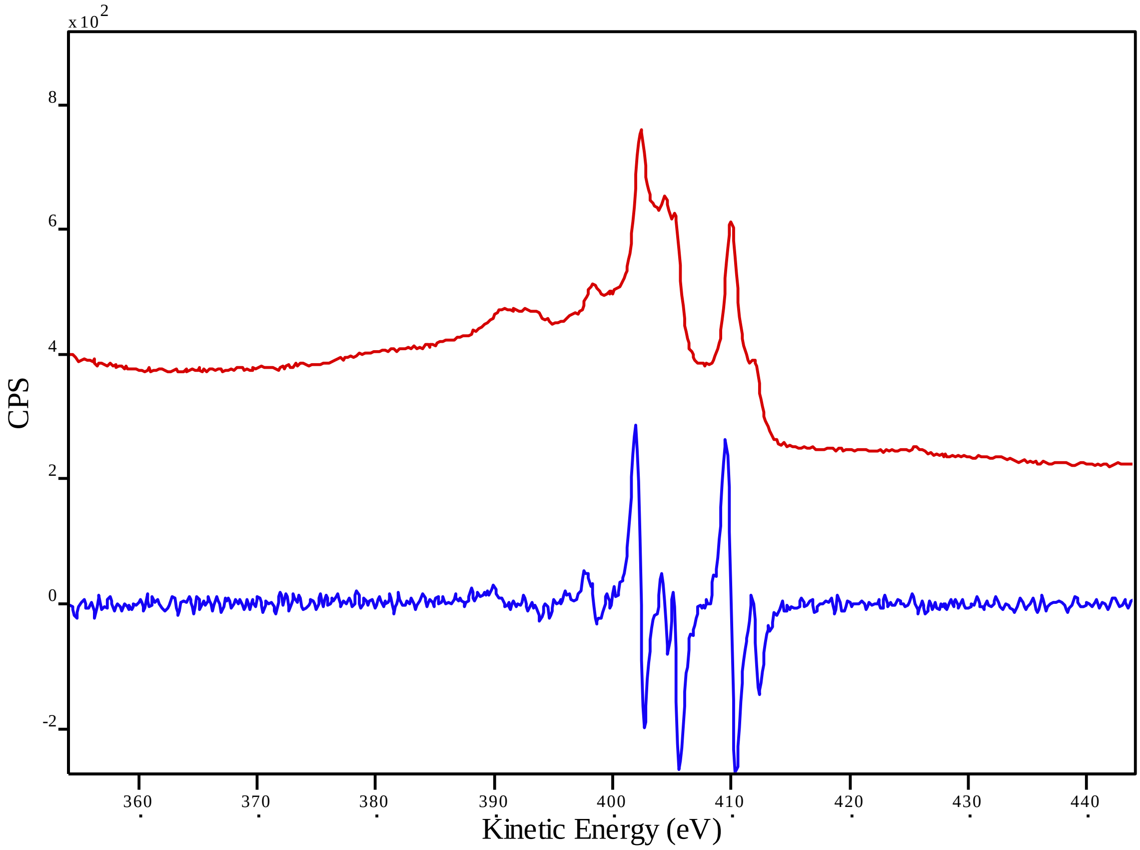

Fig. 4.9: The direct $M_{4,5}N_{4,5}N_{4,5}$ Auger spectrum of metallic In (red), and the differential form of the same spectrum (blue) obtained by the Savitzky-Golay method with smoothing width of 5 data bins. The background (not subtracted in the direct spectra is supressed by differentiation, whereas the main spectroscopic peaks stand out.

4.3 Elemental Sb Spectra:

The same procedure used with the elemental indium in (Sec.4.2) is used here. A general view of the features of the raw spectra will be made first.

4.3.1 Overview of the raw data:

A broadscan was performed on the Sb sample as received without any surface preparation. It shows a contamination with carbon and oxygen (Fig. 4.10). The specimen was, then, Ar^+ ion bombarded for 40 minutes which resulted in a clean surface as shown in the spectrum in (Fig. 4.10). Features associated with plasmons are observed in the spectrum after cleaning. These arise from the excitation of the “the free electron gas” of conduction electrons.

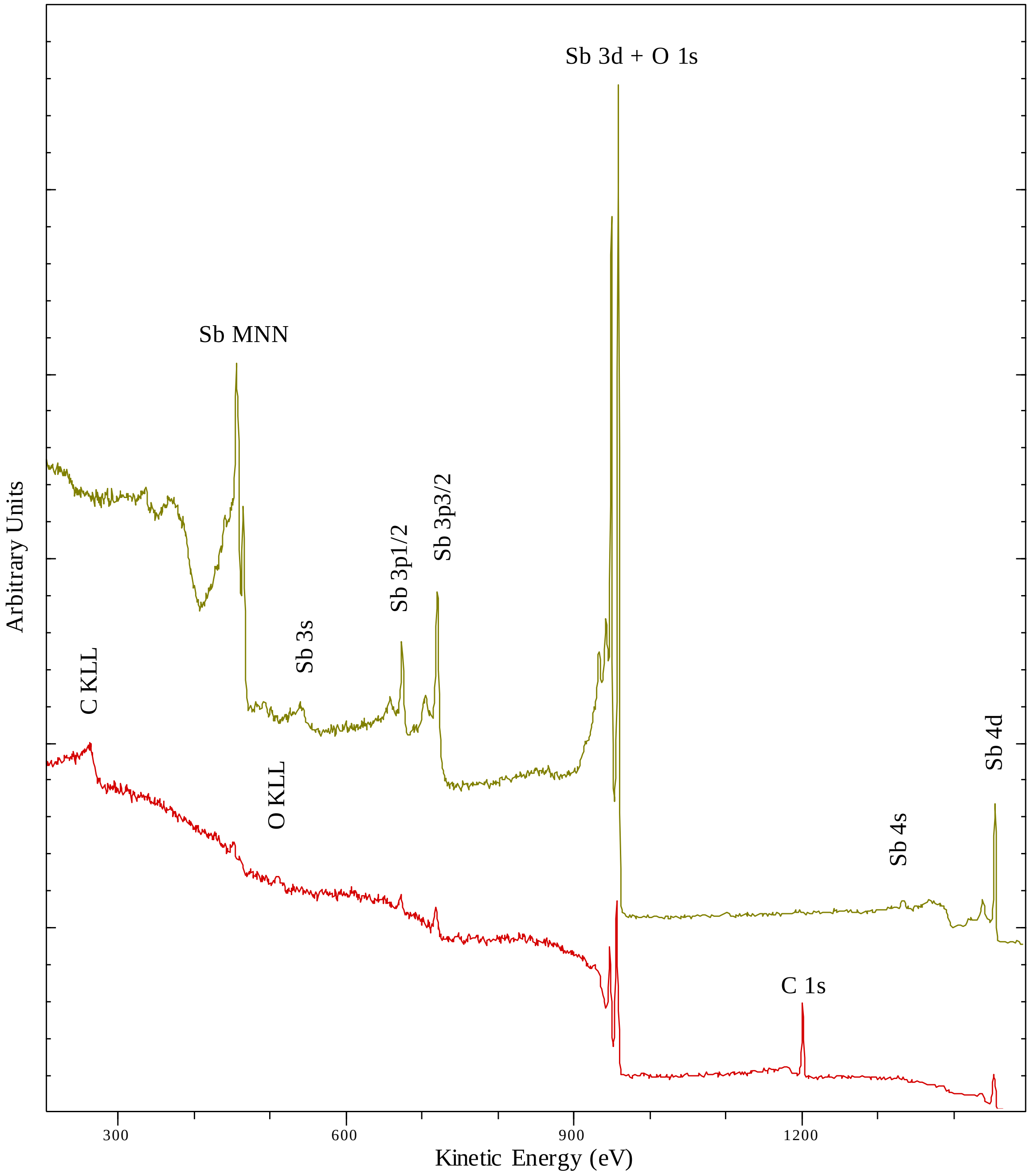

Fig.4.10: Broad scans of the Sb specimen before any treatment (bottom), and after performing an Ar^+ ion bombardment for 40 *minutes* (top). Strong presence of C 1s before bombardment is clear in addition to the oxygen and carbon KLL Auger spectra. O 1s line is known to overlap with the Sb $3d_{5/2}$ [1-3]. After cleaning, C and O spectra did not appear, the Sb lines became sharper, and the plasmon loss peaks appeared (the unannotated peaks to the lower energy side of Sb peaks).

The spectra of the 3d region before and after the Ar^+ bombardment (Fig. 4.11) provide more information about the chemical state of the Sb specimen before and after cleaning.

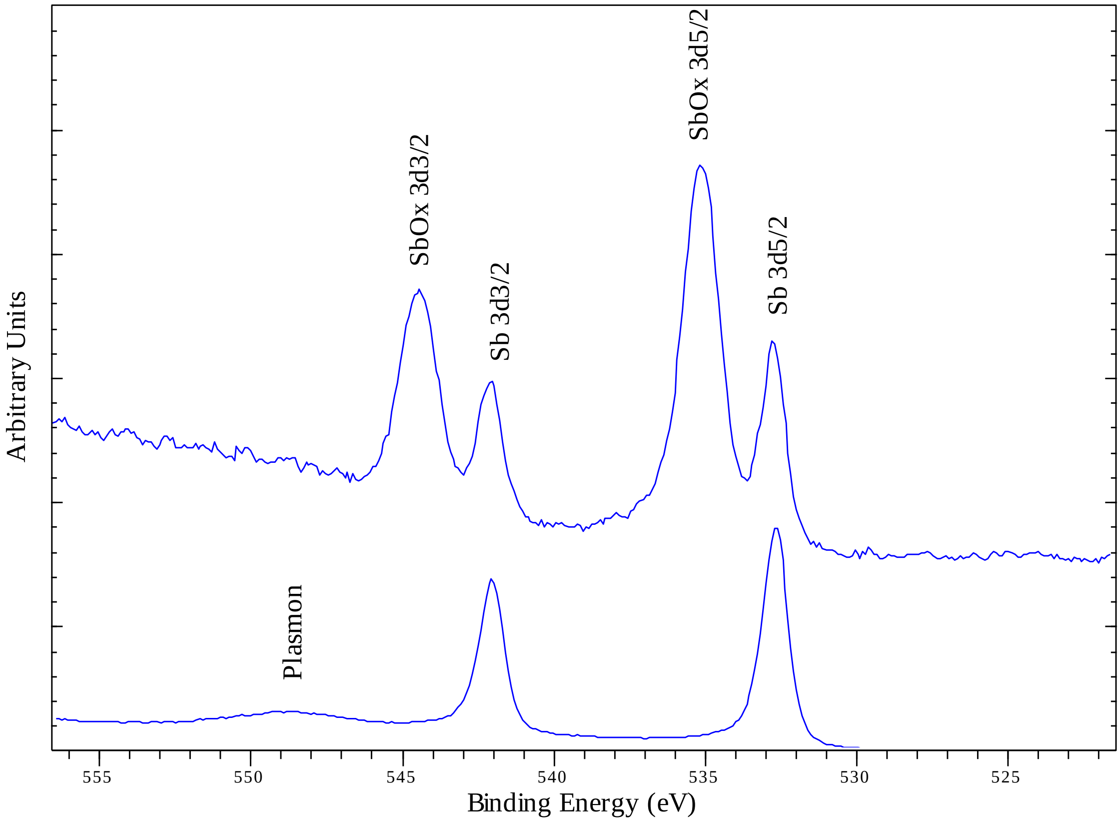

Fig. 4.11: Narrow scans of the Sb 3d region before (top) and after (bottom) cleaning. Before cleaning, there were Sb oxide (SbOx) peaks which are more intense than those of the pure Sb. The Oxide was completely removed by the Ar ion bombardment, which led to the appearance of the plasmon peak at $\sim 16.17\ eV$ from the $3d_{5/2}$ peak. The Sb bulk plasmon loss has been reported to be $16.0\ eV$ [4].

The spectrum before cleaning contains two species, one of which can be associated with a pure Sb as it is in the same position as a single component in the spectrum after cleaning (Fig.4.11), whereas the other is shifted by $\sim 2.4 \pm 0.07\ eV$ to higher binding energy and associated with surface oxide. The disappearance of the latter species suggests that the antimony was completely reduced by the Ar^+ bombardment. An oxide shift of Sb in Sb_2O_3 has been reported to be $2.29 \pm 0.2\ eV$ [6] which is equal to the shift found in this work before cleaning, considering the uncertainties. In the as-received specimen, the higher binding-energy $3d$ species is more intense than the other (Fig.4.11) which indicates that most of the Sb atoms at the surface were initially oxidised.

The positions of the $M_4N_{4,5}N_{4,5}$ and $M_5N_{4,5}N_{4,5}$ groups were determined from the differential form of the spectrum (Fig.4.12) produced as described in (Sec.4.2.3). These are further discussed in (Sec.4.3.3).

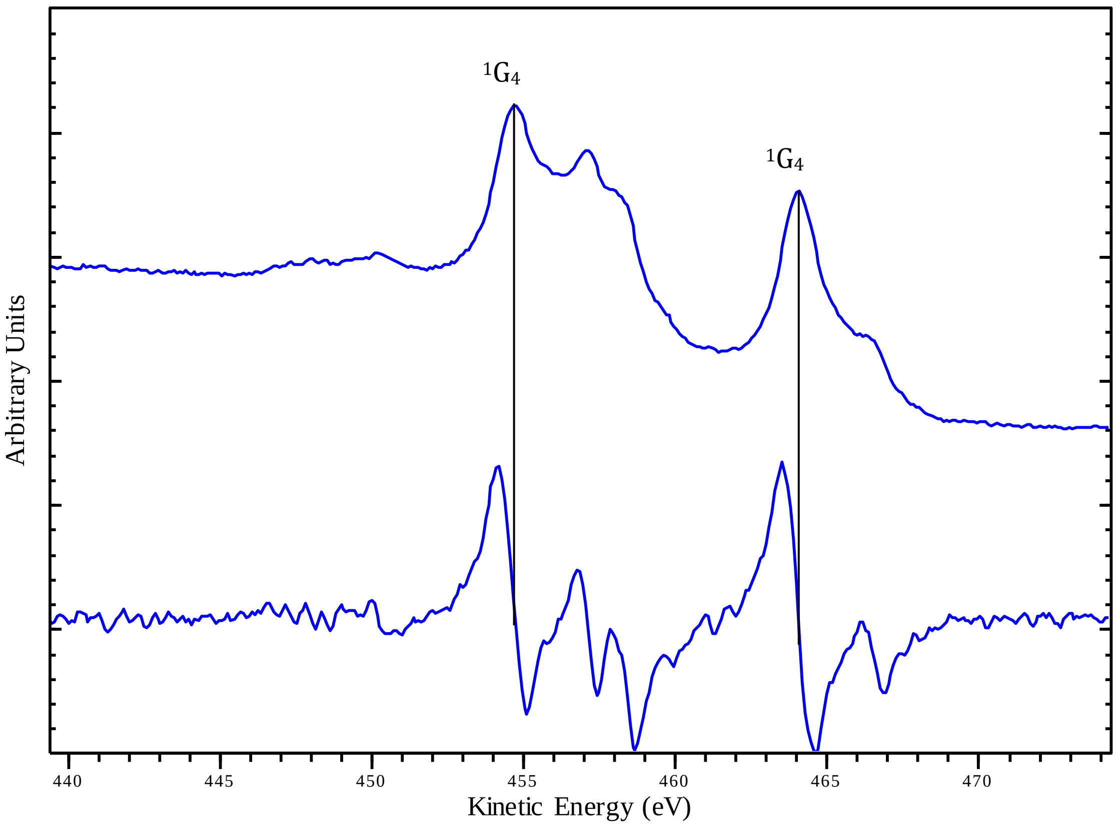

Fig. 4.12: Top: the direct $M_{4,5}N_{4,5}N_{4,5}$ Auger spectrum of the metallic elemental Sb cleaned by Ar ion bombardment for $40\ minutes$. The highest peak of each of the two Auger groups, which is associated with the $^1G_4$ component, is annotated. Bottom: the differential form of the same spectrum produced using the Savitzky-Golay method. Vertical lines are drawn between the positions of the $^1G_4$ components in the direct and the differential forms. These are the downward-going zero-crossings in the differential form.

The energy scale correction that was determined from the Au $4f_{7/2}$ to be $4.36\ eV$ in (Sec. 2.2.3) and used to correct all the Sb spectra mentioned above accounts for the instrument work function only. The Sb line positions obtained after the Ar^+ ion bombardment must be referenced to the Fermi level measured in the same circumstances in order to be reliable to use in comparing the atomic structure of the metallic elemental Sb with those of Sb in the other chemical environments.

The Fermi level was determined by CasaXPS (Fig.4.13) using the same method used for indium (Sec.4.2.1) and described in (Sec.2.3.4).

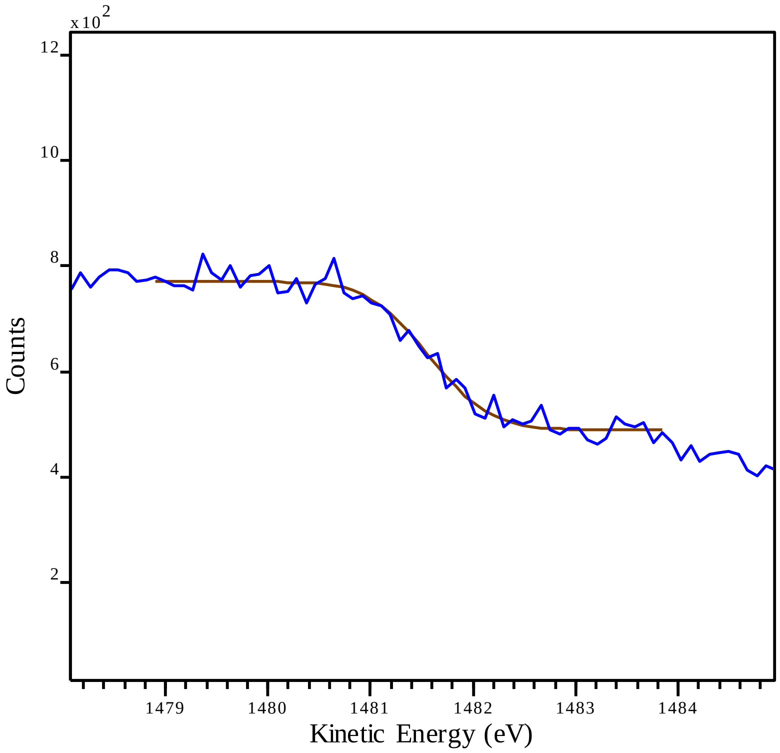

Fig. 4.13: The Fermi edge of the metallic elemental Sb (blue) scanned after cleaning the specimen by Ar^+ ion bombardment. The black line is the fit of the step function, described in (Sec.2.3.4), to the Fermi edge. The Fermi level was located at $KE = 1481.57 \pm 0.05\ eV$.

The kinetic energy of the Fermi level of Sb was found to be:

$$KE_{Fermi} = 1481.57 \pm 0.05\ eV \qquad (4.4)$$

hence, the correction that must be applied to the measured KEs of Sb spectra is:

$$KE_{correction} = h\nu - KE_{Fermi}$$

$$= 1486.6 - 1481.57 \pm 0.05 = 5.03 \pm 0.05\ eV \qquad (4.5)$$

This value will be used to correct the elemental Sb spectra for the rest of this chapter.

4.3.2 The Sb surface spectra:

Narrow scans were performed on the $3d$ region at different takeoff angles ($0°$ and $75°$). Normalising and overlaying the two spectra reveals a broadening at the lower binding energy side of the peaks that are taken at the surface sensitive takeoff angle which indicates the existence of extra components due to the surface core-level shift (Fig. 4.14).

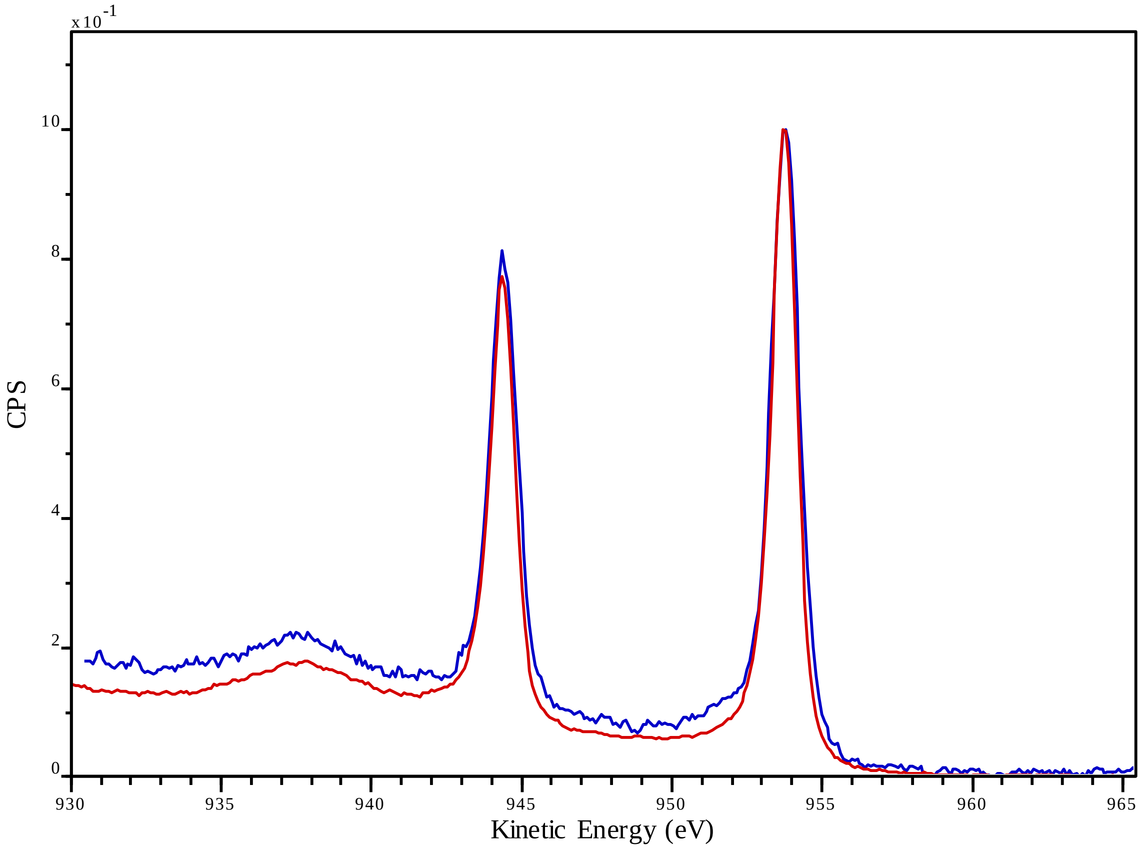

Fig. 4.14: $3d$ region of metallic elemental Sb scanned at $0°$ (red) and $75°$ (blue) takeoff angles after cleaning. Bulk plasmons appear in both spectra. The surface-sensitive peaks (at the $75°$ takeoff angle) involve a broadening at the lower binding energy side. This is due to a contribution from the core-level shift at the surface. Extra peaks must be added when fitting the spectrum to account for this shift (Fig.4.17).

The splitting between the Sb $3d_{5/2}$ and $3d_{3/2}$ lines has been reported around $9.40\ eV$ [3, 5]. For such a separation, it is common that the Shirley background crosses through the data [18]. To avoid this, two separate regions are used to evaluate the background (Fig.4.15). After that, the peaks in the two regions are fitted. If the peak areas satisfy the intensity condition ($3{:}\,2$ in the case of $3d$ components (Eq.4.3)), then the background subtraction is correct [18]. This procedure was applied to the surface sensitive Sb $3d$ spectrum, and resulted in a good fit (Fig.4.17).

Regions are created in CasaXPS with specific *start* and *end* points (Fig.4.16), and then the type of background is chosen from a drop list. The limits (the ends) of the regions can be varied, and up and down offsets can be applied at both sides.

A model was constructed to fit the surface sensitive spectrum using the method described in (Section.4.2.2) assigning two peaks to each component of the $3d$ doublet to account for the species arising from the surface core-level shift as well as that from the bulk. The ratio between the areas of each of these $3d_{3/2}$ and $3d_{5/2}$ pair of components was set to $2{:}\,3$ in

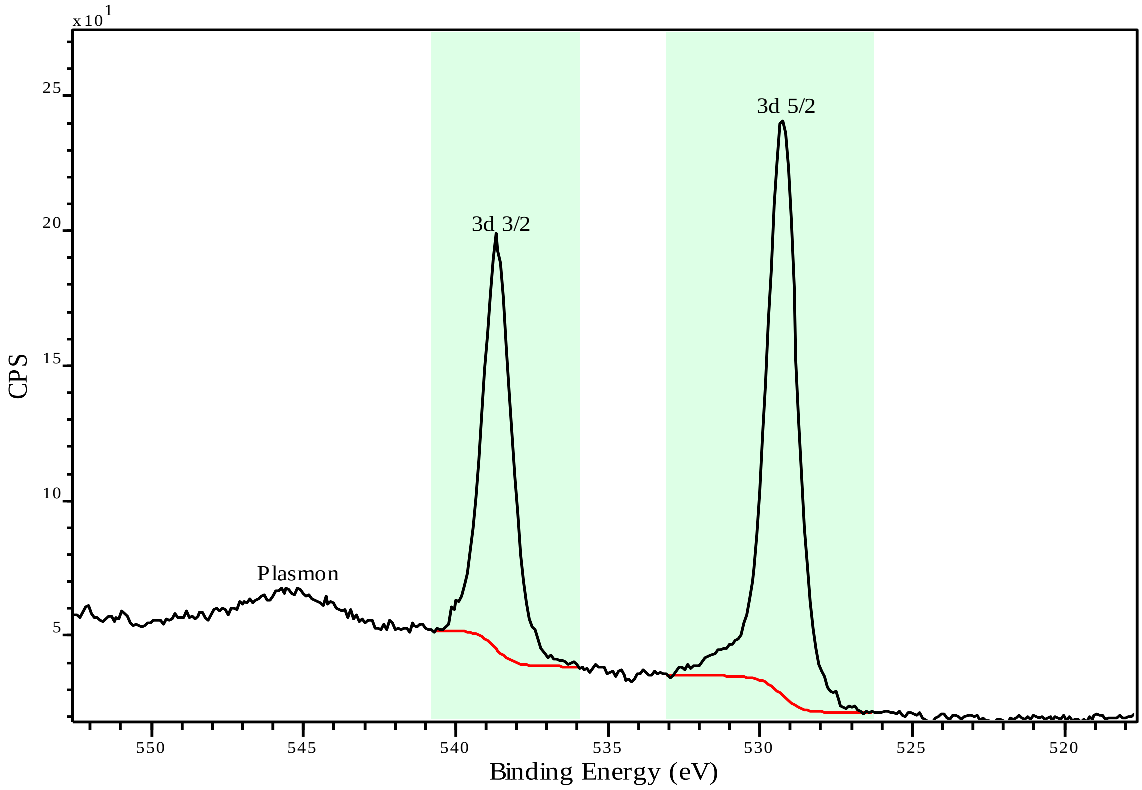

Fig. 4.15: The surface sensitive spectrum of Sb $3d$ (black). The spectrum is noisy, and there are sudden fall of intensity near the tails of the peaks. The red lines are Shirley backgrounds computed separately in CasaXPS by creating two regions (green shade) in the spectrum. The components created in the two regions to fit the spectrum must be constrained so that the total area in the $3d_{3/2}$ region is $2/3$ of the area in the $3d_{5/2}$ region. If this condition applies, then the background subtraction is corrected.

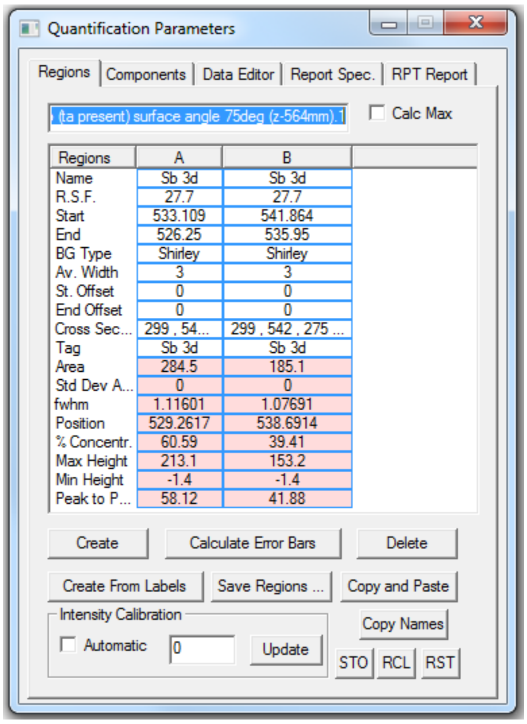

(ta present) surface angle 75deg (z-564mm).1

Regions	A	B
Name	Sb 3d	Sb 3d
R.S.F.	27.7	27.7
Start	533.109	541.864
End	526.25	535.95
BG Type	Shirley	Shirley
Av. Width	3	3
St. Offset	0	0
End Offset	0	0
Cross Sec...	299 , 54...	299 , 542 , 275 ...
Tag	Sb 3d	Sb 3d
Area	284.5	185.1
Std Dev A...	0	0
fwhm	1.11601	1.07691
Position	529.2617	538.6914
% Concentr.	60.59	39.41
Max Height	213.1	153.2
Min Height	-1.4	-1.4
Peak to P...	58.12	41.88

Intensity Calibration: 0

Fig.4.16. The “Quantification Parameters” dialog window in CasaXPS. It shows the two regions created for the Sb 3d spectrum (Fig.4.15). The beginning and the end points of the region are entered as well as the background type.

accordance with the electron population of the $3d_{3/2,5/2}$ levels. This facilitates a physically meaningful fit to the experimental spectra as discussed in (Sec. 4.2.2). The result of this fitting procedure is shown in (Fig.4.17).

The signal to noise ratio of the surface sensitive scan (Fig. 4.15) is not ideal and there is a sudden fall of the intensity at the high binding energy side of the $3d_{3/2}$ component.

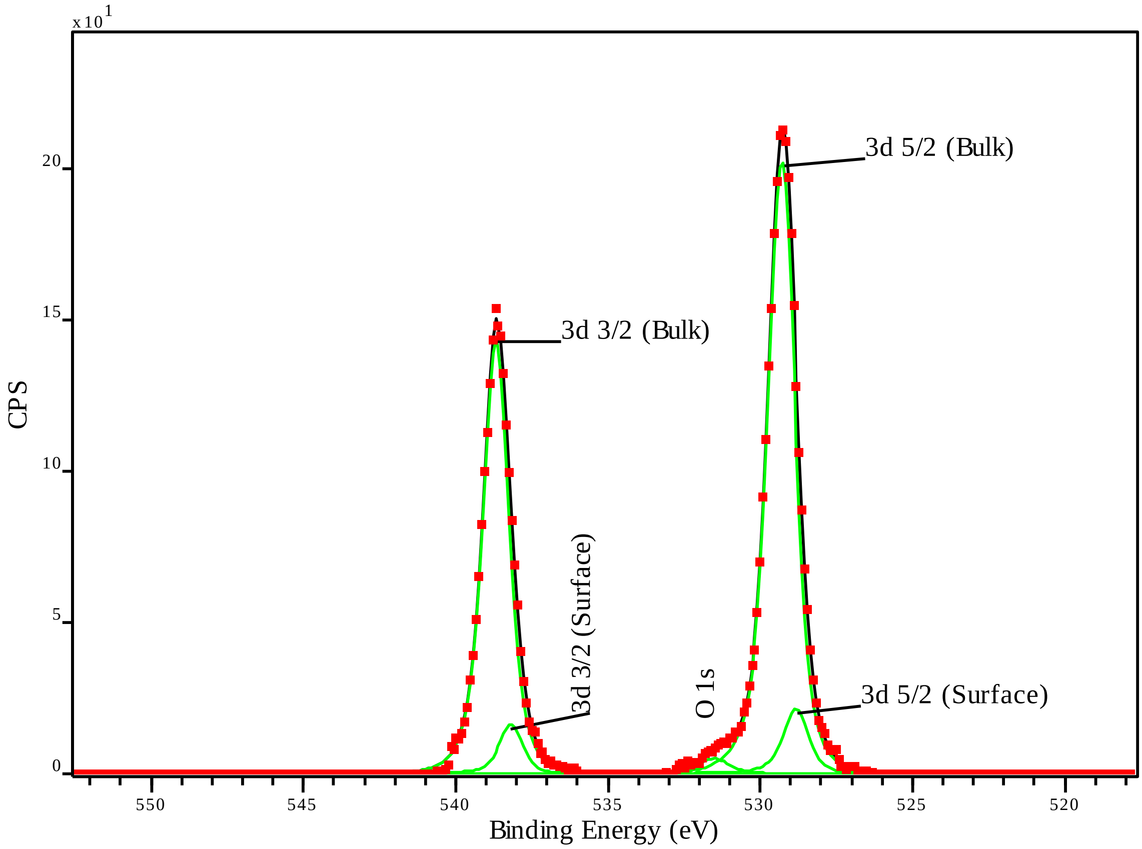

Fig. 4.17: Red squares: the surface-sensitive Sb $3d$ spectrum after the subtraction of the background shown in (Fig.4.15). Green: the synthetic peaks created to account for the spectrum. Two peaks were created for each $3d$ doublet components to account for the bulk and the surface emission. A weak O $1s$ peak was detected. The black line is the synthetic spectrum resulting from the synthetic peaks. The areas of the $3d_{5/2}$ and $3d_{3/2}$ bulk components are 253.7 and 172.5, respectively, while the areas of the bulk components are 24.9 and 17.0. These areas achieve the $3:2$ intensity condition for a d level mentioned in the text.

The binding energies of the bulk and the surface components of the $3d_{5/2}$ peak are $528.61 \pm 0.07\ eV$ and $528.13 \pm 0.07\ eV$ respectively, whereas the binding energies of the corresponding $3d_{3/2}$ peaks are $538.00 \pm 0.07\ eV$ and $537.49 \pm 0.07\ eV$. The surface core-level shift is then $0.48 \pm 0.07\ eV$ toward lower binding energy for $3d_{5/2}$ and $0.51 \pm 0.07\ eV$ for $3d_{3/2}$.

A weak O $1s$ peak was detected at $530.85 \pm 0.07\ eV$ (Fig. 4.17).

In the Shirley-background subtracted surface Sb $M_{4,5}N_{4,5}N_{4,5}$ Auger spectrum (Fig. 4.18) the peaks associated with the $^{1}G_4$ term of the $M_5N_{4,5}N_{4,5}$ and $M_4N_{4,5}N_{4,5}$ groups were located at $455.08 \pm 0.07\ eV$ and $464.47 \pm 0.07\ eV$ respectively. The splitting between the two groups is $9.39 \pm 0.07\ eV$ which is equal to the splitting between the $3d_{3/2,5/2}$. These splittings were found by Pessa et al [5] to be $9.39 \pm .21\ eV$ and $9.41 \pm .21\ eV$ respectively. The $3d$ doublet splitting has been reported at values ranging between $9.30\ eV$ and $9.50\ eV$ [6].

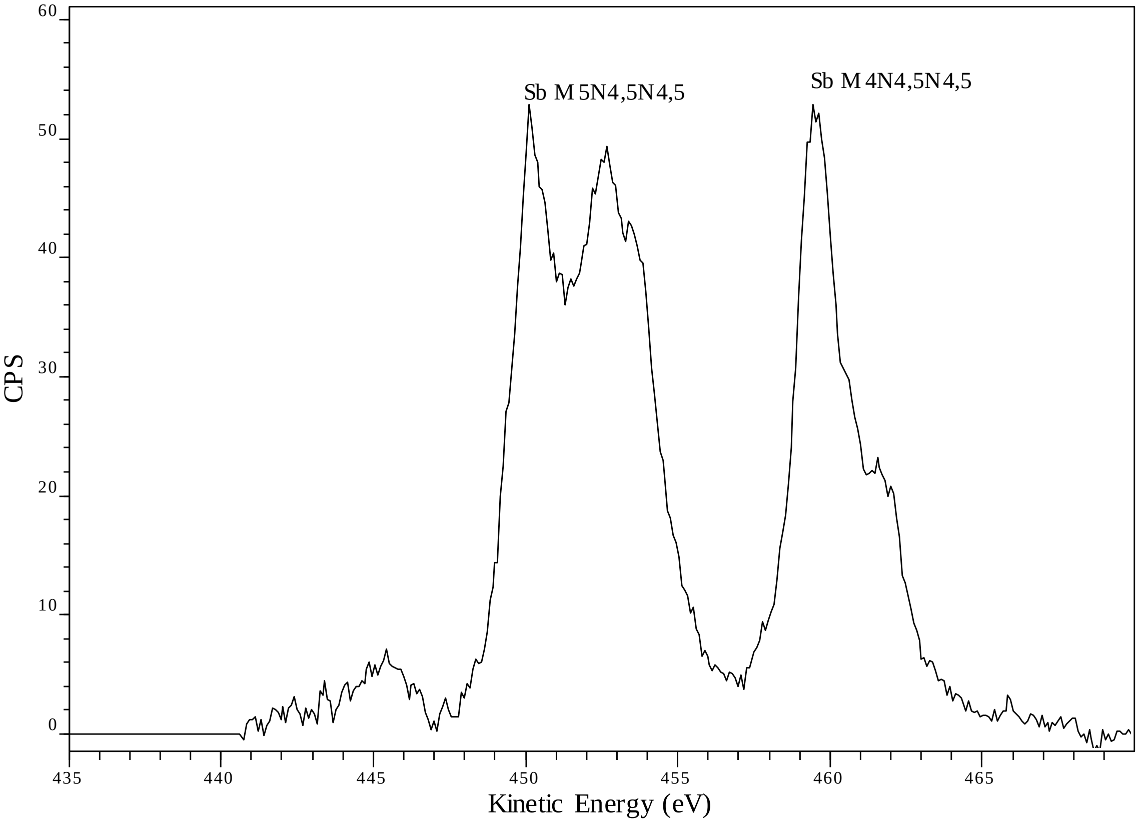

Fig. 4.18: Surface-sensitive Sb $M_{4,5}N_{4,5}N_{4,5}$ Auger spectrum. Background was corrected by Shirley method. This spectrum is similar to that obtained at the normal emission (Fig.4.20).

4.3.3 The Sb bulk spectra:

A synthetic peak model of the Sb $3d$ spectrum taken at a normal takeoff (Fig. 4.19) was constructed by the same method used for the In $3d$ (Section. 4.2.2). The model contains a species that arises from the surface core-level shift as well as that from the bulk. The O $1s$ did not appear in this spectrum, which indicates that the oxygen is within a thin layer on the surface of the pure metallic Sb. The binding energies of the bulk and the surface $3d_{5/2}$ components are $527.81 \pm 0.07\ eV$ and $527.41 \pm 0.07\ eV$, whereas those of $3d_{3/2}$ are $537.18 \pm 0.07\ eV$ and $536.77 \pm 0.07\ eV$ respectively. The surface core-level shift is therefore

$0.40 \pm 0.07\ eV$ of $3d_{5/2}$, and $0.41 \pm 0.07\ eV$. The $3d$ spin-orbit splitting is $9.37 \pm 0.07\ eV$ for the bulk components, and $9.36 \pm 0.07\ eV$ for the surface components.

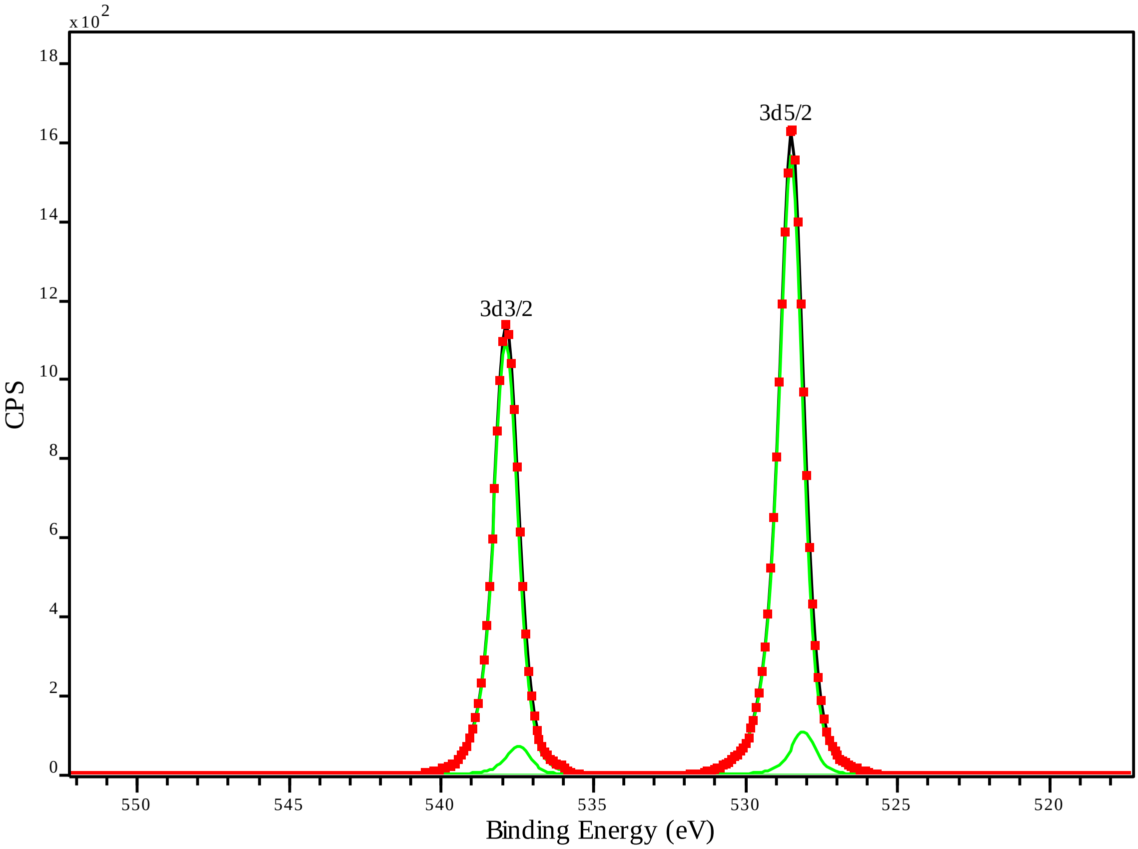

Fig. 4.19: The red squares: the Sb $3d$ spectrum at normal emission scan after the subtraction of a Shirley-type background similar to that used for the surface sensitive spectrum (Fig.4.15). There synthetic peaks (green) are created to account for different components. There are two peaks for each of the $3d$ doublet components. The black line is the resulting synthetic spectrum which aligns with the data (the real spectrum).

The positions of the highest peaks in the $M_5N_{4,5}N_{4,5}$ and the $M_4N_{4,5}N_{4,5}$ Auger groups at the normal emission (Fig.4.20) were $455.41 \pm 0.07\ eV$ and $464.74 \pm 0.07\ eV$ respectively. These peaks are associated with the $^1G_4$ components as mentioned in (Sec.4.2.3), and located using the differential form of the spectrum (Fig.4.12). The values taken at normal emission differ from those taken at the surface sensitive measurements (Sec 4.3.2). Both sets of values were referenced to the Fermi level measured during the normal emission scan, therefore, and as mentioned in (Sec 4.3.1) the normal emission values are reliable. The surface sensitive scan did not show a clear Fermi edge (Fig 4.21).

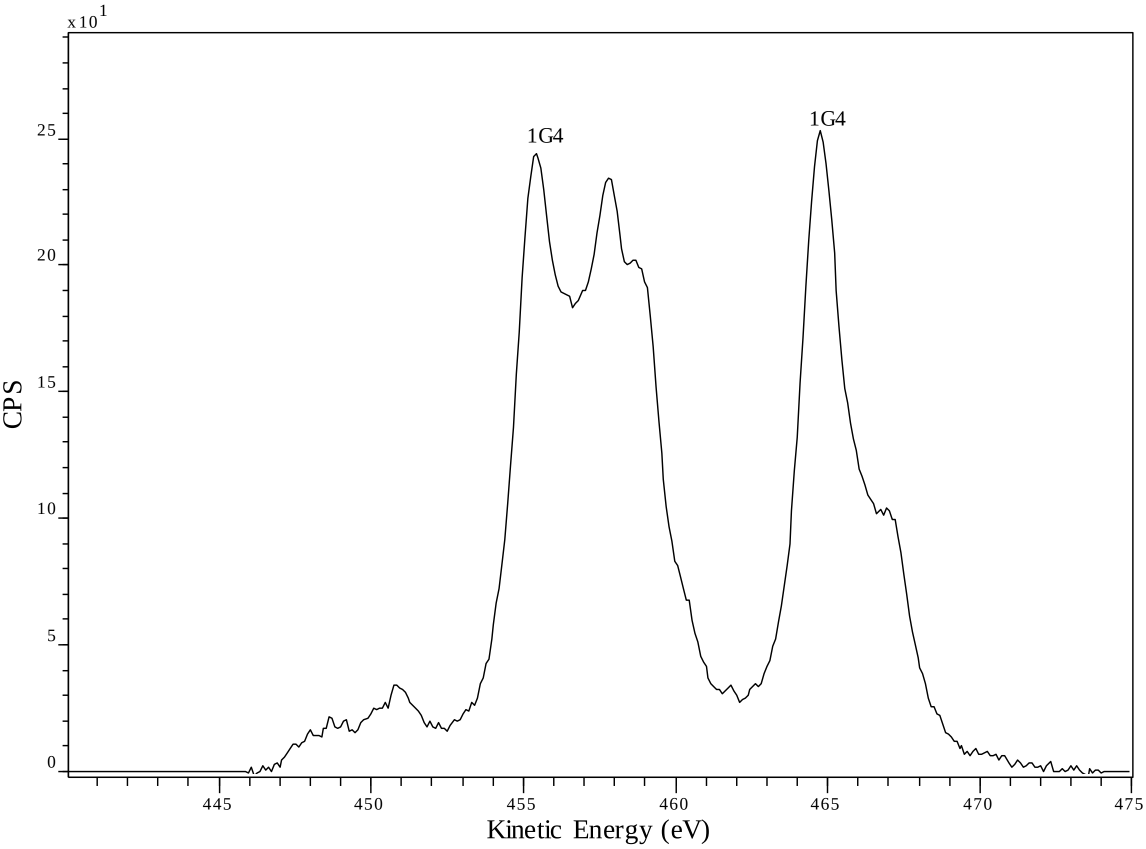

Fig. 4.20: The Sb $M_{4,5}N_{4,5}N_{4,5}$ Auger spectrum obtained at Normal emission after the Ar^{+} ion bombardment. A correction is made by subtracting a Shirley background. The highest peaks at both of the Auger groups, which are associated with the $^{1}G_{4}$ components, are annotated. The same spectrum was shown before the background subtraction in (Fig.4.12).

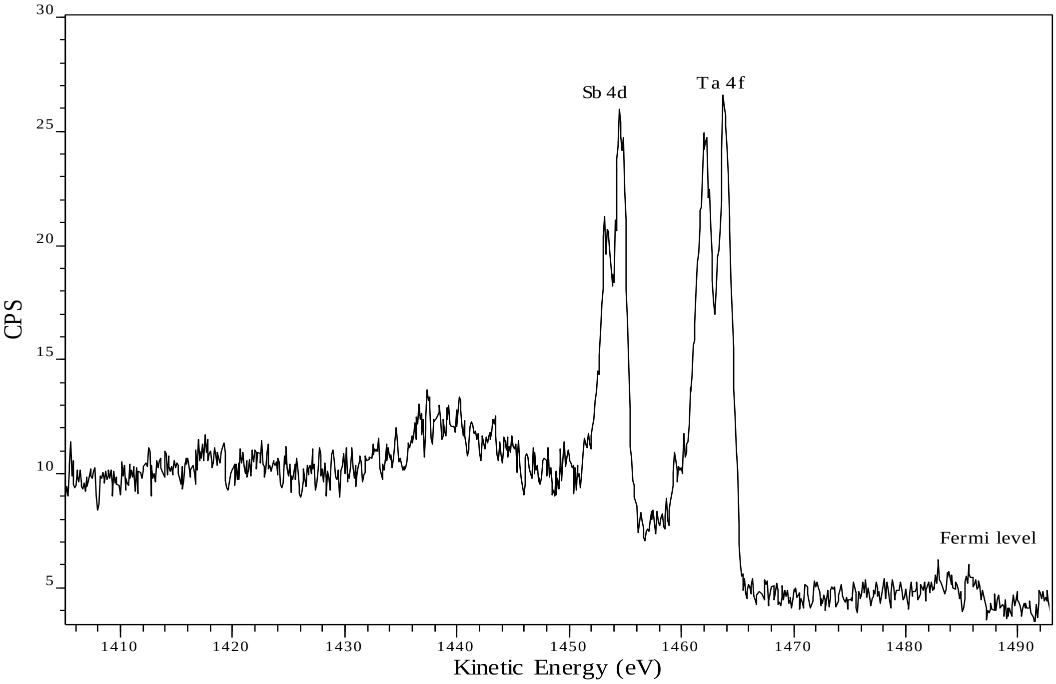

Fig. 4.21: The surface sensitive spectrum of the Sb valence band and Fermi level obtained after cleaning. The Fermi level is not clear. Ta $4f$ photoelectron lines are detected from the tantalum specimen holder.

4.4 Summary:

The Auger and photo-electron spectra of metallic In and Sb have been analysed, and the characteristic $3d$ and $^1G_4$ components have been precisely located. (Table. 4.1) lists the spectroscopic values of these components obtained by this work and those obtained by [5].

Transition	In		Sb	
	This work	**[5]**	**This work**	**[5]**
$\boldsymbol{3d_{5/2}}$	444.04	443.84	527.81	528.02
$\boldsymbol{3d_{3/2}}$	451.58	451.44	537.18	537.43
$\boldsymbol{M_5N_{4,5}N_{4,5}\ (^1G_4)}$	402.56	402.85	455.41	454.90
$\boldsymbol{M_4N_{4,5}N_{4,5}\ (^1G_4)}$	410.22	410.41	464.74	464.29
$\boldsymbol{\alpha}$	854.26	854.25	992.55	992.31

Table. 4.1. The BE of $3d_{5/2}$ and $3d_{3/2}$ lines, and the KE of the $^1G_4$ components of the $M_5N_{4,5}N_{4,5}$ and $M_4N_{4,5}N_{4,5}$ Auger transitions of In and Sb obtained by this work and by [5]. α is the Auger parameter calculated as $KE_{M_4N_{4,5}N_{4,5}}(^1G_4) + BE_{3d_{5/2}}$.

The values of the Auger parameters of metallic elemental In and Sb (Table.4.1), $854.26 \pm 0.07\ eV$ and $992.55 \pm 0.07\ eV$ respectively, will be used in the potential model, described in (Sec.1.4.2), to analyse the electronic structure of InSb in (Ch.9).

References

1. Linarez Pérez, O.E., M.D. Sánchez, and M. López Teijelo, *Characterization of growth of anodic antimony oxide films by ellipsometry and XPS.* Journal of Electroanalytical Chemistry, 2010. **645**(2): p. 143-148.
2. Honma, T., et al., *Electronic polarizability, optical basicity and XPS spectra of Sb 2 O 3–B 2 O 3 glasses.* Journal of non-crystalline solids, 2000. **272**(1): p. 1-13.
3. Tang, X., et al., *Oxidation of the InSb surface at room temperature.* Semiconductor science and technology, 1986. **1**(6): p. 355.
4. Paliwal, V.K., A. Vedeshwar, and S. Shivaprasad, *Sb induced (7× 7) to (1× 1) surface phase transformation of the Si (111) surface.* Solid state communications, 2003. **127**(1): p. 7-11.
5. Pessa, M., et al., *Solid-state effects inM4,5N4,5N4,5Auger spectra of elements fromIn49toTe52.* Physical Review B, 1979. **20**(8): p. 3115-3123.
6. NIST, X., *Database,< h ttp.* srdata. nist. gov/xps/Default. aspx.
7. Williams, R., et al., *Angle-and energy-dependent core-level photoelectron energy loss studies in Al and In.* Journal of Electron Spectroscopy and Related Phenomena, 1977. **12**(4): p. 477-492.
8. Bouslama, M., et al., *AES and EELS analysis of the interaction between phosphorus and metallic indium.* Journal of electron spectroscopy and related phenomena, 1994. **68**: p. 377-382.
9. Krischok, S., et al., *Investigations of MBE grown InN and the influence of sputtering on the surface composition.* Surface Science, 2004. **566-568**: p. 849-855.
10. Legare, P., L. Hilaire, and G. Maire, *The superficial oxidation of indium, Sb and InSb (111)-a LEED, AES, XPS and UPS study.* JOURNAL DE MICROSCOPIE ET DE SPECTROSCOPIE ELECTRONIQUES, 1980. **5**(6): p. 771-782.
11. Sen, P., M. Hegde, and C. Rao, *Surface oxidation of cadmium, indium, tin and antimony by photoelectron and Auger spectroscopy.* Applications of Surface Science, 1982. **10**(1): p. 63-74.
12. Parry-Jones, A., P. Weightman, and P. Andrews, *The M4, 5N4, 5N4, 5 Auger spectra of Ag, Cd, In and Sn.* Journal of Physics C: Solid State Physics, 1979. **12**(8): p. 1587.
13. Aksela, S., et al., *M4, 5N4, 5N4, 5 Auger electron spectrum of In from In, InCl and InCl3 vapours.* Journal of Physics B: Atomic and Molecular Physics, 1980. **13**(19): p. 3745.
14. Aksela, S., et al., *Free-atom—metal shifts in theM4,5N4,5N4,5Auger spectra of Ag, Cd, In, Sn, Sb, and Te.* Physical Review B, 1981. **23**(9): p. 4362-4368.
15. Seah, M., *Quantitative Auger electron spectroscopy: Via the energy spectrum or the differential?* Surface and Interface Analysis, 1979. **1**(3): p. 86-90.
16. Harris, L., *Miscellaneous topics in Auger electron spectroscopy.* Journal of Vacuum Science and Technology, 1974. **11**(1): p. 23-28.
17. Briggs, D. and J.T. Grant, *Surface analysis by Auger and x-ray photoelectron spectroscopy*. 2003, Chichester, West Sussex, U.K.: IM Publications. xi, 899 p.
18. John Walton, P.W., Neal Fairley, Alan Carrick, *Peak Fitting with CasaXPS*. 2011, Cheshire: Acolyte Science. 132.

Chapter 5

Electron Spectroscopic Analysis of Sb/InSb

5.1. Introduction:

XPS and AES were performed on the $\mathrm{Sb/InSb}$ specimen as received and after decapping by heating at $150\ °C$, $250\ °C$, $300\ °C$, $325\ °C$, $350\ °C$, $375\ °C$. Broadscans were performed at each stage and narrow scans were performed when new spectroscopic features were detected.

The resolution and the energy step of the analyser were set to $1.67\ eV$ and $0.49\ eV$ respectively in all the broadscans; and $0.33\ eV$ and $0.09\ eV$ in the narrow scans.

The choice of cleaning and decapping the specimen by heating is preferred over ion sputtering, although the latter is more effective. This is because ion bombardment is known to cause change to the surface topography [4] and crystal structure as well as selective segregation of some components [6, 7].

The specimen was grown in The University of Warwick by molecular beam epitaxy (MBE). The surface orientation of the InSb is (001). The Sb overlayer was made by leaving the surface exposed to the Sb flux and switching off the substrate heater. The Sb flux is switched off some time after the substrate has cooled to room temperature. So, amorphous Sb forms on the surface.

5.2. Overview of the spectra:

Raw spectra will be analysed to develop an overview of the species present and their relative intensities and energy splittings. After that, in (Sec.5.3), peak models will be made to fit the $3d$ spectra and determine line positions.

5.2.1. The broadscans:

In the broadscan that was taken on the specimen as received the Sb $M_{4,5}N_{4,5}N_{4,5}$ Auger and level $3d$ and $4d$ photoelectron lines appear. There is a contamination of carbon and oxygen as can be noticed from the O KLL Auger and C $1s$ lines (Fig.5.1).

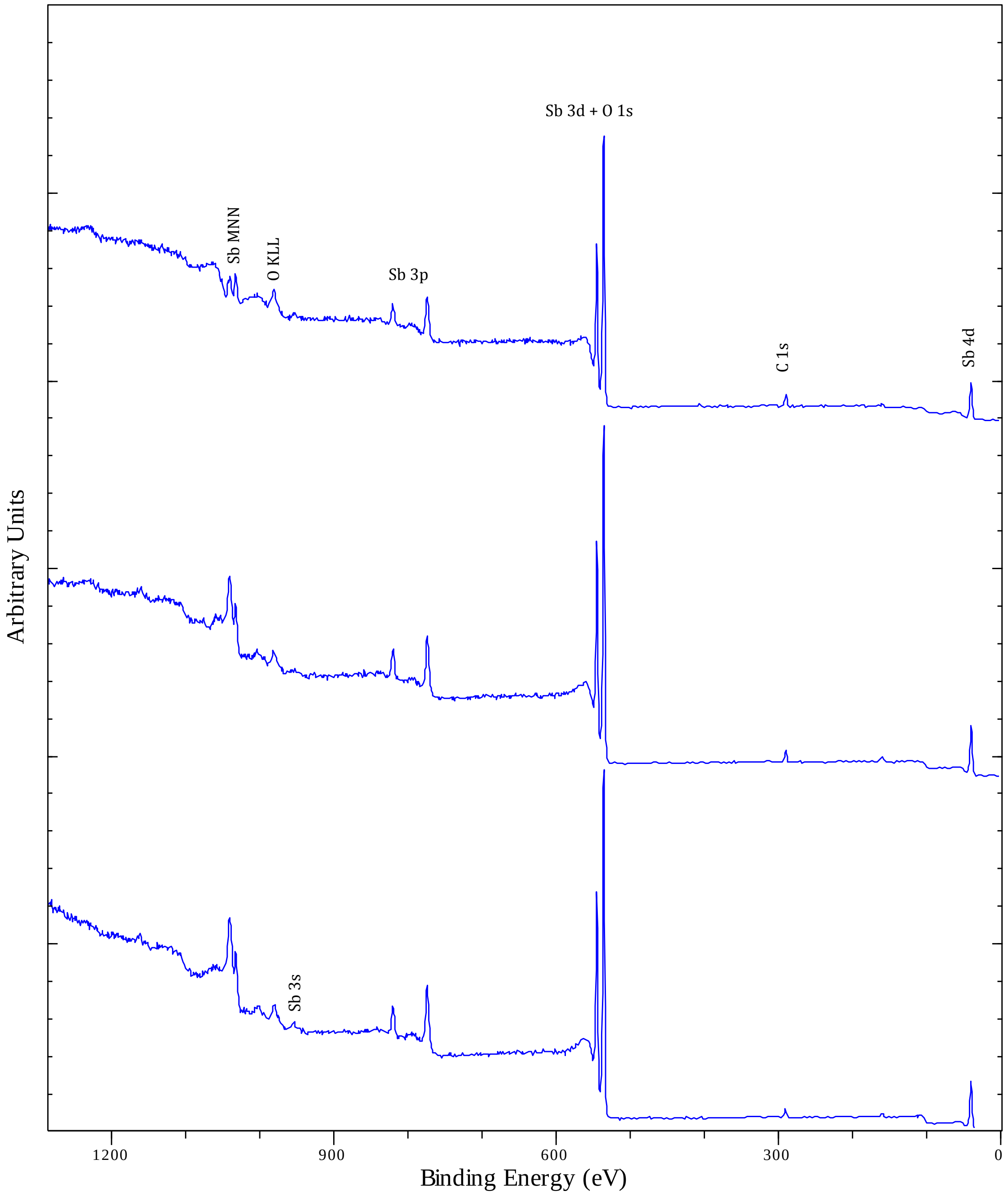

Fig. 5.1: Broadscans of Sb/InSb specimen as received (top), after heating at $150\ °C$ for 2 hours (middle) and after heating at $250\ °C$ for 2 hours (bottom). O KLL Auger and C $1s$ were reduced by heating. O $1s$ is known to overlap with Sb $3d_{5/2}$ line. The Sb $M_{4,5}N_{4,5}N_{4,5}$ spectrum became sharper by heating.

After heating (decapping) the specimen at $150\ °C$ for $2\ hours$ the following can be noticed at the broadscan (Fig.5.1):

- The $M_{4,5}N_{4,5}N_{4,5}$ is more intense and their appears to be a new species at lower kinetic energy which can be attributed to plasmon loss that occurred because of the presence of free electron gas after the specimen was deoxidised by heating .

- $\mathrm{O}\ KLL$ and $\mathrm{C}\ 1s$ are weaker. That is linked to the previous point.
- The $\mathrm{Sb}\ 3p$ lines are more intense.

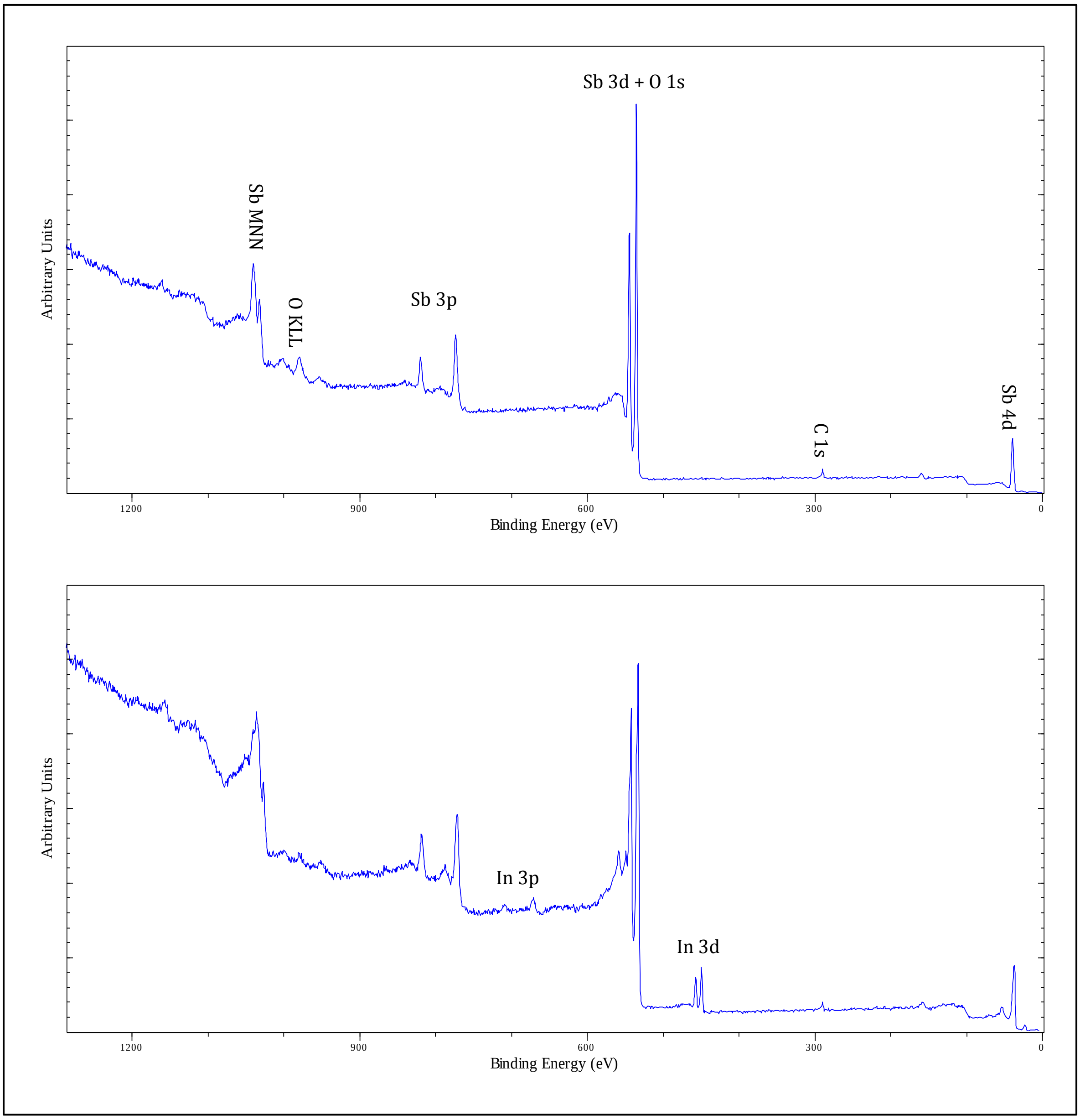

Fig. 5.2: The broadscans of Sb/InSb after heating at 250 $°C$ for 2 hours (top), and at 300 $°C$ for 2 hours (bottom). It shows the presence of indium spectrum and the significant reduction of oxygen.

After further heating the specimen at 250 ℃ for 2 $hours$, no significant changes could be seen (Fig. 5.1).

After heating at 300 ℃ for 2 $hours$ significant changes to the spectra appeared (Fig. 5.2):

- In lines ($3d$, $3p$ and $4d$) are present which suggests, with hindsight, that the InSb layer has been exposed.

- The intensity of O KLL decreased significantly resulting in more intense Sb plasmon loss peaks.
- The Sb $M_{4,5}N_{4,5}N_{4,5}$ Auger peaks are broader probably due to an overlap between the lines of the Sb cap and the Sb in the InSb layer. This becomes clear when the narrow scans are analysed (Sec.5.2.4).

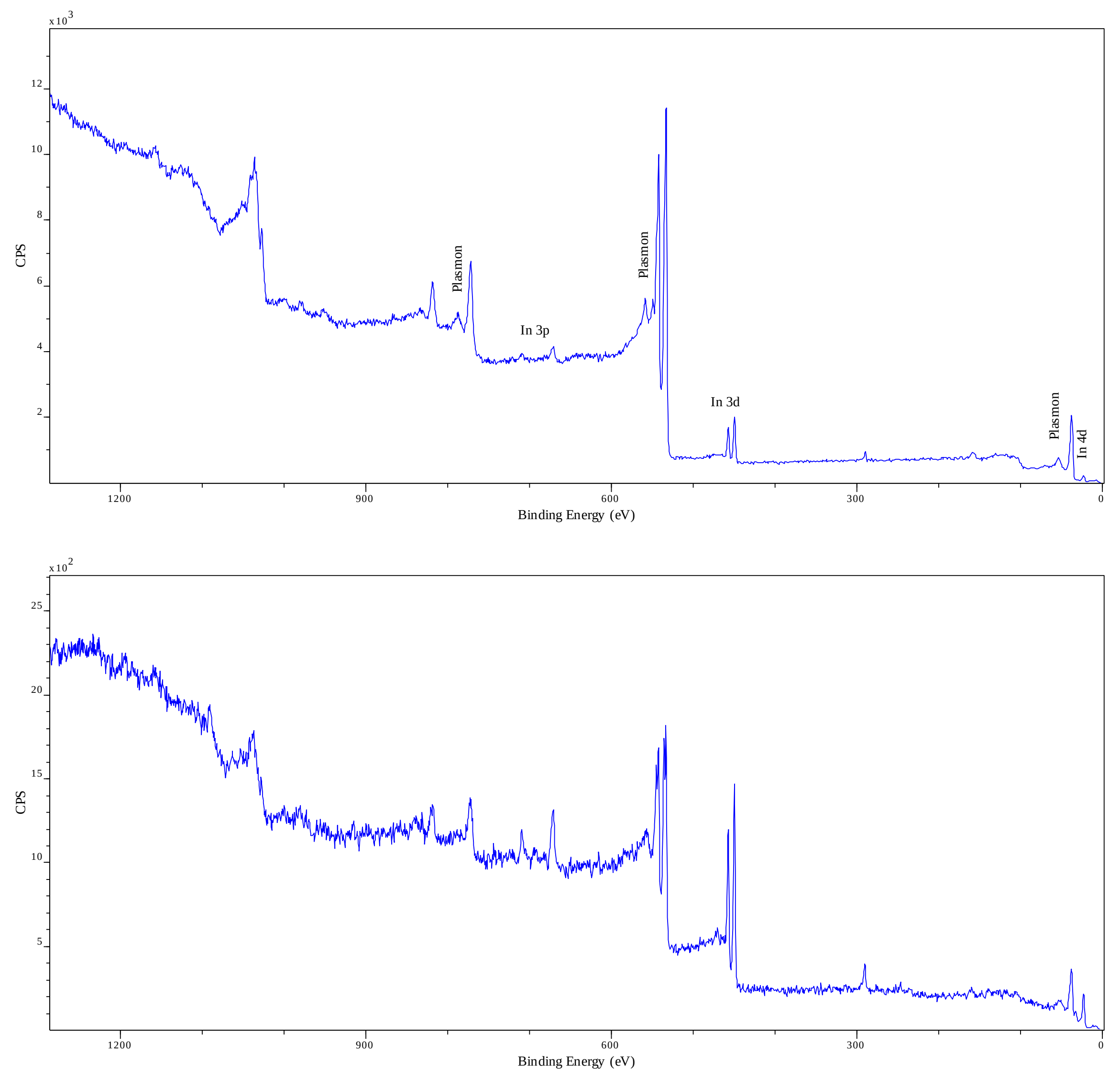

Fig. 5.3: Top: the Sb/InSb broad scan spectrum acquired at normal emission (0° takeoff angle relative to the perpendicular to the surface) after heating the specimen at 300 °C for 2 hours. Bottom: the surface-sensitive broadscan (obtained at 80° takeoff angle). The intensity of the In $3d$ at the surface is considerably higher than in the bulk which suggests the diffusion of In from the InSb substrate to the surface of the specimen.

A surface-sensitive scan (at 80° takeoff angle) taken after the 300℃ heating exhibits more intense In photoelectron lines and C $1s$. The Sb $3d$ plasmons are less intense suggesting that an SbOx layer is still present on the surface of the specimen (Fig. 5.3).

By zooming on the Sb $3d$ region in the surface-sensitive broadscan taken after the 300 ℃ heating, it can be seen that this line has doubled (Fig. 5.4).

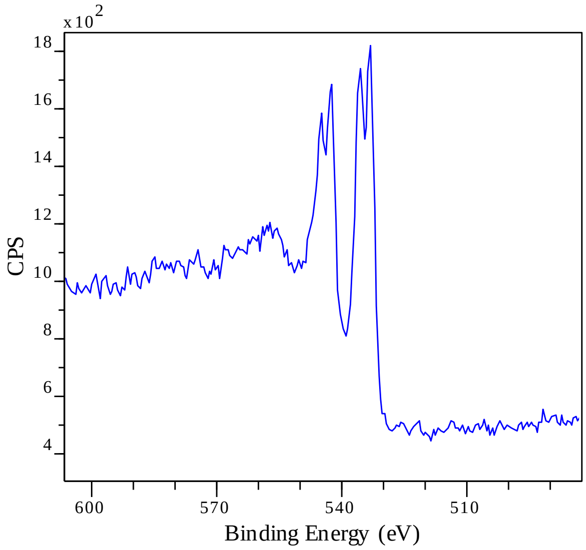

Fig. 5.4: The Sb $3d$ region within the surface-sensitive broadscan obtained after the heating at 300 ℃. It shows the existence of two species of $3d$.

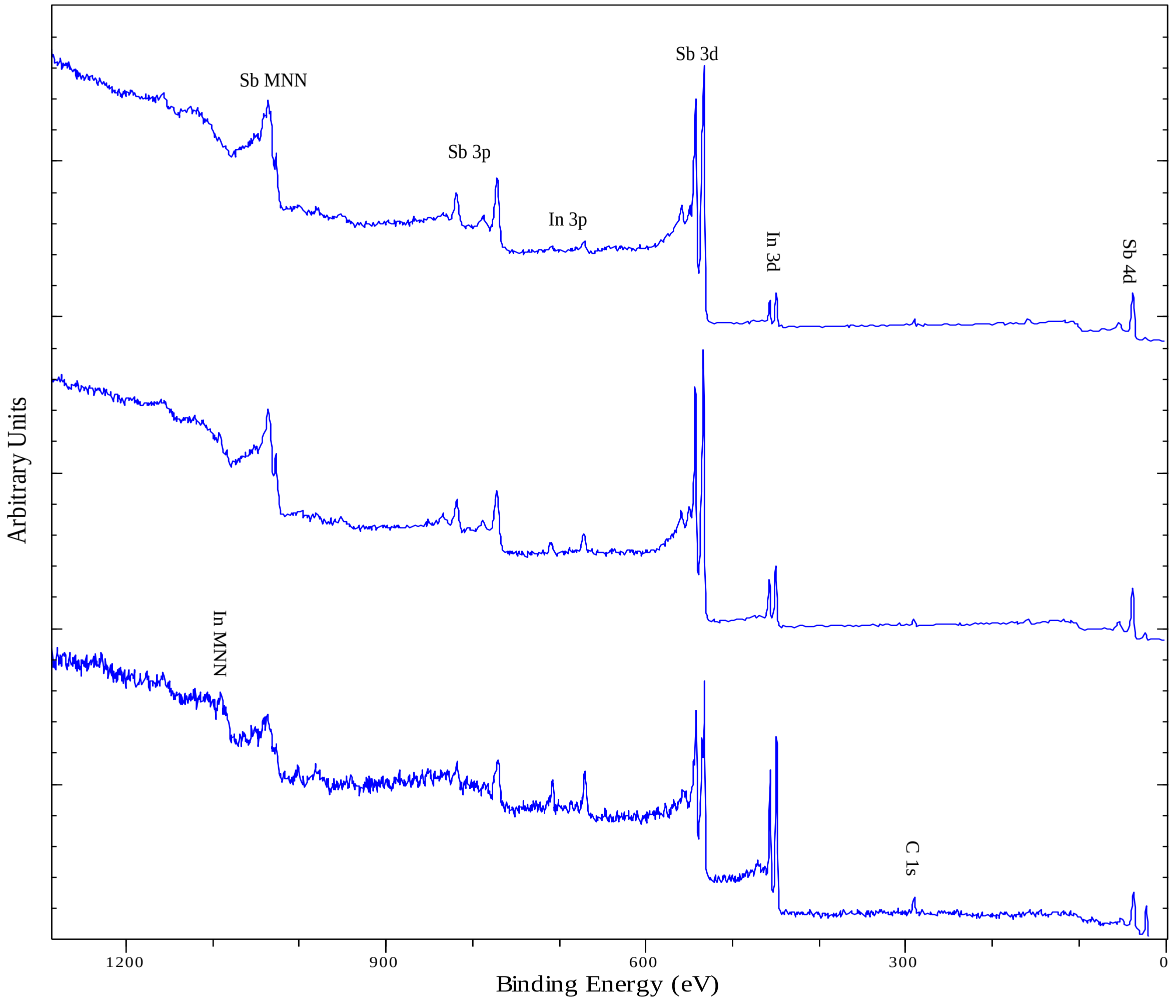

Fig. 5.5: The normal emission broadscans of Sb/InSb after decapping at 300 °C for 2 hours (top), at 350 °C for 1 *hour* (middle) and the surface sensitive scan at the latter. In spectrum is more intense after heating at 350 °C, and considerably more intense in the surface-sensitive spectrum. The peak of the lowest binding energy in the spectra (next to Sb $4d$) is the In $4d$.

After heating the specimen at $350\ ^{\circ}\mathrm{C}$ for $1\ hour$ the $\mathrm{In}\ 3p$, $3d$ and $4d$ became stronger (Fig 5.5). Taking a surface-sensitive broadscan at the same stage (Fig 5.5) reveals the same properties as those observed after the $300\ ^{\circ}\mathrm{C}$ heating. However, indium lines are considerably stronger in the surface sensitive spectra. This is an indication of the formation of an In rich surface. This will be further investigated when the narrow scans are analysed (Sec.5.2.3).

After heating the specimen at $375\ ^{\circ}\mathrm{C}$ for $1\ hour$ no significant change has occurred (Fig. 5.6).

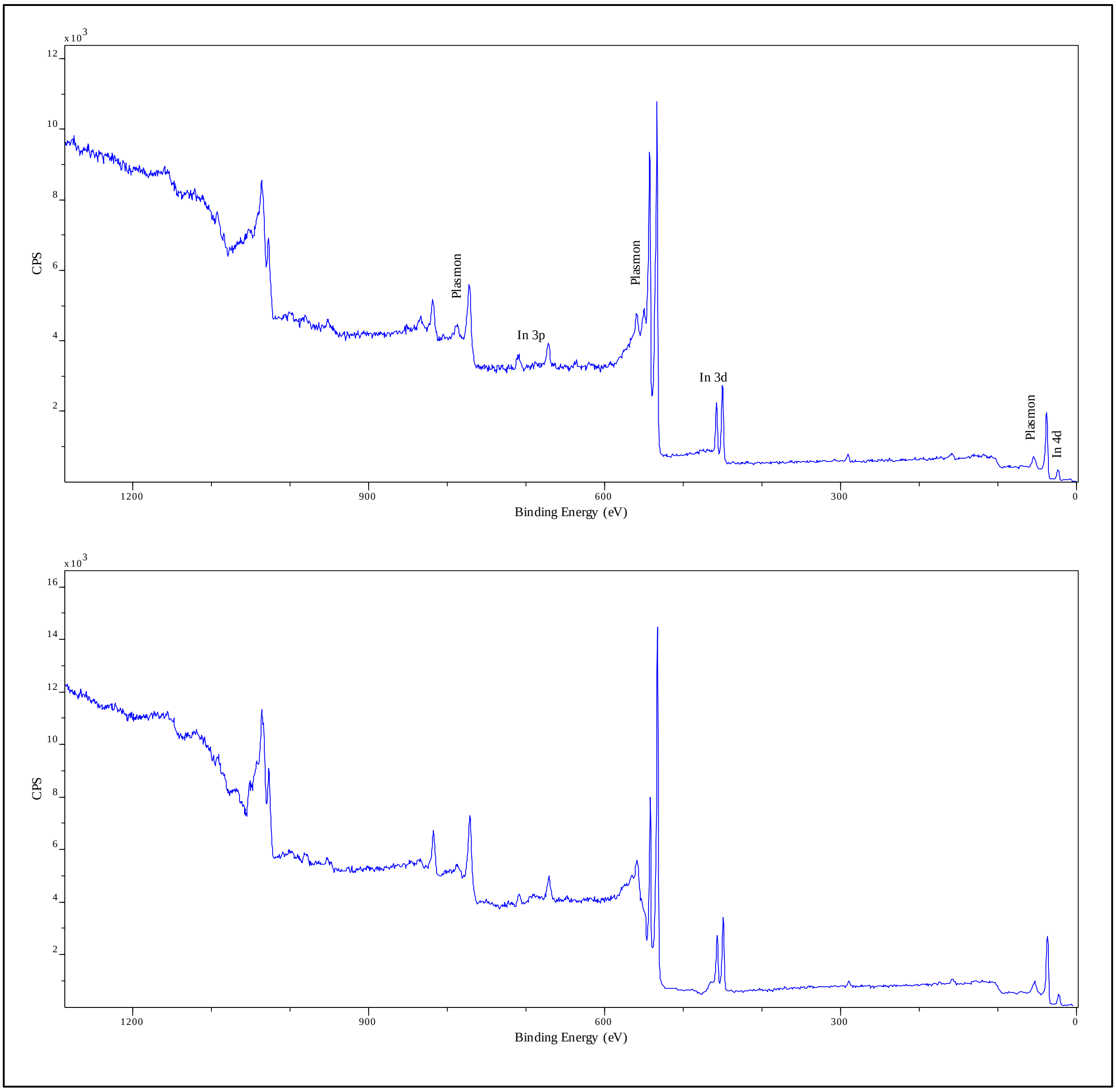

Fig. 5.6: The broadscans of $\mathrm{Sb/InSb}$ after decapping at $350\ ^{\circ}C$ for 2 hours (top), and at $375\ ^{\circ}C$ for $1\ hour$ (bottom). The two spectra ae similar which means that the heating at $375\ ^{\circ}C$ did not change the structure of the specimen.

5.2.2. Valence band and the Fermi level:

After each annealing, if the Fermi edge was clear and reliable it was modelled by the error function. It was then used to reference the spectroscopic lines.

(Fig.5.7) shows the valence band scans made before heating the specimen and after heating it at $300\ ^\circ\mathrm{C}$. The $\mathrm{Sb}\ 4d$ region consists of two components separated by $\sim 2.6\ eV$. The higher BE one can be associated with an oxidised Sb in the Sb cap while the other is associated with pure Sb. The latter became considerably more intense after the heating showing the expected $\mathrm{Sb}\ 4d$ doublet splitting of $\sim 1.2\ eV$ [8], while the former was reduced to a shoulder in the higher BE side. The as-received spectrum shows what appears to be the Fermi edge at $\sim 1479\ eV$, close to which there is a noise due to an electric spike in the detector. Nevertheless, the Fermi edge was fitted (Fig.5.8) and the Fermi level was determined at $1479.47 \pm 0.05\ eV$ in the kinetic energy scale, which is equivalent to binding energy of $7.13 \pm 0.05\ eV$. This large work function is due to a contribution from the surface charging of the contaminated, hence less conductive, specimen.

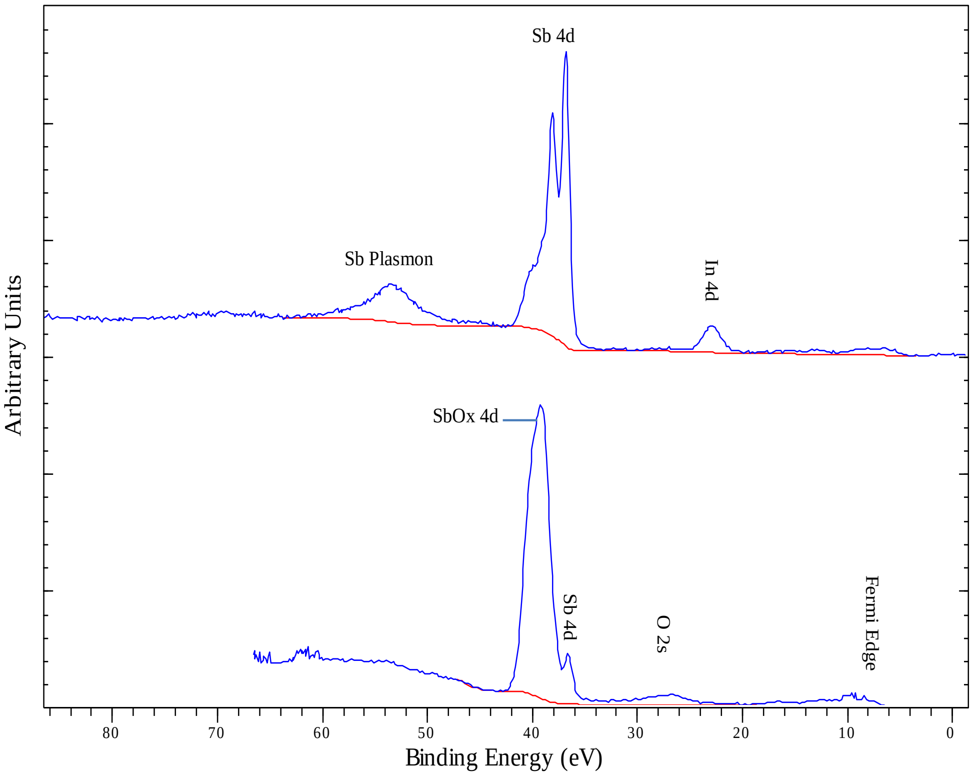

Fig. 5.7: The valence band and the Fermi edge spectra of Sb/InSb specimen before heating (bottom) and after heating at 300 °C (top). Most of the Sb was oxidised before heating as appears from the intense SbOx $4d$ peak, compared to a faint elemental Sb peak. This is reversed after heating where the pure Sb 4d doublet is clear and the SbOx appears as a small shoulder at the higher binding energy side. Sb plasmon peak is present after heating because of the existence of a free electron gas. In 4d peak appears after the heating which is consistent with the observation of In spectrum in the broad scan after the heating at 300 °C. The red lines are Shirley-type backgrounds.

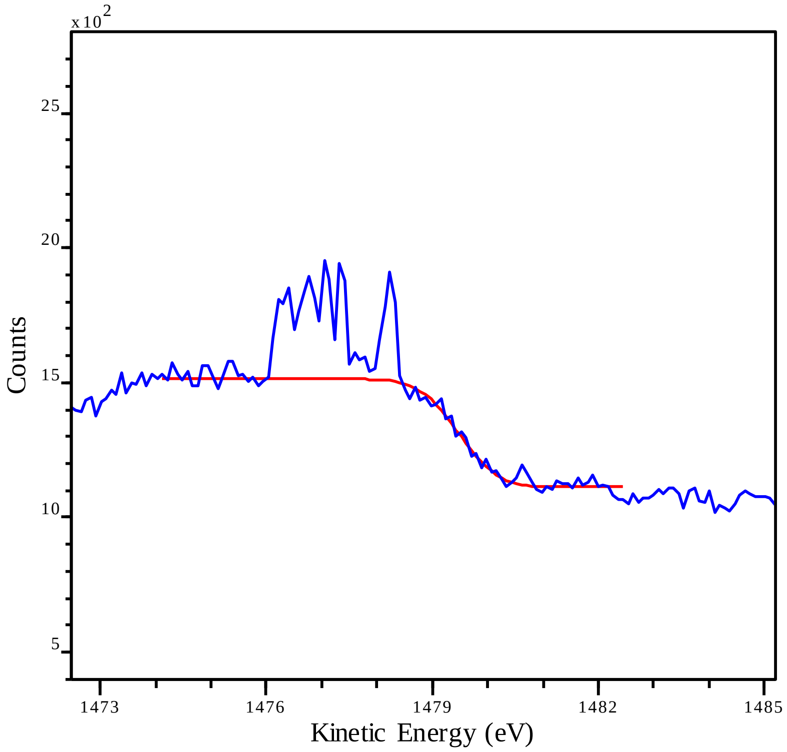

Fig. 5.8: The Fermi edge of $\mathrm{Sb/InSb}$ measured as received (blue). There is a noise (to the lower energy side of the edge) due to an electric spike in the detector. The red line is the fit of the step function to the Fermi edge. The position of the Fermi level (at $KE = 1479.47 \pm 0.05\ eV$) is chosen during the fitting process alongside the instrumental Gaussian contribution as described in (Sec.2.3.4).

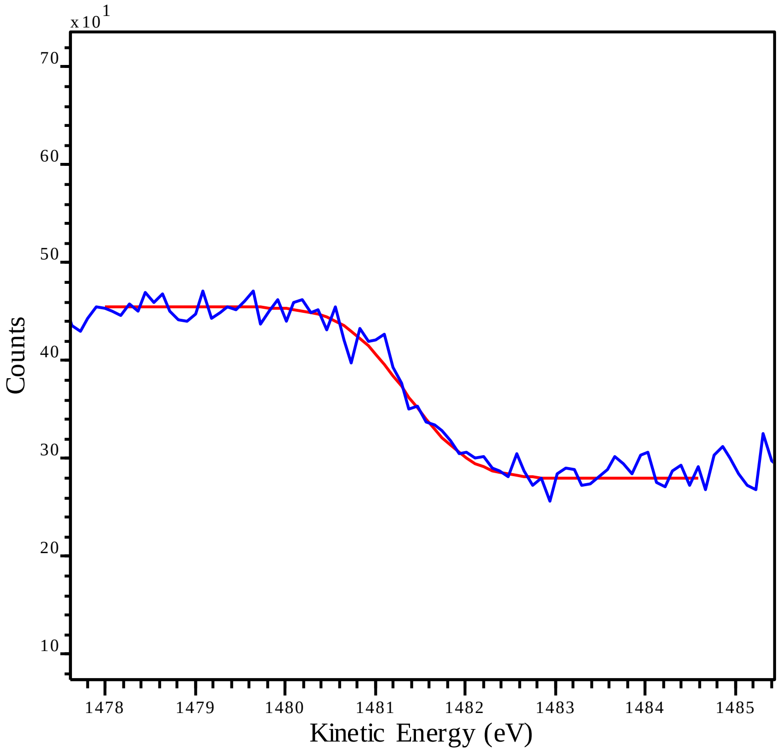

Fig. 5.9: The Fermi edge of $\mathrm{Sb/InSb}$ after heating at $300\ ^{\circ}\mathrm{C}$ (blue), and the error function fit (red) described in (Sec.2.3.4). The Fermi level was located at $KE = 1481.34 \pm 0.05\ eV$.

The work function after heating at $300\ ^{\circ}\mathrm{C}$ derived from fitting the Fermi level (Fig.5.9) is $5.26 \pm 0.05\ eV$.

(Fig.5.11) shows the valence band normal and surface-sensitive spectra after heating at $300\ ^{\circ}\mathrm{C}$. The Fermi edge at the latter has low signal to noise rate, but fitting it provides insight into the behaviour of the whole spectra throughout the experiment. By doing so, the Fermi level was located at $5.38 \pm 0.05\ eV$ (Fi.5.10).

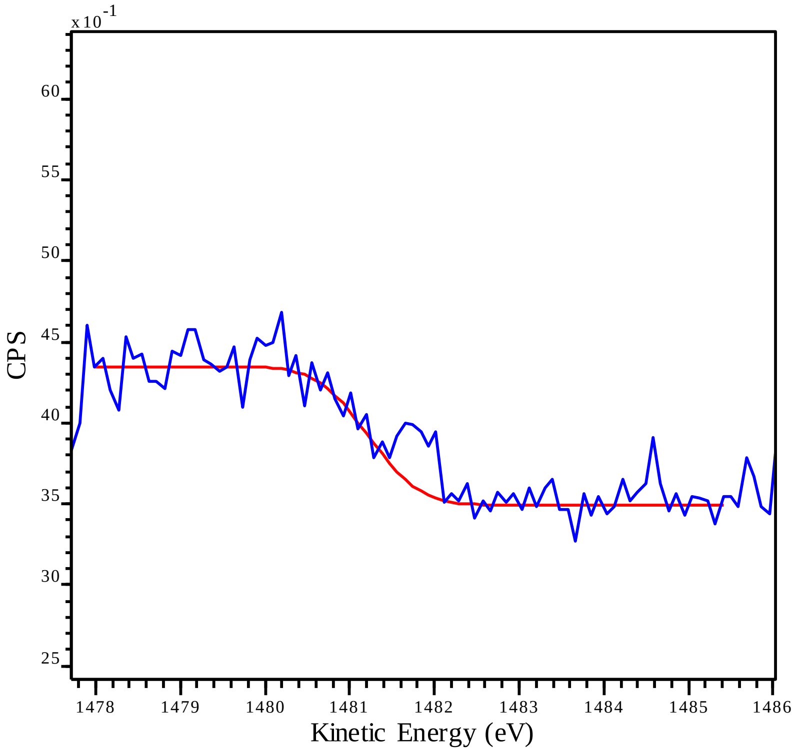

Fig. 5.10: Surface-sensitive Fermi edge spectrum of Sb/InSb obtained after heating at $300\ ^{\circ}\mathrm{C}$ (blue). The red line is the error function fit obtained by the same way as for the normal emission spectrum (Fig.5.9) and of the specimen before treatment (Fig.5.8). The Fermi level was located at $KE = 1481.22 \pm 0.05\ eV$. Although the signal to noise is not ideal, locating the Fermi level provides a reference point for the spectra measured at the same circumstances.

In the surface-sensitive spectrum (Fig.5.11), there are two peaks at BE of $\sim 26.12\ eV$ and $\sim 28.12\ eV$ (referenced to the Fermi level). They are identified as $\mathrm{Ta}\ 4f$ doublet from the Ta specimen holder.

(Fig.5.12) compares the valence band spectra taken after heating at $300\ ^{\circ}\mathrm{C}$ and $350\ ^{\circ}\mathrm{C}$. The apparent binding energy of the Fermi level after heating at $350\ ^{\circ}\mathrm{C}$ is $5.43 \pm .05\ eV$ (Fig.5.13).

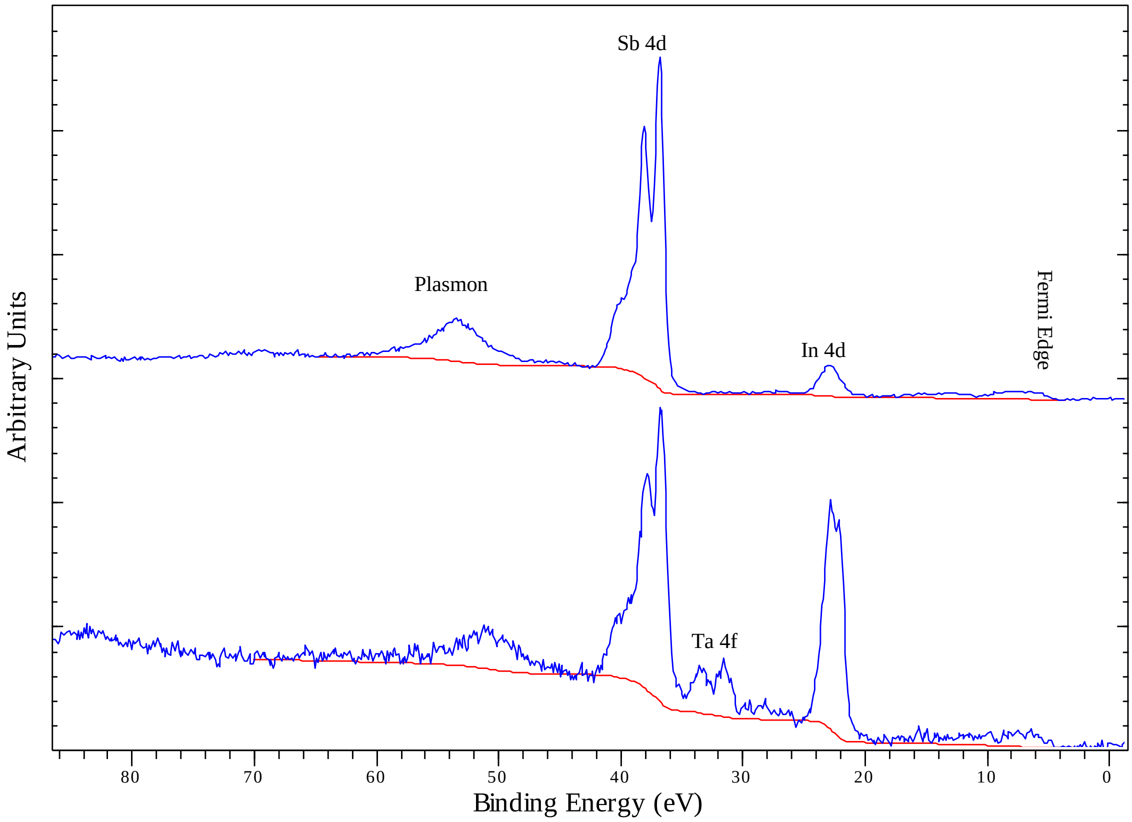

Fig. 5.11: Top: the valence band and Fermi edge spectrum of Sb/InSb obtained at normal emission after the 300 ℃ heating. Bottom: the same spectrum obtained at an emission angle of 80° making it surface sensitive. The In $4d$ is considerably more intense at the surface spectrum. A shoulder at the higher binding energy side of Sb $4d$ is due to the Sb oxide components. Ta 4f peaks are from the tantalum specimen holder. The red lines are the backgrounds of the spectra obtained by the Shirley method.

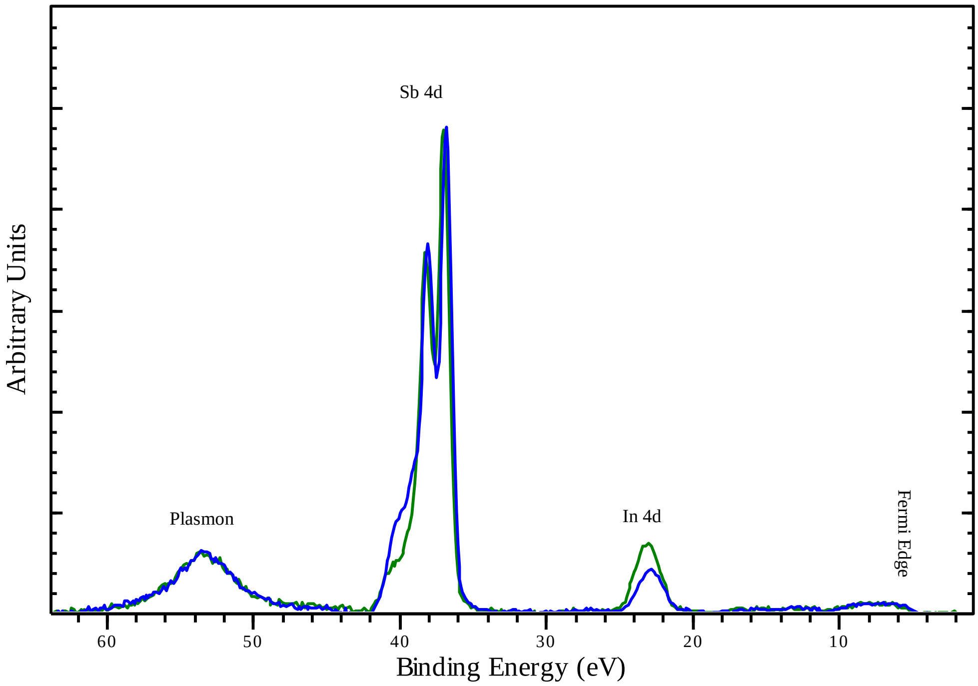

Fig. 5.12: The Valence band and Fermi level spectra of Sb/InSb taken after heating at 300 ℃ (blue) and 350 ℃ (green). Backgrounds similar to those in (Fig.5.11) were subtracted. The intensities of both spectra were normalised with respect to the highest peak of Sb $4d$ to detect differences in the shapes and widths of the peaks. The two spectra are identical apart from two features appear after heating at 350 ℃; the In $4d$ is more intense, and the shoulder at the higher BE side of Sb $4d$ is less intense. This shoulder is due to SbOx components as clear from (Fig.5.7).

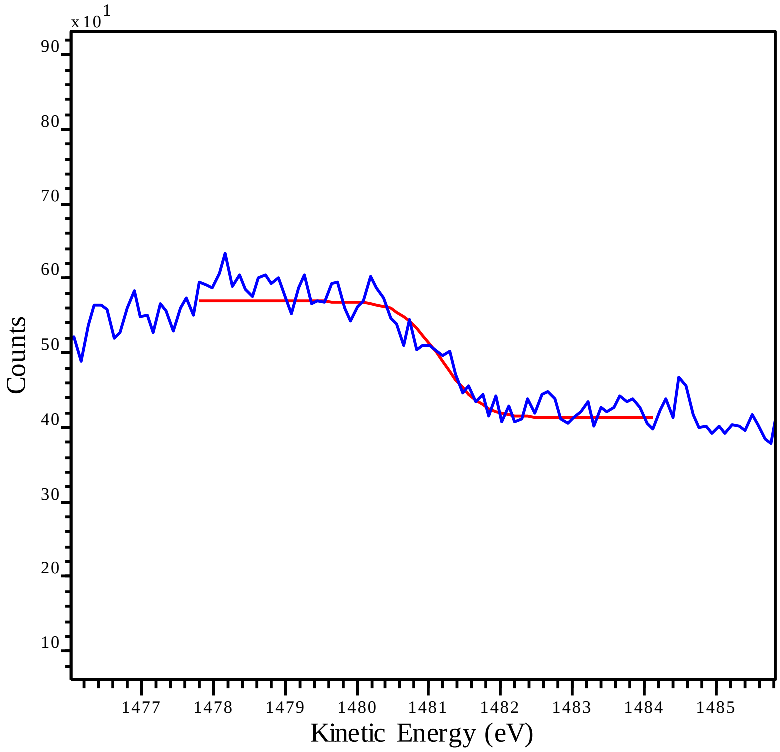

Fig. 5.13: Fermi edge of $\mathrm{Sb/InSb}$ (after heating at $350\ ℃$) (blue), and the error function fit (red) described in (Sec.2.3.4). The Fermi level was located at $KE = 1481.17 \pm 0.05\ eV$.

The surface measurement after the heating at $350\ ℃$ shows the same features observed after heating at $300\ ℃$ (Fig. 5.14). This spectrum is shifted to lower binding energy with respect to the bulk measurement. The most likely explanation to that is that the latter is irradiated by slightly different x-ray beam, that is the monochromated beam has a narrow line width. The Sb oxide shoulder in $4d$ is more clear at the surface. The Fermi edge is not sufficiently intense to be modelled by the error function. However, the $C\ 1s$ correction is $5.59 \pm 0.24\ eV$.

The spectrum did not change after heating the specimen at $375\ ℃$ (Fig.5.15). The only difference from that obtained after heating at $350\ ℃$ is that the SbOx shoulder in the $\mathrm{Sb\ 4d}$ peak was removed; suggesting the removal of the oxide from the bulk of the sample.

The Fermi edge measured after heating at $375\ ℃$ is weak, because of the less number of scans performed during the measurement of this spectrum, but modelling it (Fig.5.16) reveals that the Fermi level is at $4.82 \pm .05\ eV$.

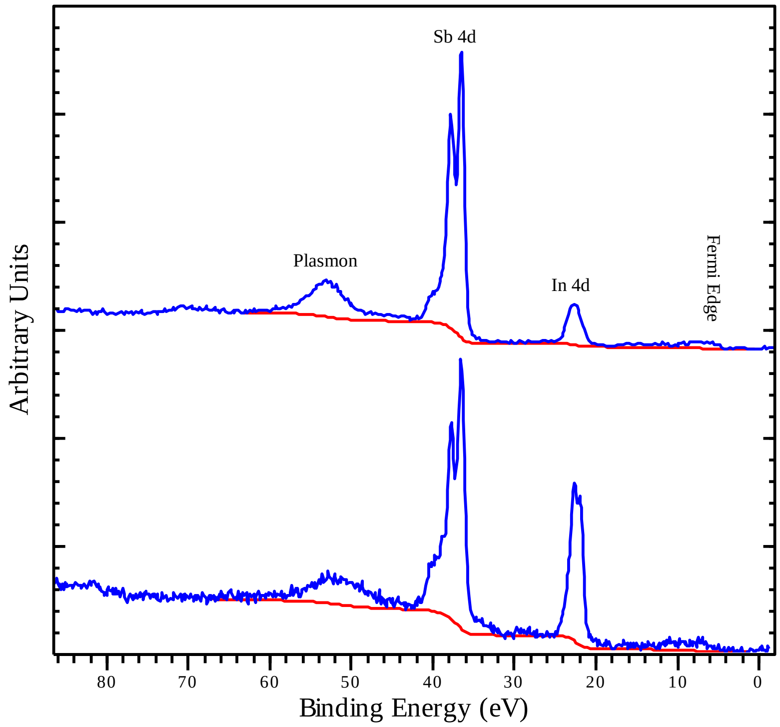

Fig. 5.14: Top: the valence band and Fermi level spectrum of Sb/InSb obtained at normal emission after the 350 ℃ heating. Bottom: the same spectrum obtained at an emission angle of 80°. The spectral features are similar to those obtained after heating at 300 ℃. The In $4d$ is more intense at the surface, while the SbOx shoulder at Sb $4d$ is less intense. The Fermi level at the surface spectrum is unclear. The red lines are the backgrounds of the spectra obtained by the Shirley method.

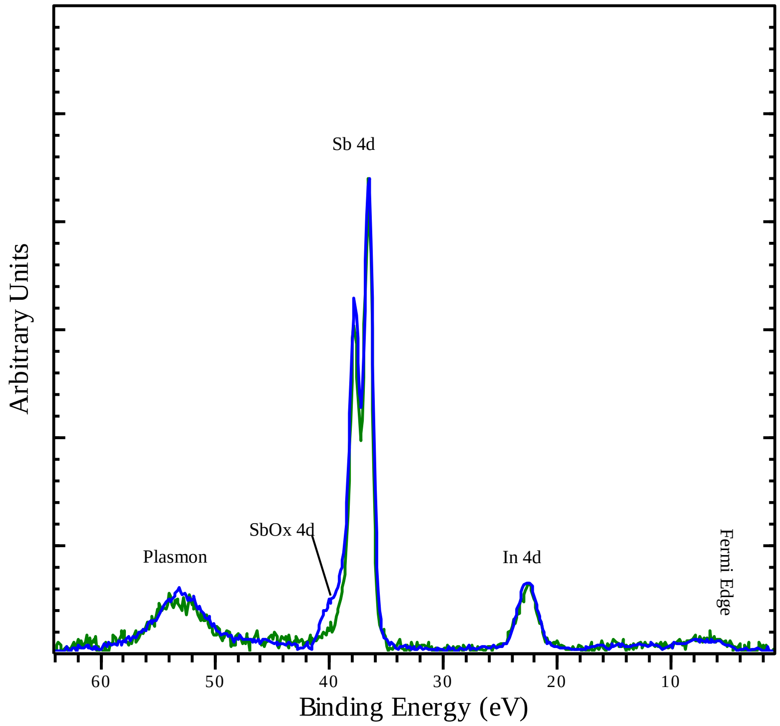

Fig. 5.15: The valence band and the Fermi edge spectra obtained after heating at 350 ℃ (blue) and 375 ℃ (green). The spectroscopic features are explained in (Fig.5.12). The noticeable change after heating at 375 ℃ is the disappearance of the SbOx shoulder in Sb 4d, which indicates the removal of oxygen from the bulk of the sample.

The obtained values of the Fermi level are most reliable at the normal-emission spectra obtained after heating at $300\ ^{\circ}\mathrm{C}$ and $350\ ^{\circ}\mathrm{C}$ since the Fermi edge is more intense and has a better signal to noise ratio.

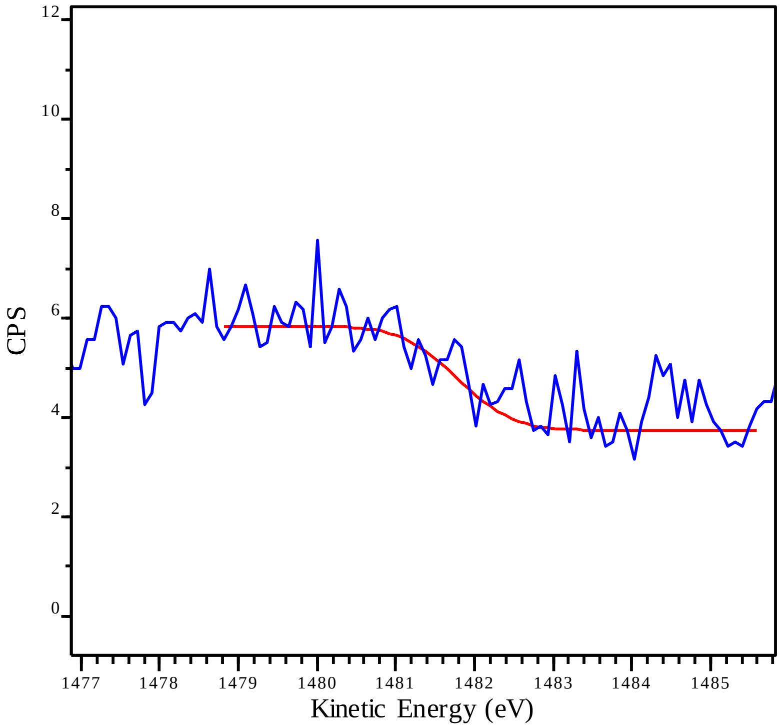

Fig.5.16. The Fermi edge scanned after heating at $375\ ^{\circ}\mathrm{C}$ (blue), and the error function fit to it (red) made using the method described in (Sc.2.3.4). The Fermi level was located at $KE = 1481.78 \pm 0.05\ eV$.

5.2.3. $3d$ Spectra:

The analysis of the broadscans of $\mathrm{Sb/InSb}$ (Sec.2.1) and the $4d$ spectra of Sb and In in the same sample (Sec.2.2) shows that the indium spectrum appeared after heating at $300\ ^{\circ}\mathrm{C}$, and that this spectrum is significantly more intense at the surface of the specimen. It also shows the removal of oxygen from the bulk of the specimen after heating at $375\ ^{\circ}\mathrm{C}$. However, it is not yet clear what the contributions of the Sb cap (overlayer) and the Sb in InSb (underlayer) are to the Sb spectrum. It is also not clear how the In in the InSb layer contributes to the observed In spectrum. Especially that it is clear that there is diffusion of In to the surface of the specimen by heating. Analysing the raw spectra of the In and Sb $3d$ gives a closer insight of the nature of the spectroscopic features.

5.2.3.1. Sb $3d$:

A scan performed before heating the specimen shows a strong Sb $3d$ doublet and each of the doublet components is accompanied by a very weak peak at a lower binding energy (Fig.5.17). O $1s$ is known to overlap with Sb $3d_{5/2}$ [9]. This becomes clear in (Fig.5.xx, xx) where the spectrum is fitted.

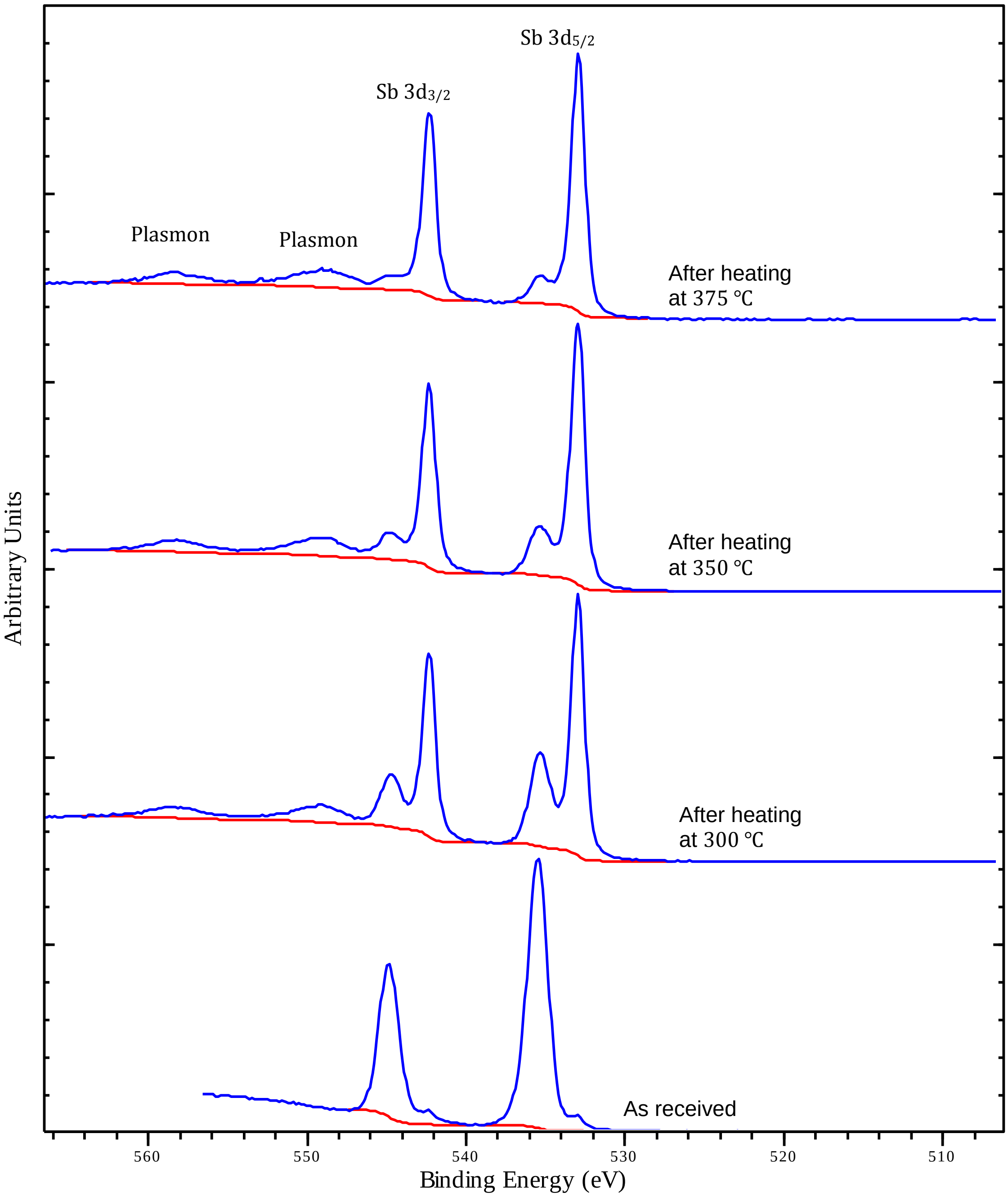

Fig. 5.17: Sb $3d$ spectrum observed from Sb/InSb sample as received (before any treatment) and after the heating at 300 °C, 350 °C, 375 °C. There are to peaks for each of the doublet components ($3d_{5/2}$ and $3d_{3/2}$), which indicates the presence of two species of Sb. The separation between these two species is $\sim 2.6\ eV$ before heating and $\sim 2.4\ eV$, $\sim 2.5\ eV$, $\sim 2.3\ eV$ after heating at 300 °C, 350 °C, 375 °C respectively. Plasmon peaks which are associated with the Sb bulk [2] appeared at $16\ eV$ higher binding energies from the lower binding energy Sb species.

After the sequence of heating processes at $300\ ℃, 350\ ℃, 375\ ℃$ the intensities of the two Sb species changed dramatically so the species at the lower binding energy became more intense than that at the higher binding energy (Fig. 5.17).

The peaks from the two species are close together for their positions to be shifted slightly as their relative intensities vary, with the position of the weak peak being pulled towards the position of the stronger peak. However, the separation between the $3d_{3/2}$ components of the two species is $\sim 2.6\ eV$ before heating, and $\sim 2.4\ eV$, $\sim 2.5\ eV$, $\sim 2.3\ eV$ after heating at $300\ ℃$, $350\ ℃$, $375\ ℃$ respectively.

The binding energies of $\mathrm{Sb}\ 3\mathrm{d}$ lines in $\mathrm{Sb_2O_3}$ have been reported to be shifted by $2.29 \pm 0.2\ eV$ [8] to higher binding energy relative to $\mathrm{Sb}\ 3\mathrm{d}$ lines in metallic Sb. Such a shift has been also reported to be $2.5\ eV$ [9]. This shows that the two Sb species observed in this experiment (Fig.5.17) are from the metallic Sb of the cap (on top of the InSb layer) and from an $\mathrm{Sb_2O_3}$ layer on the surface of the cap.

The broadscans analysed in (Sec.5.2.1) show the presence of indium spectrum after heating at $300\ ℃$. If this spectrum had originated from the InSb layer, then the corresponding $\mathrm{Sb}\ 3d$ lines (from InSb) should be present. These lines are shifted towards lower BE by $0.7\ eV$ relative to the metallic Sb cap [3]. $3d_{3/2}$ lines (Fig. 5.17) are separated by $\sim 2.60\ eV$ in the specimen as received, and by $\sim 2.40\ eV$ after the heating, which does not suggest the presince of Sb component from the InSb layer.

Comparing the bulk and the surface-sensitive scans (at $0°$ and $80°$ emission angle, respectively, relative to the perpendicular to the surface) performed at the same stage (after heating at $300\ ℃$) shows that the SbOx peaks are more intense on the surface which means that they originate from a thin oxide layer on top of the elemental Sb cap (Fig.5.18). The shift between the two species on the surface did not change from that observed at normal emission in the sample as received.

The surface-sensitive spectrum at the $350\ ℃$ stage (Fig.5.19) is consistent with that at $300\ ℃$ in which the SbOx species is more intense than in the normal incidence spectrum.

If there were $\mathrm{Sb}\ 3d$ components originating from the InSb layer and obscured by overlapping with the $\mathrm{Sb}\ 3d$ components from the elemental Sb, they would appear (as a result of the shift of $0.7\ eV$ mentioned above) as brodenings in the latter. The $\mathrm{Sb}(\mathrm{InSb})$ components would be more intense at the scans of normal emission than at the surface-sensitive scans since they originate from a sublayer. However, overlaying the normal and the surface-sensitive scans,

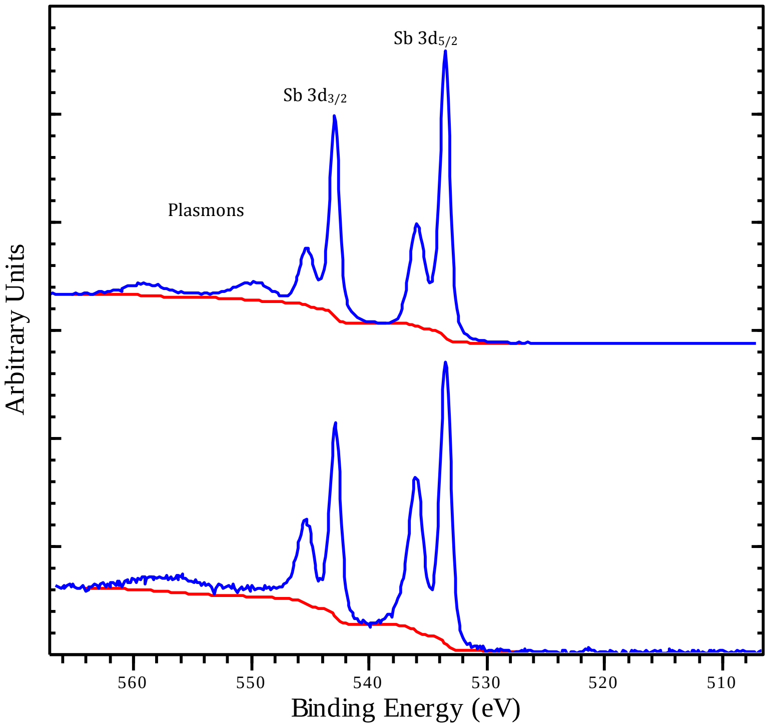

Fig. 5.18: Sb $3d$ region scanned at normal emission (top) and a surface-sensitive emission angle (bottom) after heating at 300 °C. Two Sb $3d$ species are present: one (at lower binding energy) originating from the elemental Sb cap, and the other is from SbOx. The latter is more intense at the surface than at the bulk, which indicates that the SbOx is a thin layer on top of the Sb cap.

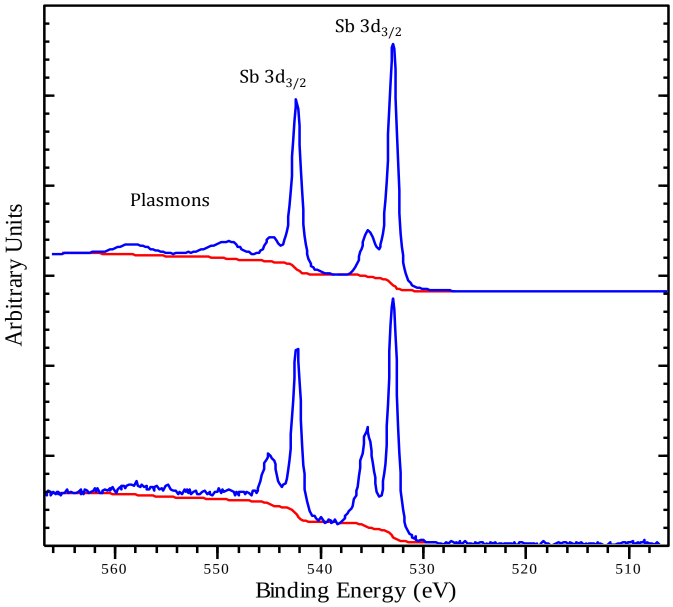

Fig.5.19: Top: Sb 3d spectrum obtained at normal emission after heating the Sb/InSb sample at 350 °C. Bottom: the same spectrum obtained at emission angle of 80° (surface sensitive). The two spectra show the same features as those obtained after heating at 300 °C; the SbOx components, at the higher binding energies, are more intense in the surface than in the bulk.

made after heating at 350 ℃ (Fig.5.20), does not show such broadenings in the normal emission spectrum.

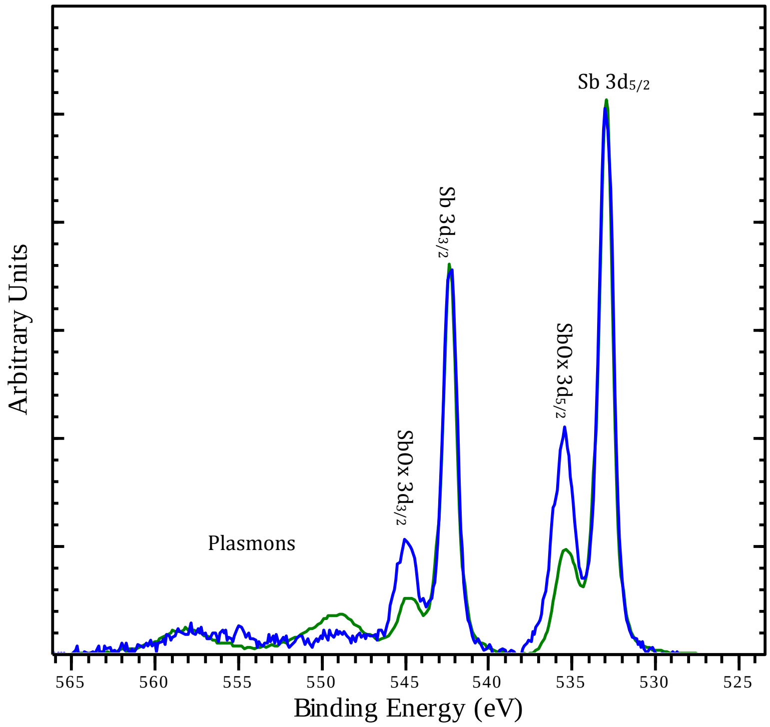

Fig.5.20. The Sb $3d$ region scanned after heating the Sb/InSb specimen at 350 ℃. The green spectrum was taken at normal emission, while the blue spectrum was taken at 80° from the normal. The $3d$ doublets associated with the elemental metallic Sb (in the Sb cap) were overlaid to detect any broadening due to components from the Sb in the InSb layer. Such components were reported to be at 0.7 *eV* to the lower BE side from the elemental components [3], and should be (has they had appeared) more intense in the normal emission since the surface of the specimen was still dominated by the elemental Sb and the SbOx as concluded above. The normal and the surface-sensitive elemental Sb components are identical which does not indicate the existence of components from the InSb underlayer which would have made the normal-emission components broader. The relative intensities of the SbOx were commented on in (Fig.5.19). The Shirley backgrounds, shown in (Fig.5.19), were subtracted. There are characteristic Sb bulk plasmons (at 16 *eV* higher BE) from the elemental Sb peaks obtained at normal emission, whereas no clear plasmon structure at the surface-sensitive spectrum.

During the course of the experiment, it was concluded that the In spectrum that appeared after heating at 300 ℃ (and became more intense after heating at 350 ℃) had originated from the InSb layer and that the Sb cap (overlayer) was removed. Moreover, the spectra did not significantly change after heating at 375 ℃. Consequently, the experiment was ended, and no surface-sensitive scans were made after heating at 375 ℃.

Desorption of a 250 Å thick Sb cap on InSb(001) has been reported to occur by heating at 330 ℃ for 5 min, while the desorption of a 2000 Å thick one was by heating at 450 ℃ for 10 min [3]. Complete removal of Sb cap on InAlSb/InSb by heating at 490 ℃ has been reported [10]. Both specimens had In rich surfaces after decapping.

5.2.3.2. In $3d$:

There was no sign of In in the broadscans made on the Sb/InSb specimen as received and after heating at 150 ℃, 250 ℃ (Fig. 5.1). In $3d$ peaks first appeared after heating at 300 ℃ (Fig.5.2), and changed in intensity with heating and varyation of the emission angle.

Overlaying the In $3d$ spectra obtained after heating at 300 ℃ and 350 ℃ (Fig.5.21) reveals no significant difference between them. A change in the width or the shape would indicate the emergence (or change of the intensity) of a species other than the In diffused to the surface (Fig.5.3).

The In $3d$ spectrum obtained after heating at 375 ℃ has a poor signal.

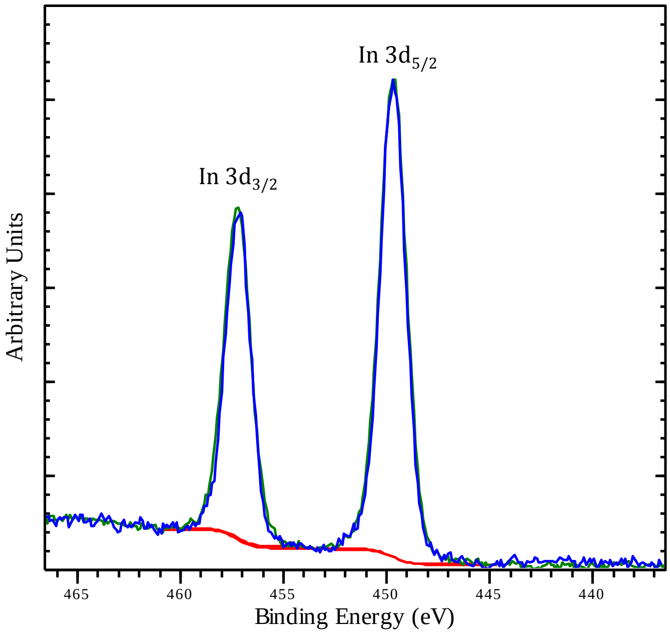

Fig.5.21. In 3d spectra obtained at normal emission after heating at 300 ℃ (blue) and at 350 ℃ (green). The two spectra were normalised (with respect to the intensities of the $3d_{3/2}$ peaks) and overlaid to detect any difference of shapes or widths which would indicate the existence of more than one species. None of this can be seen. The red lines are Shirley backgrounds.

5.2.4. Auger $M_{4,5}N_{4,5}N_{4,5}$:

(Fig. 5.22) shows the background subtracted $M_{4,5}N_{4,5}N_{4,5}$ Auger spectrum of the solid elemental Sb obtained by [1]. The multiplet structures of both Auger groups ($M_4N_{4,5}N_{4,5}$ and $M_5N_{4,5}N_{4,5}$) were modelled by six components with the $^1G_4$ line (overlapping with the $^1D_2$ line) forming the most intense feature in each group. Similar Auger profiles were obtained for solid elemental Ag through Te [11], and for elements Ag through Sn [12].

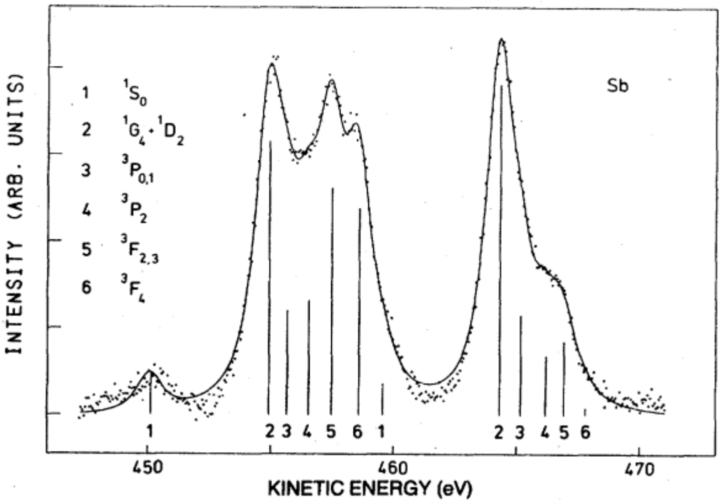

Fig.5.22: The Auger $M_{4,5}N_{4,5}N_{4,5}$ spectrum of metallic Sb (dots). Solid line is the synthetic model. Vertical lines indicate the positions of the multiplet structure components used to model (fit) the spectrum) [1].

Depending on the observations of the $\mathrm{Sb}\ 3d$ region (Sec.5.2.3) it is expected to observe Auger lines originating from the elemental Sb overlayer and from the SbOx

(Fig.5.23) shows the Auger spectra obtained before heating and afterheating at $300\ ℃$, $350\ ℃$, and $375\ ℃$. It supports the assumption made in (Section. 5.2.3) in identifieng the species present in the $\mathrm{Sb/InSb}$ specimen. The Sb Auger species present bfore heating (Fig.5.23) is associated with SbOx. After heating at $300\ ℃$ this species became unclear and another one, which appeared at higher kinetic energy, is assumed to originate from the elemental Sb(cap). plasmon peaks, also, appeared after heating. The Sb bulk and surface plasmons have been reported at $16\ eV$ and $11\ eV$ respectively [2].

Heating the specimen at $350\ ℃$ then at $375\ ℃$ did not significantly change the Sb Auger spectrum, apart from the $M_5N_{4,5}N_{4,5}$ group of the elemental Sb being sharper because of the reduction of the overlapping SbOx $M_4N_{4,5}N_{4,5}$ group (annotated at (Fig.5.23)).

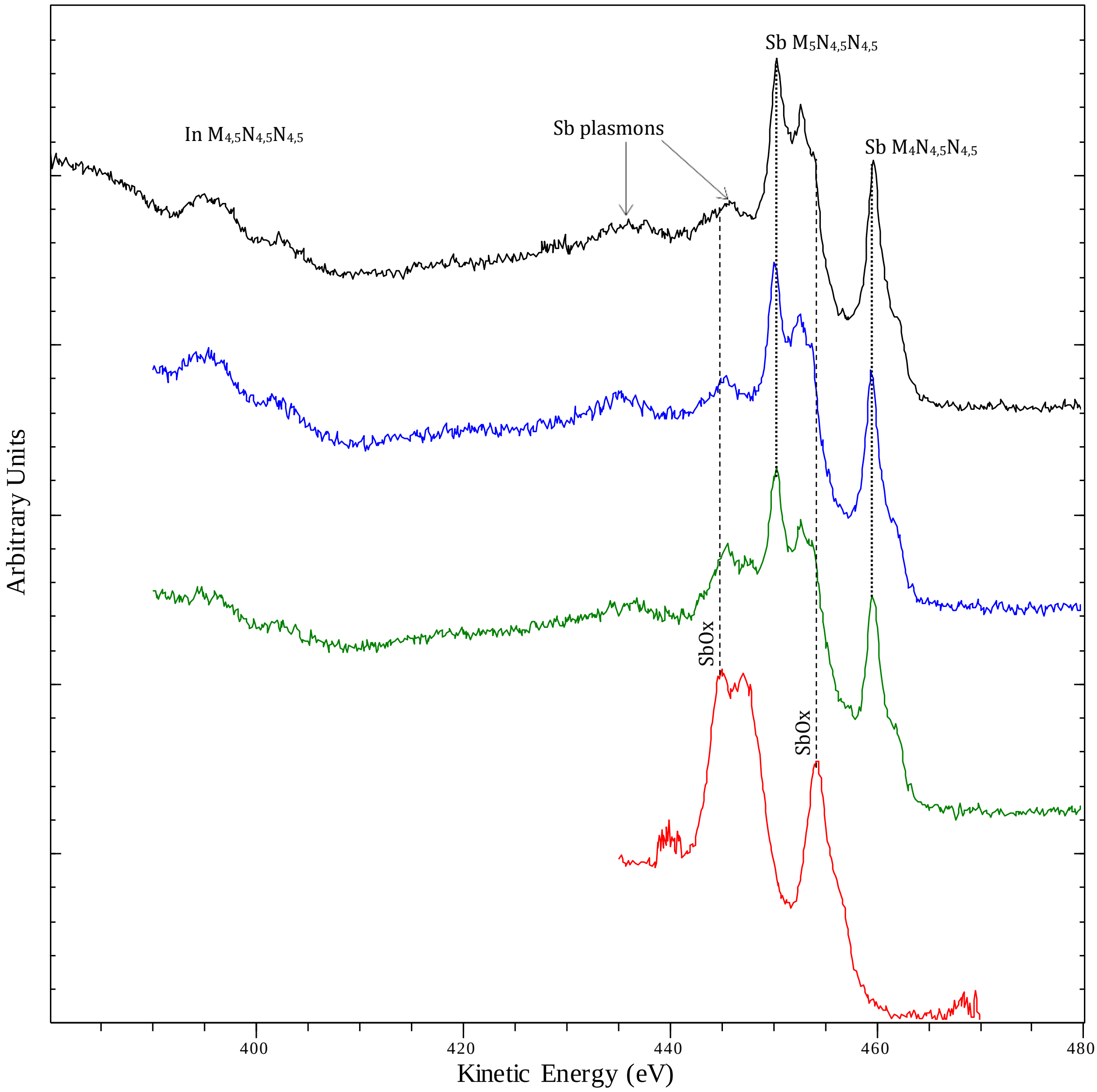

Fig.5.23: The Auger $M_{4,5}N_{4,5}N_{4,5}$ region of In and Sb (in Sb/InSb) scanned before heating (red) and after heating at 300 ℃ (green), 350 ℃ (blue), and at 375 ℃ (black). The In spectrum (around $KE = 400\ eV$) is faint. The Sb spectrum (at $KE \sim 430\ eV$ to $465\ eV$) has, before heating, a profile similar to that obtained by [1], and consists of one species due to SbOx as concluded from the analysis of the $3d$ region (Sec.5.2.3). The highest peaks in the $M_5N_{4,5}N_{4,5}$ and $M_4N_{4,5}N_{4,5}$ groups of SbOx are annotated with dashed lines. SbOx spectrum became unclear after heating (the green, blue and black spectra) and a new species, appeared at higher KE, is due to the elemental Sb overlayer (the cap). The highest peaks of this species are annotated with dotted lines. Plasmon peaks, which appeared after heating, overlap with the SbOx peaks. There is a spike at the position of the $^1S_0$ line in the spectrum obtained before heating. The spectra observed after heating are complicated, because they contain two species as well as the plasmons of the elemental Sb. The position of the highest peak of the $M_4N_{4,5}N_{4,5}$ group of the elemental Sb is easy to determine since it does not overlap with the plasmons or the SbOx spectrum. The spectra in this figure are not energy corrected.

The positions of the $^1G_4$ lines are annotated in (Fig.5.23). They were identified by considering the facts that this line is associated with the most intense peak in the Sb

$M_{4,5}N_{4,5}N_{4,5}$ profile [1, 11, 12] , and that the separation between the two Auger groups was reported to be $9.39 \pm 0.15\ eV$ [1].

The position of the $^1G_4$ line of the $M_4N_{4,5}N_{4,5}$ group is used in calculating the Auger parameter of Sb for chemical analysis (Eq.5.1). In the spectrum originating from SbOx before heating, the peak associated with $^1G_4(M_4N_{4,5}N_{4,5})$ is at KE of $461.11 \pm 0.07\ eV$, while $^1G_4(M_5N_{4,5}N_{4,5})$ is at KE of $451.68 \pm 0.07\ eV$. Hence, the separation between the two groups is $9.43 \pm 0.07\ eV$. The SbOx peaks became weak after heating; and the $^1G_4$ lines originating from the elemental Sb are at $464.45 \pm 0.07\ eV$ and $455.12 \pm 0.07\ eV$ as read from the spectrum obtained after the heating at $375\ ℃$ (Fig.5.23) and corrected by the value of the Fermi level determined at the same stage of experiment. The position of $^1G_4(M_4N_{4,5}N_{4,5})$ of elemental Sb is more accurate than that of $^1G_4(M_5N_{4,5}N_{4,5})$, since the latter overlaps with the SbOx spectrum and with the plasmons. The spectrum obtained after heating at $375\ ℃$ was chosen to study the Auger parameter of the Sb cap because it contains the least intense SbOx contribution.

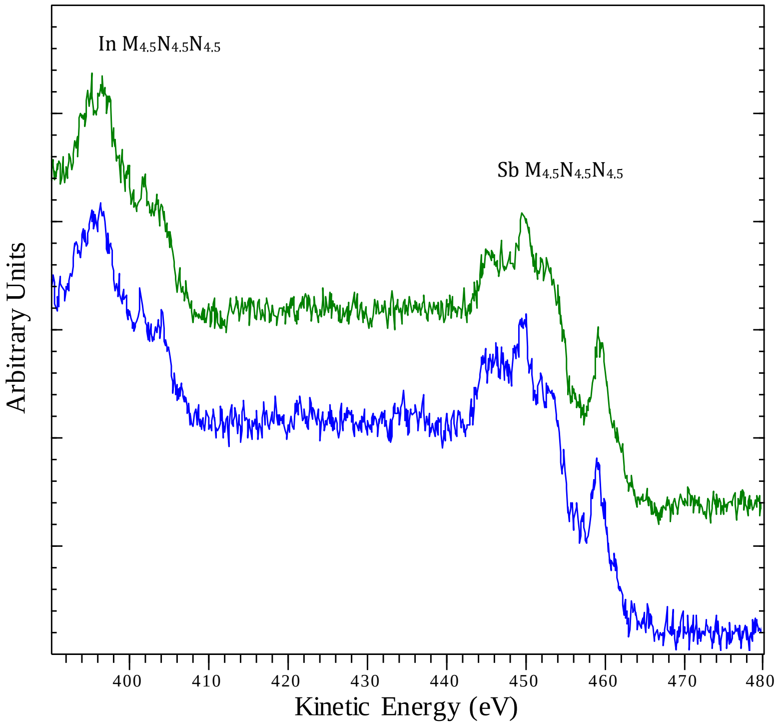

Fig.5.24: The Auger $M_{4,5}N_{4,5}N_{4,5}$ spectra of In and Sb (in Sb/InSb) scanned at takeoff angle of 80° after heating at 300 ℃ (blue), and after heating at 350 ℃ (green). The spectra of both elements show similar profiles after heating at 300 ℃ and at 350 ℃ . However, the signals are too weak for line positions to be determined, especially knowing that two species exist for both elements (Fig.5.X, X).

The Auger process is more sensitive to the chemical state than the photoemission because of the greater extra-atomic relaxation (Sec.1.2.2.1); hence the shift between the Sb and the SbOx Auger lines is $3.34 \pm 0.07\ eV$, while the shift between the $3d$ lines is $2.46 \pm 0.07\ eV$ (Sec.5.3.1).

The $\mathrm{In}\ M_{4,5}N_{4,5}N_{4,5}$ Auger spectra obtained at normal emission are very weak (Fig.5.23). Surface-sensitive $\mathrm{In}\ M_{4,5}N_{4,5}N_{4,5}$ spectra (obtained at emission angle of $80°$) (Fig.5.24) are stronger than those obtained at normal emission. However, they are not strong enough for reliable line positions to be located, especially knowing that two species are present as concluded in (Sec.5.2.3). Looking at the $M_{4,5}N_{4,5}N_{4,5}$ Auger spectrum of metallic In (Fig.2.25) and to elemental In spectrum obtained by this work (Fig.4.8), no similarity can be seen with the In spectra in (Fig.5.24).

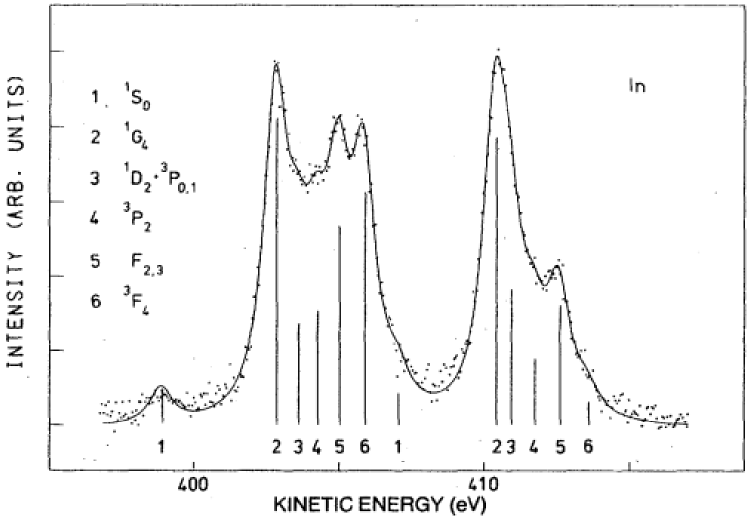

Fig.5.25: Metallic In $M_{4,5}N_{4,5}N_{4,5}$ Auger spectrum (dots). Solid line is the synthetic model. Vertical lines indicate the positions of the components of the model [1].

5.3. $3d$ models:

Models were made to fit the Sb and $\mathrm{In}\ 3d$ spectra, in order to identify and precisely locate the constituent peaks.

5.3.1. $\mathbf{Sb}\ 3d$ models:

It was concluded from the analysis in (Sec.5.2.3) that the two $\mathrm{Sb}\ 3d$ species present throughout the experiment are due to the elemental Sb, of the Sb overlayer (the cap), and SbOx on the surface of the specimen. The oxide was greatly (but not completely) removed by the sequence of heating processes (Fig.5.17). By fitting the $\mathrm{Sb}\ 3d$ spectrum obtained of the specimen as received (before heating) the positions of the $3d_{5/2}$ and $3d_{3/2}$ components (in the binding energy scale) were determined (Table.5.1). The BE of O $1s$ was found to be $528.71 \pm .07\ eV$.

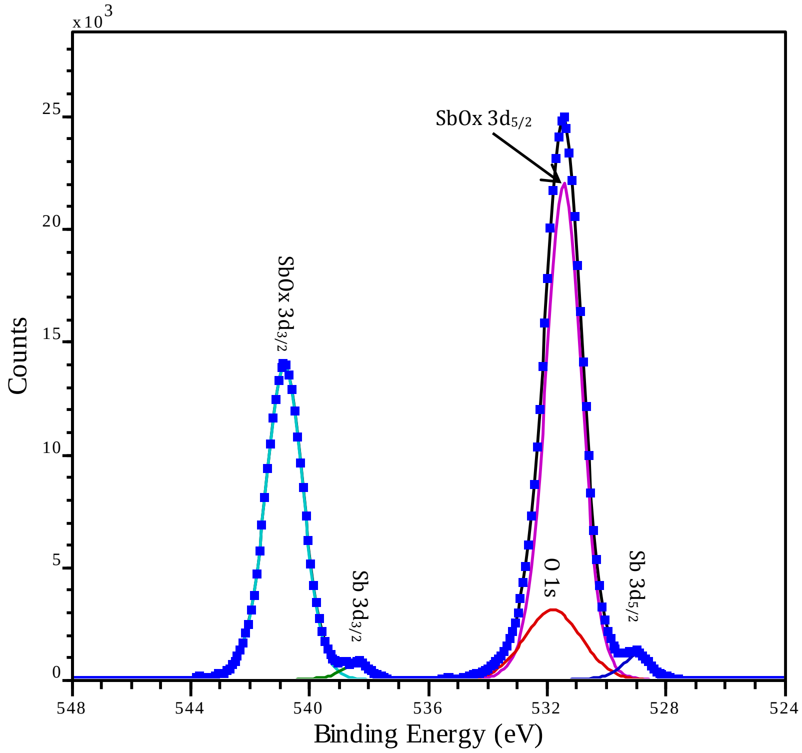

Fig. 5.26: The Sb $3d$ spectrum of Sb/InSb specimen as received (squares). The Shirley background, shown in (Fig.5.17), was subtracted. The fitting procedure described in (Sec.4.2.2 and 4.3.2) was followed. The coloured peaks are the synthetic peaks created to fit the spectrum. These synthetic peaks resulted in a synthetic spectrum (black line) which matches the real spectrum. SbOx components are intense while those of the elemental Sb are weak, which indicates that most of the Sb overlayer (the cap) was oxidised. O $1s$ peak is clear despite the small cross section of this line (see text).

Species	$3d_{3/2}$	$3d_{5/2}$	**S-O Splitting**
SbOx	537.71	528.30	9.41
Sb	535.26	525.82	9.44
Chemical Shift	2.45	2.48	---

Table 5.1: BEs, spin-orbit splittings and the chemical shifts of Sb $3d$ doublet components observed in the Sb/InSb specimen as received. The error in the listed values is $\pm 0.07\ eV$.

The chemical shift of $3d_{5/2}$ between the elemental Sb and the SbOx is $2.48 \pm .07\ eV$. A shift of $2.5\ eV$ has been reported between metallic Sb and Sb_2O_3 [9].

(Fig.5.27) shows the Sb $3d$ spectrum, obtained after the heating at 375 ℃, and the model constructed to fit it. The BEs of the $3d$ components are listed in (Table.5.2). O $1s$ peak could not be detected, because of its small cross section in addition to its very low intensity which is clear from the intensities of the Sb(SbOx) peaks. The O $1s$ cross section is 2.93 [13]. This is 0.18 relative to the cross section of Sb $3d_{5/2}$ which is 16.39 [13].

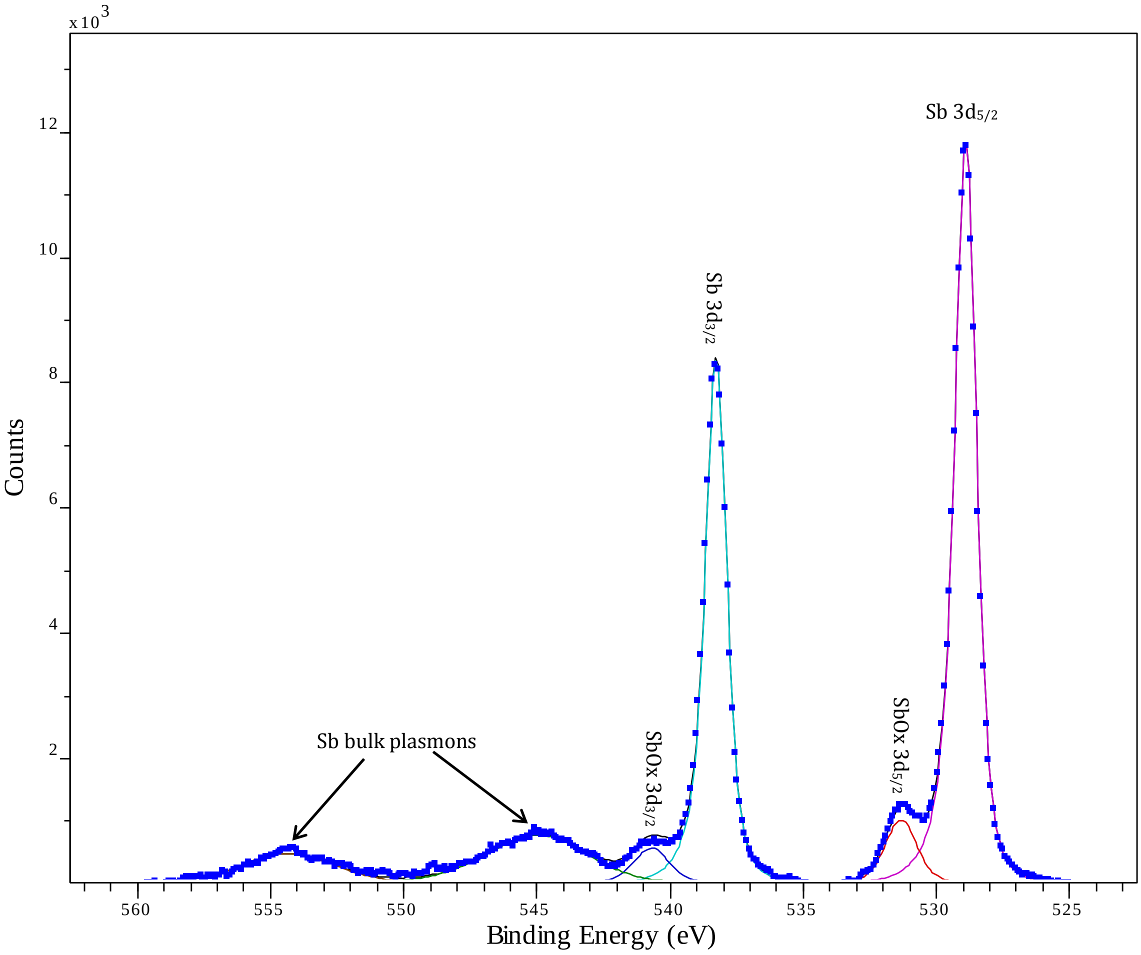

Fig. 5.27: The Sb $3d$ spectrum of Sb/InSb specimen after the heating at 375 ℃ (squares). The Shirley background, shown in (Fig.5.17), was subtracted. The fitting procedure described in (Sec.4.2.2 and 4.3.2) was followed. The coloured peaks are the synthetic peaks created to fit the spectrum. The synthetic peaks resulted in a synthetic spectrum (black line) which matches the real spectrum closely. The peaks of the elemental Sb are dominant, while the SbOx components are weak. O $1s$ peak could not be detected, due to its low cross section in addition to its low intensity (see text). Plasmon loss peaks characteristic to elemental Sb are present at $16.00 \pm 0.07\ eV$ from the associated peaks (elemental Sb $3d_{5/2}$ and $3d_{3/2}$).

Characteristic plasmon peaks appear at $16.00 \pm 0.07\ eV$ higher binding energies from the $3d$ components of the elemental Sb. These plasmons are characteristic to the Sb bulk [2].

Species	$3d_{3/2}$	$3d_{5/2}$	**S-O Splitting**
SbOx	539.90	530.54	9.36
Sb	537.46	528.08	9.38
Chemical Shift	2.44	2.46	---

Table. 5.2: BEs, spin-orbit splittings and chemical shifts of the Sb $3d$ spectrum observed in the Sb/InSb specimen after the heating at 375 °C. The error in the listed values is $\pm 0.07\ eV$.

Comparing the BEs of the Sb lines before and after the heating can be misleading because the Fermi level observed before the heating was weak due to the oxidisation of most of the Sb cap (Fig.5.7). The chemical shifts within the same spectrum, however, are independent to referencing. The shift between the two Sb $3d$ species did not change by the heating processes considering the errors (Table.5.1, 2).

5.3.2. In $3d$ models:

In spectrum first appeared after heating the Sb/InSb specimen at 300 °C (Sec. 5.2.1), and became slightly more intense by heating at 350 °C (Fig.5.5). In $3d$ spectrum obtained after the heating at 350 °C is similar in the shape and width to that obtained after the heating at 300 °C (Fig.5.21). The latter was fitted to detect its spectroscopic features. Two asymmetric peaks at BEs of $451.89 \pm 0.07\ eV$ and $444.38 \pm 0.07\ eV$ fit the spectrum well (Fig.5.28).

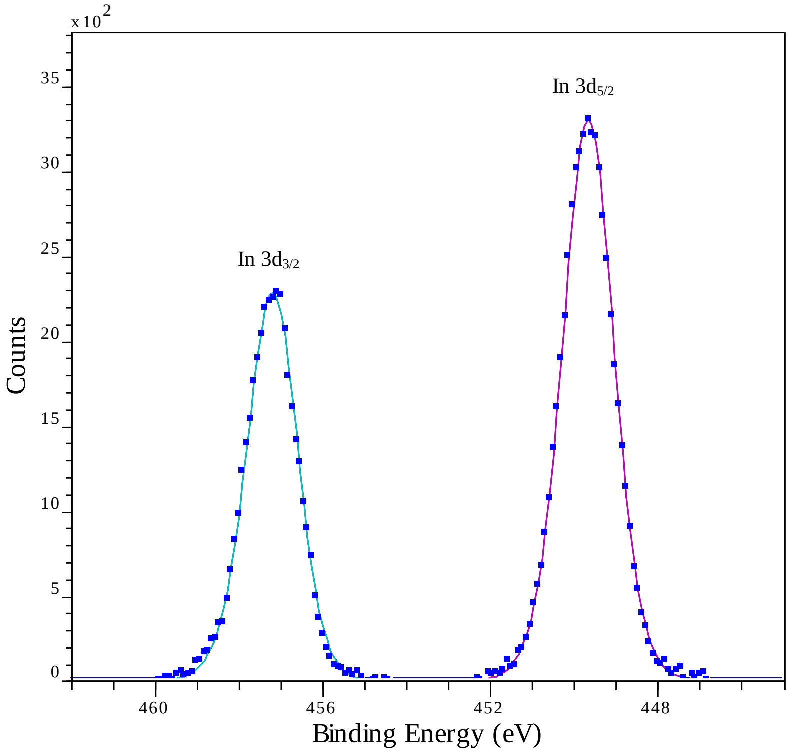

Fig. 5.28: In $3d$ spectrum obtained after heating Sb/InSb at 300 °C (blue squares). The background shown in (Fig.5.21) was subtracted. The spectrum was fitted with one species. The energy scale is not corrected for the work function.

These peaks account for one species of the $\mathrm{In}\ 3d_{3/2,5/2}$ doublet components respectively. The splitting between the two peaks is $7.51 \pm 0.07\ eV$. $3d$ doublet splitting for solid elemental In has been reported at $7.6\ eV$ [1, 14, 15] and at $7.5\ eV$ [16].

The spectra in (Fig. 5.3 and 5) show that In is considerably more intense at the surface of the specimen. The surface-sensitive $\mathrm{In}\ 3d$ spectrum (obtained at emission angle of $80°$) obtained after the heating at $300\ ℃$ (Fig.5.29) could not be fitted with one peak for each of the doublet components i.e. one species. Since In is a metal, it is not unexpected that part of it is oxidised. Two $3d_{3/2}$ peaks separated by $0.86 \pm 0.07\ eV$, and two $3d_{5/2}$ peaks separated by $0.84 \pm 0.07\ eV$ made a good fit to the spectrum. These separations are similar to the reported values of the shift of $\mathrm{In_2O_3}\ 3d$ lines from those of elemental In [8]. The BEs of the $3d_{3/2}$ and $3d_{5/2}$ components originating from the elemental In are 451.53 ± 0.07 and $443.99 \pm 0.07\ eV$ respectively, while those of the InOx components are 452.39 ± 0.07 and $444.83 \pm 0.07\ eV$.

5.4. Overall results:

(Table. 5.3) lists the binding energies of the In and $\mathrm{Sb}\ 3d_{5/2}$ lines, and the kinetic energies of the $^1G_4$ components in the $M_4N_{4,5}N_{4,5}$ Auger groups as well as the Auger parameters (α) at the different chemical states studied in this chapter and in (Ch.4). The Auger parameter (AP) was calculated using the following formula which defines the modified Auger parameter [4]:

$$\alpha = KE_{M_4N_{4,5}N_{4,5}} + BE_{3d_{5/2}} \quad (5.1)$$

where $KE_{M_4N_{4,5}N_{4,5}}$ was taken as the kinetic energy of the highest peak in the $M_4N_{4,5}N_{4,5}$ Auger group consisting of the $^1G_4$ in indium and ($^1G_4 + {}^1D_2$) in antimony [1].

Material	$3d_{5/2}$	$^1G_4\ (M_4N_{4,5}N_{4,5})$	α
In$_{\mathrm{metallic}}$	444.04	410.22	854.26
In (Sb/InSb Heated at 300 ℃)	444.38	---	---
In (Sb/InSb Heated at 300 ℃) Surface measurement	443.99	---	---
InOx (Sb/InSb Heated at 300 ℃) Surface measurement	444.83	---	---
Sb$_{\mathrm{metallic}}$	527.81	464.74	992.55
SbO$_x$ (Sb/InSb As Received)	528.30	461.11	989.41
Sb(Cap) (Sb/InSb Heated at 375 ℃)	528.08	464.45	992.53

Table. 5.3: The BEs of the In and $\mathrm{Sb}\ 3d_{5/2}$, KEs of the $^1G_4$ ($M_4N_{4,5}N_{4,5}$), and the Auger parameters (α) as defined in (Eq.5.1) in all the studied Sb/InSb spectra. The data of $\mathrm{In_{metallic}}$ and $\mathrm{Sb_{metallic}}$ are those obtained from pure elements in (Ch. 4). All BEs and KEs are referenced to the Fermi levels measured in the same conditions. All the results are in unit eV, and have ± 0.07 uncertainty in their values.

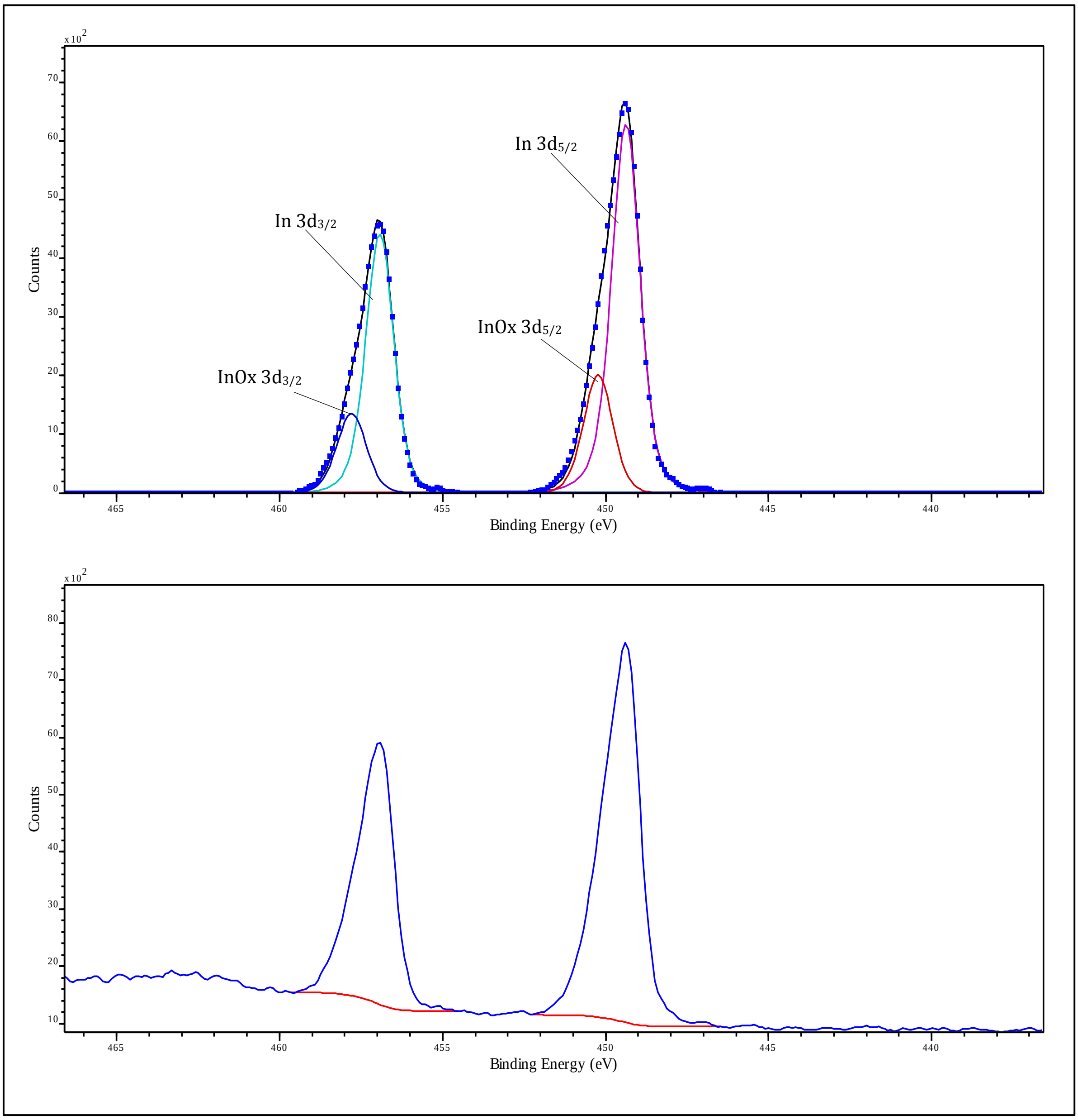

Fig.5.29: Bottom: In $3d$ spectrum obtained at 80° emission angle of Sb/InSb sample after the heating at 300 ℃. The red lines are Shirley backgrounds calculated separately. Top: the same spectrum (squares) after the subtraction of the backgrounds. This spectrum was fitted with two peaks for each of the $3d$ doublet components. The more intense components are due to elemental In, while the other two peaks are due to indium oxide (InOx). In(InOx) $3d_{3/2}$ component is shifted by $0.86 \pm 0.07\ eV$ to higher binding energy compared to the $3d_{3/2}$ of the elemental In. The shift of the In(InOx) $3d_{5/2}$ component is $0.84 \pm 0.07\ eV$. The black line is the overall result of the fit. Surface related plasmon peaks of In have been reported at $8.6\ eV$ [5]. Therefore, if such peaks exist, then that of $3d_{5/2}$ should partly overlap with $3d_{3/2}$. Relative areas (intensities) under the $3d_{5/2}$ and $3d_{3/2}$ regions (bottom) are 1.48. This is consistent with the electron population in the two levels, which does not suggest the existence of plasmon peaks.

Looking at the spectroscopic values (Table.5.3), it can be noticed that the AP of the elemental Sb observed after heating at 375 ℃ is equal to that of the metallic Sb discussed in (Ch.4). This is an expected result which shows that the Sb(cap) was still thick enough to attenuate the electrons emitted from the Sb interface with the InSb layer. Such an interface is a unique chemical environment whose spectrum is expected to be different from that of pure Sb and the Sb in InSb.

As for In, that diffused to the surface of the $\mathrm{Sb/InSb}$ specimen is expected to be in a metallic state. However, the weak Auger lines do not enable the calculation of the AP which is the trustable tool to compare the chemical sates. BE of $\mathrm{In}\ 3d_{5/2}$ at the surface measurement is equal to that of the metallic In considering the measurement error of $0.07\ eV$. BE of $\mathrm{In}\ 3d_{5/2}$ measured at normal emission is $0.34 \pm 0.10\ eV$ higher than that of metallic In. This shift can be due to the contact with Sb, or just a result of the different referencing.

5.5. Conclusion:

The recommendation for future studies is heating the specimen further at steps of $25\ ℃$ until the spectrum of Sb-InSb interface is observed, and then heating further at the same step for complete removal of the Sb overlayer. This would provide data to investigate the electronic structure at the metal-semiconductor interface, as well as the electronic structure of the semiconductor (InSb).

To achieve the aim of this work, which is the study of the electronic structure of InSb, (Ch.6) presents the electron spectroscopy, of this material, obtained through different method.

References

1. Pessa, M., et al., *Solid-state effects inM4,5N4,5N4,5Auger spectra of elements fromIn49toTe52.* Physical Review B, 1979. **20**(8): p. 3115-3123.
2. Paliwal, V.K., A. Vedeshwar, and S. Shivaprasad, *Sb induced (7× 7) to (1× 1) surface phase transformation of the Si (111) surface.* Solid state communications, 2003. **127**(1): p. 7-11.
3. Evans, S., et al., *Protective overlayer techniques for preparation of InSb (001) surfaces.* Surface science, 1990. **226**(1): p. 169-179.
4. Briggs, D. and J.T. Grant, *Surface analysis by Auger and x-ray photoelectron spectroscopy*. 2003, Chichester, West Sussex, U.K.: IM Publications. xi, 899 p.
5. Bouslama, M., et al., *AES and EELS analysis of the interaction between phosphorus and metallic indium.* Journal of electron spectroscopy and related phenomena, 1994. **68**: p. 377-382.
6. Liu, W. and M. Santos, *Characterization of oxide desorption from InSb (001) substrates.* Journal of Vacuum Science & Technology B, 1996. **14**(2): p. 647-651.
7. Bouslama, M., C. Jardin, and M. Ghamnia, *The InSb (100) surface change during the argon ion bombardment and the electron stimulated oxidation.* Vacuum, 1995. **46**(2): p. 143-146.
8. NIST, X., *Database,< h ttp.* srdata. nist. gov/xps/Default. aspx.
9. Linarez Pérez, O.E., M.D. Sánchez, and M. López Teijelo, *Characterization of growth of anodic antimony oxide films by ellipsometry and XPS.* Journal of Electroanalytical Chemistry, 2010. **645**(2): p. 143-148.
10. Clark, S., et al., *Antimony capping and decapping of InAlSb (100).* Surface science, 1995. **336**(1): p. 193-198.
11. Aksela, S., et al., *Free-atom—metal shifts in theM4,5N4,5N4,5Auger spectra of Ag, Cd, In, Sn, Sb, and Te.* Physical Review B, 1981. **23**(9): p. 4362-4368.
12. Parry-Jones, A., P. Weightman, and P. Andrews, *The M4, 5N4, 5N4, 5 Auger spectra of Ag, Cd, In and Sn.* Journal of Physics C: Solid State Physics, 1979. **12**(8): p. 1587.
13. Scofield, J.H., *Hartree-Slater subshell photoionization cross-sections at 1254 and 1487 eV.* Journal of Electron Spectroscopy and Related Phenomena, 1976. **8**(2): p. 129-137.
14. Sen, P., M. Hegde, and C. Rao, *Surface oxidation of cadmium, indium, tin and antimony by photoelectron and Auger spectroscopy.* Applications of Surface Science, 1982. **10**(1): p. 63-74.
15. Tang, X., et al., *Oxidation of the InSb surface at room temperature.* Semiconductor science and technology, 1986. **1**(6): p. 355.
16. Legare, P., L. Hilaire, and G. Maire, *The superficial oxidation of indium, Sb and InSb (111)-a LEED, AES, XPS and UPS study.* JOURNAL DE MICROSCOPIE ET DE SPECTROSCOPIE ELECTRONIQUES, 1980. **5**(6): p. 771-782.

Chapter 6

Electron Spectroscopic Analysis of InSb

6.1. Introduction:

A careful analysis of the results reported in Ch.5 showed that at a late stage in the PhD programme I had failed to completely remove the Sb cap and obtain data on the clean InSb surface. After discussion with my supervisors it was arranged for measurements to be taken on a new InSb specimen by Dr David Hesp of the Stevenson Institute for Renewable Energy, University of Liverpool under the direction of Dr Vin Dhanak and Dr Tim Veal. I acknowledge the contribution of my collaborators in providing the results described in this chapter. This specimen was grown at The University of Warwick.

The measurements of the x-ray excited Auger and photoelectron spectra were obtained with unmonochromated Mg and Al $K\alpha$ x-rays.

The analyser pass energy was set to $100\ eV$ at the broadscans and $50\ eV$ for the narrow region scans. The energy steps were set to $0.50\ eV$ and $0.025\ eV$ respectively.

Measurements were performed on the sample as received and after two consecutive sputtering with Ar^+ ion of $500\ eV$ and $\sim 7\ \mu A$ for $10\ min$. Followed by another measurement after annealing at $\sim 250\ ℃$.

Sputtering is more effective in removing surface contamination than the annealing treatment adopted earlier [2] , but it is known to cause damage to the surface including crystal defects and selective segregation of some components (particularly anions in III-V semiconductors) [3, 4]. However, the energy of the Ar^+ in this experiment was moderate and not expected to cause a significant damage [2, 5]. This damage can be reversed by annealing [5].

A general view of the spectroscopic features before and after the surface treatments will be made first, followed by precise determination of the line positions. These line positions will be used to calculate the Auger parameters of In and Sb in InSb. The shifts between these Auger parameters and the Auger parameters of metallic In and Sb (Ch.4) are calculated. These shifts will be analysed through the potential model to study the electronic structure of InSb in (Ch.9).

6.2. Overview of the spectra:

A broadscan performed on the sample as received (Fig.6.1) shows a clear presence of C and O contaminants. There were two Sb species visible in the $3d$ region which is clearer in (Fig. 6.3). The specimen became clean after repeating the Ar ion sputtering for $10\ min$ twice (Fig. 6.1). The $\mathrm{Mg}\ K\alpha$ anode was used in these surveys and in the narrow region scans that followed them.

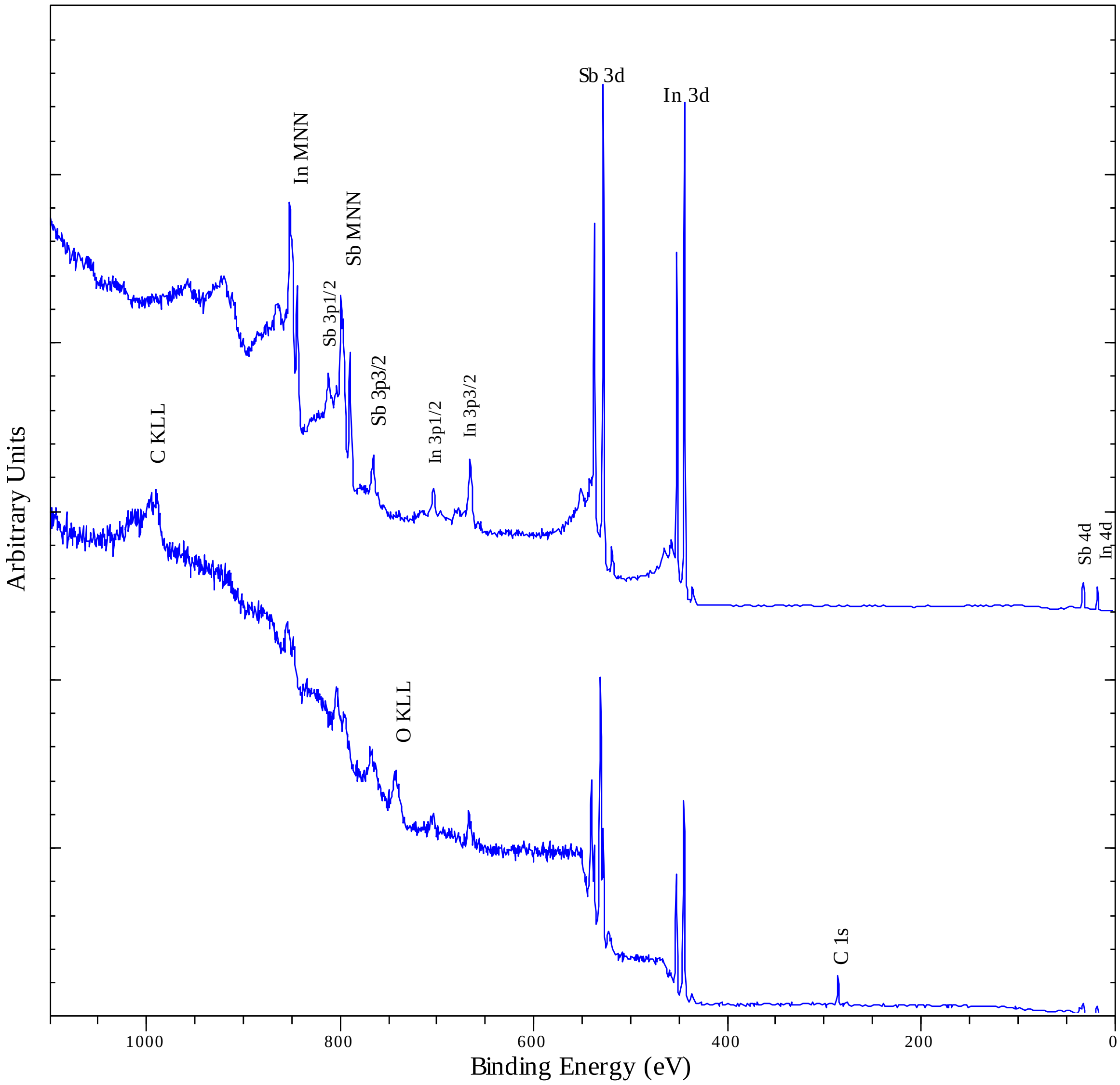

Fig. 6.1. Broadscans performed on the InSb sample as received (bottom), and after two Ar^{+} ion sputtering processes, each at $500\ eV$ for $10\ min$. The x-ray source used was unmonochromated $\mathrm{Mg}\ K\alpha$. $\mathrm{C}\ 1s$ as well as C and $\mathrm{O\ KLL}$ were present before the sputtering, and completely removed after it. There are two Sb species visible in the $3d$ region. Peaks due to the x-ray satellites can be seen at lower binding energies from $3d$ lines.

Annealing at ~ 250 ℃ was, then, carried out. Followed by instrument degassing to $1 \times 10^{-6}\ Pa$. After that, the sample was measured using the $\mathrm{Al}\ K\alpha$ anode. (Fig. 6.2) shows the broadscan spectrum made after the annealing and the broadscan made of $\mathrm{Sb/InSb}$ after heating at 375 ℃ as explained in (Ch. 5). The energy scales of both spectra were calibrated by correcting the binding energy of the $1s$ photoelectric line of adventitious carbon (to the recommended value of $284.8\ eV$ [6]) which was present in the $\mathrm{Sb/InSb}$ after heating at 375 ℃ and in the InSb sample as received. The energy scale corrections were $4.51\ eV$ and $0.67\ eV$ of $\mathrm{Sb/InSb}$ and InSb respectively.

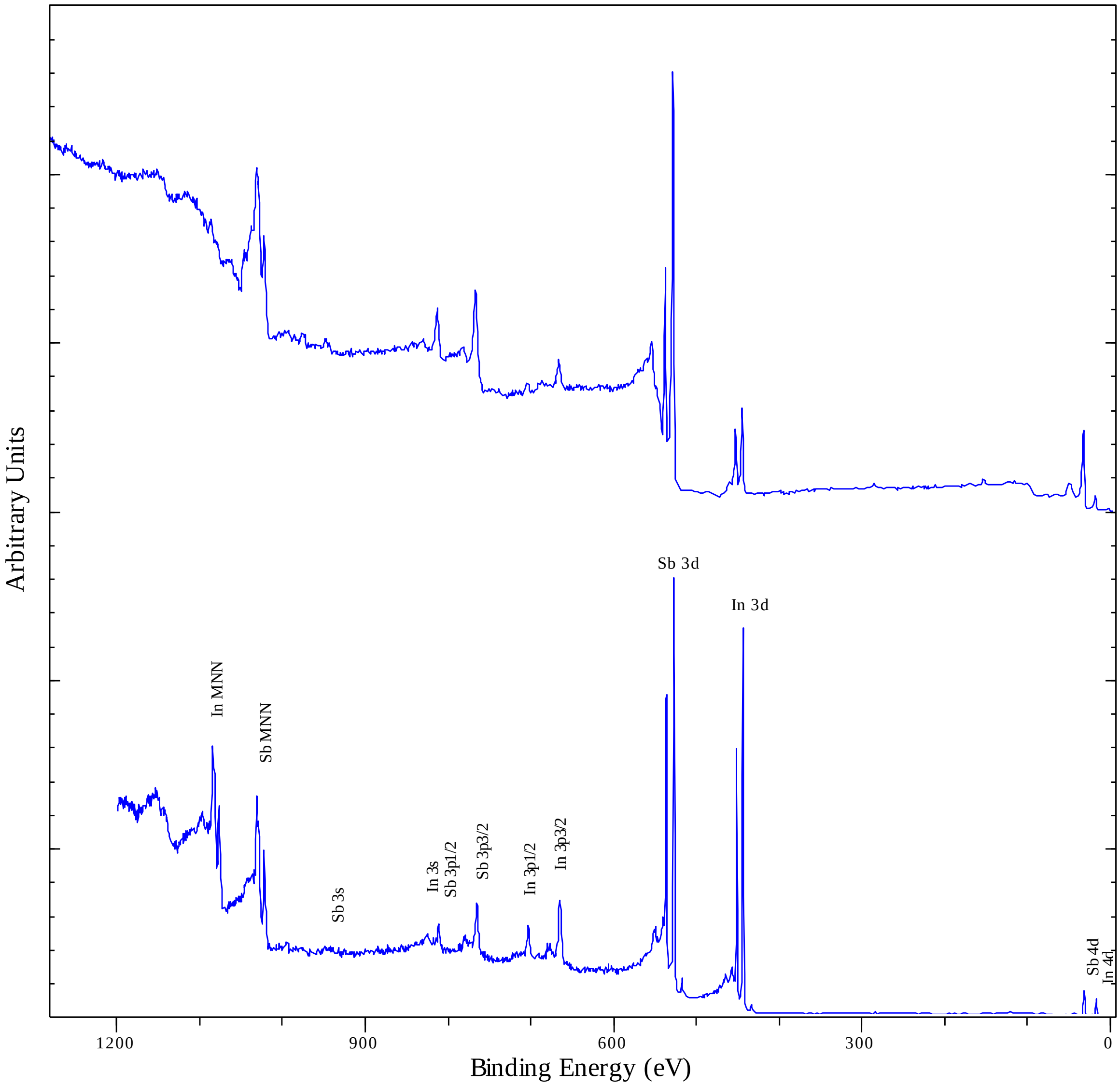

Fig.6.2. The broadscans of $\mathrm{Sb/InSb}$ made after heating at 375 ℃ (top) with use of monochromated $\mathrm{Al}\ K\alpha$ (Ch. 5), and InSb after two Ar^{+} sputtering at $500\ eV$ for $10\ min$, then annealing at 250 ℃, excited with unmonochromated $\mathrm{Al}\ K\alpha$ (bottom). Energy scales of both spectra are corrected using the $1s$ BE of adventitious carbon detected in the same measurement of $\mathrm{Sb/InSb}$ and the measurement of InSb as received (Fig. 6.1).

At first sight, Sb and In lines in the annealed InSb appear to have similar intensities, in contrast to the results obtained in the studies of Sb/InSb reported earlier following gradual annealing up to 375 °C. In the earlier experiment the In lines were less intense because they originated from In diffusion to the surface rather than the InSb layer.

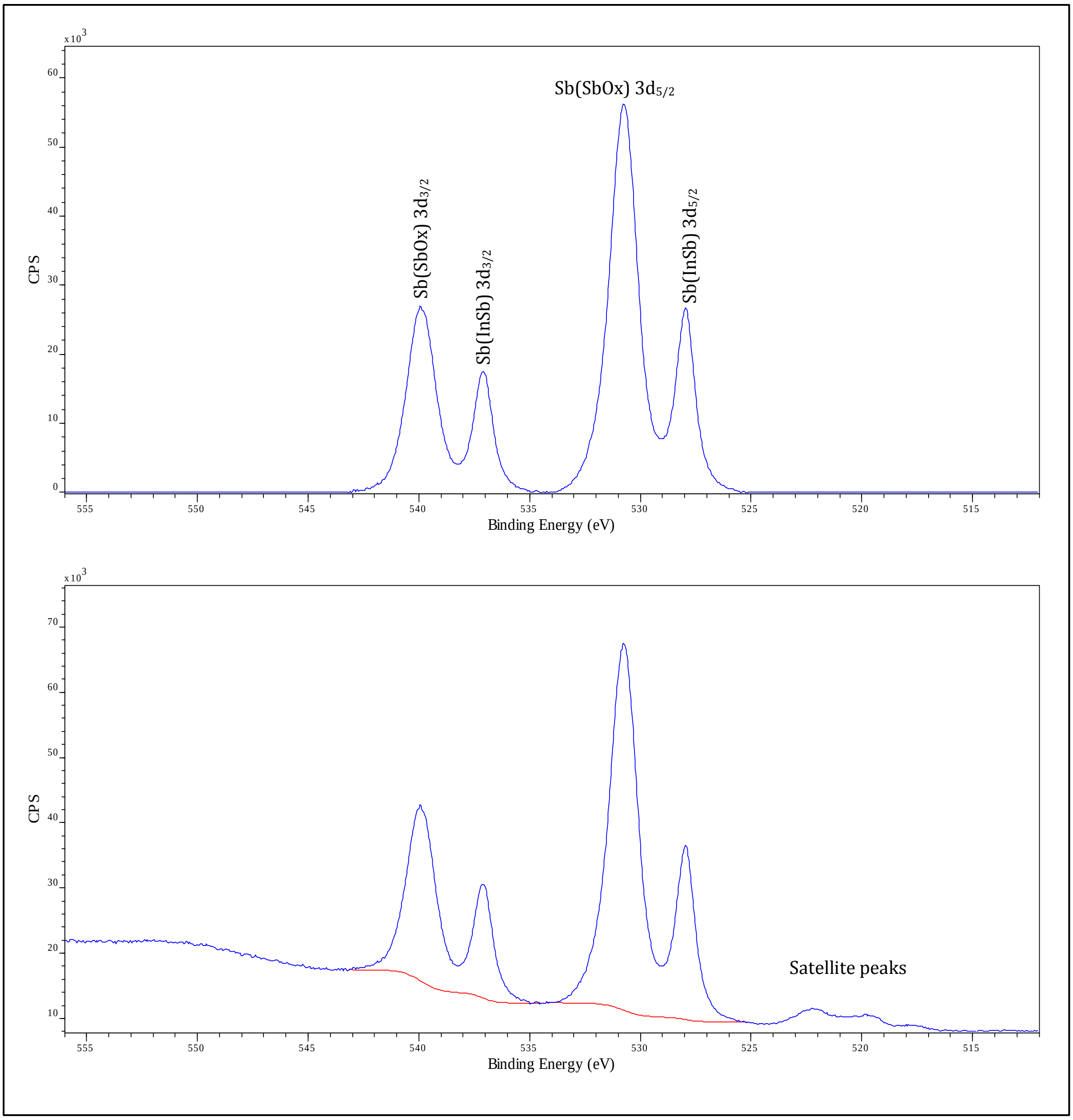

Fig. 6.3. Top: the Sb $3d$ region of the InSb sample as received. Two species are present. The higher binding energy one is due to an oxide layer which was removed by sputtering (Fig.6.4). Bottom: the same spectrum before the subtraction of the background (red). This spectrum was excited by unmonochromated Mg $K\alpha$ x-ray. Therefore, extra peaks appear at 8.4 eV lower binding energy due to a character x-ray satellites [1].

The $\mathrm{Sb}\ 3d$ region shows the presence of two components separated by $\sim 2.83\ eV$. The higher BE species is due to an oxide layer which was removed by the sputtering processes (Fig. 6.4). The $\mathrm{O}\ 1s$ line is known to overlap with the $3d_{5/2}$ component of Sb oxide [2]. The BE of the two Sb 3d doublet peaks and the energy shifts are accurately determined when the spectrum is fitted in the next section.

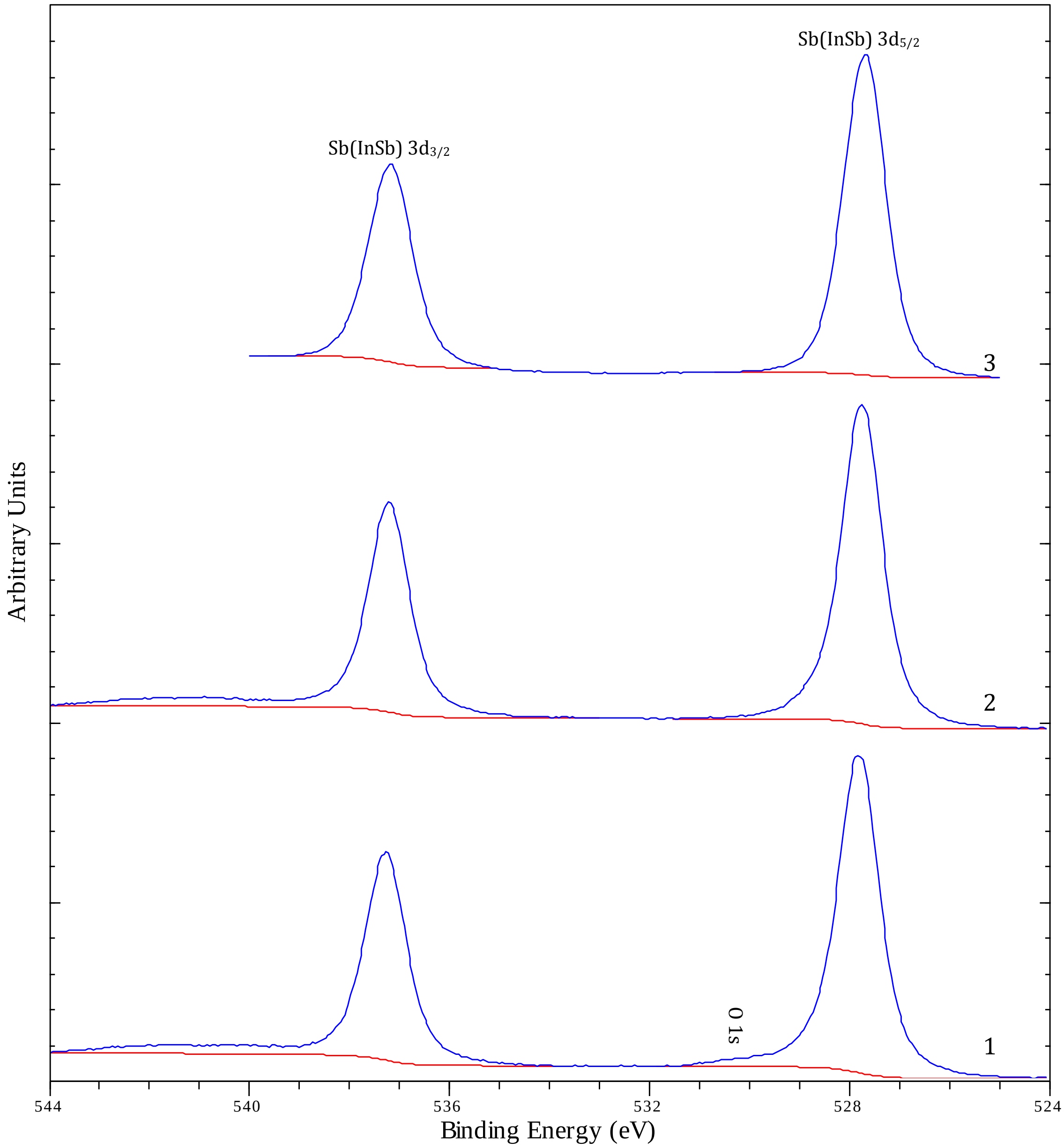

Fig. 6.4. The $\mathrm{Sb}\ 3d$ spectra after the first and the second sputtering (1,2), and after annealing at 250 ℃ (3). The oxide components were removed by the first sputtering, but a small amount of oxygen remained. Backgrounds calculated by Shirley method are shown. The doublet components have similar width and shape in the three spectra. The spectroscopic features are clearer after subtracting the backgrounds (Fig.6. 9, 10).

As for In, the reported $3d$ oxide shift is smaller than that of Sb. The former was reported to be $0.76\ eV$ [6], whereas the latter is $\sim 2.5\ eV$ [7]. A clear broadening at the higher binding energy side of $\mathrm{In}\ 3d$ peaks measured in InSb as received indicates the existence of the oxide components (Fig. 6.5). This broadening was did not appear in the spectrum obtained after the sputtering and annealing (Fig.6.5), which means the removal of the In oxide as was observed for Sb (Fig.6.4).

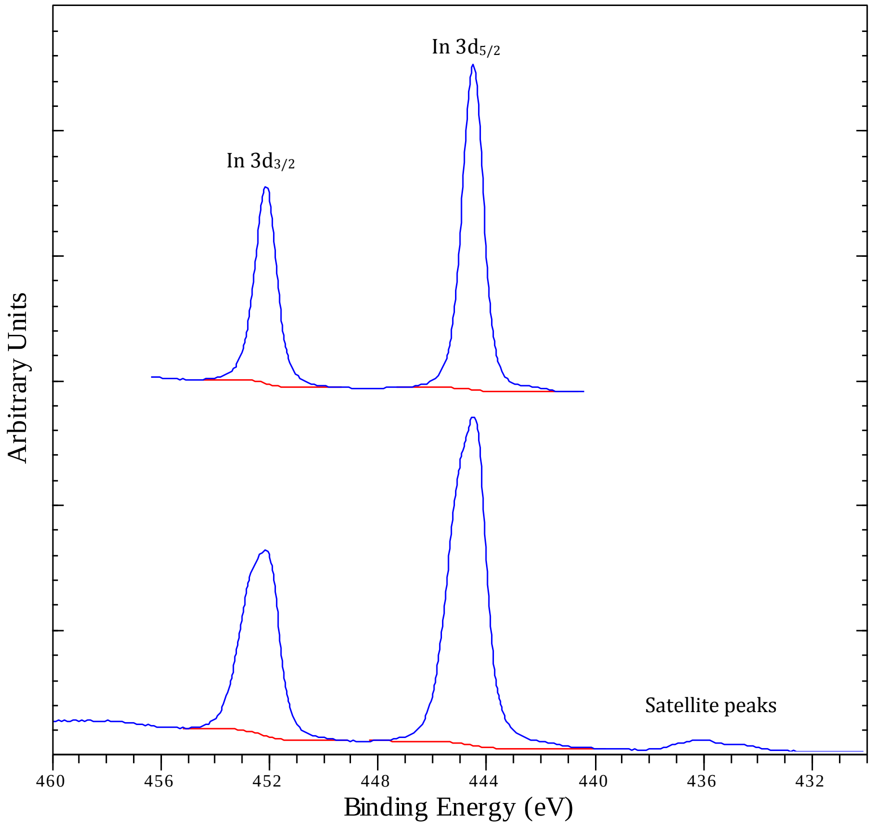

Fig. 6.5. Bottom: In $3d$ spectrum observed from InSb as received. This spectrum was excited with the unmonochromated Mg $K\alpha$ x-ray, and shows characteristic satellite peaks of this line at $8.4\ eV$ lower binding energy. Top: the same spectrum obtained after sputtering twice and annealing. This spectrum was excited with the unmonochromated Al $K\alpha$ x-ray. The broadening at the higher BE side in the spectrum obtained before the surface treatments is due to the oxide components. The red lines are Shirley-type backgrounds.

The Sb (InSb) $M_{4,5}N_{4,5}N_{4,5}$ Auger spectrum (Fig. 6.6) has a similar shape to those observed from elemental Sb (Sec.4.3.1) and from $\mathrm{Sb/InSb}$ (Sec.5.2.4). The profile of the Sb $M_{4,5}N_{4,5}N_{4,5}$ Auger process originating from pure InSb became sharp and clearer after the surface treatment of sputtering and annealing as the oxide components were absent. The same is true for the In $M_{4,5}N_{4,5}N_{4,5}$ Auger spectra (Fig. 6.7).

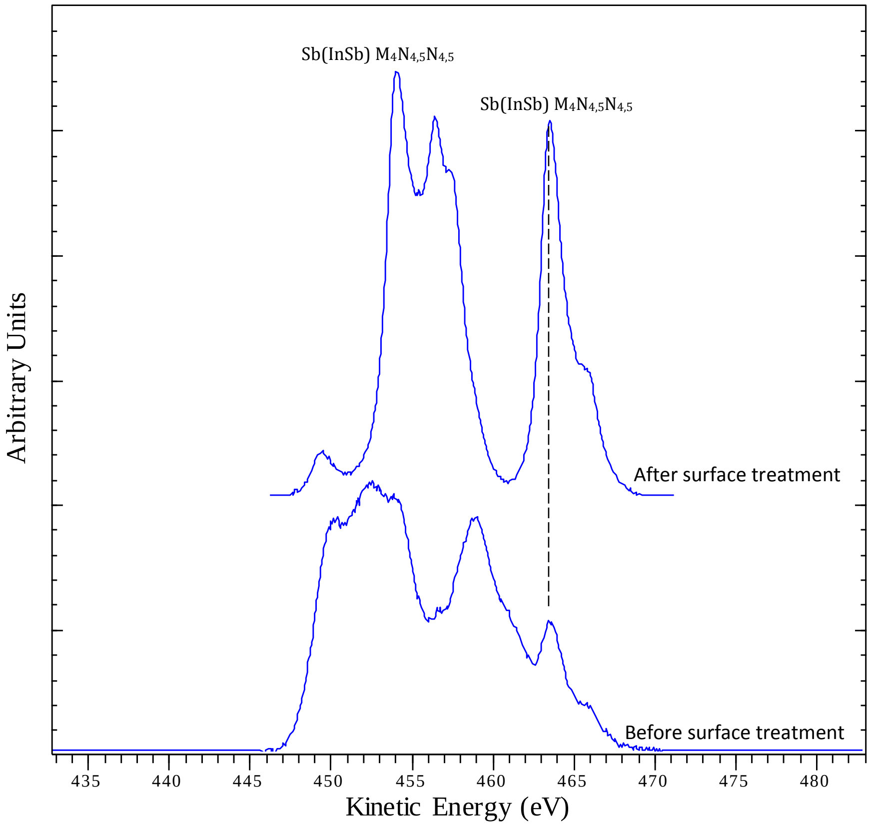

Fig. 6.6. Top: Sb $M_{4,5}N_{4,5}N_{4,5}$ Auger spectrum from InSb obtained after the surface treatments by Ar^+ bombardment and annealing. It has a similar profile to the spectrum of metallic Sb (Fig.4.12) and (Fig.5.22). The spectrum in the bottom was obtained of the InSb specimen as received. It does not exhibit the same distinct peaks, because of the existence of Sb oxide spectrum which was removed by the surface treatment. The dashed line designates the highest peak in the $M_4N_{4,5}N_{4,5}$ Auger group of Sb in InSb. The backgrounds subtracted from both spectra are similar to that shown in (Fig.6.11).

6.3. Peak analysis:

All the line positions in the binding energy scale are corrected by subtracting $0.67 \pm 0.02\ eV$ which is determined from the binding energy of C $1s$ photoelectron from the adventitious carbon detected in the sample as received.

The Sb and In $3d$ spectra were fitted using the method described in (Sec.4.2.2).

6.3.1. Sb $3d$:

Synthetic peak models were constructed to fit the Sb $3d$ spectra obtained from the InSb sample as received and after each surface treatment. The model made for the as-received

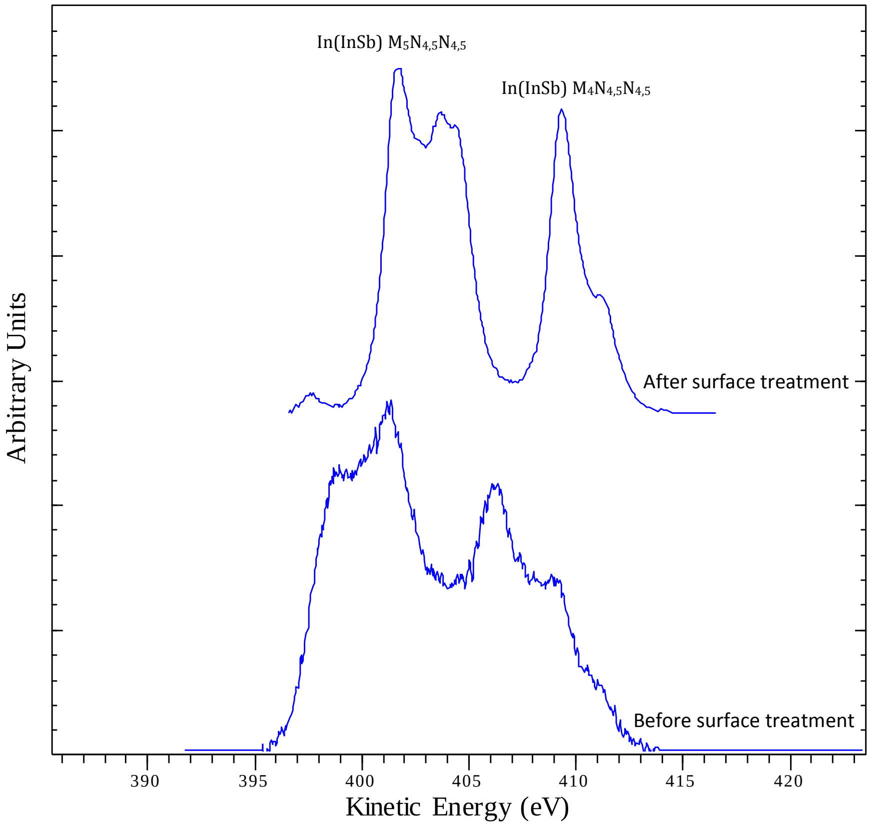

Fig. 6.7. Top: In $M_{4,5}N_{4,5}N_{4,5}$ Auger spectrum of InSb obtained after the surface treatments by Ar^+ bombardment and annealing. It has a similar profile to the spectrum of metallic In (Fig.4.9) and (Fig.5.25). The spectrum in the bottom was obtained of the InSb specimen as received. It does not have the same profile as the spectrum of the clean sample, because of the existence of In oxide spectrum. The backgrounds subtracted from both spectra are similar to that shown in (Fig.6.12).

sample (Fig. 6.8) shows the expected O $1s$ peak which overlaps with the Sb $3d_{5/2}$ peak of InSbOx. BE of the Sb $3d_{5/2}$ line of the oxide and that of InSb were $530.07 \pm 0.02\ eV$ and $527.30 \pm 0.02\ eV$ respectively, whereas the BE of the corresponding $3d_{3/2}$ components were $539.23 \pm 0.02\ eV$ and $536.43 \pm 0.02\ eV$. The shift between the two species in the $3d_{3/2,5/2}$ doublet components is then $2.80 \pm 0.02\ eV$ and $2.77 \pm 0.02\ eV$ respectively. The BE of O $1s$ is $530.31\ eV$. The accuracy of this fit can be affected by the overlap between Sb $3d_{5/2}$ and O $1s$.

After the first sputtering, the Sb(InSbOx) $3d$ doublet disappeared, but a weak O $1s$ peak remained (Fig. 6.9). The BE of $3d_{3/2,5/2}$ were 536.60 ± 0.02 and $527.14 \pm 0.02\ eV$ respectively. After the second sputtering, O $1s$ was not detected (Fig. 6.10). The binding

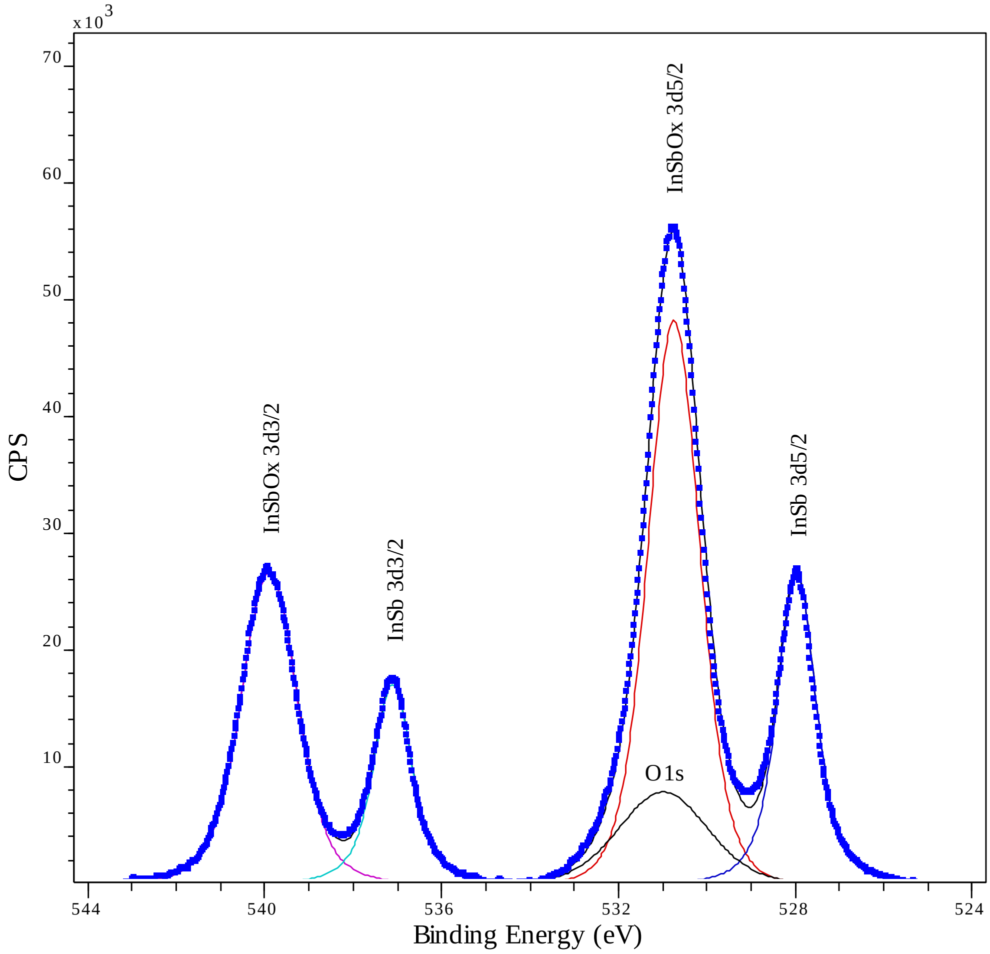

Fig. 6.8. The Sb 3d (InSb) spectrum (blue squares) fitted with a model of two specie accounting for pure and oxidised InSb, as well as the O $1s$. The widths of the $3d_{3/2,5/2}$ doublet components are $1.02\ eV$ and $1.03\ eV$ for InSb, and $1.49\ eV$ and $1.39\ eV$ for InSbOx.

energies of the Sb $3d$ doublet components were 536.54 ± 0.02 and $527.07 \pm 0.02\ eV$. After annealing, Sb $3d$ spectrum did not change (Fig. 6.10). The BE of $3d_{3/2,5/2}$ became $536.51 \pm 0.02\ eV$ and $527.02 \pm 0.02\ eV$.

6.3.2. In $3d$:

(Fig. 6.5) showed a broadening in the higher BE side of In $3d$ peaks due to the InSbOx. The relative intensities of the In $3d$ components, $I(3d_{5/2})/I(3d_{3/2})$, after subtracting Shirley type backgrounds is 1.76, much greater than 1.5 the value expected from the electron population of the $3d_{5/2}$, $3d_{3/2}$ subshells. This is due to a contribution from the satellites of the unmonochromated x-ray source. The broadening did not appear in the peaks obtained after sputtering and annealing which is expected since the O KLL was absent from the broadscan, and O 1s was not detected in the Sb $3d$ region. The peak positions of the In $3d_{3/2,5/2}$

components after annealing are 451.12 ± 0.02 and $443.47 \pm 0.02\ eV$ in the binding energy scale.

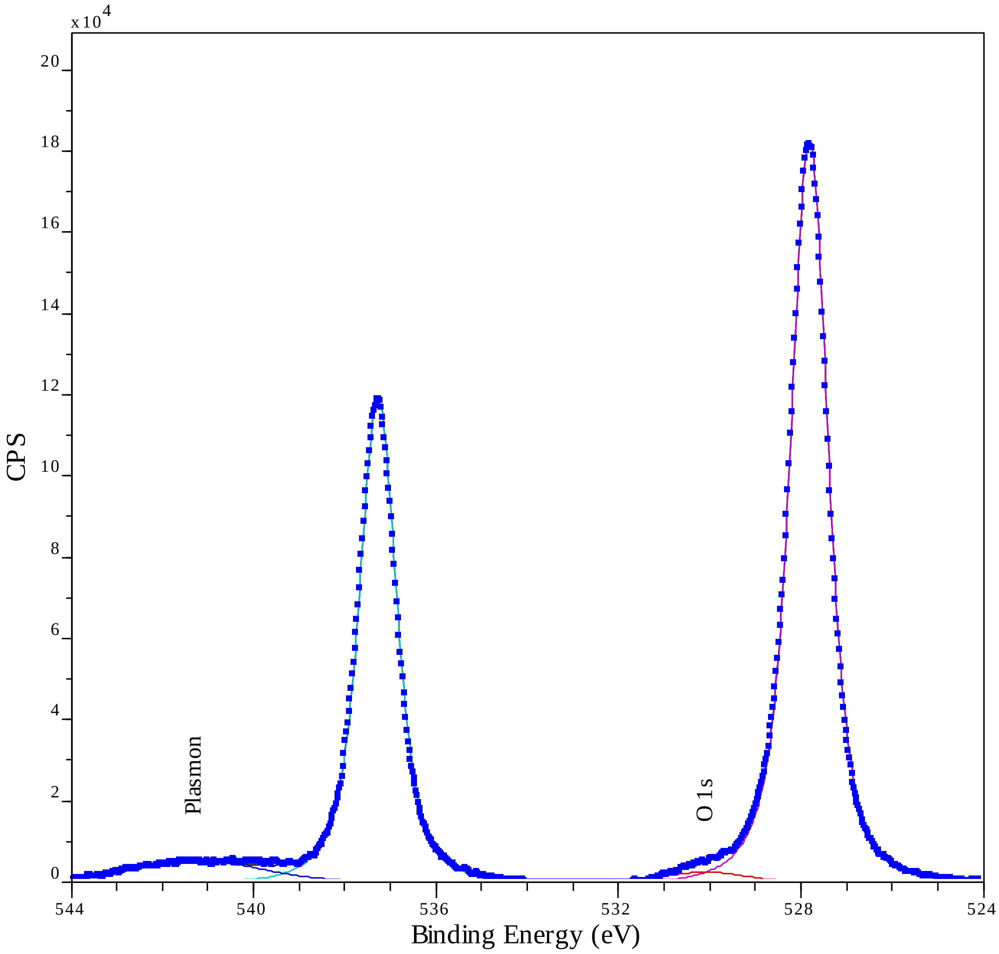

Fig. 6.9. Sb $3d$ region after the first sputtering (squares). The oxide peaks disappeared, but a weak O $1s$ still existed. InSb bulk plasmon (at $13.41\ eV$ from $3d_{5/2}$) partially overlaps with $3d_{3/2}$. The widths of $3d_{3/2,5/2}$ components are $0.96\ eV$ and $0.97\ eV$.

6.3.3. Sb $M_{4,5}N_{4,5}N_{4,5}$ Auger:

The positions of the $^1G_4$ lines of the multiplet structure of the $M_{4,5}N_{4,5}N_{4,5}$ groups are usually quoted in comparing the chemical shifts of In and Sb [8, 9]. This component is associated with the most intense peaks in each group [9, 10] and is easier to obtain from the differential form as described in (Sec.4.2.3). The Sb Auger spectrum measured before any surface treatment was dominated by the oxide spectrum and had a poor signal to noise ratio (Fig 6.6). The positions of the most intense peaks in the $M_5N_{4,5}N_{4,5}$ and $M_4N_{4,5}N_{4,5}$ groups in the kinetic energy scale after annealing (Fig. 6.11) are 455.12 ± 0.06 and $464.61 \pm 0.06\ eV$. The splitting between the two groups is $9.49 \pm 0.07\ eV$ which is equal to the spin-orbit is splitting between the $3d$ doublet components (Sec.6.3.1) as expected since the $3d_{3/2}$ and $3d_{5/2}$ hole states are the initial states of the $M_4N_{4,5}N_{4,5}$ and $M_5N_{4,5}N_{4,5}$ Auger processes respectively.

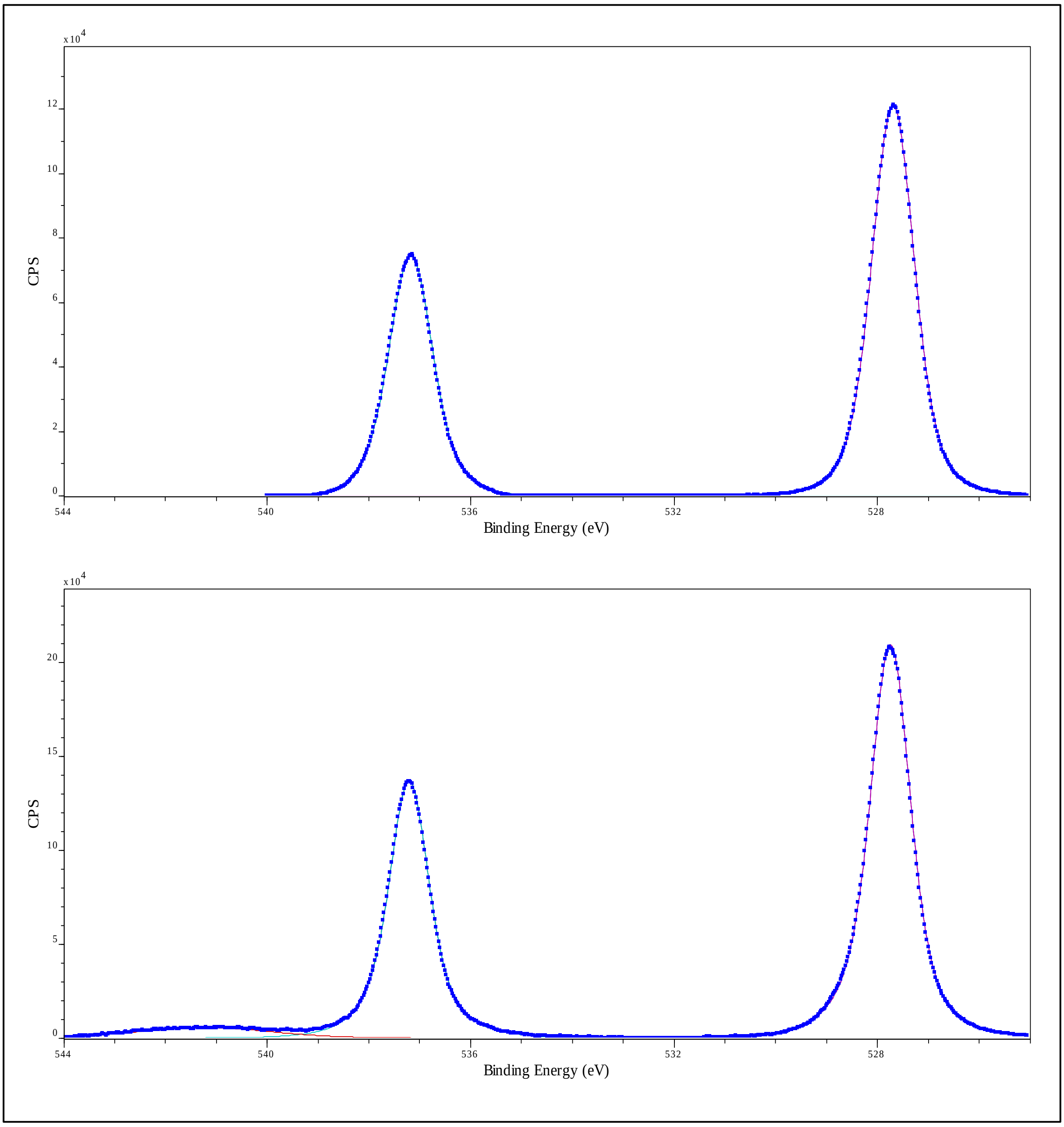

Fig. 6.10. Bottom: Sb $3d$ spectrum obtained after the second sputtering (squares) and the peak model. O $1s$ peak no longer existed. InSb bulk plasmon (at $13.51\ eV$ from $3d_{5/2}$) partially overlaps with $3d_{3/2}$. The widths of the $3d_{3/2,5/2}$ components are 0.94 and $0.95\ eV$. Top: The Sb $3d$ spectrum scanned after annealing. The widths of $3d_{3/2,5/2}$ components are 1.02 and $0.99\ eV$ respectively.

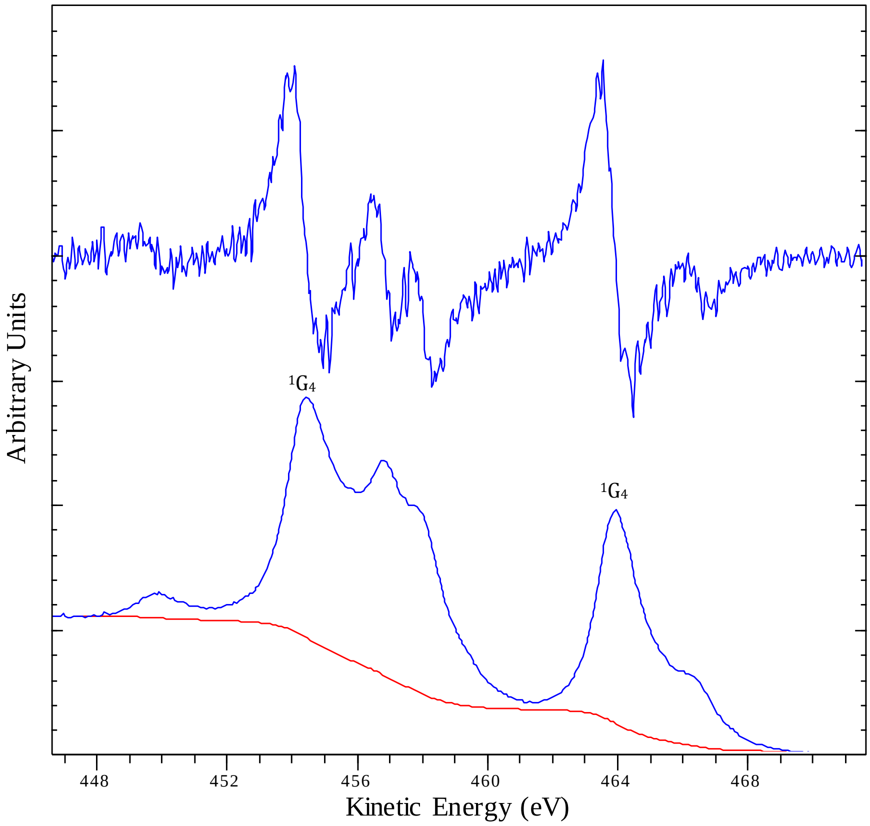

Fig. 6.11. The direct and the differential form of Sb $M_{4,5}N_{4,5}N_{4,5}$ Auger spectrum in InSb measured after two Ar⁺ sputtering then annealing. The KE of the highest peak in each of the two Auger groups (annotated in the spectrum as $^1G_4$) is determined through the position of the most intense downward-going zero-crossing in the differential form. The red line is a Shirley background.

6.3.4. In $M_{4,5}N_{4,5}N_{4,5}$ Auger:

By analysing the In $M_{4,5}N_{4,5}N_{4,5}$ Auger spectrum the way described in the previous section, the energies of the two $^1G_4$ lines measured after sputtering and annealing were found to be 402.30 ± 0.06 and $409.97 \pm 0.06\ eV$ respectively (Fig.6.12). The splitting between the two lines is, then, $7.67 \pm 0.08\ eV$ compared to spin-orbit splitting of $7.65 \pm 0.02\ eV$ between the In $3d$ components obtained after the same surface treatment (Sec.6.3.2). The difference between the two splittings is within the measurement error.

6.4. Conclusion:

Having obtained the BE($3d_{5/2}$) and the KE of the most intense peaks in the $M_4N_{4,5}N_{4,5}$ group of Sb and In in the clean InSb prepared by Ar⁺ sputtering and annealing, these results are

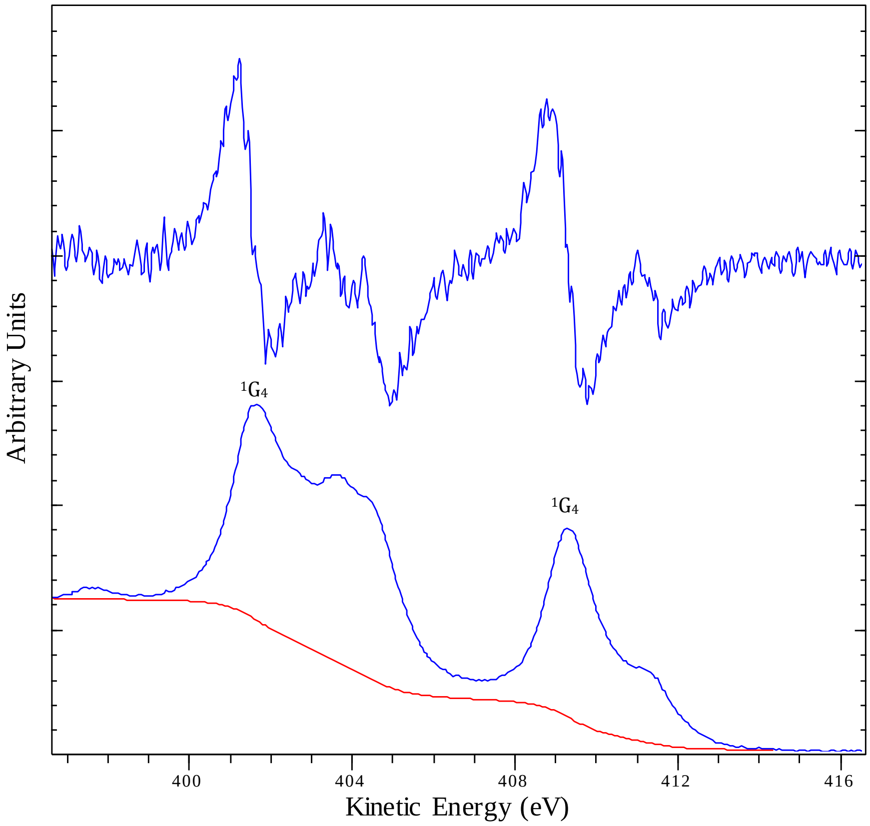

Fig. 6.12. The direct and the differential form of In $M_{4,5}N_{4,5}N_{4,5}$ Auger spectrum in InSb measured after two Ar$^+$ sputtering then annealing. The KE of the highest peak in each of the two Auger groups (annotated in the spectrum as $^1G_4$) is determined through the position of the most intense downward-going zero-crossing in the differential form. The red line is a Shirley background.

now used to calculate the Auger parameters AP($3d_{5/2}$,$M_4N_{4,5}N_{4,5}$) using the following formula [1]:

$$\alpha = KE_{M_4N_{4,5}N_{4,5}} + BE_{3d_{5/2}} \quad (6.1).$$

Substituting the values obtained in (Sec.6.1-4) in this equation, the AP (α) of Sb was found to be $991.63 \pm 0.06\ eV$, and the AP of In is $853.44 \pm 0.06\ eV$. These are reliable values, obtained of clean InSb. Therefore, they can be used together with the AP values of metallic Sb and In obtained in (Ch.4) to apply the potential model explained in (Sec.1.4.2) to investigate the electronic structure of InSb.

(Ch.7) involves the derivation of the potential model parameters (a, b, d) of In and Sb atoms, which are necessary to formulate (Eq.1.54) for both elements.

References

1. Briggs, D. and J.T. Grant, *Surface analysis by Auger and x-ray photoelectron spectroscopy*. 2003, Chichester, West Sussex, U.K.: IM Publications. xi, 899 p.
2. Iwanowski, R., et al., *XPS analysis of surface compositional changes in InSb 1− x Bi x (111) due to low-energy Ar+ ion bombardment.* Applied surface science, 2000. **153**(4): p. 193-199.
3. Liu, W. and M. Santos, *Characterization of oxide desorption from InSb (001) substrates.* Journal of Vacuum Science & Technology B, 1996. **14**(2): p. 647-651.
4. Bouslama, M., C. Jardin, and M. Ghamnia, *The InSb (100) surface change during the argon ion bombardment and the electron stimulated oxidation.* Vacuum, 1995. **46**(2): p. 143-146.
5. Woodruff, D.P. and T.A. Delchar, *Modern techniques of surface science*. 2nd ed. Cambridge solid state science series. 1994, Cambridge ; New York: Cambridge University Press. xviii, 586 p.
6. NIST, X., *Database,< h ttp.* srdata. nist. gov/xps/Default. aspx.
7. Liu, W.K., *Characterization of oxide desorption from InSb(001) substrates.* Journal of Vacuum Science & Technology B: Microelectronics and Nanometer Structures, 1996. **14**(2): p. 647.
8. Aksela, S., et al., *Semiempirical Solid State Shifts in the Auger-and Photoelectron Energies.* Physica Scripta, 1982. **25**(1A): p. 45.
9. Pessa, M., et al., *Solid-state effects inM4,5N4,5N4,5Auger spectra of elements fromIn49toTe52.* Physical Review B, 1979. **20**(8): p. 3115-3123.
10. Parry-Jones, A., P. Weightman, and P. Andrews, *The M4, 5N4, 5N4, 5 Auger spectra of Ag, Cd, In and Sn.* Journal of Physics C: Solid State Physics, 1979. **12**(8): p. 1587.

Chapter 7

Derivation of the Potential model Parameters For In and Sb

7.1. Introduction:

The potential model produced by Cole and co-workers [1] was introduced in (Sec. 1.4.2). The value of k, the change in the core potential by the removal of a valence electron, depends on five parameters:

$$k(N_{nl}, q) = a + bN_{nl} + c{N_{nl}}^2 + (d + eN_{nl})q \qquad (7.1)$$

These parameters are derived and explained for In and Sb in the following sections. They are, then, used in (Ch. 8, 9) to describe screening and valence charge in In, Sb and InSb.

7.2. The potential parameters for the In atom:

Atomic structure calculations were carried out by the Dirac-Fock self-consistent field (SCF) program [2] for In and Sb atoms at the $3d$ core level occupancies N from 0 to -4. For each value of N the calculation was repeated for all values of valence charge q, from $q = 0$ (equivalent to configuration $\mathrm{Kr\ 5s^0\ 5p^0}$) to $q = -8$ (equivalent to $\mathrm{Kr\ 5s^2\ 5p^6}$). The eigenvalue (orbital energy) of the $3d_{5/2}$ subshell was read, from the program output (Fig.2.10), for each $3d$ occupancy and valence level configuration (Table. 7.1). The following step was calculating the difference between the $3d$ orbital energy V_{3d} for the ground state configuration ($\mathrm{Kr\ 5s^2\ 5p^1}$ for In and $\mathrm{Kr\ 5s^2\ 5p^3}$ for Sb) and all other configurations (ΔV_{3d}). (Graph.7.1) shows the relation between ΔV_{3d} and q at different N_{3d} values for In. k was then derived as the derivative $d(\Delta V_{3d})/dq$ for each value of N_{3d} (Graph.7. 2).

$\boldsymbol{3d}$ $\boldsymbol{Occupancy}$	$\boldsymbol{Valence\ Level}$ $\boldsymbol{Configuration}$	$\boldsymbol{V(3d_{5/2})}$ $\boldsymbol{(eV)}$	$\boldsymbol{V(3d_{3/2})}$ $\boldsymbol{(eV)}$	$\boldsymbol{N_{3d}}$	$\boldsymbol{\Delta V_{3d}(N_{3d},q)}$ $\boldsymbol{(eV)}$	$\boldsymbol{q}$	$\boldsymbol{k_{3d}}$ $(Volt)$
$3d^{10}$	$5s^2\ 5p^1$	−468.47	−476.2	0	0	−3	7.39
	$5s^2\ (5p^0)$	−475.86	−483.59	0	7.39	−2	8.885
	$5s^1$	−486.24	−493.97	0	17.77	−1	10.945
	$4d^{10}\ (5s^0)$	−497.75	−505.48	0	29.28	0	11.51
$3d^9$	$5s^2\ 5p^3$	−495.53	−503.42	−1	−13.67	−5	5.77
	$5s^2\ 5p^2$	−501.3	−509.19	−1	−7.9	−4	6.835
	$5s^2\ 5p^1$	−509.2	−517.09	−1	0	−3	8.625
	$5s^2$	−518.55	−526.45	−1	9.35	−2	10.59
	$5s^1$	−530.38	−538.27	−1	21.18	−1	12.305
	$4d^{10}$	−543.16	−551.05	−1	33.96	0	12.78
$3d^8$	$5s^2\ 5p^4$	−528.56	−536.62	−2	−24.71	−6	6.56
	$5s^2\ 5p^3$	−535.12	−543.18	−2	−18.15	−5	7.475
	$5s^2\ 5p^2$	−543.51	−551.57	−2	−9.76	−4	9.075
	$5s^2\ 5p^1$	−553.27	−561.33	−2	0	−3	10.325
	$5s^2$	−564.16	−572.22	−2	10.89	−2	11.985
	$5s^1$	−577.24	−585.3	−2	23.97	−1	13.515
	$4d^{10}$	−591.19	−599.24	−2	37.92	0	13.95
$3d^7$	$5s^2\ 5p^5$	−562.5	−570.74	−3	−37.51	−7	7.23
	$5s^2\ 5p^4$	−569.73	−577.96	−3	−30.28	−6	8.055
	$5s^2\ 5p^3$	−578.61	−586.84	−3	−21.4	−5	9.515
	$5s^2\ 5p^2$	−588.76	−597	−3	−11.25	−4	10.7
	$5s^2\ 5p^1$	−600.01	−608.24	−3	0	−3	11.735
	$5s^2$	−612.23	−620.46	−3	12.22	−2	13.225
	$5s^1$	−626.46	−634.69	−3	26.45	−1	14.62
	$4d^{10}$	−641.47	−649.71	−3	41.46	0	15.01
$3d^6$	$5s^2\ 5p^6$	−597.3	−605.71	−4	−51.87	−8	7.81
	$5s^2\ 5p^5$	−605.11	−613.52	−4	−44.06	−7	8.575
	$5s^2\ 5p^4$	−614.45	−622.86	−4	−34.72	−6	9.95
	$5s^2\ 5p^3$	−625.01	−633.42	−4	−24.16	−5	11.08
	$5s^2\ 5p^2$	−636.61	−645.02	−4	−12.56	−4	12.08
	$5s^2\ 5p^1$	−649.17	−657.58	−4	0	−3	12.99
	$5s^2$	−662.59	−671	−4	13.42	−2	14.35
	$5s^1$	−677.87	−686.29	−4	28.7	−1	15.655
	$4d^{10}$	−693.9	−702.31	−4	44.73	0	16.03

Table. 7.1. Column 1 is the In $3d$ occupancy. Column 2 is the valence level configuration. Column 3,4 are the eigenvalues of $3d_{5/2,\ 3/2}$. ΔV_{3d} is the difference between $3d$ eigenvalue for the corresponding valence level configuration and the ground state configuration $5s^2\ 5p^1$. ΔV is the same for $3d_{5/2}$ and $3d_{3/2}$. q is the valence charge which is the number of valence level electrons multiplied by -1. k is the derivative of ΔV_{3d} with respect to q for each N_{3d} separately.

It can be noticed in (Table. 7. 1) that k_{3d} was not obtained for some configurations. This is due to the SCF procedure not converging to a solution for the reason explained in (Sec. 3.2.1.1.1).

(Eq. 7.1) was solved analytically to obtain the values of the five parameters a, b, c, d, e. The solution was obtained by running a multiple linear regression of the (k_{3d} vs. q) spread of points in (Table.7.1) in five terms and four independent variables as illustrated in the following equation:

$$k(N_{3d}, q) = a + bx_1 + cx_2 + dx_3 + ex_4 \qquad (7.2)$$

where $x_1 = N_{nl}$, $x_2 = {N_{nl}}^2$, $x_3 = q$, $x_4 = N_{nl}q$ and a is the intercept which is the value of k_{3d} corresponding to $N_{nl} = q = 0$. The values of the parameters c and e were found to be of considerably smaller magnitudes than a, b and d, therefore they can be neglected [3]. Therefore, (Eq. 7.1) is rewritten as:

$$k(N_{nl}, q) = a + bN_{nl} + dq \qquad (7.3)$$

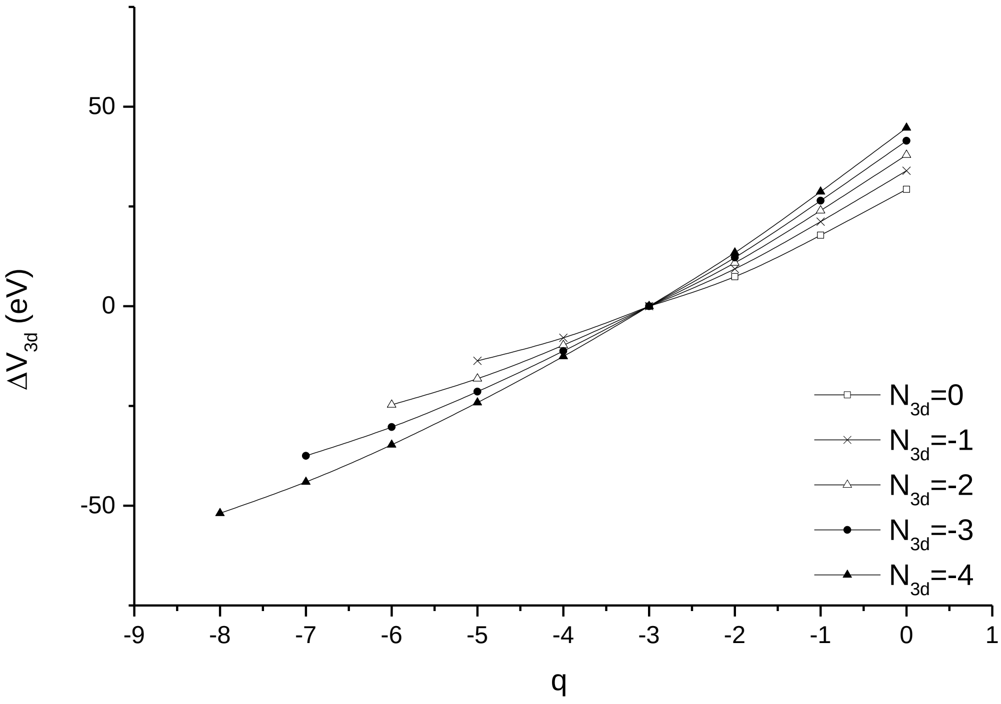

Graph.7.1. The abscissa is the valence charge of In atom and the ordinate is the corresponding shift of the $3d$ eigenvalue (ΔV_{3d}) from its value for the ground state configuration $5s^2$ $5p^1$ ($q = -3$) at different $3d$ occupancies N_{3d}.

b is of a negative value. So, as $k \approx 1/\langle r_v \rangle$ (Eq. 1.44), b expresses the compression of the valence level by the creation of a core hole. d determines the compression/expansion of the valence level by the reduction/addition of valence charge.

Parameter	Value	Standard Error
a	11.99812	0.1813
b	-1.28716	0.15287
c	-0.04805	0.03711
d	1.58932	0.06922
e	0.12877	0.02233

Table. 7.2. The coefficients of (Eq. 7.1) for In atom, derived analytically by linear regression of (k_{3d}, q) points with five terms as in (Eq. 7.2).

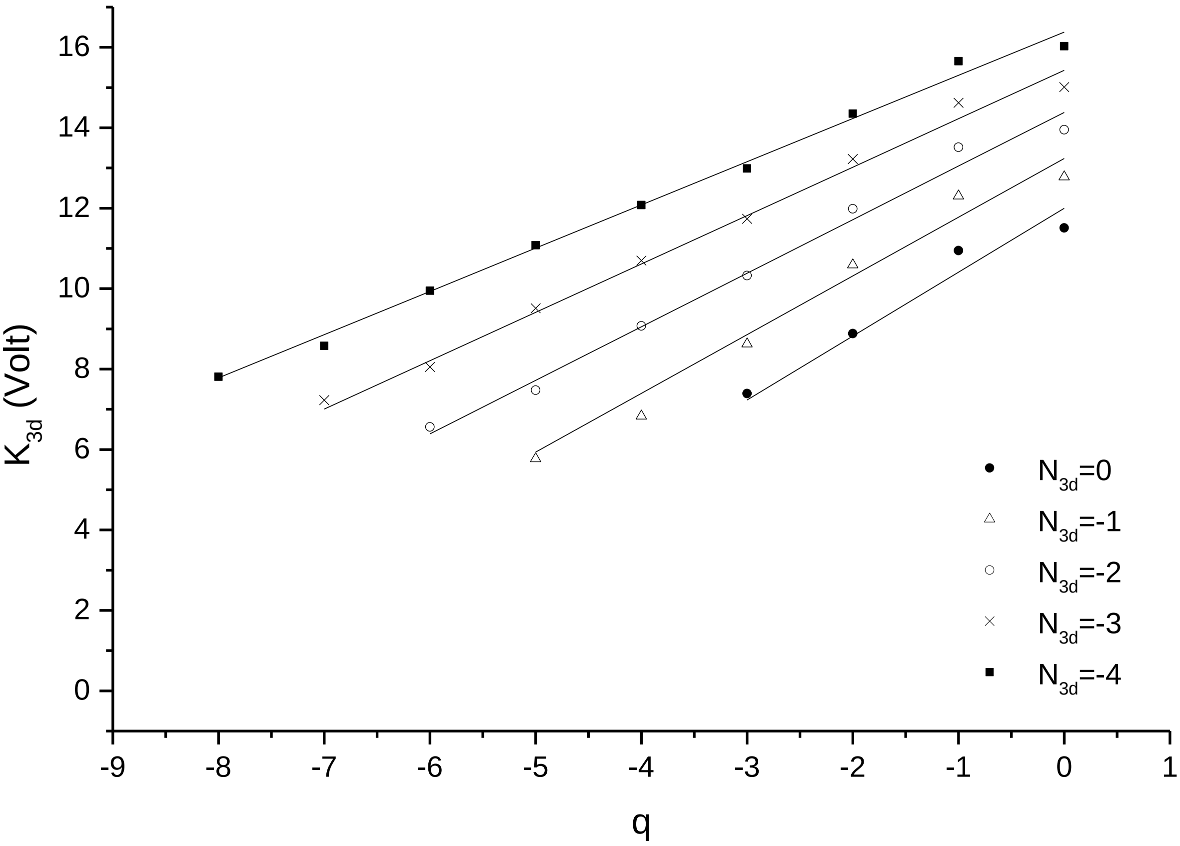

Graph. 7.2. Points: k_{3d} value vs. valence charge for In at different $3d$ occupancies from (Table. 7.1). The lines are the linear fits of the whole (k_{3d}, q) spread in five terms as in (Eq. 7.2).

Substituting the values from (Table. 7.2) in (Eq. 7.3) the following expression is obtained for the core potential of In:

$$k(N_{nl}, q) = 12 - 1.29N_{nl} + 1.59q \qquad (7.4)$$

From (Eq. 1.54), the chemical shift of the Auger parameter is expressed as a function of the change in the core hole screening and local charge as follows:

$$\Delta\alpha = \Delta\left\{-1.29q + \frac{dq}{dN}\left[14.58 + 1.59\left(q - \frac{dq}{dN}\right)\right] + \frac{dV^{ea}}{dN}\right\} \qquad (7.5)$$

The essence of the potential model is the derivation of an equation similar to (Eq.7.5) for each element in a material. The equations are, then, solved together to obtain information about screening and local charges of the constituent atoms. This requires knowledge of the Auger parameter shifts ($\Delta\alpha$) between the state of the elements in the studied material and their states in simple (well-known) other materials. The other material is ideally the elemental gaseous state. This is demonstrated in (Ch.8, 9).

7.3. The potential parameters for Sb atom:

To obtain the potential parameters for Sb, the same procedure used for In (Sec. 7.2) was followed. In and Sb are in the same period in the periodic table, so they have the same number of core electrons, whereas their valence levels are 5s 5p.

k_{3d} for Sb was obtained as in (Table. 7.3).

(Graph. 7.3) shows the shift of $3d$ eigenvalue due to the change of the valence configuration from the ground state one which is $5s^2\,5p^3$ for Sb. (Graph. 7.4) shows a plot of k_{3d} values from (Table. 7.3) against the valence charge values q, as well as a linear regression fitting of k_{3d} using (Eq. 7. 2). This results in an analytical solution of (Eq. 7.1) for Sb atom with the values of the five coefficient listed in (Table. 7. 4). By neglecting the small coefficients c and e, (Eq. 7.1) is written for Sb as follows:

$$k(N_{nl}, q) = 14.62 - 1.17N_{nl} + 1.34q \qquad (7.6)$$

From (Eq.1.54), the chemical shift of the Auger parameter of Sb is expressed as a function of the change in the core hole screening and local charge as follows:

$$\Delta\alpha = \Delta\left\{-1.17q + \frac{dq}{dN}\left[16.96 + 1.34\left(q - \frac{dq}{dN}\right)\right] + \frac{dV^{ea}}{dN}\right\} \qquad (7.7)$$

$3d$ $Occupancy$	$Valence\ Level\ Configuration$	$V(3d_{5/2})$ eV	$V(3d_{3/2})$ eV	N_{3d}	$\Delta V_{3d}(N_{3d},q)$ eV	q	k_{3d} (Volt)
3d^{10}	5s^2 5p^4	-547.3	-556.85	0	-6.63	-6	6.63
	5s^2 5p^3	-553.93	-563.49	0	0	-5	7.58
	5s^2 5p^2	-562.46	-572.01	0	8.53	-4	9.22
	5s^2 5p^1	-572.37	-581.92	0	18.44	-3	10.485
	5s^2 (5p^0)	-583.43	-592.98	0	29.5	-2	12.21
	5s1	-596.79	-606.34	0	42.86	-1	13.795
	4d^{10} (5s^0)	-611.02	-620.57	0	57.09	0	14.23
3d^9	5s^2 5p^5	-581.95	-591.7	-1	-16.33	-7	7.32
	5s^2 5p^4	-589.27	-599.02	-1	-9.01	-6	8.165
	5s^2 5p^3	-598.28	-608.03	-1	0	-5	9.665
	5s^2 5p^2	-608.6	-618.34	-1	10.32	-4	10.87
	5s^2 5p^1	-620.02	-629.77	-1	21.74	-3	11.92
	5s^2 (5p^0)	-632.44	-642.19	-1	34.16	-2	13.47
	5s^1	-646.96	-656.7	-1	48.68	-1	14.92
	4d^{10} (5s^0)	-662.28	-672.03	-1	64	0	15.32
3d^8	5s^2 5p^6	-617.65	-627.6	-2	-28.12	-8	7.92
	5s^2 5p^5	-625.57	-635.51	-2	-20.2	-7	8.7
	5s^2 5p^4	-635.05	-644.99	-2	-10.72	-6	10.1
	5s^2 5p^3	-645.77	-655.72	-2	0	-5	11.255
	5s^2 5p^2	-657.56	-667.51	-2	11.79	-4	12.275
	5s^2 5p^1	-670.32	-680.26	-2	24.55	-3	13.2
	5s^2 (5p^0)	-683.96	-693.9	-2	38.19	-2	14.615
	5s^1	-699.55	-709.5	-2	53.78	-1	15.97
	4d^{10} (5s^0)	-715.9	-725.85	-2	70.13	0	16.35
3d^7	5s^2 5p^6	-662.64	-672.78	-3	-33.2	-8	9.93
	5s^2 5p^5	-672.57	-682.72	-3	-23.27	-7	10.525
	5s^2 5p^4	-683.69	-693.84	-3	-12.15	-6	11.635
	5s^2 5p^3	-695.84	-705.99	-3	0	-5	12.62
	5s^2 5p^2	-708.93	-719.09	-3	13.09	-4	13.53
	5s^2 5p^1	-722.9	-733.05	-3	27.06	-3	14.37
	5s^2 (5p^0)	-737.67	-747.82	-3	41.83	-2	15.69
	5s^1	-754.28	-764.44	-3	58.44	-1	16.97
	4d^{10} (5s^0)	-771.61	-781.77	-3	75.77	0	17.33
3d^6	5s^2 5p^6	-710.82	-721.18	-4	-37.45	-8	11.5
	5s^2 5p^5	-722.32	-732.69	-4	-25.95	-7	12.01
	5s^2 5p^4	-734.84	-745.2	-4	-13.43	-6	12.975
	5s^2 5p^3	-748.27	-758.63	-4	0	-5	13.855
	5s^2 5p^2	-762.55	-772.92	-4	14.28	-4	14.68
	5s^2 5p^1	-777.63	-788	-4	29.36	-3	15.46
	5s^2 (5p^0)	-793.47	-803.84	-4	45.2	-2	16.71
	5s^1	-811.05	-821.43	-4	62.78	-1	17.92
	4d^{10} (5s^0)	-829.31	-839.69	-4	81.04	0	18.26

Table. 7.3. Column 1 is the Sb $3d$ occupancy. Column 2 is the valence level configuration. Column 3,4 are the eigenvalues of $3d_{5/2,\,3/2}$. ΔV_{3d} is the difference between 3d eigenvalue for the corresponding valence level configuration and the ground state configuration 5s^2 5p^3. ΔV is the same for $3d_{5/2}$ and $3d_{3/2}$. q is the valence charge which is the number of valence level electrons multiplied by -1. k is the derivative of ΔV_{3d} with respect to q for each N_{3d} separately.

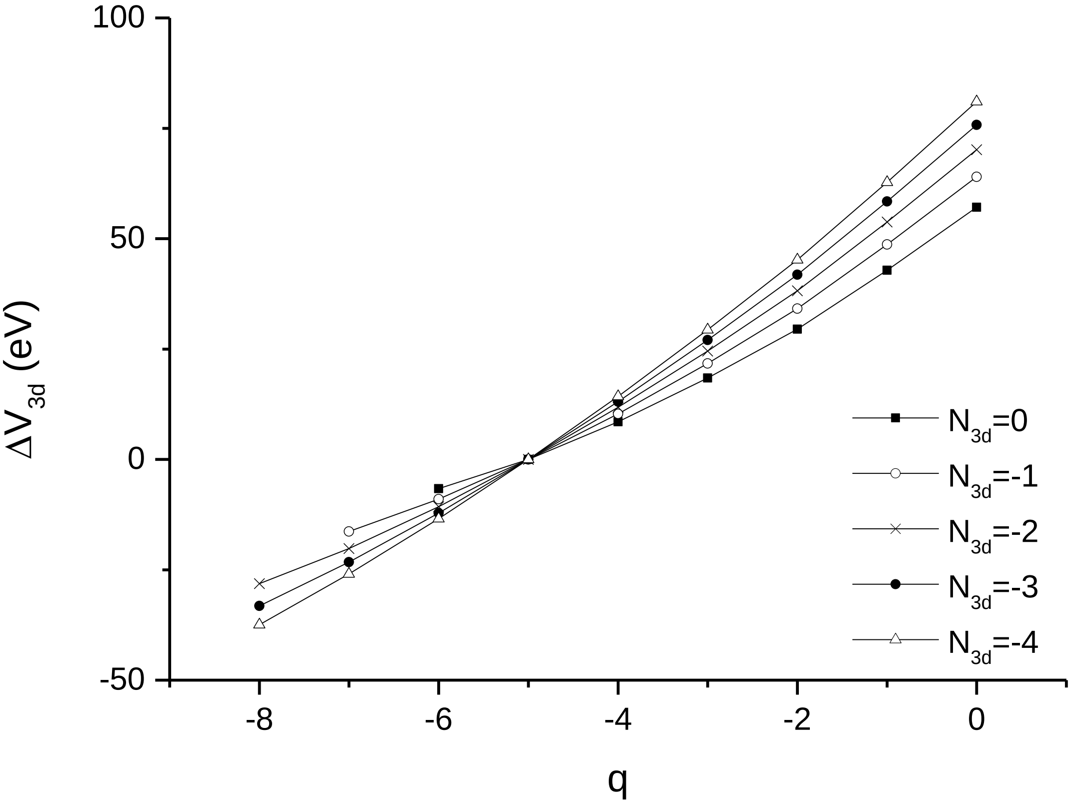

Graph. 7.3. The abscissa is the valence charge of Sb atom, and the ordinate is the corresponding shift of the $3d$ eigenvalue (ΔV_{3d}) from its value for the ground state configuration $5s^2$ $5p^3$ ($q = -5$) at different $3d$ occupancies N_{3d}.

Parameter	Value	Standard Error
a	14.62276	0.13018
b	-1.17468	0.10238
c	-0.06085	0.02325
d	1.34189	0.03192
e	0.11506	0.01195

Table. 7.4. The coefficients of (Eq.7.1) for Sb atom, derived analytically by linear regression of k_{3d} points with five terms as in (Eq. 7.2).

7.4. Summary:

This chapter included the derivation of the formulas that link the chemical shifts of the Auger parameters of In and Sb to the change of the electronic structure of the materials they are part of (Eq.7. 5 and 7). Such formulas are based on the potential model [1] explained in

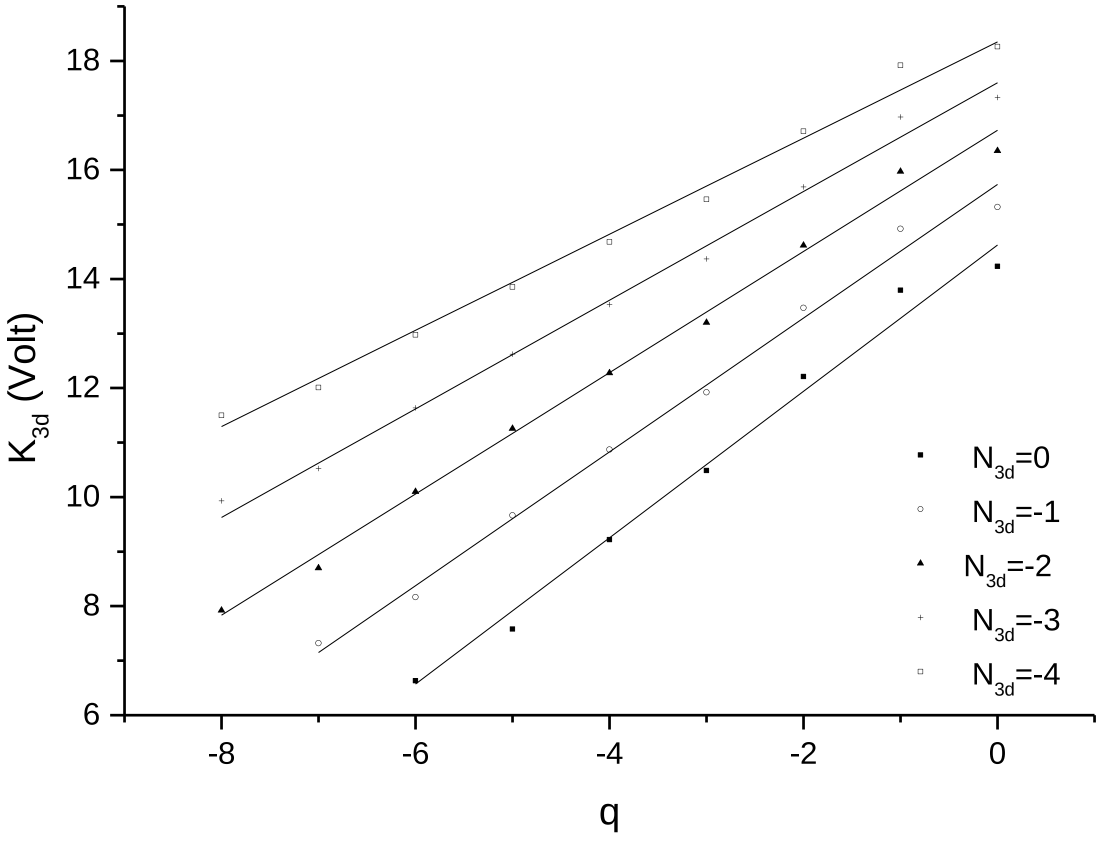

Graph.7.4: Points: k_{3d} value vs. valence charge for Sb atom at different $3d$ occupancies from (Table. 7.3). The lines are the linear fits of the whole (k_{3d}, q) spread in five terms as in (Eq. 7.2).

(Sec.1.4.2). No attempt has been made, before this work, to apply this model to compound semiconductors. (Ch.9) includes the application of this model to InSb. This became possible because of the determination of precise values of the Auger parameters of In and Sb in their metallic states and in InSb (Ch.4 and 6). So, the shifts of the Auger parameters determined in (Ch.4 and 6) substitute $\Delta\alpha$ in (Eq.7.5) and (Eq.7.7) which are, then, solved together to obtain information about screening and local charge of In and Sb in InSb.

Before that, (Ch.8) examines the validity of applying the potential model, together with a different type of the Auger parameter, for the determination of physically meaningful values of screening in a relatively simpler case which is the metallic state of In and Sb.

References

1. Cole, R.J., D.A.C. Gregory, and P. Weightman, *Analysis of Auger-parameter and XPS shifts: Application of potential models.* Physical Review B, 1994. **49**(8): p. 5657-5661.
2. Desclaux, J. and P. Indelicato, *The relativistic atomic program MCDFGME V 2005.10.* Published at http://dirac. spectro. jussieu. fr/mcdf/on August, 2005. **17**: p. 2005.
3. Cole, R. and P. Weightman, *Separating ground state and screening contributions to chemical shifts.* Journal of Physics: Condensed Matter, 1994. **6**(29): p. 5783.

Chapter 8

Separating Valence Charge and Relaxation Effects in the Chemical Shifts of Metals

8.1. Introduction:

The chemical shifts of the atomic core photoelectron binding energy (BE) and the Auger electron kinetic energy (KE) result from the changes in valence charge and relaxation energy between the two environments [2]. From (Eq. 1.6), and relating the energy level of an electron (ϵ_i) to the core potential at that level as follows:

$$\epsilon(i) = -V(i)$$

the shift in BE(i) between a free atom and an elemental metal can be given as follows:

$$\Delta BE(i) = (V(i)_{metal} - V(i)_{atom}) - (R^{a}(i)_{metal} - R^{a}(i)_{atom}) - (R^{ea}(i)_{metal} - R^{ea}(i)_{atom})$$

$$\therefore\ \Delta BE(i) = \Delta V(i) - \Delta R^{a}(i) - \Delta R^{ea}(i) \quad (8.1)$$

where ΔV is the change in the atomic core potential due to the change in the valence charge, and R^{a} and R^{ea} are the atomic and extra-atomic relaxation energies. The R^{a} term is assumed to not be affected significantly by the chemical environment of the atom, and the R^{ea} is equal to zero in the case of a free atom [3]. Therefore, the free-atom to metal BE shift (Eq. 8.1) can be rewritten as follows:

$$\Delta BE(i) = \Delta V(i) - R^{ea}(i) \quad (8.2)$$

where $R^{ea}(i)$ is now the extra-atomic relaxation energy in the metal.

The KE of an Auger electron emitted by a process involving (ijj) core levels is:

$$KE(ijj) = BE(i) - BE(jj) \quad (8.3)$$

where $BE(i)$ is the binding energy of a core hole in the atomic level (i), and $BE(jj)$ is the binding energy of the final (jj) two-hole state.

To a first approximation, the extra-atomic relaxation, which is defined as the polarisation of the surrounding environment, can be considered to be proportional to the square of the core hole charge. It follows that:

$$R^{ea}(jj) \sim 4R^{ea}(i) \qquad (8.4)$$

Hence, from (Eq. 8.3), the relaxation energy accompanying the Auger process is expected to be:

$$R^{ea}(ijj) \sim 3R^{ea}(i) \quad (8.5)$$

From (Eq. 8.2) in (Eq. 8.3) and assuming that ΔV is equal for all atomic core levels, the chemical shift of the $KE(ijj)$ between two atomic environments is expected to be:

$$\Delta KE(ijj) \approx \Delta V - \Delta R^{ea} - 2\Delta V + 4\Delta R^{ea} \qquad (8.6)$$

Considering the case of a free-atom to metal shift, (Eq. 8.6) becomes:

$$\Delta KE(ijj) \approx -\Delta V + 3R^{ea}_{metal} \qquad (8.7)$$

Cole and Weightman [2] introduced two types of the Auger parameter (AP) by using different combinations of ΔKE and ΔBE as defined in (Eq. 8.2, 7):

$$\Delta\beta(ijj) \equiv \Delta KE(ijj) + \Delta BE(i) + 2\Delta BE(j) \approx 2\Delta V \qquad (8.8)$$

$$\Delta\xi(ijj) \equiv \Delta KE(ijj) - \Delta BE(i) + 2\Delta BE(j) \approx 2\Delta R^{ea} \qquad (8.9)$$

The first AP (Eq. 8.8) is sensitive to the shift of the core potential of the atomic ground state; hence it can be described as an initial state AP. While the second AP (Eq. 8.9) is sensitive to the shift in the screening of the core hole states and is called the final state AP.

The development of the potential model for interpreting chemical shifts led to the following expression of the potential ($V_{nl}^{valence}$) experienced by the core electron in the nl atomic level, due to the valence charge, q, during the existence of N_{nl} core holes [2]:

$$V_{nl}^{valence}(N_{nl},q) = \int_0^q k(N_{nl},\acute{q})d\acute{q} \qquad (8.10)$$

where:

$$k(N_{nl},q) = a + Nb + dq \qquad (8.11)$$

as described in (Sec. 7.2), omitting the parameters d and e as they are relatively small [3].

Cole and Weightman [2] derived the following expressions which relate the chemical shifts to the valence charge of the ground state, q, expressed in units of $|e|$, and the core hole screening dq/dN through the parameters obtained from the atomic structure calculations (a, b and d):

$$\Delta\xi = \Delta\left\{qb + \frac{dq}{dN}\left[a - 2b + d\left(q - \frac{dq}{dN}\right)\right] + \frac{dV^{ea}}{dN}\right\} \qquad (8.12)$$

$$\Delta\beta = \Delta\left\{2aq + dq^2 - \frac{2}{3}\frac{dq}{dN}\left[2b + d\frac{dq}{dN}\right] + 2V^{ea}\right\} \qquad (8.13)$$

$$\Delta BE = \Delta\left\{\left(a - \frac{b}{2}\right)q + \frac{d}{2}q^2 + \frac{dq}{dN}\left[\frac{b}{3} - \frac{a}{2} + d\frac{dq}{dN}\left(\frac{1}{6} - \frac{q}{2}\right)\right] + V^{ea} - \frac{1}{2}\frac{dV^{ea}}{dN}\right\} \qquad (8.14)$$

$$\Delta KE = \Delta\left\{\left(\frac{3b}{2} - a\right)q - \frac{d}{2}q^2 + \frac{dq}{dN}\left[\frac{3a}{2} - \frac{7b}{3} + d\frac{dq}{dN}\left(\frac{3q}{2} - \frac{7}{6}\right)\right] - V^{ea} - \frac{3}{2}\frac{dV^{ea}}{dN}\right\} \qquad (8.\ 15)$$

where dq/dN is the amount of charge attracted to an atom due to the creation of a core hole, i.e. core-hole screening by conduction electrons. This is equal to zero in a free atom. V^{ea} is the core hole screening by polarisation of the surrounding environment.

Assuming that screening in metals is completely local by attracting conduction electrons to the core ionised atomic site, then:

$$V_{metal}^{ea} = 0 \qquad (8.16)$$

and

$$\frac{dq_{metal}}{dN} = 1 \qquad (8.17)$$

For free-atom to metal shifts (Eq. 8.12-15) are rewritten as follows:

$$\Delta\xi = b\left(q_{metal} - q_{gas}\right) + \frac{dq_{metal}}{dN}\left(a - 2b + dq_{metal}\right) - d\left(\frac{dq_{metal}}{dN}\right)^2 \qquad (8.18)$$

$$\Delta\beta = 2a\left(q_{metal} - q_{gas}\right) + d\left(q_{metal}^2 - q_{gas}^2\right) - \frac{4b}{3}\frac{dq_{metal}}{dN} - \frac{2d}{3}\left(\frac{dq_{metal}}{dN}\right)^2 \qquad (8.19)$$

$$\Delta BE = \left(a - \frac{b}{2}\right)\left(q_{metal} - q_{gas}\right) + \frac{d}{2}\left(q_{metal}^2 - q_{gas}^2\right) + \left(\frac{b}{3} - \frac{a}{2}\right)\frac{dq_{metal}}{dN}$$

$$+d\left(\frac{1}{6} - \frac{q_{metal}}{2}\right)\left(\frac{dq_{metal}}{dN}\right)^2 \qquad (8.20)$$

$$\Delta KE = \left(\frac{3b}{2} - a\right)\left(q_{metal} - q_{gas}\right) - \frac{d}{2}\left(q_{metal}^2 - q_{gas}^2\right) + \left(\frac{3a}{2} - \frac{7b}{3}\right)\frac{dq_{metal}}{dN}$$

$$+d\left(\frac{3q}{2} - \frac{7}{6}\right)\left(\frac{dq_{metal}}{dN}\right)^2 \qquad (8.21)$$

(Eq.8.18-21) can be solved numerically for (q_{metal}, dq_{metal}/dN) If experimental values of the shifts ($\Delta\xi$, $\Delta\beta$, ΔBE or ΔKE) are available as in (Table. 8.1), and “Selection of any two of these equations gives a closed system from which a graphical separation of initial and final state effects can be made” [2]. Physically acceptable values of q and dq/dN for metallic Na, Mg and Zn were determined by Cole and Weightman using this approach [2]. By repeating the calculations of Cole and Weightman they were found to be in error, since the values they reported for the spectroscopic values ($\Delta\xi$, $\Delta\beta$, ΔBE, ΔKE) and the potential parameters (a, b, d) do not result in the same solutions (q, dq/dN) they reported. The graphical solution made by this work is demonstrated in the following section.

8. 2. Empirical determination of dq/dN:

A graphical representation of (Eq.8.18-21) for Na is produced first using the same potential parameters and AP shifts used by [2]. Then, the solution determined by the intersection of the curves of $\Delta\xi$ and $\Delta\beta$ is compared to that obtained by the same reference. The method is then applied to In and Sb.

8.2.1. Na:

(Table. 8.1) lists the values used by [2] to determine q and dq/dN for Na and Mg.

	Na	**Mg**
$\Delta \boldsymbol{BE}\ (\boldsymbol{eV})$	-4.6	-4.8
$\Delta \boldsymbol{KE}\ (\boldsymbol{eV})$	14.3	15
$\Delta \boldsymbol{\xi}\ (\boldsymbol{eV})$	9.7	10.2
$\Delta \boldsymbol{\beta}\ (\boldsymbol{eV})$	0.5	0.6
$\boldsymbol{a}\ (\boldsymbol{V})$	8.81	13
$\boldsymbol{b}\ (\boldsymbol{V})$	-2.91	-2.24
$\boldsymbol{d}\ (\boldsymbol{V})$	2.35	2.91

Table.8.1. The spectroscopic values and the potential parameters of Na and Mg as reported by Cole and Weightman [2].

By substituting the values of a, b, d and $\Delta\xi$ for Na in (Eq.8.18), the following quadratic polynomial results:

$$9.7 = -2.91(q_{metal} + 1) + \frac{dq_{metal}}{dN}(8.81 + 5.82 + 2.35q_{metal}) - 2.35\left(\frac{dq_{metal}}{dN}\right)^2 \qquad (8.22)$$

which was then solved for dq_{metal}/dN at q_{metal} values of ($-2 \leq q_{metal} \leq 0$) with step 0.1 (Table. 8.2). The polynomials resulting from (Eq. 8.19-21) were solved by the same way (Table. 8.2). The procedure was repeated for (Eq. 8.19) at steps of $q = 0.002$ due to the great sensitivity of the initial state AP ($\Delta\beta$) to the ground state charge.

(Fig.8.1) shows that the curves of $\Delta\xi$ and $\Delta\beta$ intersect at $q = -1.14$ and $dq/dN = 0.96$. Cole and Weightman reported the value of q and dq/dN to be -1.11, 1.04 respectively.

$\boldsymbol{q_{metal}}$ $(\boldsymbol{e})$	$\boldsymbol{dq_{metals}/dN}$ $(\boldsymbol{e})$ **from** $\Delta\xi$		$\boldsymbol{dq_{metals}/dN}$ $(\boldsymbol{e})$ **From** $\Delta\boldsymbol{\beta}$		$\boldsymbol{dq_{metals}/dN}$ $(\boldsymbol{e})$ **From** $\Delta\boldsymbol{KE}$		$\boldsymbol{dq_{metals}/dN}$ $(\boldsymbol{e})$ **From** $\Delta\boldsymbol{BE}$	
−2	0.858008	3.367524	i	i	0.267454	1.77561	2.299873	−0.33939
−1.9	0.872663	3.452869	i	i	0.325334	1.794026	2.307803	−0.25953
−1.8	0.886375	3.539157	i	i	0.387846	1.813732	2.313287	−0.16901
−1.7	0.89922	3.626312	i	i	0.455346	1.835085	2.315667	−0.06593
−1.6	0.911265	3.714267	i	i	0.528182	1.858574	2.313979	0.052125
−1.5	0.922574	3.802958	i	i	0.606664	1.884877	2.306751	0.188413
−1.4	0.933206	3.892326	i	i	0.691001	1.914948	2.291584	0.347532
−1.3	0.943211	3.98232	i	i	0.78121	1.950158	2.264207	0.536488
−1.2	0.95264	4.072892	i	i	0.876965	1.992507	2.21586	0.767489
−1.1	0.961535	4.163997	0.602254	1.874342	0.977361	2.044923	2.123067	1.068423
−1	0.969937	4.255595	0.136376	2.34022	1.080625	2.111662	1.796138	1.634713
−0.9	0.977882	4.34765	−0.19485	2.671446	1.183857	2.198699	i	i
−0.8	0.985404	4.440128	−0.47155	2.94815	1.283102	2.313842	i	i
−0.7	0.992532	4.533	−0.71702	3.193618	1.374113	2.466233	i	i
−0.6	0.999296	4.626236	−0.94183	3.418425	1.453709	2.665372	i	i
−0.5	1.00572	4.719812	−1.15181	3.62841	1.520805	2.920638	i	i
−0.4	1.011827	4.813704	−1.35059	3.827181	1.576279	3.242268	i	i
−0.3	1.01764	4.907892	−1.54055	4.017146	1.62204	3.643588	i	i
−0.2	1.023178	5.002354	−1.7234	4.2	1.660156	4.144003	i	i
−0.1	1.028458	5.097074	−1.90039	4.376986	1.692416	4.772976	7.000333	3.556132
0	1.033498	5.192034	−2.07245	4.549044	1.720222	5.576435	10.34448	3.378921

Table. 8.2: The values of dq_{metals}/dN obtained from (Eq.8.18-21) for metallic Na at different values of the ground state charge (q_{metal}). The valence charge of the Na vapour (q_{gas}) was assumed to be always -1. i indicates an imaginary number.

For the ideally expected value of the valence charge of metallic Na atom ($q_{metal} = -1$) (Eq. 8.22) becomes:

$$-2.35\left(\frac{dq_{metal}}{dN}\right)^2 + 12.28\left(\frac{dq_{metal}}{dN}\right) - 9.7 = 0 \qquad (8.23)$$

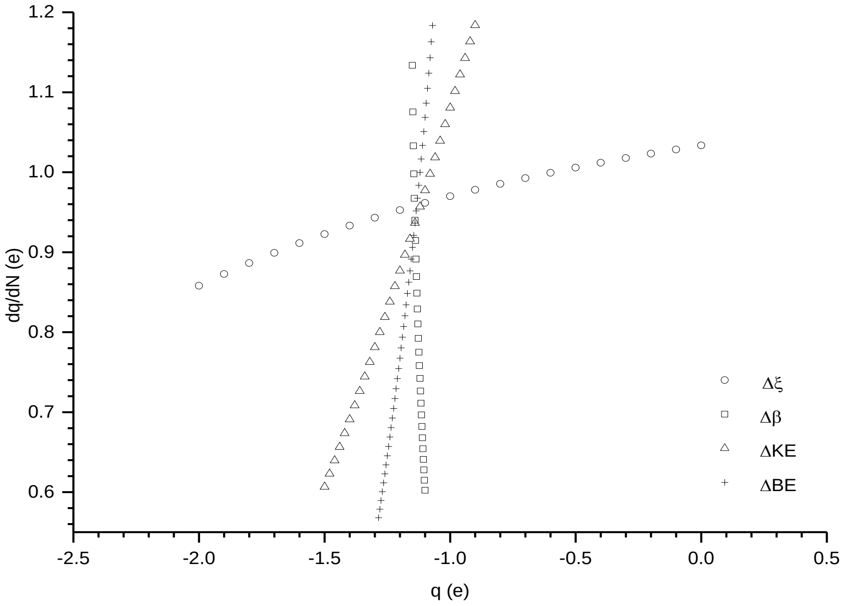

Fig. 8.1: Four plots for the four different relations between q and dq/dN (for Na) represented by (Eq.8.18-21). The values of q and dq/dN were obtained from (Table.8.2) as explained in the text. The point of intersection between the four plots is a graphical solution of the set of equations (Eq.8.18-21). The plot that results from (Eq.8.19) which is represented by (□) shows the great sensitivity of the shift of the initial state AP ($\Delta\beta$) to the ground state charge (q). Small changes to this value results in a big change to the resulting dq/dN value. The opposite is true for the shift of the final state AP ($\Delta\xi$) which is represented by (Eq.8.18). This equation is sensitive to change of dq/dN, a small change of which results in a significant change to the value of q as clear from the (○) plot. The other two plots (+, Δ) represent different solutions of (Eq.8.20, 21) respectively. ΔBE and ΔKE are less sensitive to both q and dq/dN. More importantly, these two shifts are less reliable due to the energy referencing problem [2]. Therefore, the point where □ and ○ plots intersect represents a reliable solution of (Eq.8.18, 19) from which the values of q and dq/dN are obtained. The same method is followed to find q and dq/dN for In and Sb (Fig.8.2,3).

which is a quadratic equation of one variable whose solutions are

$$\frac{dq_{metal}}{dN} = 0.97 \text{ and } 4.26$$

The latter solution is nonphysical so it was discarded.

Similarly to (Eq. 1.51), (Eq. 8.18) can be used to evaluate the compression of the valence wave function in solids [3]. Considering the valence charge of the ground state of free atom and elemental solid to be equal (-1 for Na) and imposing the value of perfect screening in metals ($dq/dN = 1$), (Eq. 8.18) is written as follows:

$$\Delta\xi = qb(\gamma - 1) + \gamma[a - 2b + d(q - 1)] \qquad (8.24)$$

Substituting for $\Delta\xi$ and the potential parameters from (Table. 8.1), γ^{Na} is found to be 0.98. This value is less than one which is nonphysical. This might be due to an error in the values (of $\Delta\xi$ and the potential parameters) reported by [2]. 1.03 is the value reported by [2].

8.2.2. In:

The free-atom to metal shifts of In and Sb reported by [1], as well as the a, b and d potential parameters calculated by this work are listed in (Table. 8.3).

	In	**Sb**
$\Delta\boldsymbol{BE}$ $(\boldsymbol{eV})$	$-3.80(15)$	$-3.90(15)$
$\Delta\boldsymbol{KE}$ $(\boldsymbol{eV})$	$13.1(25)$	$13.10(15)$
$\Delta\boldsymbol{\xi}$ $(\boldsymbol{eV})$	$9.30(29)$	$9.20(21)$
$\Delta\boldsymbol{\beta}$ $(\boldsymbol{eV})$	$1.70(51)$	$1.40(47)$
$\boldsymbol{a}$ $(\boldsymbol{V})$	$12.00(18)$	$14.62(13)$
$\boldsymbol{b}$ $(\boldsymbol{V})$	$-1.29(15)$	$-1.17(10)$
$\boldsymbol{d}$ $(\boldsymbol{V})$	$1.59(07)$	$1.34(03)$

Table.8.3. The free-atom to metal chemical shifts of In and Sb as reported by [1]; and a, b, d potential parameters calculated by this work. The numbers between brackets are the experimental errors in the spectroscopic values, and the standard errors in the potential parameters.

(Eq. 8.18, 19) were solved for In using the parameters in (Table. 8.3) using the same procedure followed for Na in (Sec. 8.2.1).

(Fig. 8.2) shows that the two APs intersect at $q = -2.92 \pm 0.001$ and $dq/dN = 1.16 \pm 0.10$. The uncertainty in the value of q is due to the step in the values of q_{metals} entered in evaluating dq_{metals}/dN. This step was set to 0.1 in (Table. 8.4) to avoid too many data. The uncertainty in dq/dN arises from the experimental uncertainties in $\Delta\xi$ and $\Delta\beta$ values, as well as the standard errors in the values of the potential parameters listed in (Table. 8.3). This

q_{metal}	dq_{metals}/dN **from** $\Delta\xi$		dq_{metals}/dN **From** $\Delta\beta$	
-4	1.30	3.87	i	i
-3.9	1.28	3.98	i	i
-3.8	1.27	4.10	i	i
-3.7	1.25	4.22	i	i
-3.6	1.237832	4.33	i	i
-3.5	1.22	4.44	i	i
-3.4	1.21	4.56	i	i
-3.3	1.20	4.67	i	i
-3.2	1.19	4.78	i	i
-3.1	1.18	4.89	i	i
-3	1.17	5.00	i	i
-2.9	1.16	5.11	0.15	1.47
-2.8	1.15	5.22	-0.55	2.17
-2.7	1.14	5.33	-1.00	2.62
-2.6	1.14	5.43	-1.37	2.99
-2.5	1.13	5.54	-1.69	3.31
-2.4	1.12	5.65	-1.98	3.60
-2.3	1.12	5.75	-2.24	3.87
-2.2	1.11	5.86	-2.49	4.12
-2.1	1.10	5.97	-2.73	4.35
-2	1.10	6.07	-2.96	4.58

Table.8.4. Core hole screening dq/dN of metallic In calculated using (Eq. 8.18, 19) for different values of q_{metal}, whereas q_{gas} is -3. i indicates an imaginary number.

uncertainty was calculated by substituting the values of q and dq/dN in (Eq. 8.25) which results from multiplying (Eq. 8.19) by $-3/2$ and adding the result to (Eq. 8.18):

$$\frac{dq_{metal}}{dN} = \left[\frac{\Delta\xi - \frac{3}{2}\Delta\beta - (b-3a)(q_{metal} - q_{gas}) + \frac{3}{2}d(q_{metal}^{2} - q_{gas}^{2})}{a + dq_{metal}}\right] \qquad (8.25)$$

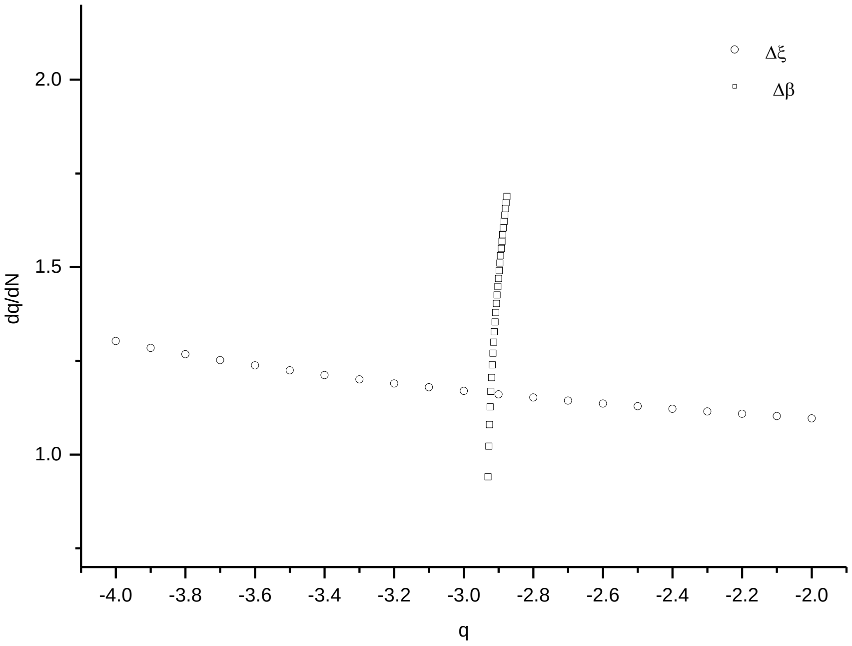

Fig. 8.2: A graphical solution of (Eq. 8.18, 19) for the variables (q, dq/dN) for metallic In. The values plotted for the two variables are listed in (Table. 8.4). The point of intersection between the two plots is the solution of the two equations. The projections of the point are the local charge (q) and the core-hole screening (dq/dN) (see the legend of (Fig.8.1)). The solution was found to be $q = -2.92$ and $dq/dN = 1.16$.

The solid state parameter of In γ^{In} was found from (Eq. 8.24) to be 1.08, which indicates the compression of the wave function of the valence level due to interaction with neighbouring atoms. This was explained in detail (Sec.1.4.2).

8.2.3. Sb:

The value of the core hole screening dq/dN in metallic Sb was determined by solving (Eq. 8.18, 19) in the same way described in (Sec. 8.2.1). (Table. 8.5) lists the values of dq/dN obtained for values of the ground state charge of metallic Sb q_{metal} ranging between -4 and -6 at a step of 0.10. Then repeated for (Eq. 8.19) at step of 0.005 at the range within which it intersects with the solution of (Eq. 8.18) between -4.90 and -5 to account for the greater sensitivity of $\Delta\beta$ to the ground state charge.

q_{metal}	dq_{metals}/dN from $\Delta\xi$		dq_{metals}/dN from $\Delta\beta$	
-6	1.07	5.58	i	i
-5.9	1.07	5.69	i	i
-5.8	1.06	5.79	i	i
-5.7	1.06	5.90	i	i
-5.6	1.06	6.00	i	i
-5.5	1.05	6.10	i	i
-5.4	1.05	6.21	i	i
-5.3	1.05	6.31	i	i
-5.2	1.04	6.41	i	i
-5.1	1.04	6.52	i	i
-5	1.04	6.62	i	i
-4.9	1.03	6.72	-0.12	1.86
-4.8	1.03	6.82	-0.80	2.55
-4.7	1.03	6.93	-1.28	3.03
-4.6	1.03	7.03	-1.68	3.43
-4.5	1.02	7.13	-2.03	3.78
-4.4	1.02	7.24	-2.35	4.09
-4.3	1.02	7.34	-2.64	4.39
-4.2	1.02	7.44	-2.91	4.66
-4.1	1.01	7.54	-3.17	4.92
-4	1.01	7.64	-3.42	5.17

Table.8.5. Core hole screening dq/dN of metallic Sb calculated using (Eq. 8.18, 19) for values of q_{metal} ranging between -4 and -6, whereas q_{gas} is -5. i indicates an imaginary number. dq/dN obtained from (Eq. 8.19) is very sensitive to the ground state charge so it was calculated at a step of q_{metal} equal to 0.005 between $q_{metal} = -4.9$ and -5.

(Fig. 8.3) shows the plots of the solutions of (Eq. 8.18, 19) for Sb. The curve of $\Delta\beta$ (Eq. 8.19) has a discontinuity close to the intersection with the curve of $\Delta\xi$ (Eq. 8.18). The values of the ground state charge q and core hole screening dq/dN were read at the plots (Fig. 8.3) and found to be $\sim -4.95 \pm 0.0025$ and $\sim 1.04 \pm 0.10$. The uncertainties were calculated in the same way described in (Sec. 8.2.2).

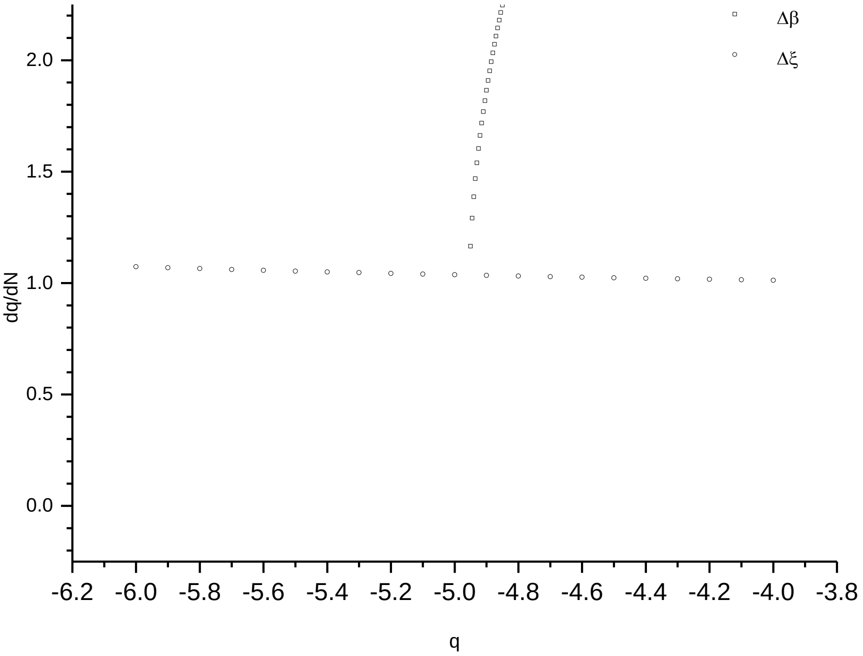

Fig. 8.3: A graphical solution of (Eq. 8.18, 19) for the variables (q, dq/dN) for metallic Sb. The values plotted for the two variables are listed in (Table. 8.5). The point of intersection between the two plots is the solution of the two equations. The projections of the point are the local charge (q) and the core-hole screening (dq/dN) (see the legend of (Fig.8.1)). The curve of $\Delta\beta$ (Eq. 8.19) has a discontinuity close to the intersection with the curve of $\Delta\xi$ (Eq. 8.18). The two curves are close to intersection at $q = -4.95$ and $dq/dN = 1.04$.

The solid state parameter of Sb γ^{Sb} was found from (Eq. 8.24) to be 1.02. This value satisfies the prediction of compression of the valence level in solids, although it is smaller than that obtained for In in the previous section. The explanation of such a difference is that the valence level of Sb is more localised than that of In because of the larger nuclear charge of the former.

8.3. Discussion:

In this chapter, physically meaningful values of local charge (q_{metal}) and core-hole screening (dq/dN) of In and Sb have been obtained using the potential model [2, 3]. Moreover, the calculations showed that the model is capable of producing realistic results of the solid state parameter (γ).

(Table.8.6) lists the values of local charge and screening for Na, In, and Sb. The values calculated for Na (by this work) deviate from those reported by [2] as explained in (Sec.8.2.1). However, the values of screening obtained for In and Sb are close to the prediction made in (Sec.8.1), where core-hole screening in metals was predicted to be solely by the attraction of a free electron (Eq.8.17). Local charge of In and Sb were found to be -2.92 and -4.95 respectively. These values are close to those of a free atom. This is also expected, since the atoms in an elemental solid are similar. So, bonding between them does not involve charge transfer. Explanation of the small deviation of local charges from -3 and -5 for In and Sb requires further consideration to the nature of the valence level wave function and the band structure.

In (Ch.9), application of the potential model is taken further by using it to describe screening in the InSb semiconductor.

	q		dq/dN	
	This Work	**Cole and Weightman**	**This Work**	**Cole and Weightman**
Na	-1.14	-1.11	0.96	1.04
In	-2.92	--	1.16(10)	--
Sb	-4.95	--	1.04(10)	--

Table. 8.6. Ground state charge (local charge) q and core hole screening dq/dN of Na determined using the values of the chemical shifts and potential parameters reported by [2], along with the results reported by the same reference which were found to be in different. q and dq/dN for metallic In and Sb were calculated using the chemical shits reported by [1], and the potential parameters determined by this work (Ch. 7). The numbers between brackets are the values of the errors.

References

1. Aksela, S., et al., *Semiempirical Solid State Shifts in the Auger-and Photoelectron Energies.* Physica Scripta, 1982. **25**(1A): p. 45.
2. Cole, R. and P. Weightman, *Separating ground state and screening contributions to chemical shifts.* Journal of Physics: Condensed Matter, 1994. **6**(29): p. 5783.
3. Cole, R.J., D.A.C. Gregory, and P. Weightman, *Analysis of Auger-parameter and XPS shifts: Application of potential models.* Physical Review B, 1994. **49**(8): p. 5657-5661.

Chapter 9

Core Hole Screening and Charge Transfer in InSb

9.1. Introduction:

It was shown in (Sec.1.2.4) that the shift in the Auger parameter is the most accurate method of probing the difference in the atomic core potential between different chemical states. This was formalised [1] by linking the shift of the Auger parameter to three factors; the difference in the ground state charge Δq, the change in the core hole screening by attracting a free electron $\Delta(dq/dN)$ and the change in the screening by polarisation of the surrounding environment $\Delta(dV^{ea}/dN)$. These three factors are linked to the change in the atomic core potential via the a, b and d parameters described in (Sec.1.4.2) and (Ch. 7) as follows:

$$\Delta\xi = \Delta\left\{qb + \frac{dq}{dN}\left[a - 2b + d\left(q - \frac{dq}{dN}\right)\right] + \frac{dV^{ea}}{dN}\right\} \quad (9.1)$$

In the extreme case of metals or metallic alloys, screening of the core hole is assumed to be completely local by free electron gas ($V^{ea} = 0$ and $dq/dN = 1$), whereas in the case of insulators screening is completely by polarisation of the surrounding environment, and $dq/dN = 0$ [2].

A series of approximations will be followed to solve (Eq. 9.1) in order for the best picture of the core-hole screening and the ground state charge to be reached. The analysis will be applied to indium and antimony as elemental solids and in InSb using the values of the Auger parameter ξ obtained in (Ch. 4, 6) and the potential parameters determined in (Ch. 7).

9.2. Screening analysis:

9.2.1. First approximation: a completely local screening approach:

If a core hole is screened by the attraction of a free electron to the valence level of the core ionised site, then, screening is described to be completely local with no contribution from the surrounding environment:

$$\frac{dV^{ea}}{dN} = 0 \qquad (9.2)$$

and (Eq. 9.1) becomes

$$\Delta\xi = b\Delta q + (a-2b)\Delta\left(\frac{dq}{dN}\right) + d\Delta\left(q\frac{dq}{dN}\right) - d\Delta\left(\frac{dq}{dN}\right)^2 \qquad (9.3)$$

Assuming that both environments are metal-like as described in (Sec. 9.1), then (Eq. 9.3) becomes:

$$\Delta\xi = (b+d)\Delta q \qquad (9.4)$$

Applying (Eq. 9.4) to the chemical shift between metallic In and In in InSb, it becomes:

$$\Delta\xi_{InSb-In} = (b+d)\Delta q_{In} \qquad (9.5)$$

Substituting for $\Delta\xi_{InSb-In}$, b and d from (Table. 9.1):

$$-0.82 = 0.30\Delta q_{In}$$

$$\Delta q_{In} = -2.73$$

Applying the same method to Sb, Δq_{Sb} is found to be -5.41. Where the valence charge (q) and the change in it (Δq) are given in units of $|e|$.

Clearly the application of this complete local screening approximation does not produce physically meaningful results since both elements are predicted to gain substantial amounts of charge on the formation of InSb.

	In	**Sb**
$\Delta\xi$	-0.82 ± 0.09	-0.92 ± 0.09
$\boldsymbol{a}$	12 ± 0.18	14.62 ± 0.13
$\boldsymbol{b}$	-1.29 ± 0.15	-1.17 ± 0.10
$\boldsymbol{d}$	1.59 ± 0.07	1.34 ± 0.03

Table. 9.1. The Auger parameter shifts between elemental In and Sb obtained in (Ch. 4) and InSb (Ch. 6) ($\xi_{InSb} - \xi_{metal}$). a, b and d are the potential parameters obtained in (Ch. 7).

In order to depart from the perfect local screening picture of the core hole to screening by polarisation of the surrounding environment, the concept of the Jost cavity model is introduced.

9.2.2. The Jost cavity model:

The response of a solid medium to the creation of a core atomic hole has been described by the Jost cavity model [3] in which the core ionised site is screened by a charge q'' on a spherical cavity with a radius (R) centred in the ion, in an infinite medium with dielectric constant ϵ (Fig. 9.1). Assuming that the medium was initially unpolarised, the induced charge is described as follows:

$$q'' = \frac{1}{R}(1 - \frac{1}{\epsilon})q' \qquad (9.6)$$

where q' is the core hole charge and ϵ is the dielectric constant of the medium.

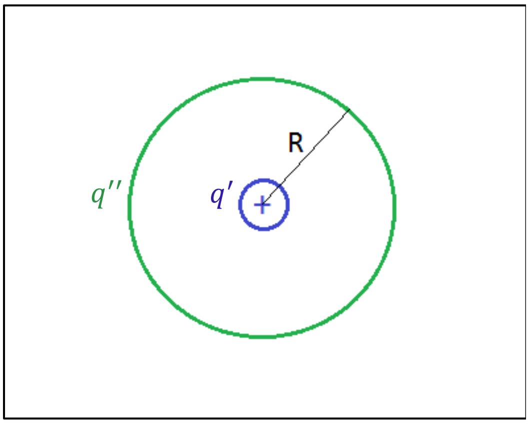

Fig. 9.1. The Jost cavity (green) centred in the ion (blue) with core hole charge q'. q'' is the induced charge at the surface of the cavity.

9.2.3. Second approximation: Screening charge on the outer surface of the ion:

The media in the first approximation were assumed to be metal-like with screening charge attracted to the valence level of the core ionised atom. In this second approximation, screening is still assumed to be local, however the induced charge is assumed to be less than complete but still on the outer surface of the ion. Therefore, applying the Jost cavity model and considering the screening charge to be on the outer surface of the ion, (Eq. 9.6) becomes:

$$\left(\frac{dq}{dN}\right) = 1 - \frac{1}{\epsilon_\infty} \qquad (9.\ 7)$$

where ϵ_∞ is the high frequency optical dielectric constant which is equal to infinity in metals and metallic alloys.

Substituting (Eq. 9.7) in (Eq. 9.3) and substituting the subscript in ϵ_∞ with the relevant symbol of the material results in the following expression of the AP shift:

$$\Delta\xi = b\Delta q - (a-2b)\Delta\left(\frac{1}{\epsilon}\right) + d\left[q_{In}^{InSb}\left(1-\frac{1}{\epsilon_{InSb}}\right) - q_{In}^{metal}\left(1-\frac{1}{\epsilon_{In}}\right)\right] - d\left[\left(\frac{1}{\epsilon_{InSb}^2}-\frac{2}{\epsilon_{InSb}}\right) - \left(\frac{1}{\epsilon_{In}^2}-\frac{2}{\epsilon_{In}}\right)\right] \quad (9.8)$$

$$\Delta\xi = b\Delta q - (a-2b)\Delta\left(\frac{1}{\epsilon}\right) + d\Delta q - d\Delta\frac{q}{\epsilon} - d\Delta\frac{1}{\epsilon^2} + d\Delta\frac{2}{\epsilon} \quad (9.9)$$

$$\Delta\xi = (b+d)\Delta q - (a-2b-2d)\Delta\left(\frac{1}{\epsilon}\right) - d\Delta\left(\frac{q}{\epsilon}+\frac{1}{\epsilon^2}\right) \quad (9.10)$$

Let ϵ equal infinity in the elemental In and Sb, and equal to the reported value of 15.68 in InSb [4]. Then, applying (Eq. 9.10) to In it becomes:

$-0.82 = 0.30\Delta q - 11.4 \times 0.06 - 0.10 q_{In}^{InSb} - 0.01$

$-0.82 = 0.90 + 0.30 q_{In}^{InSb} - 0.68 - 0.10 q_{In}^{InSb} - 0.01$

$-0.82 = 0.21 + 0.20 q_{In}^{InSb}$

$q_{In}^{InSb} = -5.15$

∴ The charge transferred to the In site in InSb $\Delta q_{In} = -2.15$

and applying (Eq. 9.10) to Sb gives:

$\Delta\xi = (b+d)\Delta q - (a-2b-2d)\Delta\left(\frac{1}{\epsilon}\right) - d\Delta\left(\frac{q}{\epsilon}+\frac{1}{\epsilon^2}\right)$

$-0.92 = 0.17\Delta q - 14.28 \times 0.06 - 0.09 q_{Sb}^{InSb} - 0.01$

$-0.92 = 0.17 q_{Sb}^{InSb} + 0.85 - 0.86 - 0.09 q_{Sb}^{InSb} - 0.01$

$-0.92 = 0.08 q_{Sb}^{InSb} - 0.02$

$q_{Sb}^{InSb} = -11.25$

∴ The charge transferred to the Sb site $\Delta q_{Sb} = -6.25$.

The assumption of local onsite screening in InSb thus leads to the contradiction that both sites gain electrons. The values are also unphysically large.

9.2.4. Third approximation:

A third approximation within the local screening model is to assume that the screening in the In and Sb sites in InSb is equal (but unknown). It is also assumed that the screening in the metal site is perfect.

$$\left(\frac{dq}{dN}\right)_{In}^{metal} = \left(\frac{dq}{dN}\right)_{Sb}^{metal} = 1 \qquad \text{(9.11a)}$$

$$\left(\frac{dq}{dN}\right)_{In}^{InSb} = \left(\frac{dq}{dN}\right)_{Sb}^{InSb} \qquad \text{(9.11b)}$$

The values of the charge transfer are equal and opposite:

$$\Delta q_{Sb} = -\Delta q_{In} \qquad \text{(9.11c)}$$

(Eq. 9.3) for In and Sb respectively becomes:

$$-0.82 = -1.29\Delta q_{In} + 14.58\Delta\left(\frac{dq}{dN}\right) + 1.59\Delta\left(q\frac{dq}{dN}\right) - 1.59\Delta\left(\frac{dq}{dN}\right)^2 \qquad \text{(9.12)}$$

$$-0.92 = -1.17\Delta q_{Sb} + 16.96\Delta\left(\frac{dq}{dN}\right) + 1.34\Delta\left(q\frac{dq}{dN}\right) - 1.34\Delta\left(\frac{dq}{dN}\right)^2 \qquad \text{(9.13)}$$

From (Eq. 9.11a,b) in (Eq. 9.12,13):

$$-82 = -1.29\left(q_{In}^{InSb} + 3\right) + 14.58\left(\frac{dq}{dN} - 1\right) + 1.59\left(q_{In}^{InSb}\frac{dq}{dN} + 3\right) - 1.59\left[\left(\frac{dq}{dN}\right)^2 - 1\right] \qquad \text{(9.14)}$$

$$-0.92 = -1.17\left(q_{Sb}^{InSb} + 5\right) + 16.96\left(\frac{dq}{dN} - 1\right) + 1.34\left(q_{Sb}^{InSb}\frac{dq}{dN} + 5\right) - 1.34\left[\left(\frac{dq}{dN}\right)^2 - 1\right] \qquad \text{(9.15)}$$

From (Eq. 9.11c), the ground state charge of Sb atom in InSb is related to that of In as follows:

$$q_{Sb}^{InSb} = q_{Sb}^{metal} + \Delta q_{Sb} = q_{Sb}^{metal} - \Delta q_{In} = -5 - \Delta q_{In} = -5 - \left(q_{In}^{InSb} + 3\right) = -q_{In}^{InSb} - 8 \qquad \text{(9.16)}$$

From (Eq. 9.16), (Eq. 9.15) becomes:

$$-0.92 = -1.17\left(-q_{In}^{InSb} - 3\right) + 16.96\left(\frac{dq}{dN} - 1\right) + 1.34\left[\left(-q_{In}^{InSb} - 8\right)\frac{dq}{dN} + 5\right] - 1.34\left[\left(\frac{dq}{dN}\right)^2 - 1\right]$$

$$= 1.17q_{In}^{InSb} + 3.51 + 16.96\frac{dq}{dN} - 16.96 - 1.34q_{In}^{InSb}\frac{dq}{dN} - 10.72\frac{dq}{dN} + 6.7 - 1.34\left(\frac{dq}{dN}\right)^2 + 1.34$$

$$= 1.17q_{In}^{InSb} - 1.34q_{In}^{InSb}\frac{dq}{dN} + 6.24\frac{dq}{dN} - 1.34\left(\frac{dq}{dN}\right)^2 - 5.41$$

$$\therefore \quad 1.17q_{In}^{InSb} - 1.34q_{In}^{InSb}\frac{dq}{dN} + 6.58\frac{dq}{dN} - 1.34\left(\frac{dq}{dN}\right)^2 - 4.49 = 0 \qquad (9.17)$$

This is a simplified expression of the factors affecting the shift of the potential in the Sb atom core between the metallic state and InSb. It contains two variables which can be determined if a similar equation is produced for In. To do so, (Eq. 9.14) is simplified as follows:

$$-82 = -1.29\left(q_{In}^{InSb} + 3\right) + 14.58\left(\frac{dq}{dN} - 1\right) + 1.59\left(q_{In}^{InSb}\frac{dq}{dN} + 3\right) - 1.59\left[\left(\frac{dq}{dN}\right)^2 - 1\right]$$

$$-82 = -1.29q_{In}^{InSb} - 3.87 + 14.58\frac{dq}{dN} - 14.58 + 1.59q_{In}^{InSb}\frac{dq}{dN} + 4.77 - 1.59\left(\frac{dq}{dN}\right)^2 + 1.59$$

$$= -1.29q_{In}^{InSb} + 14.58\frac{dq}{dN} + 1.59q_{In}^{InSb}\frac{dq}{dN} - 1.59\left(\frac{dq}{dN}\right)^2 - 12.09$$

$$\therefore \quad -1.29q_{In}^{InSb} + 1.59q_{In}^{InSb}\frac{dq}{dN} + 14.58\frac{dq}{dN} - 1.59\left(\frac{dq}{dN}\right)^2 - 11.27 = 0 \qquad (9.18)$$

(Eq. 9.17) is multiplied by 1.186 then added to (Eq. 9.18) to cancel the second term (of $q_{In}^{InSb}\frac{dq}{dN}$). (Eq. 9.17) is rewritten as follows:

$$1.39q_{In}^{InSb} - 1.59q_{In}^{InSb}\frac{dq}{dN} + 7.80\frac{dq}{dN} - 1.59\left(\frac{dq}{dN}\right)^2 - 5.32 = 0 \qquad (9.19)$$

Adding to (Eq. 9.18):

$$-3.18\left(\frac{dq}{dN}\right)^2 + 22.38\frac{dq}{dN} + 0.10q_{In}^{InSb} - 16.59 = 0 \qquad (9.20)$$

This is a quadratic polynomial of $\frac{dq}{dN}$ whose solution is as follows:

$$\frac{-b\pm\sqrt{b^2-4ac}}{2a} = \frac{-22.38\pm\sqrt{500.9+12.72\left(0.10q_{In}^{InSb}-16.59\right)}}{-6.36} = \frac{-22.38\pm\sqrt{289.9+1.27q_{In}^{InSb}}}{-6.36}$$

$$\therefore \quad \frac{dq}{dN} = 3.52 \pm \frac{\sqrt{289.9+1.27q_{In}^{InSb}}}{\sqrt{40.45}} = 3.52 \pm \sqrt{7.17 + 0.03q_{In}^{InSb}} \qquad (9.21)$$

Substituting from (9.21) in (9.18) to find q_{In}^{InSb}:

$$-1.29q_{In}^{InSb} + 1.59q_{In}^{InSb}\left(3.52 \pm \sqrt{7.17 + 0.03q_{In}^{InSb}}\right) + 14.58\left(3.52 \pm \sqrt{7.17 + 0.03q_{In}^{InSb}}\right) -$$

$$1.59\left(3.52 \pm \sqrt{7.17 + 0.03q_{In}^{InSb}}\right)^2 - 11.27 = 0$$

$$-1.29q_{In}^{InSb} + 5.60q_{In}^{InSb} \pm 1.59q_{In}^{InSb}\sqrt{7.17 + 0.03q_{In}^{InSb}} + 51.32 \pm 14.58\sqrt{7.17 + 0.03q_{In}^{InSb}} -$$

$$1.59\left(12.39 + 7.17 + 0.03q_{In}^{InSb} \pm 7.04\sqrt{7.17 + 0.03q_{In}^{InSb}}\right) = 0$$

$$4.26q_{In}^{InSb} + 20.22 + \left(1.59q_{In}^{InSb} + 3.39\right)\sqrt{7.17 + 0.03q_{In}^{InSb}} = 0$$

$$\left(4.26q_{In}^{InSb} + 20.22\right)^2 = \left[-\left(1.59q_{In}^{InSb} + 3.39\right)\sqrt{7.17 + 0.03q_{In}^{InSb}}\right]^2$$

$$18.15\left(q_{In}^{InSb}\right)^2 + 172.27q_{In}^{InSb} + 408.8 = \left(1.59q_{In}^{InSb} + 3.39\right)^2\left(7.17 + 0.03q_{In}^{InSb}\right)$$

$$18.15\left(q_{In}^{InSb}\right)^2 + 172.27q_{In}^{InSb} + 408.8 = \left[2.53\left(q_{In}^{InSb}\right)^2 + 10.78q_{In}^{InSb} + 11.49\right]\left(7.17 + 0.03q_{In}^{InSb}\right)$$

$$18.15\left(q_{In}^{InSb}\right)^2 + 172.27q_{In}^{InSb} + 408.8 = \left[18.14\left(q_{In}^{InSb}\right)^2 + 0.08\left(q_{In}^{InSb}\right)^3 + 77.29q_{In}^{InSb} + 0.32\left(q_{In}^{InSb}\right)^2 + 82.38 + 0.34q_{In}^{InSb}\right]$$

$$0.08\left(q_{In}^{InSb}\right)^3 + 0.31\left(q_{In}^{InSb}\right)^2 - 94.64q_{In}^{InSb} - 326.4 = 0 \qquad (9.22)$$

The physically meaningful solution of this equation was found numerically to be -3.44 ,

$\therefore$ $q_{In}^{InSb} = -3.44$ and from (Eq. 9.16) $q_{Sb}^{InSb} = -4.56$

$\therefore$ $\Delta q_{In}^{InSb} = -0.44$ and $\Delta q_{Sb}^{InSb} = +0.44$

This predicts that charge is transferred from Sb to In in InSb which is contrary to that expected from the electronegativity of the two atoms.

Substituting the value of q_{In}^{InSb} in (Eq. 9.21), the value of $\frac{dq}{dN}$ was found to be 0.86 or 6.18. The latter value is not physically meaningful. The 0.86 value indicates that as expected the on-site screening is less efficient in InSb than in the metals. (Eq. 9.21) shows that, in this approximation, the value of the ground state charge does not significantly affect the value of screening.

9.2.5. Fourth approximation: Screening in InSb is extra-atomic:

In this approximation, screening in InSb is assumed to be by polarisation of the surrounding environment, while the screening in the metallic In and Sb remains completely local. This means that as previously:

$$\left(\frac{dq}{dN}\right)_{In}^{metal} = \left(\frac{dq}{dN}\right)_{Sb}^{metal} = 1 \qquad (9.23)$$

It is also assumed that the In and Sb sites in InSb are screened equally. To describe the polarisation energy in InSb (the contribution to the AP shift by the relaxation of the medium surrounding the core ionised atom) the Jost cavity model is applied by considering the screening charge to be at a distance (R) from the ion whether this is In or Sb. Then, (Eq. 9.6) becomes:

$$\left(\frac{dV^{ea}}{dN}\right)_{InSb} = \frac{1}{4\pi\varepsilon_0}\frac{e}{R}\left(1-\frac{1}{\epsilon}\right) \qquad (9.24)$$

e is the hole charge which is equal to 1 in the atomic units, ε_0 is the permittivity of free space, ϵ is the dielectric constant of the medium. Using the atomic units, (Eq. 9.24) becomes:

$$\left(\frac{dV^{ea}}{dN}\right)_{InSb} = \frac{1}{R}\left(1-\frac{1}{\epsilon}\right) \qquad (9.25)$$

hence, the extra-atomic relaxation energy in eV is:

$$\left(\frac{dV^{ea}}{dN}\right)_{InSb} = 27.21\frac{1}{R}\left(1-\frac{1}{\epsilon}\right) \qquad (9.26)$$

From (Eq. 9.23), (Eq. 9.1) becomes:

$$\Delta\xi = b\Delta q + \left(\frac{dV^{ea}}{dN}\right)_{InSb} - [a - 2b + d(q_{metal} - 1)] \qquad (9.27)$$

Substituting from (Eq. 9.26) into (Eq. 9.27), the following expressions are obtained for In and Sb respectively:

$$-0.82 = -1.29\Delta q_{In} + \frac{27.21}{R_{In}^{InSb}}\left(1-\frac{1}{15.68}\right) - 8.22 \qquad (9.28)$$

$$-0.92 = -1.17\Delta q_{Sb} + \frac{27.21}{R_{Sb}^{InSb}}\left(1-\frac{1}{15.68}\right) - 8.92 \qquad (9.29)$$

where the chemical shift between the metallic environment and InSb is linked to the change of the ground state charge and the screening length around the core-ionised atom in InSb. To solve (Eq. 9.28, 29) it is necessary to make approximations.

a) Assuming zero charge transfer between In and Sb atoms in InSb ($\Delta q_{In} = \Delta q_{In} = 0$), (Eq. 9.28) is reduced to:

$$-0.82 = \frac{27.21}{R_{In}^{InSb}}\left(1 - \frac{1}{15.68}\right) - 8.22$$

$$-0.82 = \frac{25.47}{R_{In}^{InSb}} - 8.22$$

$$\therefore R_{In}^{InSb} = 3.44\, Bohr = 1.82\ \text{Å}$$

Similarly for Sb from (Eq. 9.29):

$$-0.92 = \frac{27.21}{R_{Sb}^{InSb}}\left(1 - \frac{1}{15.68}\right) - 8.92$$

$$-0.92 = \frac{25.47}{R_{Sb}^{InSb}} - 8.92$$

$$R_{Sb}^{InSb} = 3.18\, Bohr = 1.68\ \text{Å}$$

This approximation simplifies the equations but unreasonably assumes that there is no charge transfer. It predicts that screening is significantly non-local and slightly larger for the In site than for the Sb site in InSb.

b) We now make the reasonable assumption that the changes of valence charge of In and Sb are equal and opposite. This makes it possible to solve (Eq. 9.28 and 29):

$$\Delta q_{In} = -\Delta q_{Sb} \qquad (9.30.a)$$

and that the screening lengths (the radii of the Jost cavity) around both core-ionised atoms are equal:

$$R_{In}^{InSb} = R_{Sb}^{InSb} \qquad (9.30.b)$$

Then, (Eq. 9.28,29) are rewritten as follows:

$$-0.82 = -1.29\Delta q_{In} + \frac{27.21}{R^{InSb}}\left(1 - \frac{1}{15.68}\right) - 8.22 \qquad (9.31)$$

$$-0.92 = 1.17\Delta q_{In} + \frac{27.21}{R^{InSb}}\left(1 - \frac{1}{15.68}\right) - 8.92 \qquad (9.32)$$

Multiplying (Eq. 9.32) with 1.103 and adding to (Eq. 9.31):

$$-1.83 = \frac{53.57}{R^{InSb}} - 18.06$$

$$R^{InSb} = 3.30 \pm 0.10\, Bohr = 1.75 \pm 0.05\ \text{Å}$$

Substituting for R^{InSb} in (9.31):

$$-0.82 = -1.29\Delta q_{In} + 7.72 - 8.22$$

$$\therefore \Delta q_{In} = 0.25 \pm 0.41$$

and from (Eq. 9.30a):

$$\Delta q_{Sb} = -0.25 \pm 0.41$$

where the unit of the charge transfer is $|e|$ as described in (Sec. 9.2.1).

The great uncertainty on the value of the charge transfer (Δq) is due to the large standard errors on the values of the potential parameters (Table.9.1). Using (Eq.9.32) to obtain the value of Δq results in a slightly smaller uncertainty (± 0.34) because this equation was derived for the Sb atom whose potential parameters have smaller errors.

Comparing these values of charge transfer with the values obtained by the first and second approximations shows “that in environments of limited screening efficiency it is dielectric differences that may dominate $\Delta\xi$ rather than ground-state charge transfer, although of course the two processes are not totally uncorrelated” [2]. (Table. 9.2) lists the values of the charge transfer $|\Delta q|$ and screening length R calculated from (Eq. 9.31, 32) for different values of the dielectric constant. It shows that the charge transfer is an atomic property which is insensitive to the environment, whereas the screening length is weakly related to the environment (Graph.9.1).

ϵ	$\lvert\Delta q\rvert$	R(Å)
14	0.246	1.732
15	0.246	1.741
16	0.246	1.749
17	0.246	1.756
18	0.246	1.762

Table. 9.2. $|\Delta q|$ and R in InSb calculated for different values of ϵ using (Eq. 9. 31,32).

Describing the screening in InSb in terms of extra-atomic relaxation clearly gives sensible estimates of the charge transfer between In and Sb atoms and the screening length around the core ionised sites. The relations between these results and the other structural properties of InSb are analysed in the following section.

9.3. Analysis of the electronic properties of InSb:

The zinc blend structure of InSb (Fig. 9.2) has a lattice parameter (a) of 6.479 Å [5]. The basis consists of two tetrahedrally bonded atoms, so that if an In atom is on the origin (0,0,0), there is an Sb atom at $(1/4,\ 1/4,\ 1/4)$ in the units of the lattice parameter.

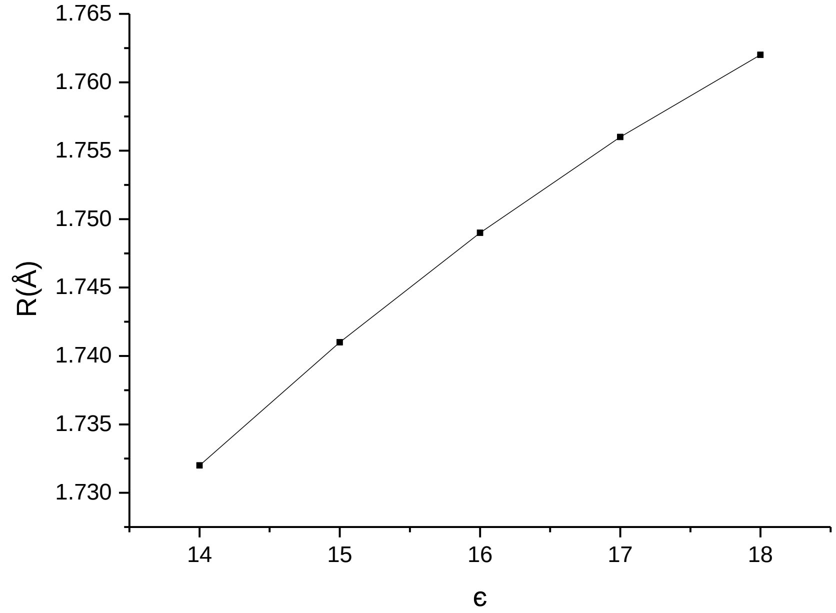

Graph. 9.1. The screening length in InSb (R) calculated for different values of ϵ using (Eq. 9, 31, 32). This shows the little sensitivity of R to the change in the dielectric constant.

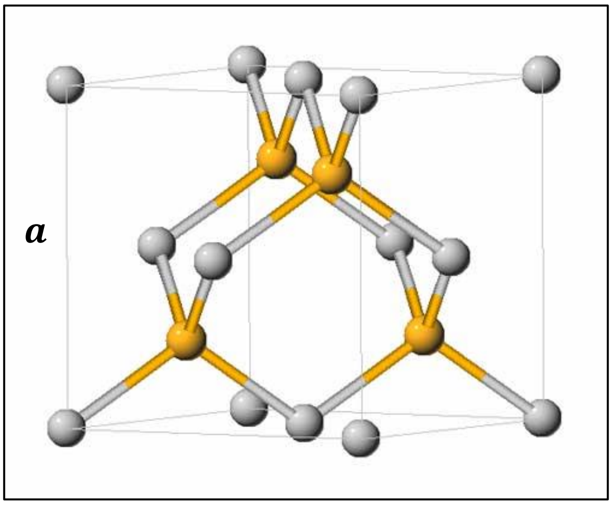

Fig. 9.2: Zinc blende structure which is an fcc lattice where the basis consists of two different atoms bounded tetrahedrally. Source of the picture: www.ciss.iis.u-tokyo.ac.jp

The nearest neighbours of an atom are at a distance of $\frac{\sqrt{3}}{4}a$ which is equal to 2.81 Å in the undoped InSb.

The value found for charge transfer of 0.25 ± 0.41 from In to Sb in InSb agrees with the direction of charge transfer deduced from the intensity of quasi-forbidden x-ray reflections from InSb crystals [6] and is in reasonable agreement with the magnitude of the charge transfer, 0.16 electrons [7] deduced from such studies, given how differently this property is defined in the x-ray diffraction work.

It is clear from the analysis of (Sec. 9.2.3, 4) that the assumption of on-site screening in InSb, $dq/dN = 1$, fails to yield reasonable results. This is in keeping with the expectation that due to the low number of charge carriers the screening length in semiconductors is significantly longer than in metals. The analysis of (Sec. 9.3.5) was based on the assumption of non-local, but equal screening, of In and Sb sites in InSb and gave a screening length of 1.75 ± 0.05 Å. This is $\sim 20\%$ larger than half the inter-nuclear distance in InSb. This off-site screening of core holes is expected to arise from contributions from the low concentration of charge carriers and the polarisation of the nearest neighbour ions.

9.4. Conclusion:

It has already been shown that the potential model [1] gives reasonable results of screening in metals [8]. (Ch.8) showed that the model is also able to describe the contraction of the valence level in metals. This chapter took the model further by applying it to a compound semiconductor which, unlike pure metals, involves charge transfer between different atoms, as well as a complicated core hole screening mechanism.

Obtaining reasonable results of charge transfer and screening length in InSb (Sec.9.3) establishes the potential model as a method of analysing the electronic structures of materials using electron spectroscopy. Potential applications of such a model were discussed in (Sec.1.5). Concluding remarks are made in (Ch.10).

References

1. Cole, R.J., D.A.C. Gregory, and P. Weightman, *Analysis of Auger-parameter and XPS shifts: Application of potential models.* Physical Review B, 1994. **49**(8): p. 5657-5661.
2. Waddington, S.D., et al., *Charge transfer and core-hole screening in PbTe.* Physical Review B, 1989. **39**(14): p. 10239-10245.
3. Briggs, D. and J.T. Grant, *Surface analysis by Auger and x-ray photoelectron spectroscopy*. 2003, Chichester, West Sussex, U.K.: IM Publications. xi, 899 p.
4. Palik, E.D. and G. Ghosh, *Handbook of optical constants of solids*. 1998, San Diego: Academic Press.
5. Kasap, S.O. and P. Capper, *Springer handbook of electronic and photonic materials*. 2006, New York: Springer. xxxii, 1406 p.
6. Saravanan, R., S. Mohanlal, and K. Chandrasekaran, *Anomalous dispersion effects, anharmonic thermal vibrations and bonding charges in indium antimonide.* Journal of Physics and Chemistry of Solids, 1991. **52**(7): p. 879-886.
7. Bilderback, D. and R. Colella, *X-ray determination of valence-electron charge density and its temperature dependence in indium antimonide.* Physical Review B, 1976. **13**(6): p. 2479.
8. Cole, R. and P. Weightman, *Separating ground state and screening contributions to chemical shifts.* Journal of Physics: Condensed Matter, 1994. **6**(29): p. 5783.

Chapter 10
Conclusion

10.1. Overall achievement:

Despite the advancement of the instrumentation of electron spectroscopy in the second half of the twentieth century [1, 2], and the great deal of research on the interpretation of spectroscopic results, no definitive model has been established to harness the capability of Auger and photoelectron spectroscopy of probing the electronic structure of materials [3-6].

In this work the electronic structure of InSb has been investigated by interpreting shifts in the photoelectron and Auger electron energies of transitions involving atomic core levels in terms of a model of the potential in the atomic core [7] which is parameterised using the results of atomic structure calculations. Unlike treatments based on the results of empirical scales of electronegativity and ionicity [8, 9], this puts the treatment of charge transfer on a firm quantum mechanical basis [10]. However, in interpreting the results of this analysis it is important to remember that the values of the charge transfer and electron screening deduced from the model refer to their influence on the potential in the core of the atoms [7, 11].

10.2. How can this work be used for future projects?

(Ch.1) provides the knowledge needed for understanding the theory of the x-ray excited Auger and photo-electron spectroscopy. It, also, provides the full basic atomic structure theory underlying the electron spectroscopy and the theoretical calculations using the MCDFGME program [12].

The potential model, that links the shift of the Auger parameter to the electronic structure of matter, is explained in (Ch.1) and formulated for In and Sb atoms in (Ch.7).

(Ch.3) demonstrates how the MCDFGME program is run, and how its output is interpreted through various In and Sb atomic structure calculations.

(Ch.4-6) contains thorough analysis of electron spectroscopic data of elemental solids (In and Sb) and of compounds (InSb).

(Ch.8) shows how the potential model is applied to describe screening and valence level contraction in metals.

(Ch.9) shows how different scenarios of core-hole screening are drawn to interpret the chemical shifts of elements from their elemental states and their states in a compound semiconductor (InSb).

10.3. Suggestions for further research:

This work has established a new approach to the study of the electronic structure of semiconductors. There are two obvious extensions to further work. One is to investigate the variation of the screening length with doping level in a particular compound. This would provide insight into the screening of impurities in semiconductors. The second is to extend the approach to the III-V and II-VI systems. This latter systematic approach would make it possible to compare the screening response in different compounds and investigate how variations in the polarisation of ions contributed to the screening length in compounds with a significant mismatch in the size of ions.

In general the approach developed here should yield fundamental insights into the factors controlling the electronic structure and behaviour of semiconductor devices.

References

1. Briggs, D. and J.T. Grant, *Surface analysis by Auger and x-ray photoelectron spectroscopy*. 2003, Chichester, West Sussex, U.K.: IM Publications. xi, 899 p.
2. Weightman, P., *X-ray-excited Auger and photoelectron spectroscopy.* Reports on Progress in Physics, 1982. **45**(7): p. 753.
3. Wagner, C. and A. Joshi, *The auger parameter, its utility and advantages: a review.* Journal of electron spectroscopy and related phenomena, 1988. **47**: p. 283-313.
4. Moretti, G., *Auger parameter and Wagner plot in the characterization of chemical states by X-ray photoelectron spectroscopy: a review.* Journal of electron spectroscopy and related phenomena, 1998. **95**(2): p. 95-144.
5. Moretti, G., *The Wagner plot and the Auger parameter as tools to separate initial- and final-state contributions in X-ray photoemission spectroscopy.* Surface Science, 2013. **618**: p. 3-11.
6. Cole, R., B. Macdonald, and P. Weightman, *Relative core level shifts in XPS: a theoretical study.* Journal of electron spectroscopy and related phenomena, 2002. **125**(2): p. 147-152.
7. Cole, R.J., D.A.C. Gregory, and P. Weightman, *Analysis of Auger-parameter and XPS shifts: Application of potential models.* Physical Review B, 1994. **49**(8): p. 5657-5661.
8. Phillips, J., *Dielectric definition of electronegativity.* Physical Review Letters, 1968. **20**(11): p. 550.
9. Phillips, J., *Bonds and bands in semiconductors*. 2012: Elsevier.
10. Jackson, M., et al., *Potential parameters for analysis of chemical shifts for the elements Lithium to Argon.* Journal of electron spectroscopy and related phenomena, 1995. **72**: p. 261-266.
11. Cole, R., J. Matthew, and P. Weightman, *Extra-atomic relaxation energy calculations using an extended potential model.* Journal of electron spectroscopy and related phenomena, 1995. **72**: p. 255-259.
12. Desclaux, J. and P. Indelicato, *The relativistic atomic program MCDFGME V 2005.10.* Published at http://dirac. spectro. jussieu. fr/mcdf/on August, 2005. **17**: p. 2005.